Manipulating Wavepacket Dynamics with Half-Cycle Pulses

Jason George Zeibel
Charlottesville, Virginia

B.S. Duke University, May 1997
M.A. University of Virginia, May 2001

A Dissertation presented to the Graduate Faculty
of the University of Virginia in Candidacy for the Degree of
Doctor of Philosophy

Department of Physics

University of Virginia
May 2003

_____

_____

_____

_____

Abstract

Novel electronic wavepackets have been created and probed through multistep laser excitations and electric field pulse interactions. Three experiments are presented here, each of which uses a half cycle pulse of THz radiation (HCP) as a tool for manipulating wavepacket dynamics. In the first experiment, a HCP field recombines a continuum electron with a nearby ion in the presence of a static field. The relative alignment of the HCP and the static field turns out to be a crucial factor in determining recombination rates. In a second experiment, a HCP influences the rate of autoionization (AI) in a doubly excited Rydberg state. Some suppression of the AI rate is observed due to HCP redistribution of the Rydberg population. In the final experiment, the time dependent momentum space probability distribution of a recombined electronic wavepacket is measured by observing the response of the recombined wavepacket to a HCP field. A highly localized three dimensional electronic wavefunction is created through the recombination process and the dynamics of this distribution are measured. A new technique of lock-in impulse momentum retrieval (IMR) is developed to improve signal to noise in the recovered momentum distribution. Both classical and quantum mechanical simulations are performed which reproduce measured spectra.

Contents

List of Tables

List of Figures

Chapter 0

Acknowledgments

Just trying to think about all the people that have helped me along the way to this point in my life is difficult. First and foremost, I must thank my Mom and Dad. Without your support for the last 27 years, none of this would have been possible. You guys are awesome!

Thanks must also go to my grandparents: Don and Jane Sterrett and George and Florence Zeibel. I have been incredibly blessed to have all four of you in my life pushing me along... sometimes gently, sometimes not so. Your love and support has meant a lot to me. I also want to thank Joe Mozer... you were like a grandfather to me and that meant a lot. Expect me to visit as soon as I can find a plane back to the islands!

Thanks to the St. Thomas Montesorri school for instilling in me a love of numbers. Thanks to Dr. Bill Cross for instilling in me a love of mathematics. Thanks to Mona Hedrick for instilling in me a love of physics. None of you knew it at the time, but you each played a major role in my career path.

To my oldest friend Judd, 5^{th} grade seems so long ago. Have we really been friends for 18 years now? I'm really glad we finally got that trip to Spain together. Hopefully you can finally find a nice girl down there in Winston-Salem. To Chris, I finally made it to my Ph.D.... hah! Just remember that when all else fails, we'll still have llove and llamas. To Amy, I owe you a visit or two back to Durham to reminiss about the good ol' TIP days. Thanks for your support through my four years at the Gothic Wonderland. To Marlo, thanks for talking me into grad school. You're going to be the best pediatrician ever! Just watch out for Peter...

To all my friends in TAWVFCI/OP(?)MPB&CSRU!!!, thanks for six years of extending my college lifestyle. From day one, you guys made me feel at home. Its hard to

believe that I am now the old sketchy guy. Beth, despite making me wait two months to meet you, it was worth it. Good luck with that whole Econ thing. Renee, you made me smile when I needed it most. Derek, sorry about breaking your nose... it was an accident. Dan, sorry about breaking your ankle... it was an accident. Ian and Wendy, you guys rock. Thanks for all the fun times. Let's try not to live too far apart. Jenner, count on Audra and me visiting you many more times. Greg, Tony, and Tom, thanks for always saving a spot for me at wings. To my band family, carry on my traditions. Look for me and my sax to wander by every now and then.

Next, I want to thank my girlfriend of these last five years, Audra Burchfield. You listened to me when I was frustrated, calmed me when I was upset, laughed with me when I was funny (or funny looking as the case may be), and supported me thoughout everything. I don't know if I would have made it to this point without you, but I know that without you I wouldn't have enjoyed it. Therefore, I'll just say that writing this thesis started with you. You are 1 in 1×10^6.

This work was made a lot easier by all the amazing folks in the Physics Department. Thank you Suzie, Brenda, Tammie, Pam, Teresa, Beverly, Faye, Lucille, Bobby, Chris, and Harvey for your help with everything imaginable. You guys are the ones that are really in charge here. Thanks Jim for the library help, as well as the countless discussions about women's ACC basketball. Thanks Shawn and Bryan for always bailing me out of my computing conundrums.

Tom and Matt, thanks for making sure I survived my first year in the lab. You both are great teachers. Supriya, thanks for getting me through the quals and making me laugh when I needed it most. Eric, your patience for my rambling amazes me. Thanks for all the thoughtful discussions and especially for the help editing this thesis. You are going to make a great professor. Thanks to John, Shella, Tim, Cherice, Wenhui, Merrick, Victor, Fred, Warren, Michael, and many others for the help with six years of physics learning. A big thanks to my labmate Santosh. I've always been amazed by how quickly physics comes to you. I've also been amazed at how fast you can crash a computer. Your friendship the past six years has meant a lot to me. To Dan, Jeremy, and Brett: keep an open mind and remember to always question what was done previously. Its a great lab to work in, so have fun with it.

Thanks to Dr. Tom Gallagher for introducing me to the Society of Fellows and for your straightforward approach to atomic physics. Thanks to Dr. Michael Fowler for your support and for letting me help with the stereo. Thanks to Dr. Blaine Norum for selling me on UVA.

Finally, I want to express my sincere thanks to Dr. Bob Jones. I am consistently amazed by your ability to figure out what is wrong with an experiment in 30 seconds or less. Thank you for putting up with all my questions and for teaching me how to be an experimentalist. Now, if I can only convince you that GENPLOT can't do everything. This work has been supported by the AFOSR, the NSF, and the Packard Foundation.

Chapter 1

Introduction and Motivation

In the time since the days of Democritus, man has been fascinated with the atom. For nearly 2000 years, the fascination was considered "philosophy" as no methods existed to directly investigate individual atoms. That all changed with the discovery of the electron in 1897. Since that point, the field of atomic physics has evolved into one of the most investigated areas in all of science. Developments such as the laser and the transistor both have their roots firmly in atomic physics and many new developments are on the horizon.

Current research in atomic physics focuses largely on the response of atomic systems to electromagnetic fields. The electromagnetic fields used in these studies come from a variety of sources. Examples include externally applied fields (like from a laser or pulse generator) as well as fields from other passing atoms or from the atom itself.

The response of an atom to these fields is of significant interest due to the inherent electromagnetic structure of the atom. As experimental advances are made in the types of electromagnetic fields which can be produced, new discoveries are made in how atomic systems respond when exposed to the new fields. Furthermore, the atomic response to new and novel types of electromagnetic fields can be used to characterize properties of the field itself.

The response of atomic systems to electromagnetic fields can be measured from two different points of view. From the discovery of quantized electron energy levels up through the 1980s, the prevailing picture of the atom was taken from the frequency domain. Experiments proceeded by shining specific colors of light upon a given atom and measuring how much of the light was absorbed. Since the energy corresponding to a given frequency of light is known, the energy spacing between levels can be determined. If an atom did absorb a given color of light, then it was known that the atom must be in an excited state. Furthermore, the atom must then contain a given amount of energy above its ground state. Such measurements are known as frequency domain spectroscopic measurements. With the invention of narrow bandwidth lasers in the 1960s and 1970s, it became possible to perform spectroscopic measurements in precise detail and determine the positions of the energy levels of any given atom very exactly.

With the introduction of very short laser pulses in the mid 1980s, it became possible to start looking at atomic systems in the time domain. In typical time domain

spectroscopy, an electromagnetic field interacts with an atom at some known time. The field may contain many different frequencies which each excite slightly different states of the atom. Therefore, after interaction the atom takes on time dependent or "non-stationary" characteristics. A variable time delay after the initial field interaction, a short field pulse probes the state of the system. By varying the time delay of the probe, the time evolution of the system can be measured. For time domain spectroscopy to be most effective, the electron being measured must move very little during the time the probe pulse interacts with it. This requirement is why advances in time-domain spectroscopy have coincided with the development of extremely short laser pulses. Since the shortest pulses are still several atomic units long, time domain spectroscopy usually focuses on excited states of atoms. The properties of excited atoms will be discussed in the following section.

Even though the atomic response is measurable with both frequency-domain and time-domain techniques, certain experiments which are technically impossible through frequency domain spectroscopy become much simpler in the time domain [1]. Furthermore, time domain spectroscopy is very closely related to the classical concept of following the trajectory of an orbiting electron [2]. This typically produces a more intuitive understanding of the time domain measurements.

The main goal of this thesis is to develop methods to control atomic processes and manipulate wavepackets. To this end, we use time domain spectroscopy to measure

the response of an atom to changes in its environment. In each experiment presented, combinations of time dependent electromagnetic fields are applied which alter the surroundings of an atomic system in some manner. Through these fields, we are able to exert control over the evolution of an atomic system. Both extremely short optical pulses and unipolar bursts of terahertz electromagnetic radiation are used as control pulses. The subsequent time evolution of the system is then probed with time-domain spectroscopic techniques to characterize the effects generated by the time dependent fields. Information about the fields themselves is also recovered from the measured atomic responses.

We are able to specify the properties of the control pulses in each experiment. This can be done in a repeatable manner. By applying these fields, we are able to control several atomic processes. Some examples which are presented in this work are: simulated atomic collisions (chapters 4 and 6), configuration interactions (chapter 5), and wavepacket localization (chapters 6 and 7). Many other areas may also be studied with the techniques developed here. These include the areas of quantum control [3] and quantum information [4].

1.1 The Alkali Rydberg Atom

Scientists tend to study the simplest possible system which exhibits a certain property of interest. From there, results are extended to more complex systems. In atomic

physics, the simplest system to study is the neutral hydrogen atom. Some of the first experimental atomic physics was done with hydrogen, and certainly much of theoretical atomic physics begins with the hydrogen atom. In general however, hydrogen is experimentally difficult to work with.

To investigate atomic structure of hydrogen, its electron must be transferred from the ground state to some higher lying excited state. The field free energy levels of hydrogen are given by

$$E(n) \;=\; \frac{-13.6\ eV}{n^2}\ , \tag{1.1}$$

where n is the principle quantum number of the n^{th} energy level. The first excited state of hydrogen lies 10.2 eV above the ground state. To perform a photoexcitation from the ground state of hydrogen to the first excited state requires 10.2 eV of energy, corresponding to a ultraviolet light pulse with a wavelength of 121.6 nm. The generation and manipulation of coherent light with such short wavelengths presents a daunting experimental obstacle. Furthermore, hydrogen typically comes as a diatomic molecular gas. Creating a sample of monatomic hydrogen can done in various ways (for example, by colliding a proton beam with an atomic or molecular target [5] or with RF discharge techniques). However, the experimental complexities in creating monatomic hydrogen add an unwelcome level of difficulty prior to beginning the study of any electron dynamics. Despite these difficulties, the isolated hydrogen atom has been studied extensively over the past 100 years and its dynamics are fairly well understood both

theoretically and experimentally.

We then turn our focus to the alkali earth elements. We choose alkali earth elements instead of the alkalis due to the two valence electrons. The complexity of the electron - electron interactions in a non-hydrogenic system is of much interest. Furthermore, alkali earth elements have relatively small binding energies and are readily available in monatomic form. Compared to hydrogen, the alkali earth elements can be optically excited quite easily. For example, an excited state of calcium lies only 2.93 eV above the ground state. A 423 nm photon generated from a easily obtainable dye laser can populate this state (and does so in each of the experiments in this thesis). Furthermore, with two optically accessible valence electrons alkali earth elements provide a nice system for investigating the effects of varying external field environments on electron - electron dynamics. In the work presented here, we use an alkali earth system (specifically calcium) to investigate the effect of time dependent electromagnetic fields on both atomic dynamics in general and electron - electron dynamics in specific.

In a each experiment performed in this thesis, ground state electrons are photoexcited to high lying states with $n > 20$. Such highly excited electrons are known as Rydberg electrons [6]. The orbital period of a Rydberg electron is very large when compared with either the orbit time of a ground state electron or the duration of the current shortest ultrafast laser pulses. This property will be exploited in each experiment presented in this work. Several other properties of Rydberg electrons also make

Property	n **dependence**	$n = 1$	$n = 35$
Binding Energy	$-1/2n^2$	-109737.3 cm^{-1}	-89.58 cm^{-1}
Energy Between Adj. States	$1/n^3$	82303.1 cm^{-1}	4.908 cm^{-1}
Outer Turning Point $\ell = 0$	$2n^2$	2 a.u.	2450 a.u.
Orbital Period	$2\pi n^3$	0.15 fs	6516.3 fs
Adiabatic Field Ionization	$1/16n^4$	3.214×10^8 V/cm	214.2 V/cm
Stark Manifold Crossing	$1/3n^5$	$> 10^7$ V/cm	32.6 V/cm

Table 1.1: n dependence of various physical properties.

them attractive experimental entities. Some of these properties are shown in table 1.1.

Rydberg atoms have many attractive experimental properties. The lifetime of a Rydberg state is relatively long. The binding energy of a Rydberg state can be overcome easily with a common lab power supply. The transition frequencies between low lying states and Rydberg states are typically in the visible spectrum. The time period of a Rydberg orbit is much longer than the typical duration of current experimentally produced short laser pulses. Therefore, probing of the electron dynamics on a sub-orbital time scale is possible. In comparison, the 150 attosecond orbit time of a $n = 1$ ground state electron is less than $1/10^{th}$ of a single optical cycle of the electric field in a 600 nm laser pulse. Due to the exaggerated properties of Rydberg atoms, they are almost exclusively chosen for investigation of atomic time dynamics, including in all of the experimental work presented in this thesis.

1.2 Wavepackets

A great deal of both experimental and theoretical work has been performed recently on the subject of wavepacket dynamics [7–11]. A wavepacket is a quantum state which exhibits time dependence in one or more observable quantities [9]. It can be described as a coherent superposition of a number of non-degenerate stationary eigenstates [12] and written

$$\psi(\vec{r},t) \;=\; \sum_k \; a_k(t)\; e^{-i(E_k t-\delta_k)}\; \phi_k(\vec{r}) \;, \tag{1.2}$$

where k runs over all eigenstates present in the wavepacket. Here, $a_k(t)$ is the (possibly time dependent) complex state amplitude of the k^{th} state, E_k is the energy, $\phi_k(\vec{r})$ is the eigenfunction of the k^{th} eigenstate, and δ_k is the constant initial phase for that state.

Experiments presented in this thesis focus on a small subset of possible wavepackets, specifically electronic wavepackets in atomic systems. Electronic wavepackets can be generated by exposing a stationary eigenstate of an atom to a short pulse of electromagnetic radiation. The evolution of the wavepacket depends critically on the characteristics of the initial pulse. The creation of coherent electronic wavepackets is possible as long as the duration of the radiation pulse is short compared to any incoherent relaxation processes within the atom. Typically, the difficult aspect of wavepacket creation is the creation of a *particular* wavepacket which exhibits a behavior of interest, rather than the creation of any general wavepacket [9]. Once a particular type of wavepacket can be made on a consistent basis, then we can manipulate each copy of the wavefunc-

tion in a different manner and use time dependent spectroscopic techniques to observe how it responds.

The time dependent probability distribution of the wavepacket describes the time evolution of an atom after feeling the influence of a particular electromagnetic pulse. It is obtained by multiplying $\psi(\vec{r},t)$ from equation 1.2 by its complex conjugate. The resulting distribution is given by

$$|\psi(\vec{r},t)|^2 \;=\; |<\psi(\vec{r},t)|\psi(\vec{r},t)>| \;\propto\; \sum_j \sum_k \; a_j^*(t)a_k(t)\; \phi_j^*(\vec{r})\phi_k(\vec{r})\; exp[i\Delta E_{jk}t - \Delta\delta_{jk}]\;, \tag{1.3}$$

where the energy difference and phase difference are given by

$$\Delta E_{jk} \;=\; E_j - E_k \quad \text{and} \quad \Delta\delta_{jk} \;=\; \delta_j - \delta_k\;. \tag{1.4}$$

The complex phase of each component of $\psi(\vec{r},t)$ evolves at its own rate determined by the energy of that state. However, the time scales important to the wavepacket dynamics are governed by the energy differences between each of the states given in equation 1.4. As constituent eigenstates beat in and out of phase, variations in physically measurable quantities (such as the probability density) occur.

The electronic wavepackets which are investigated in this thesis are comprised of a coherent superposition of Rydberg states. The stationary eigenstates $\phi_k(\vec{r})$ from equation 1.2 are given by the $|n\ell m>$ spherical eigenstates or the $|nkm>$ parabolic eigenstates. A Rydberg wavepacket can be made up of states with different n values and similar ℓ values (radial Rydberg wavepacket), or the same n value but with different

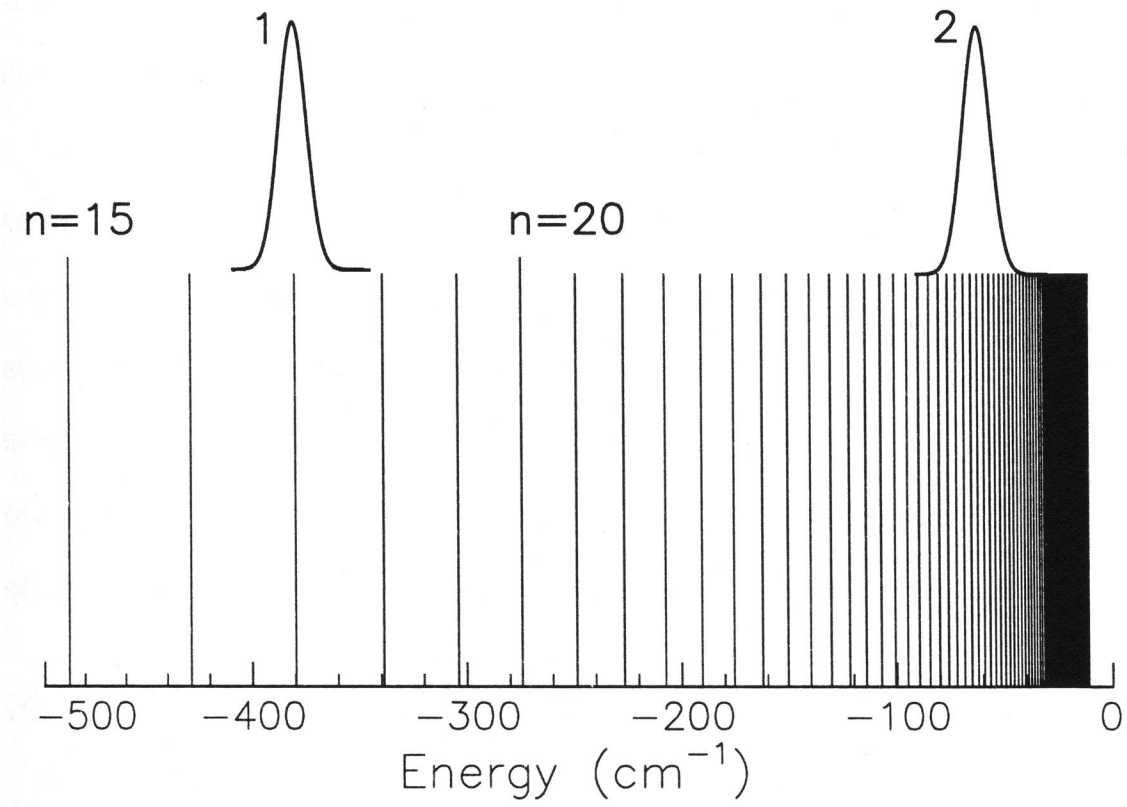

Figure 1.1: Two possible excitation possibilities to a Rydberg series. In each scenario, the frequency width of the laser pulse which makes the Rydberg transition is shown by the curves above the Rydberg levels. In the first case (marked "1"), a laser pulse with a 20 cm^{-1} bandwidth makes a transition from a low lying state to a single Rydberg eigenstate, in this case $n = 17$. In the second case (marked "2"), a laser pulse (also with a 20 cm^{-1} bandwidth) makes a transition from a low lying state to a range of Rydberg states centered around $n = 42$. Since all the Rydberg levels are excited coherently by the same laser pulse in case 2, a wavepacket is created.

ℓ values (angular Rydberg wavepacket), or many other combinations [13]. We will investigate radial Rydberg wavepacket dynamics explicitly in chapter 3 and appendix A. Both angular and radial Rydberg wavepacket dynamics are present in each of the other experiments. Since the energy spacing between individual eigenstates is small, forming a coherent wavepacket is straightforward with a short laser pulse. This is shown schematically in figure 1.1.

1.3 Ultrafast Lasers and Broad Bandwidth

The typical orbital periods of the Rydberg electrons produced for this thesis range from 1 ps to tens of picoseconds. We wish to make measurements of the motion of Rydberg wavepackets on a time scale shorter than the average orbital period of the wavepacket. Therefore, the probe pulse we use must be short in duration when compared to the orbital time of the Rydberg electrons being studied. Only in the last two decades have pulses short enough to perform these measurements become available. We use pulses which are typically on the order of 1 ps FWHM in duration to probe the time dynamics of Rydberg wavepackets. The details of how we retrieve information about a given wavepacket will be discussed in a later section.

Coherent bursts of light lasting only a few femtoseconds (10^{-15} seconds) can be generated and measured with current laser technology [14], although doing so is quite difficult. To get a feel for the time scale of a 100 fs pulse, consider that 100 fs is the

time that it takes a supersonic aircraft to travel the width of a ground state hydrogen atom [15]. Laser pulses with such extremely short durations are known as ultrafast pulses [16].

The duration of a laser pulse and the width of the frequency components contained in the pulse are related through the uncertainty principle. Since $\Delta t \Delta \nu \approx 1$, as Δt decreases, the spread in frequencies ($\Delta \nu$) must increase. For example, a 100 fs long Gaussian laser pulse has a bandwidth of approximately 150 cm^{-1}. The broad bandwidth allows the laser pulse to be resonant with many transitions at the same time. Just because many frequency components are present does not however guarantee an ultrashort pulse. The key to generating the ultrashort pulses used here is not just a generation of a large range of frequencies, but maintaining phase coherence between all the frequency components and keeping each of the frequency components oscillating in phase [17].

1.4 Half Cycle Pulses

As discussed earlier, a 100 fs laser pulse is extremely short in duration. However, a 780 nm, 100 fs pulse still contains 38 full cycles of the electric field. The time integrated electric field of this pulse is zero. A schematic of a typical short optical pulse is shown in figure 1.2. A free electron (or an electron far from the atomic core) which feels the influence of a 100 fs optical pulse wiggles back and forth due to the oscillating electric

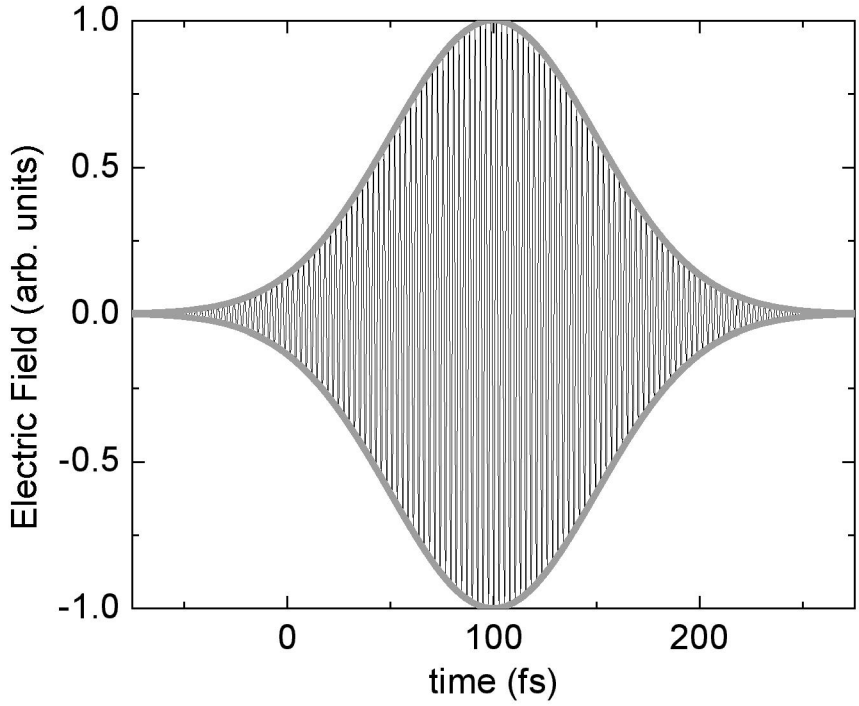

Figure 1.2: The electric field of a 100 fs FWHM, 780 nm laser pulse. Shown in grey is the Gaussian envelope which bounds the maximal values of the electric field. The time integrated electric field is zero.

field. After the pulse interaction however, the total energy of the electron is unchanged. Only when an electron is near a third body (like the atomic core) can it scatter and receive a net change in its total energy.

To create a pulse which has a nonzero time averaged effect on a free (or loosely bound) electron, the time integrated electric field must be nonzero. Two possibilities exist to satisfy this condition. First, a typical optical pulse can be reduced in duration from 100 fs to less than one full optical cycle. For a 780 nm pulse, this corresponds to a pulse with a full width at half maximum (FWHM) of less than 1 fs. While x-ray

pulses with FWHM less than 1 fs have been created and measured [14], at present no sub-single cycle optical pulses have been experimentally produced.

A second possibility for generating a nonzero time integrated electric field pulse involves using a terahertz electric field. Instead of decreasing the width of a pulse so that it encompasses less than a single optical electric field cycle, the wavelength of the radiation is chosen so that one half of a cycle fits into roughly 1 ps. The resulting pulse has a wavelength in the terahertz part of the electromagnetic spectrum. In this thesis, we use half-cycle pulses (HCPs) of terahertz radiation to both affect atomic dynamics and then to measure the subsequent response of various atomic systems. One version of a terahertz HCP is shown graphically in figure 1.3. While the true temporal profile of the experimental HCPs used in this thesis is slightly more complicated than figure 1.3 (see chapter 3 and figure 3.2), a simple comparison of the electric fields in figures 1.2 and 1.3 reveals the origin of the nonzero integrated electric field.

If the duration of the HCP is significantly less than the Kepler period of an electron, then the HCP acts like an impulsive *kick* to the electron. The component of the electron's momentum along the direction of the HCP is changed by an amount determined by the strength of the HCP field. A HCP field can even deliver enough energy to a Rydberg electron to directly ionize it [18]. Furthermore, by varying the strength of the HCP field and observing the amount of ionization, HCPs can be used to manipulate and probe the momentum distribution of Rydberg atoms and wavepackets [19]. Through

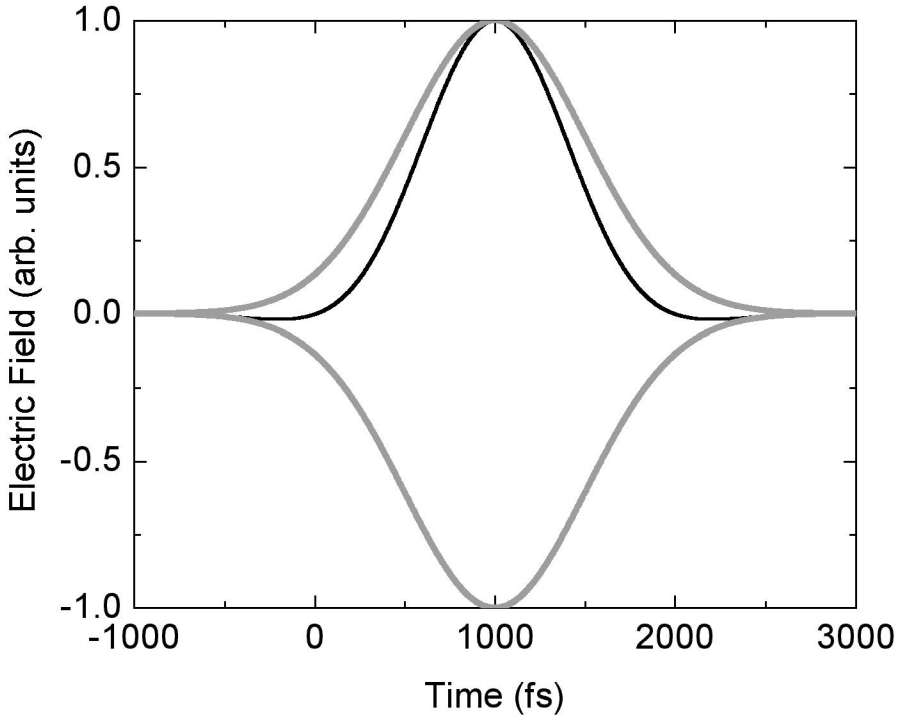

Figure 1.3: The electric field of a 1 ps FWHM, 0.5 THz pulse. Shown in grey is the Gaussian envelope which bounds the maximal values of the electric field. The time integrated electric field is not typically zero and is determined by the absolute phase of the THz oscillation.

the techniques presented in [19], the HCP field provides the basis for all momentum measurements presented in this thesis. In general, the HCP is a good tool for measuring the momentum distribution of wavepackets with principle quantum numbers $n \geq 20$. If the momentum distribution is measured, position space information can be recovered through Fourier analysis.

1.5 Discussion

This thesis is organized into three main sections. Chapters 2 and 3 discuss the tools used to study wavepacket dynamics. Chapter 2 provides a detailed overview of the laser systems and experimental setup, as well as a description of the experimental detector and data acquisition software. Chapter 3 discusses the half cycle pulse in detail. HCP production and calibration are explained, as well as how HCPs are used to recover information about the momentum distribution of a wavepacket through impulse momentum retrieval (IMR). A new variation on IMR is discussed and momentum distributions from the new method are compared to those generated with the original IMR technique.

In the second part of the thesis, three experiments are described which all center around using HCPs to manipulate and measure wavepacket dynamics. Chapter 4 presents an experiment in which a HCP is used to recombine an ion with a continuum electron in the presence of an external static field. The relative angle between the col-

lision field and the static field is shown to be an important factor in determining the probability of electron - ion recombination. Chapter 5 presents an experiment which uses HCPs to control the probability of autoionization of Rydberg eigenstates in a doubly excited configuration. Finally, chapter 6 discusses an experiment in which HCPs are used to probe the dynamics of a recombined wavepacket. In each of these chapters, novel electromagnetic fields significantly change the environment of an atomic system. We then measure the response of the atom to these changes.

The final section of this thesis concentrates on an interesting aspect of electron dynamics which occurs during HCP induced recombination. It is possible to highly localize an electron distribution far from the atomic core through the use of HCP fields. The experimental evidence for this effect is presented in chapter 6 and a full calculation of this effect is presented in detail in chapter 7.

An introductory experiment is presented in appendix A which demonstrates the large parameter space which can be investigated with the methods developed in this thesis. Many individual radial Rydberg wavepackets are created, each with a slightly different average energy. The evolution of each wavepacket is then measured. Overall trends in the evolution of an entire class of wavepackets are thereby recovered.

To aid the reader in understanding the precise methodology used in this thesis, three additional appendices are also included. An appendix is presented on the Stark effect. It contains a quantum mechanical description of the Stark effect and parabolic

coordinates, as well as several examples of computer generated Stark maps. Appendices on both the classical and quantum mechanical computer code used to simulate the experiments presented in this thesis are also included. Each appendix is designed to be a guide to someone attempting to begin similar calculations.

Bibliography

[1] J. Parker, and C.R. Stroud Jr., *Phys. Rev. Lett.* **56**, 716 (1986).

[2] P. Bellemo, C.R. Stroud Jr., D. Farrelly, and T. Uzer, *Phys. Rev. A* **58**, 3896 (1998).

[3] R.S. Judson and H. Rabitz, *Phys. Rev. Lett.* **68**, 1500 (1992); D. Meshulach and Y. Silberberg, *Phys. Rev. A* **60**, 1287 (1999); L.E.E. de Araujo and I.A. Walmsley, *ibid* **63**, 023401 (2001).

[4] J. Ahn, D.N. Hutchinson, C. Rangan, and P.H. Bucksbaum, *Phys. Rev. Lett.* **86**, 1179 (2001); C. Rangan and P.H. Bucksbaum, *Phys. Rev. A* **64**, 033417 (2001); J. Ahn, C. Rangan, D.N. Hutchinson, and P.H. Bucksbaum, *ibid* **66**, 022312 (2002).

[5] R.F. Stebbings and F.B. Dunning, *Rydberg States of Atoms and Molecules*, Cambridge University Press, Cambridge, (1983).

[6] T.F. Gallagher, *Rydberg Atoms*, Cambridge University Press, Cambridge, (1994).

[7] G. Alber, H. Ritsch, and P. Zoller, *Phys. Rev. A* **34**, 1058 (1986).

[8] L.D. Noordam and R.R. Jones, J. Mod. Optics **44**, 2515 (1997).

[9] R.R. Jones and L.D. Noordam, *Advances in Atomic, Molecular, and Optical Physics* **38**, 1 (1997).

[10] M.B. Campbell, T.J. Bensky, and R.R. Jones, *Phys. Rev. A* **58**, 514 (1998).

[11] R.R. Jones and M.B. Campbell, *Phys. Rev. A* **61**, 013403 (2000).

[12] L.D. Landau and E.M. Lifshitz, *Quantum Mechanics, 3rd ed.*, Pergamon Press, Oxford, (1977).

[13] R. Bluhm and V.A. Kostelecký *Phys. Rev. A* **51**, 4767 (1995).

[14] I.P. Christov, M.M. Murnane, and H.C. Kapteyn, *Phys. Rev. A* **57**, R2285 (1998); E. Hertz *et. al. ibid.* **64**, 051801 (2001); J. Itatani, F. Quéré, G.L. Yudin, M.Yu. Ivanov, F. Krausz, and P.B. Corkum, *Phys. Rev. Lett.* **88**, 173903 (2002).

[15] Another comparison which illustrates the relative length of 100 fs is given by M.M. Murnane at the Graduate Student Seminar for the Division of Atomic, Molecular, and Optical Physics (DAMOP) in Williamsburg, Virgina (2002). One minute is the logarithmic mean between 100 fs and the age of the universe.

[16] The term *ultrafast* is somewhat of a misnomer. The speed of light is very much a constant. Perhaps a better term would have been *ultrashort* laser pulses. Regard-

less, the terminology has already been chosen and we stick with convention in this thesis.

[17] J.C. Diels and W. Rudolph, *Ultrashort Laser Pulse Phenomena*, Academic Press, (1996).

[18] R.R. Jones, D. You, and P.H. Bucksbaum, *Phys. Rev. Lett.* **70**, 1236 (1993).

[19] R.R. Jones, *Phys. Rev. Lett.* **76**, 3927 (1996).

Chapter 2

Experimental Apparatus

2.1 Introduction

Legitimate successful completion of the experiments presented in this thesis required the coordination of several diverse apparatuses. In this chapter, each of these systems is described in some detail. We begin with a discussion of the atom source and vacuum chamber. This is followed by a discussion of the creation of ultrashort laser pulses in general, as well as the specific laser systems used in this work. A major obstacle in the field of ultrashort laser pulses is the lack of simple methods to measure the characteristics of a pulse with a FWHM of less than 1 ps. Therefore, we present a section in this chapter concentrating the methods we use to characterize ultrashort laser pulses. The chapter concludes with a discussion of the single shot detector used

to collect data and the associated data collection software.

2.2 Atomic Source

The experiments presented here are performed on calcium atoms. Calcium is chosen over the other alkali earth metals due to the location of its energy levels. A dye laser pulse is used to perform an excitation to the first excited state in calcium, the $4s4p$ state. The wavelength range that is needed to perform transitions from the $4s4p$ state to the calcium Rydberg series closely matches half the wavelength of the fundamental of a Ti:Sapphire laser. Since the Ti:Sapphire laser system provides a reliable source of broad bandwidth pulses which can be used to create Rydberg wavepackets, we concentrate our studies on calcium.

An effusive beam of neutral calcium atoms is produced in the vacuum chamber by resistively heating a 3/8 inch stainless steel tube with a small hole in the side. The stainless steel tubing is made of 316 steel and has .006 inch thick walls. A 400 μm hole is drilled into the side of a 6 inch long section of tube. The atomic beam will exit through this hole. To get the calcium into the tube, initially one end of the stainless steel tubing is crimped. Metallic calcium pellets are placed into the tube to a level just below that of the 400 μm hole. After filling, the top end of the tubing is crimped. The filled tube or "oven" is then mounted in the vacuum chamber so that the exit hole points directly towards the interaction region and the oven is electrically isolated from the rest

of the vacuum chamber. As current flows through the oven, the stainless steel heats due to its resistance to the applied current. Ca atoms in the oven are vaporized due to the heating process and leave through the exit hole and move towards the interaction region. Typically, an atomic beam is produced with a density of 10^7 - 10^8 atoms / cm^3 approximately 10 cm away from the oven.

A water cooled copper shield separates the oven from the rest of the vacuum chamber. The oven shield guards the majority of the vacuum chamber from debris and other particulate matter. The shield also prevents unwanted blackbody radiation emitted by the hot oven from reaching the rest of the chamber. A copper plate with a 5 mm by 3 mm slit is mounted on the copper shield. The plate acts as a mask for the effusive atomic beam. Only the portion of the beam directed precisely between the field plates and perpendicular to the laser propagation direction is permitted to leave the shielded area.

A high current power supply consists of a series of alternating current transformers that step down standard 120 V AC, 60 Hz to approximately 6 V AC. The output current is correspondingly increased by a factor of 20. The amount of current delivered by the transformers is regulated by a Variac AC voltage regulator. The oven typically has a resistance of approximately 0.1Ω. In order for the voltage drop to occur mainly across the oven and thereby only dissipate power in the form of oven heating, connections between the power supply and the oven are made with thick copper wiring

approximately 3/8 inch in diameter. High current 1/4 inch diameter copper voltage feedthroughs are attached to the top and bottom of the oven. Connections between the high current power supply and the voltage feedthroughs are made on the exterior of the vacuum chamber. Typically, around 80 - 100 amps of current flows through a calcium oven to produce a satisfactory effusive atomic beam density.

2.3 Vacuum Systems

The experiments presented in this work are performed in a vacuum of approximately 10^{-6} torr. The vacuum chamber is made of aluminum and approximately cylindrical, 24 inches in diameter and 12 inches tall (see figure 2.1). Eight flanges are located around the circumference which allow laser beams, electrical pulses and cooling water to enter the vacuum chamber. Vacuum pressure gauges and rotation feedthroughs are also located on various flanges. The lid of the vacuum chamber has 5 flanges. The center flange is made of plexiglass and allows visual inspection of the interior of the vacuum chamber and detector. All flanges are sealed to the vacuum chamber with Buna-type O-rings. A gate valve is located immediately below the chamber allowing the chamber to be isolated from the diffusion pump and water baffle below.

Pumping the chamber to low pressure from atmospheric pressure is a two step process. After closing the chamber, a valve is opened to an evacuated tube connected to a mechanical roughing pump. The roughing pump lowers the chamber pressure to

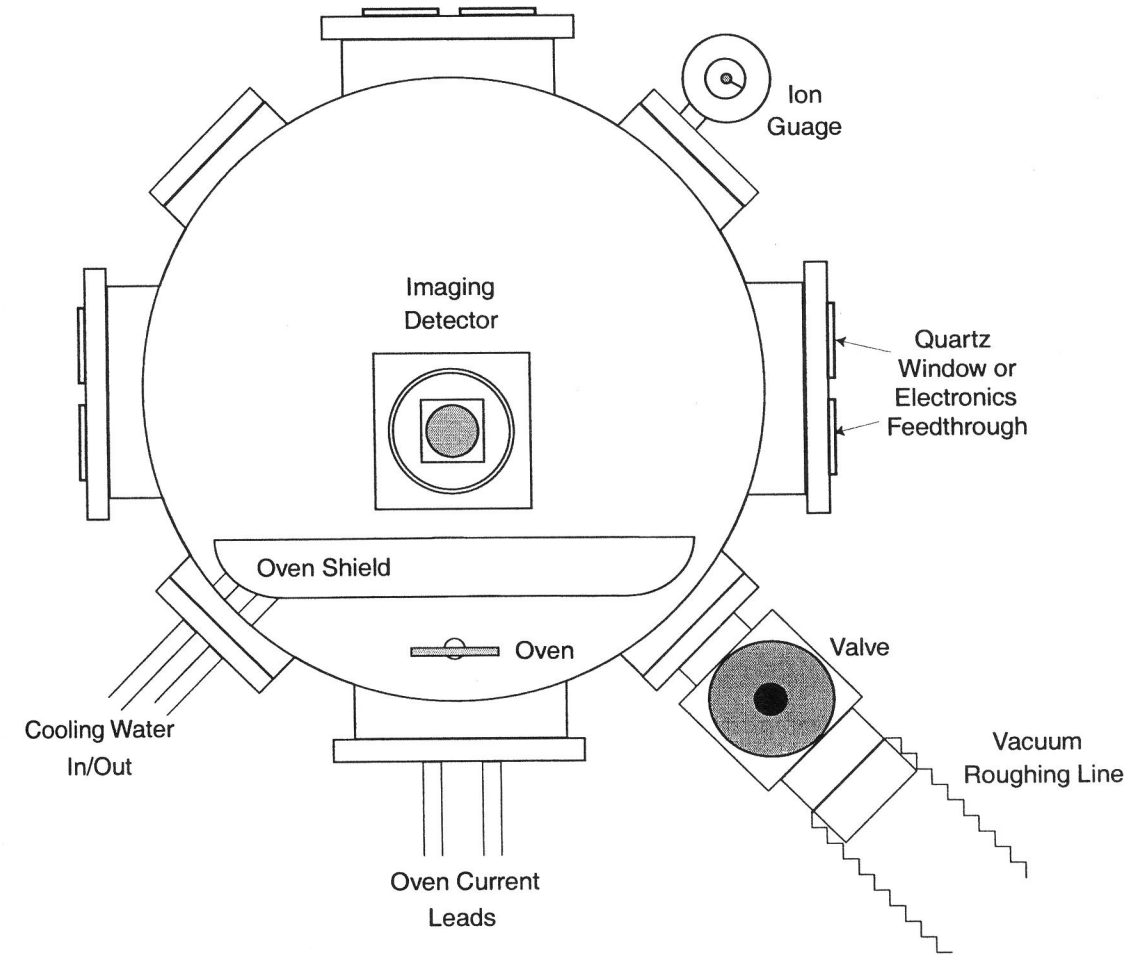

Figure 2.1: Overhead schematic diagram of the vacuum chamber. Elements shown are consistent for all experiments. Optics and other devices are placed inside the chamber depending on the specifics of each particular experiment [1].

approximately 50 mtorr in about 1 hour. Once the pressure falls to 50 mtorr, the valve to the roughing pump is closed and the gate valve is slowly opened. Below the gate valve is a Varian VHS-6 model diffusion pump and Varian model 336 water baffle. The diffusion pump contains 500 mL of vacuum pump oil (Duniway part number DS-7040) and runs continuously. The diffusion pump achieves a pressure of approximately 10^{-6} torr. The gate valve is closed to separate the chamber from the diffusion pump if the pressure in the chamber is too high. Chilled water flows through the baffle which prevents significant quantities of diffusion pump oil from contaminating the vacuum chamber during normal operation.

The diffusion pump uses approximately 2200 watts of power. To ensure that this large amount of power is properly safeguarded, the 208 V AC that powers the diffusion pump is regulated through an interlock switch. The interlock system prevents possible damage to either the lab equipment or the pump itself. Power is shut off to the diffusion pump if the pressure in the foreline of the is too high (> 100 mtorr) or the temperature of the pump is too hot. If the pump temperature is too high then the pump oil begins to crack, reducing its pumping effectiveness. Once this happens, the pump must be removed from the chamber, all the oil must be removed, the pump must be scrubbed clean, and new oil must be added. The pump may begin to overheat if the flow of cooling water to the pump or water baffle is interrupted for any reason. Once the interlock has been triggered, it must be manually reset.

Pressure in the chamber is measured with two devices. From atmospheric pressure to about 10^{-2} torr, it is measured with a thermocouple. Pressures below 10^{-2} torr are measured with an ion gauge controlled by a Varian BA2 ion gauge controller. The actual pressure is calculated by the controller and displayed on an LED readout. The first time a new oven is heated after being installed into the vacuum chamber, contaminants on the metals boil off and the pressure in the chamber rises significantly. Therefore, the current in the oven must be increased very slowly or the pressure will rise above the safe operational limits of the diffusion pump. Typically, this decontamination procedure takes about a day.

2.4 Production of Laser Pulses

An array of lasers are used to generate the many individual pulses necessary for the experiments presented in this thesis. A Nd:YAG laser is used to optically pump several tunable dye lasers. Each dye laser produces 5 ns long pulses with bandwidth of less than 1 cm^{-1}. By varying the type of dye and laser configuration, nanosecond long pulses can be created from the infared through the entire visible spectrum. A Ti:Sapphire laser is used to create 150 fs FWHM pulses from 780 nm to 786 nm. These pulses are subsequently amplified and used for a variety of purposes. This section explains the components of each laser system and provides some background information which will hopefully provide an understanding of how each system operates.

2.4.1 Lab Environment

To achieve stability of the laser system, several factors must be held constant. Among them, the temperature of the room, flow of air over the optical tables, and vibration of the surroundings. The laser systems are located on 5 optical tables which are all joined together forming one large platform. The system of optical tables is isolated from vibration by pneumatic isolation legs. Situated 4 feet above the optical tables are plywood platforms bolted to the ceiling of the lab by Unistrut. On these platforms sit various power supplies, pulse generators, and assorted other electrical devices (and a couple of dinosaur skeletons). Sheets of clear plastic are draped from the plywood platform to below the height of the optical tables. The plastic separates the air flow over the optical tables from that of the room in general. Situated on the upper platform, about 1/3 the way down the length of the optical tables is a heating unit. The thermostat on the heating unit is accurate to 0.1° F. The temperature setting of the heating unit is set higher than the ambient temperature of the surrounding room. The heater warms the air over the optical tables to a constant temperature, usually around 72.5° F.

2.4.2 Nd:YAG Lasers

In a rod of crystalline yttrium aluminum garnet, approximately 0.7% of the rare earth element yttrium is replaced by neodymium. This material has a strong lasing transition

at 1064 nm. To create a population inversion, neodymium atoms are optically excited by an external source. In the two Nd:YAG lasers used in the lab, the Nd excitation to the metastable state occurs by a pulsed flash lamp. The flashlamps typically have lifetimes of about 700 hours of operation, which equates to changing them three to four times a year [2, 3].

As the population inversion builds up, light oscillation in the cavity is prevented by the Q switch located in front of the back mirror of the cavity. The Q switch is an electronically triggered switch which varies the Q factor of the laser cavity from low to high. When the Q switch is open, loss in the cavity is high and light quickly escapes. When the Q switch is closed however, the cavity losses become low and light oscillates. As the light oscillates, the 1064 nm laser transition is stimulated in the YAG rod and the population inversion is quickly depleted. The output from the laser is a short ($<$ 10 ns) pulse of 1064 nm light with a peak power of several megawatts [4, 5]. The lasers are triggered to output pulses at 15 Hz, delivering an average power of 0.65 J per pulse.

Two KDP (Potassium Dihydrogen Phosphate) crystals are mounted directly after the output of the Nd:YAG laser. They perform frequency doubling and sum frequency mixing. The second harmonic (532 nm) and third harmonic (355 nm) of the fundamental Nd:YAG frequency are created as the 1064 nm light passes through the crystals. Varying the angles of the two crystals controls how much output power is delivered in each harmonic. The output power at 532 nm is measured with a power meter sensi-

tive to this wavelength at the start of each day and after each laser realignment. Any changes in laser output indicate a potential problem with the Nd:YAG system.

2.4.3 Dye Lasers

Several dye lasers are used in this thesis. In each of them, the second or third harmonic of the Nd:YAG laser is focused into a solution of organic dye, creating a population inversion. The dye is contained in a glass cell mounted within a laser cavity. Fluorescence from the dye cell travels along the axis of the cavity and strikes a grating. The grating is the tuning element of the cavity, removing all of the light from the cavity except that within a small frequency range. Therefore, only light at the selected frequency oscillates within the cavity. Two different styles of dye lasers are used in the experiments presented in this work. They are the Hansch type dye laser and the Littman type dye laser [6, 7] and the details of each are described below.

The dye cell is a quartz cuvette with 3/8 inch diameter glass tubes blown onto the top and bottom. Plastic tubing is clamped to the glass tubes and is connected through a pump to a dye reservoir. A solution of dye is pumped through the cell at approximately 1 L per minute. A particular dye is chosen for the laser depending on the desired output frequency. The dyes we choose for this thesis have a 30 nm to 40 nm wide range of wavelengths where lasing is possible. Each dye comes with instructions on the proper solvent and concentration to be used.

During laser operation, the Nd:YAG pump light gradually decomposes the dye molecules, which are typically large complex molecules with multiple ring structures. Degradation can be either thermal or photochemical. Pump light with higher frequencies more rapidly decompose the dye molecules. In our experiments, dye degradation is typically first observed by a noticeable decrease in the Rydberg state field ionization signal. As the dye begins to degrade, the pump light penetrates further into the dye cell. If more than the first 2 mm of the dye is illuminated by the pump light, significant dye degradation has occurred and the dye must be changed. Changing laser dye is a fairly straightforward process. First the pump light is blocked. Then the dye reservoir is removed from the pump intake. The remaining dye is allowed to drain into the reservoir. Once all the dye has been removed from the system, the reservoir is emptied and subsequently filled with fresh dye.

During alignment, dye laser performance is frequently evaluated with an étalon placed after the output coupler. The laser output is first expanded with a diverging lens, then is incident upon an étalon. Concentric interference fringes are observed on a screen placed 1 m past the étalon if the laser is properly aligned. Adjacent intensity maxima in the interference pattern are separated by $\frac{1}{2nd}$, where n is the index of refraction of the étalon and d is the étalon thickness. Small, relative changes in laser wavelength are measured by placing a photodiode at the center of the interference pattern. The voltage output of the photodiode is proportional to the amount of light

incident upon it. Varying the frequency of the laser by $\Delta\nu = \frac{1}{2nd}$ results in a change in the output voltage of the photodiode from a maximum to a minimum and back to a maximum. These changes are measured on an oscilloscope. Relative values of dye laser wavelength are calibrated in this manner.

Hansch Style

A diagram of a Hansch dye laser is shown in figure 2.2. Fluorescence from the organic dye is sent through a telescope so that the beam diameter significantly increases. After the light passes through the telescope it is incident upon a diffraction grating. The grating is tilted so that a diffraction order is sent back along its incident path. Small changes in the grating angle determine the color of the light which leaves the grating along the axis of the cavity. After passing through the dye cell a second time, the majority of the light escapes the cavity through an output coupler. A second dye cell can be placed after the output coupler for additional single pass amplification. The bandwidth of laser pulses from a Hansch dye laser is typically on the order of 1 cm^{-1}. This can be further reduced by adding a Fabry-Perot étalon within the laser cavity, however this makes the system difficult to tune during data collection.

Littman Style

A diagram of a Littman dye laser is shown in figure 2.3. Light emitted from the dye cell strikes a diffraction grating at near grazing incidence. The first order diffraction off

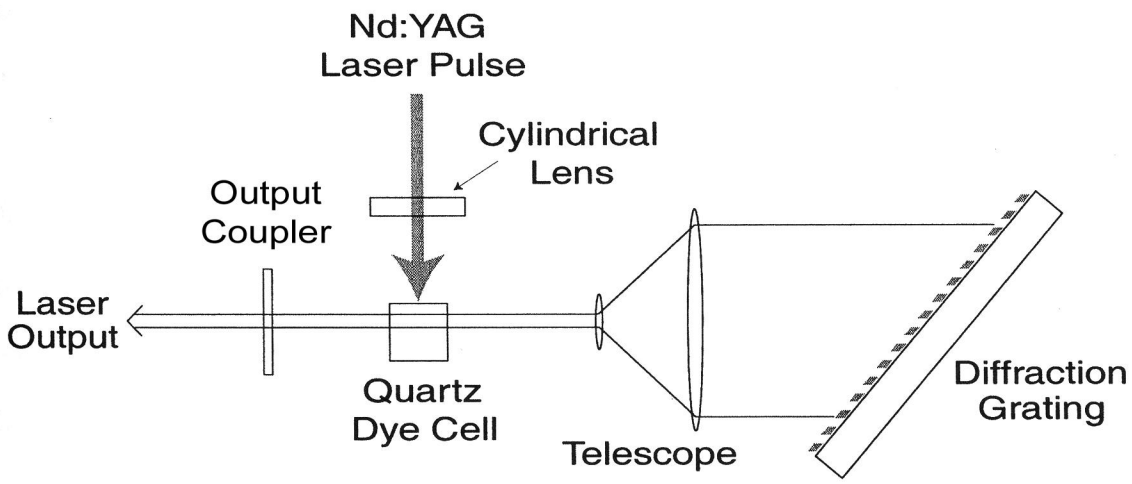

Figure 2.2: Diagram of a Hansch style dye laser [1].

the grating strikes a mirror located directly above the grating. The frequency of light which is incident upon the mirror at precisely a right angle is reflected back off the grating and through the dye cell again. Changing the angle of the mirror determines the lasing frequency as long as the chosen frequency falls within the gain profile of the laser dye. After light passes off the grating the second time and through the dye cell again, it reflects off the back mirror of the cavity and back to the dye cell. As the light again strikes the grating at grazing incidence, the 0^{th} order reflection escapes over the top of the grating. This is how light is output from the laser. Each pass off the diffraction grating further reduces the bandwidth of the light. A diagram of the angles associated with the grating - mirror system is shown in figure 2.4.

After exiting the laser cavity, the output light can be subsequently amplified by

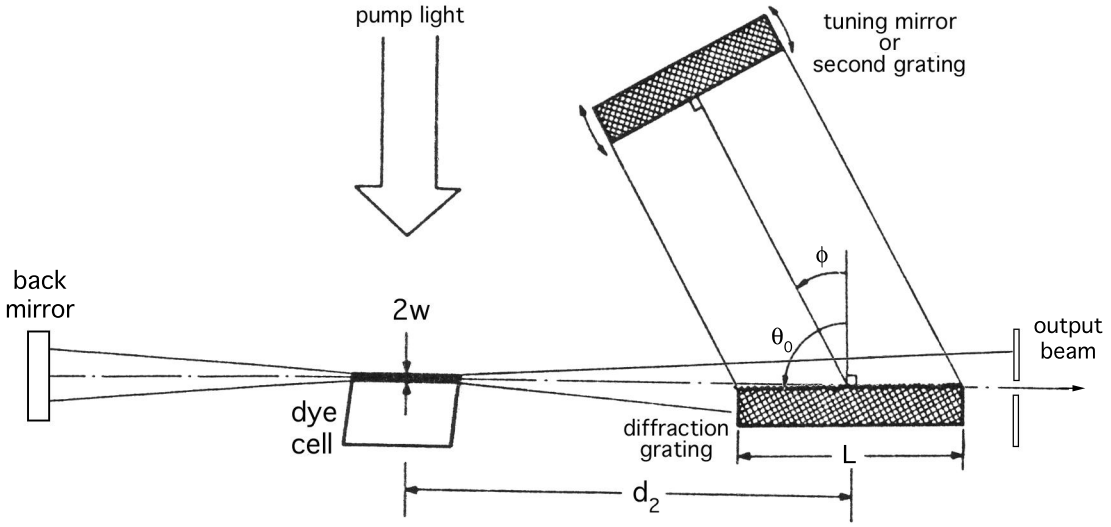

Figure 2.3: Diagram of a Littman style dye laser [7].

a single pass through a second dye cell if desired. The output power of the Littman style dye laser is less than that of the Hansch style, however the bandwidth of the Littman configuration may be considerably narrower. The bandwidth of the Littman style dye laser may be further reduced by replacing the frequency selecting mirror with a second diffraction grating. In the double grating Littman configuration, the first order diffraction off of the first grating is incident upon a second grating. The angle of the second grating is then adjusted so that the first order diffraction of the second grating reflects light back off the first grating and completes the cavity. Using a double grating Littman configuration constructed in the lab, a bandwidth of 0.14 cm^{-1} has been achieved [8].

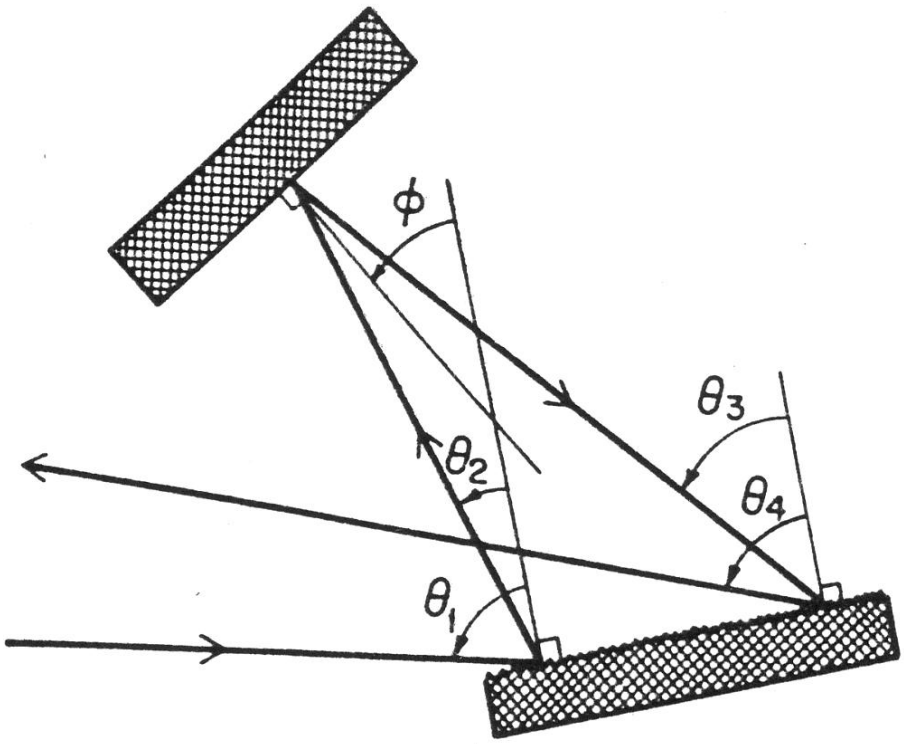

Figure 2.4: Diagram of the tuning arrangement in a Littman style dye laser illustrating the important angles in the system. The laser wavelength is determined when $\theta_1 = \theta_4$ [7].

2.4.4 Ar^+ Laser

An argon-ion laser is one of a family of noble gas ion lasers which have been developed. Singly charged argon has several emission lines in the blue-green. The strongest of these lines is the 514.5 nm Ar II line. The Ar^+ system is fairly inefficient due to the fact that the 3 eV lasing transition is approximately 36 eV above the ground state. This is offset by the ability to deliver tens of watts of continuous wave (cw) output power [4].

A long, evacuated tube is filled with approximately 1 torr of pure argon gas. The gas in the tube is excited by a high current discharge that travels the length of the tube. The discharge is confined to a cylindrical region along the center of the tube approximately 2 mm in diameter. An initial voltage pulse of a few kilovolts ionizes the argon and forms singly ionized Ar^+. Following the initial gas breakdown, the voltage falls to around 100 - 400 volts at a discharge current of between 10 amps and 60 amps. The high current density populates an upper energy state, creating a population inversion among the argon ions. Once an inversion is created, lasing begins. The tube terminates in a quartz Brewster's angle window which ensures the output beam is vertically polarized. Care must be taken to ensure that no residue builds up on the output window. If a buildup does occur, the output beam quality becomes poor and Ar^+ laser does not effectively pump the Ti:Sapphire laser. If this occurs, the output window must be cleaned using a couple drops of ammonium bi-fluoride to etch away a

surface layer from the output window and remove contaminants.

The Ar^+ laser we have used typically takes close to an hour to stabilize after being turned on. Furthermore, the output power tends to rise and fall throughout the day. The system must be aligned frequently by adjusting the back mirror of the laser cavity to obtain the maximum possible output power. Another disadvantage with the Ar^+ system is that the Argon tubes have a relatively short lifetime due to the harsh conditions that exist inside the tube during lasing. Typically this lifetime is no more than 3000 hours. Near the end of this time, the output power decreases and the beam develops complicated mode structure. Due to these considerations, the Ar^+ system has been replaced as of this writing with a solid state cw Nd:YLF laser. However, all the data presented in this thesis was collected using the Ar^+ system.

2.4.5 Short Pulse Ti:Sapphire Laser

Titanium doped sapphire (Al_2O_3) is a solid state material which is capable of lasing over a very broad range of wavelengths (700 nm - 1100 nm). In a Ti:Sapphire crystal, titanium is introduced into the crystal lattice and replaces approximately 0.05% of the aluminum [4]. Ti:Sapphire laser systems can operate in either cw or pulsed mode. The Ti:Sapphire system used in this work is a short pulse, self mode-locking system. Figure 2.5 shows a schematic diagram of the self mode-locked Ti:Sapphire laser cavity. After absorbing the light from the Ar^+ pump beam, the Ti:Sapphire crystal emits a broad

spectrum of radiation into the laser cavity. The longitudinal mode separation $\Delta\nu$ of a cavity of length d and index of refraction n is given by

$$\Delta\nu = \frac{c}{2nd}. \tag{2.1}$$

For the Ti:Sapphire laser cavity used here, the mode spacing is 78 MHz, or approximately 2.6×10^{-3} cm^{-1}. Therefore, over 100,000 longitudinal modes are possible within the gain curve of the Ti:Sapphire crystal. The fixed length of the laser cavity ensures that all the longitudinal modes have equal frequency separation. If all the supported modes are in phase (a situation referred to as being phase-locked or mode-locked), then the electric fields present add constructively at one time, creating a short pulse.

To operate the Ti:Sapphire system in pulsed mode, some source of noise is initially introduced into the laser cavity. This can be a random fluctuation over the background or an impulse generated by physically tapping on an element in the cavity. Since the disturbance is more intense than the background noise, a nonlinear process occurs in the material known as the Kerr effect which focuses the disturbance, causing it to be preferentially amplified.

When a beam of sufficiently high intensity passes through an optical material, the index of refraction of the material is altered by the intensity of the beam. This change in the index of refraction of a material is known as the optical Kerr effect. If the beam is more intense in the center than the edges, then the index of refraction of the material becomes higher at the center of the beam. Due to the Kerr effect, an intense pulse

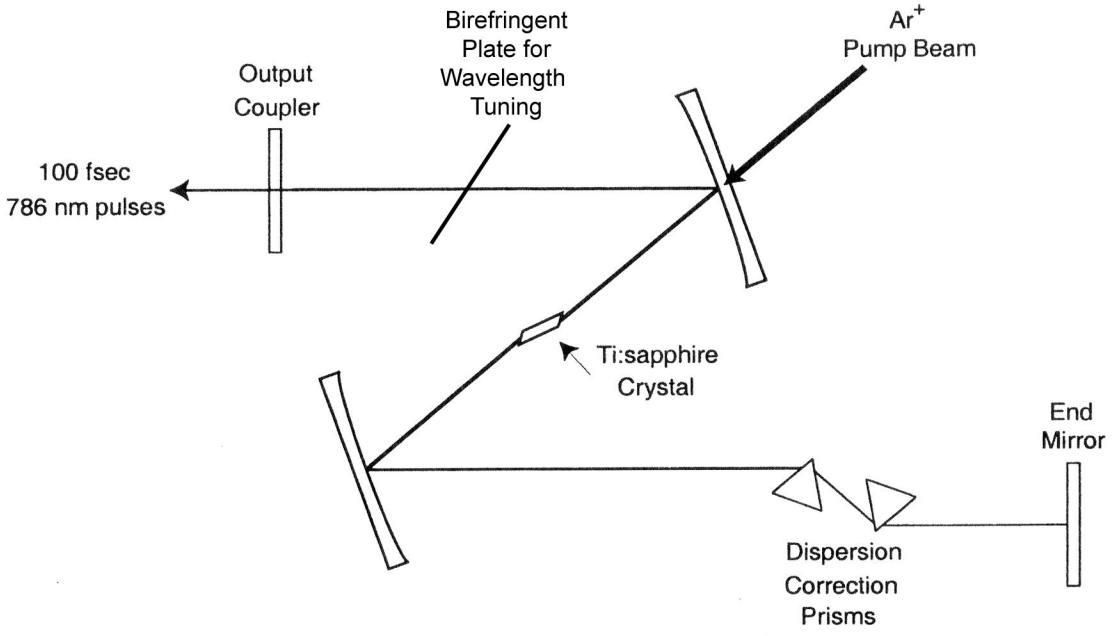

Figure 2.5: Schematic diagram of the self mode-locked Ti:Sapphire laser cavity [9].

creates a positive lens which slightly focuses itself in a material. The Kerr effect also produces self-phase modulation, broadening the frequency spectrum of the pulse [5]. As the noise pulse which was initially introduced into the laser cavity gains intensity, it self-focuses and begins to contain more and more frequency components. Eventually, the pulse exceeds the oscillation threshold of the laser cavity and begins to sweep out gain from the Ti:Sapphire crystal. The end result of this process is an ultrashort pulse.

The temporal profile of the pulse is critically dependent on the fixed, coherent relationship between the various frequency components present. However, as the pulse passes through various optical components, group velocity dispersion (GVD) occurs. As a pulse interacts with any material, each frequency component experiences a different index of refraction. Therefore, each frequency propagates at a slightly different velocity. To correct for this, two prisms are positioned in a manner which introduces an amount of negative GVD to precisely correct for the linear component of the dispersion introduced by the laser rod, mirrors, and output coupler.

The output from the Ti:Sapphire laser used for this work is a train of 100 fs transform limited pulses occurring at 78 MHz. Each pulse has approximately 1 nJ of energy and a central wavelength between 780 nm and 786 nm. Rotation of a birefringent crystal in the laser cavity controls the central output wavelength by altering the phase matching conditions of the crystal. The total output power of the Ti:Sapphire laser is approximately 200 mW. A fraction of the output of the Ti:Sapphire laser is directed

into a photodiode by a glass microscope slide. The output of the photodiode is monitored with an analog Tektronix oscilloscope. Even though the width of an individual Ti:Sapphire output pulse is on the order of 100 fs, the response time of the photodiode is a few nanoseconds. Therefore, we are able to qualitatively determine the relative intensity of individual pulses on the oscilloscope. Occasionally, the laser will support more than one transverse mode simultaneously. This results in a reduced maximum intensity and increased instability. The photodiode is used to watch for this. A cooling water line runs through the laser system. The temperature of this water is regulated by a small heater to prevent instability due to temperature fluctuations.

The relatively small pulse energy ($\approx$ 1 nJ) makes the direct output from the Ti:Sapphire laser ineffective for studying atomic systems without some form of amplification. Therefore, every 15^{th} of a second, a single pulse from the 78 MHz Ti:Sapphire pulse train is selected for amplification. Due to the high peak pulse intensity in a single 100 fs pulse, direct amplification is difficult. Instead, the short pulse is reversibly expanded by a factor of several thousand prior to being amplified to prevent damage to the optics and crystals used in amplification.

2.4.6 Expander

Figure 2.6 shows a diagram of the short pulse expander. In the expander, longer wavelengths travel a shorter distance than shorter ones, creating a frequency chirp

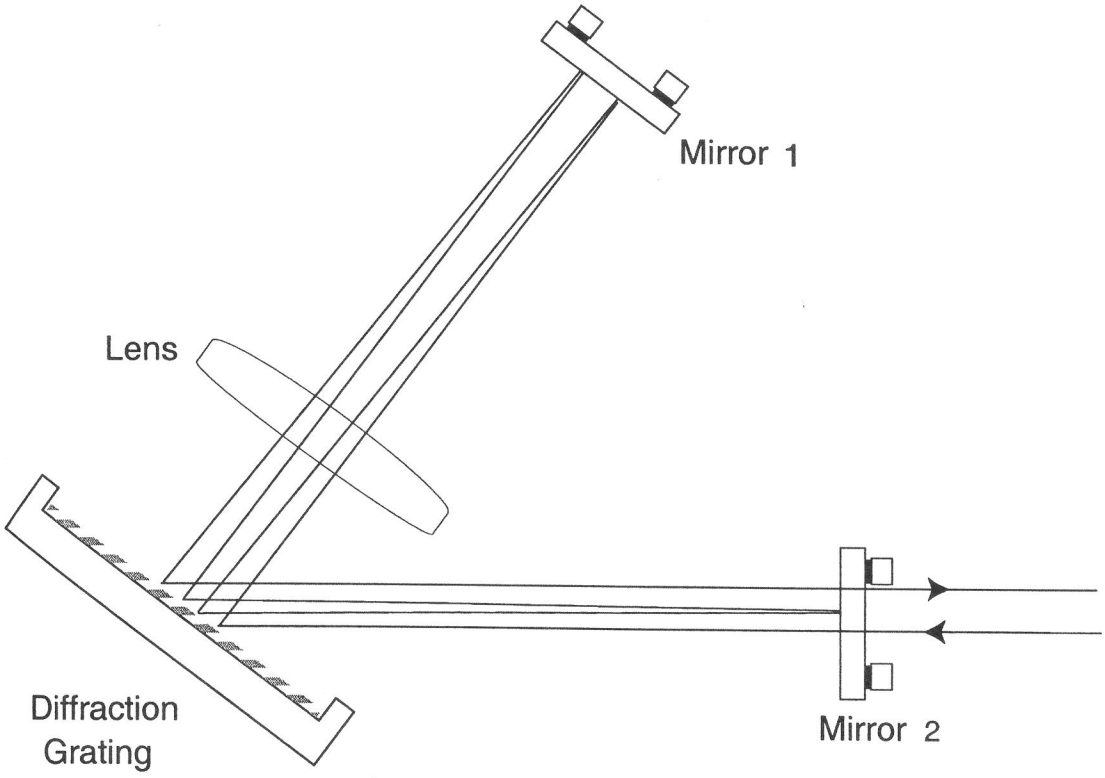

Figure 2.6: Schematic diagram of the short laser pulse expander. The beam diffracts four times off the diffraction grating. The beam path is offset in the plane of the page for clarity. Each reflection off the grating spatially separates the frequency components of the incident pulse. The expanded pulse is temporally chirped by a factor of 2000 [1].

in the pulse which effectively "expands" each pulse. When a pulse is expanded, it retains approximately half of its initial energy and the peak power is decreased by approximately three orders of magnitude. The expanded pulse may then be amplified safely without causing damage to the optical components of the amplifier. Following amplification, the frequency chirp can then be removed by the inverse process, pulse compression.

The short pulse enters the expander just above mirror 2 and diffracts from the grating. The grating is typically positioned at an angle of approximately 54° to the input pulse propagation direction. Each frequency component diffracts at a different angle determined by $sin\theta_{out} - sin\theta_{in} = \frac{\lambda}{2d}$, where λ is the wavelength of a particular frequency component and d is the line separation in the diffraction grating. The diffracted beam leaves the grating, passes through a lens, off mirror 1, back through the lens, and onto the grating again. The lens enlarges the chirped image of the input beam before it strikes the grating the second time. This allows a larger geometrical path difference between the various frequency components of the pulse. After the pulse diffracts off the grating the second time, it bounces off mirror 2, causing it to retro-reflect along its input path. Mirror 2 introduces a small vertical offset that allows the output pulse from the expander to be separated from the input pulse. In total, the pulse diffracts off the grating four times and emerges from the expander frequency chirped by about a factor of 2000 compared to the initial pulse. The reddest frequencies present in the original pulse arrive approximately 200 ps before the bluest frequencies.

2.4.7 Regenerative Amplifier

A diagram of the regenerative amplifier (regen) is shown in figure 2.7. The 532 nm second harmonic of the Nd:YAG laser creates a population inversion in a Ti:Sapphire crystal. For normal operation, approximately 0.6 W of power is input to the crystal (40

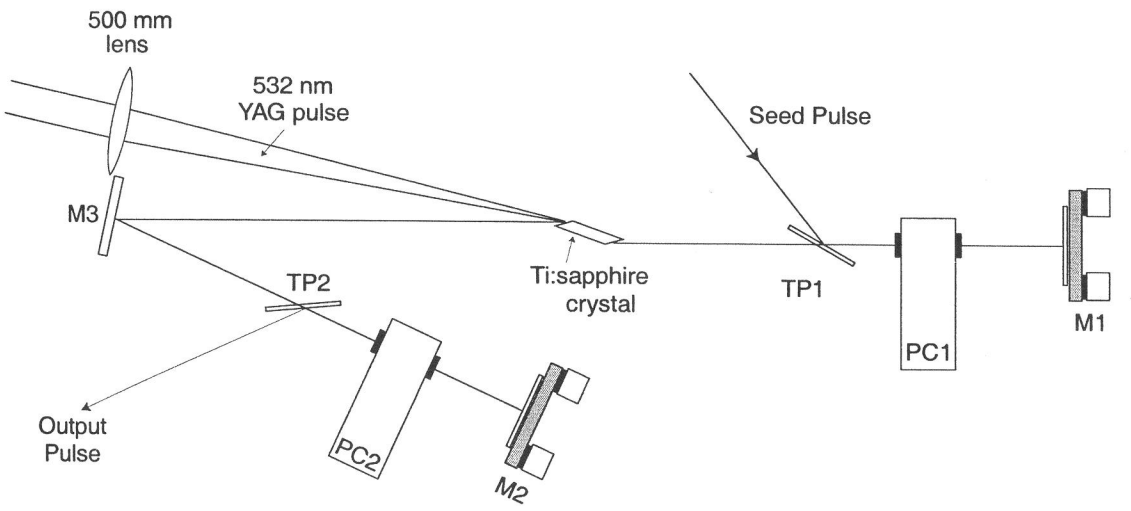

Figure 2.7: Schematic diagram of the regenerative amplifier. A thin film polarizer (TP1) directs light into a laser cavity. The polarization of the beam is rotated with a Pockels cell (PC1) so that it remains in the cavity. A population inversion is created in the Ti:Sapphire crystal by the 532 nm Nd:YAG pump light. The chirped pulse circulates through the cavity sweeping gain from the crystal on each pass. After the intensity of the pulse saturates, the polarization is rotated by PC2. The amplified pulse is deflected out of the cavity by TP2 [1].

mJ per pulse). The crystal is temperature regulated with a cooling water line. A single pulse from the Ti:Sapphire laser is sent into the regen from the first thin film polarizer (TP1). It passes through a Pockels cell (PC1) which rotates the polarization of the pulse by 45° [10]. The pulse reflects off mirror M1 and passes again through PC1 which rotates the polarization by another 45°. The pulse is now polarized orthogonal to its initial polarization and therefore passes through TP1. The voltage on the Pockels cell is now turned off, preventing further pulses from entering the regen cavity and trapping the first pulse in the cavity.

The pulse oscillates approximately 18 times in the regen. During each pass, the pulse sweeps out gain from the Ti:Sapphire crystal. The output pulse energy is increased by roughly a factor of 5×10^6 over the input energy. The second Pockels cell (PC2) is then triggered, rotating the polarization of the pulse so that the amplified pulse is ejected from the cavity by TP2.

A photodiode monitors the portion of the amplified light leaking out of the regen cavity through M1. Only during the last 4 or 5 passes through the cavity is there enough light to measure in this manner. The time delay between triggering PC1 and PC2 is adjusted so that the pulse is switched out just after the pulse energy saturates. If the pulse remains in the cavity too long, no more gain can be removed from the crystal and the pulse energy decreases. The switching is performed slightly after saturation to remove dependence on the fluctuation of the input beam. The timings of the Pockels cells are controlled by a Stanford Research Systems (SRS) DDG 535 pulse box, which is synchronized to the Nd:YAG laser. The output of the regen is typically 5.0 mJ per pulse.

The regen cavity is itself a laser cavity and must be aligned frequently for proper operation. Typically, alignment is performed at the beginning of each day and three to five times a day depending on the stability of the Ti:Sapphire laser output. To begin alignment, the input seed light from the Ti:Sapphire laser is blocked. The switching time of PC2 is then increased by 3 μs. This traps any light in the cavity for a large

number of round trips. Then, 0.2 W of 532 nm Nd:YAG pump light is sent into the Ti:Sapphire crystal in the regen cavity. The crystal fluorescence is enough to promote lasing in the cavity. A CCD camera observes the laser output reflected off of M3. The alignment of the cavity is adjusted to maximize the observed intensity. The strength of the Nd:YAG pump light is then reduced to a level where lasing in the regen cavity is barely visible. The amount of pump light is then measured with a power meter and this value is recorded as the threshold value. The typical threshold value is approximately 0.18 W. Significant deviation from this value indicates potential problems with the regen such as: poor Nd:YAG input pulse quality, problems with either PC1 or PC2, a significant misalignment of the regen cavity, or dust on the face of the Ti:Sapphire crystal. The switching time of PC2 is then reduced by 3 μs. Failure to do so may cause significant damage to the regen system. The seed light from the Ti:Sapphire laser is then reintroduced into the cavity. The alignment of the seed light is tuned to maximize the output power in the regen as seen by the photodiode. The power of the pump light is then slightly adjusted so that the system lases just at the saturation point of the regen.

2.4.8 Multipass Amplifier

The multipass amplifier provides a second amplification step for chirped laser pulses prior to compression. Output pulses from the regen are directed into the multipass

amplifier. Just like the regenerative amplifier, amplification is achieved by passing the laser pulse through a Ti:Sapphire crystal that is pumped with the 532 nm output from a Nd:YAG laser. The crystal is cooled with a chilled water line. While the regen makes use of two Pockels cells to switch a pulse in and out of a laser cavity, the multipass amplifier passes a laser pulse through a Ti:Sapphire crystal three times without retracing its path. The gain of the multipass amplifier can be continuously varied from zero up to a factor of 10 by controlling the amount of Nd:YAG pump light introduced into the Ti:Sapphire crystal. Final output pulse energy from the multipass amplifier is typically 40 mJ, with a total output power of 0.6 W.

2.4.9 Compressor

The temporal chirp which was introduced by the expander is mostly linear and reversible. Therefore, after amplification, pulses are sent through a compressor which removes the linear chirp. A schematic of the compressor is shown in figure 2.8. Functionally, it is quite similar to the expander. Input pulses are diffracted off a grating four times to reverse the frequency chirp introduced by the expander. The grating angle of the compressor is approximately 54° and exactly matches that of the expander when properly aligned. The retro-reflecting mirror pair in the compressor (the analog of mirror M2 in figure 2.6) is mounted on a translation stage so that the relative path lengths for the various frequency components can be adjusted. This adjustment allows

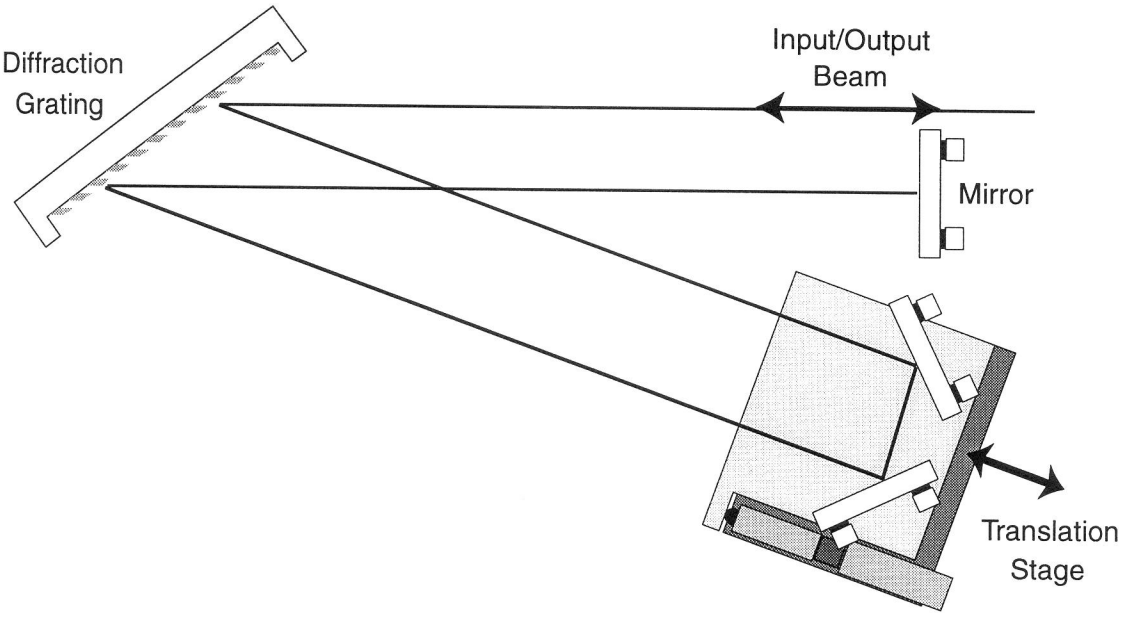

Figure 2.8: Schematic of the laser pulse compressor [1].

some "fine-tuning" of the relative path lengths of the frequency components. Proper alignment of the compressor results in zero temporal chirp of the output pulses. The output pulses from the compressor are approximately 150 fs in duration and have a pulse energy of 30 mJ. The peak power present after pulse compression is on the order of 10^{11} W.

2.5 Characterization of Laser Pulses

A typical problem that arises when trying to characterize ultrashort laser pulses is that only recently have electronic devices been developed which have response times less

than 500 ps. Measuring pulses that are typically orders of magnitude shorter than this limit can only be achieved optically. In short, only ultrashort laser pulses are short enough to measure ultrashort laser pulses. Several different techniques exist for recovering the temporal and / or frequency profile of ultrashort laser pulses. In this thesis, single shot autocorrelation is used to recover the temporal profile of ultrashort pulses. The frequency profile of each pulse is then measured with a spectrometer.

2.5.1 Single Shot Autocorrelator

In a single shot autocorrelator, a beam splitter is used to create two copies of an ultrashort laser pulse. The two pulses then cross at a small angle in a nonlinear second harmonic generation crystal. A burst of second harmonic light is created if the two input pulses are overlapped both spatially and temporally. The geometrical width of the frequency doubled light is proportional to the length of the initial pulse. A charge coupled device (CCD) camera observes the position of the second harmonic output. When a glass slide of known thickness is inserted into one leg of the autocorrelator, the slide delays one leg of the input light by an amount $\Delta t = \frac{d}{c}(n-1)$, where d is the thickness of the slide and n is the index of refraction of the glass. This time delay causes the doubled light to appear in a different spatial position. Direct comparison of the glass slide induced shift in the centroid of the doubled light to the width of the doubled light pulse leads to a calibrated value for the FWHM of the original pulse.

2.5.2 Spectrometer

A simple grating spectrometer is used to roughly measure the absolute frequency of the laser pulses used in the lab. Light is directed into the spectrometer through a 0.5 mm wide slit. The output of the spectrometer is measured with a CCD camera which is hooked up to a monochrome video monitor. A vertical line marked on the monitor indicates the alignment point of the output. To determine the frequency of the light entering the spectrometer, the frequency dial is turned until the spectrometer output, as seen on the monitor, is aligned with the calibration point marked on the monitor screen. The wavelength of the input pulse is then read off of the frequency dial. The spectrometer is accurate to 0.1 nm. The calibration point is determined by directing light from several known frequency standards into the spectrometer. The frequency dial is turned until the readout matches the known value of the frequency standard. Then a mark is made on the monitor screen at the brightest point of spectrometer output.

2.6 Single Shot Detector

Monitoring the evolution of wavepacket dynamics on the picosecond time scale can be more complicated than manipulating dynamics on that time scale. Due to the relatively slow response time of electronic measuring devices, the only method to measure events

which occur in such short times is interaction with ultrashort optical pulses. To observe wavepacket dynamics at a given instant, it is necessary to use a "camera" with a shutter that is faster than the dynamics of interest. Otherwise, the picture is blurred. This is the main idea behind time dependent spectroscopy.

In a typical pump - probe experiment, an initial short optical "pump" pulse puts the system into some state of interest. The goal is to determine the subsequent dynamics of this state. Some time delay, Δt after the pump pulse creates the state, a second "probe" pulse affects the dynamics of the system in a detectable manner. By varying Δt and observing the final state of the system after the two pulses, conclusions can be drawn about the dynamics of the initial wavepacket. Many variations of time domain spectroscopy have developed in recent years. Among them photoionization spectroscopy [11], fluorescence spectroscopy [11], the optical Ramsey method [12], impulse momentum retrieval [13], pulsed field ionization [14], and the atomic streak camera [15].

All present time domain methods are inherently destructive to the wavepacket. To recover dynamical information for a large number of time delays, many identical copies of the original wavepacket must be created. This introduces a potentially large source of error if each copy of the initial wavepacket is slightly different. Furthermore, over the course of an hour long scan of pump - probe time delays, many experimental parameters may drift by some amount. If any other parameters are to be varied as well, the amount

of time necessary to complete one measurement becomes prohibitively long.

To avoid these difficulties, a method of recording a 100 ps long window of pump - probe information in a single laser shot has been developed [1, 16]. The pump and probe pulses counterpropagate through an interaction region. Due to the finite speed of propagation, a position dependent pump - probe time delay exists along the axis of propagation. The path lengths of the pump and probe beam are arranged so that they arrive simultaneously on one edge of the interaction region.

A schematic of the single shot detector is shown in figure 2.9. The atomic beam enters a 12 mm tall region between two 7.5 cm $\times$ 7.5 cm parallel field plates. The upper field plate has a 25 mm by 2 mm slit cut in it such that the long dimension of the slit is perpendicular to the atomic beam. Ions are created in the interaction region through interaction with a combination of laser pulses and electrical pulses and fields. The ions are accelerated upward by an electric field. Ions pass through the slit in the upper field plate and are incident upon a pair of microchannel plates (MCPs) with their position along the length of the slit preserved.

The MCPs are located approximately 1 cm above the upper field plate. A steel ring assembly consisting of three rings holds the two MCPs. The first steel ring is located directly below the lowest MCP and is held at -1400 V. A second ring is located between the two MCPs and is allowed to float. The third ring is located above the top MCP and is grounded. The assembly is held together with three plastic screws. The

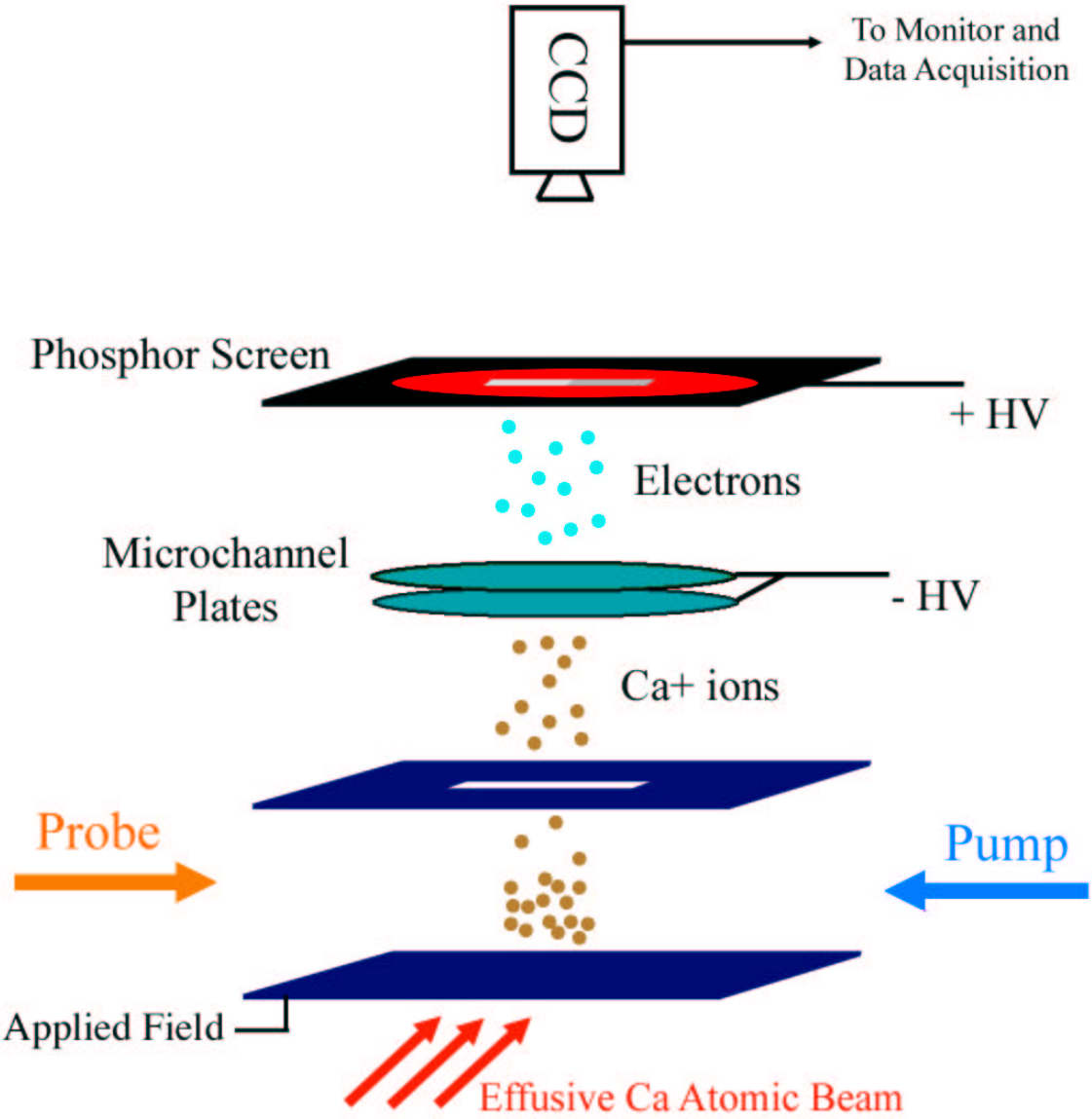

Figure 2.9: Schematic of the single shot detector when used to measure a continuous range of pump - probe time delays in a single laser shot. About 100 ps of time delay can be measured per laser shot [16].

two MCPs have matched resistances of 1.5×10^8 Ω. Each MCP provides a gain of approximately 300 with a bias voltage of -700 V. Increasing the magnitude of the bias voltage does increase the gain in the MCPs, however the MCPs begin to deviate from a linear response for bias voltages larger than 700 V in magnitude. All experiments performed in this thesis take data in "current" mode, where the total amount of ion yield is measured. This differs from "single-event" mode where each individual ion striking the MCPs is counted.

A phosphor screen with a 3 cm^2 active area is situated 3 mm above the microchannel plates. The phosphor is mounted on a piece of glass held between two stainless steel plates. The phosphor assembly is held at a bias voltage of 4500 V. Electrons leaving the microchannel plates strike the phosphor screen, causing the screen to fluoresce. The electron flux energy threshold for phosphor fluorescence is 5×10^{-5} W/cm^2. The phosphor saturates at a current of 0.3 A/cm^2 [17].

Position information observed on the phosphor screen is directly correlated to the position of ions in the interaction region. The fluorescence of the phosphor is observed by a CCD camera located directly above the phosphor screen and exterior to the vacuum chamber. The phosphor output is blue (approximately 450 nm) and the CCD camera is most sensitive to red and the near IR. One possible future improvement to the detector would be to replace the current CCD camera with one more sensitive to the wavelength of light emitted by the phosphor. The video signal from the CCD camera is recorded

by the data acquisition software (see section 2.7).

The ensemble position of the ion cloud along the laser propagation axis is preserved from the interaction region to the phosphor screen. Therefore, the pump - probe time delay information is displayed as position information on the phosphor screen. The detector can measure approximately 100 ps of time delay information in a single laser shot. Other parameters (such as laser frequency or HCP field strength) are varied between successive laser shots. The single shot detector greatly reduces the time necessary for data collection when compared with traditional pump - probe experiments.

2.7 Data Collection Software

Two different data collection programs are used to record data from the experiments presented in this thesis. The first program (DC410) is designed to record single line traces directly from an oscilloscope and was written by T.J. Bensky. The second program (HL Image) captures a standard NTSC screen image from a CCD camera through a PCI frame grabber card in a computer. The main HL Image program was purchased, however a data collection tool for HL Image unique to the current experimental setup was written by T.J. Bensky and edited by J.G. Zeibel.

2.7.1 DC410

The program "Data Collection 410" or DC410 reads voltage vs. time output from a video triggered Tektronix 410A oscilloscope through a General Purpose Interface Board (GPIB). The oscilloscope records a single digitized video line from a CCD camera image. DC410 averages a single line of data from approximately 50 successive separate laser shots together to form an averaged data file. This averaged data file is then recorded to disk. Voltage pulses are sent through the parallel port of a computer to command a stepper motor to turn a set amount after each data file is recorded. Typically, the stepper motor is connected to a micrometer dial on a delay stage or a knob on a voltage supply. In this way, an oscilloscope trace is recorded for each value of time or voltage determined by the position of the motor. The change in position or voltage between steps occurs over less than 0.5 seconds. Each motor step is considered instantaneous relative to the 15 seconds required to record each data file. The DC410 program is used primarily for daily HCP calibration, where oscilloscope traces are taken at small ($\sim$1V) steps of HCP input voltage. The HCP calibration procedure will be described fully in section 3.2.

2.7.2 HL Image

The majority of the data collected for the experiments presented in this work is taken with a frame grabbing software called HL Image. The "active" region of the phosphor

(where data signals are observed) contains approximately 600 pixels by 60 pixels when viewed by the CCD camera. The line output from the camera is connected to a frame grabbing board in a computer. HL Image translates the video input into a window on the computer desktop. A region of interest (ROI) is selected in the video window. The ROI contains the signal to be measured. Typically, some number of individual video frames are averaged together to produce an average image. This number varies depending on the signal to noise ratio of the data being taken, but is usually between 10 and 50. Data may be collected in either raw mode or integrated mode. In raw mode, the 36,000 individual points in the ROI are each recorded as a matrix for each data file. In integrated mode, data points along the shorter dimension of the ROI are added together and then saved. The result is 600 individual data points. Each point contains the integrated signal in each column of 60 points. Through this added integration step, data collected through HL Image has a 60 fold increase in signal averaging when compared to data collected with DC410. However, HL Image lacks the stepper motor controls present in DC410. A screen shot of the computer desktop while HL Image is being used to take data is shown in figure 2.10.

Real time normalization is possible with HL Image. Averaged data files are taken at the maximum and minimum signal strengths and saved to disk as S_{norm} and $S_{background}$ respectively. During data collection, the raw signal is normalized by equation 2.2 prior

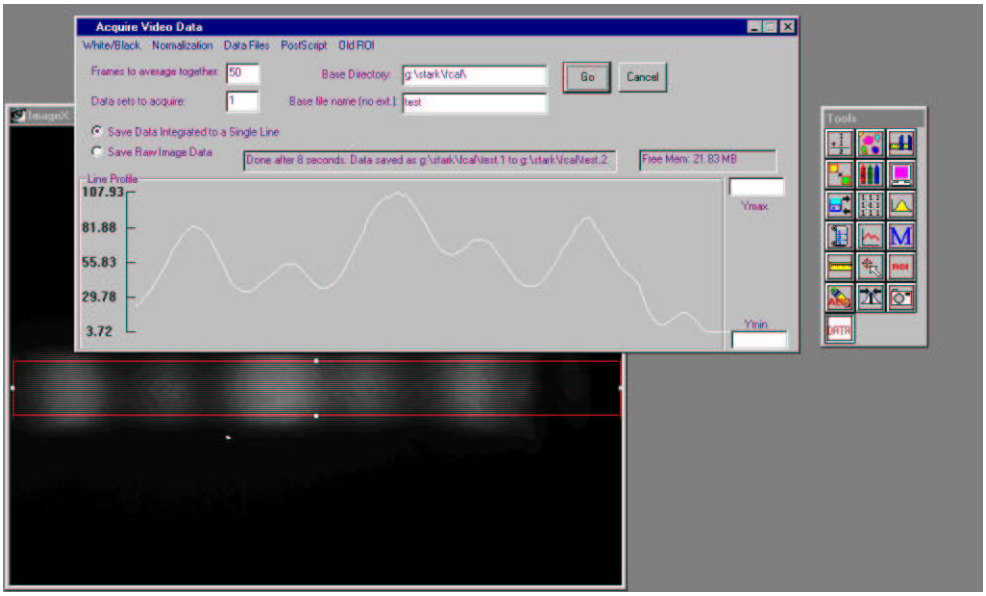

Figure 2.10: A screen shot of HL Image while taking data. The video window shows the image sent to the computer by the CCD camera. The red box in the video window is the region of interest (ROI). Light regions in the video signal correspond to areas of the interaction region where large numbers of ions are being produced. Data is being taken in integrated mode in this figure. The trace that appears in the data toolbox window is data which will be written to disk [18].

to being saved to disk.

$$S_{corrected} = \frac{S_{raw} - S_{background}}{S_{norm} - S_{background}} \tag{2.2}$$

The normalization is necessary to correct for geometrical differences in laser alignment and atomic beam position in the interaction region as well as phosphor sensitivity.

Data recorded by HL Image for this thesis is taken entirely in integrated mode. No variables are changed as a function of two spatial coordinates simultaneously. Experiments may be performed in the future which make use of the full 3 dimensional data recording capabilities of HL Image. For example, time of flight information may be encoded along the horizontal axis, orthogonal to the time delay information. Such a modification would require data to be taken in raw mode. Future improvements such as this will hopefully extend the size of the parameter spaces which may be investigated.

Bibliography

[1] M.B. Campbell, *Rydberg Wavepacket Dynamics*, Ph.D. Thesis, University of Virginia (2000).

[2] Spectra-Physics, *Nd:YAG Lasers User's Manual*, Spectra-Physics, Mountain View, CA (1994).

[3] A.E. Siegman, *Lasers*, University Science Books, Mill Valley, CA, (1986).

[4] J. Hecht, *The Laser Guidebook*, McGraw Hill, Inc., New York, (1992).

[5] W.T. Silfvast, *Laser Fundamentals*, Cambridge University Press, New York, (1996).

[6] T.W. Hansch, *Applied Optics* **11**, 895 (1972).

[7] M.G. Littman and H.J. Metcalf, *Applied Optics* **17**, 2224 (1978).

[8] S.N. Pisharody, J.G. Zeibel, and R.R. Jones, *Phys. Rev. A* **61**, 063405 (2000).

[9] J.C. Diels and W. Rudolph, *Ultrashort Laser Pulse Phenomena*, Academic Press, (1996).

[10] A. Yariv, *Quantum Electronics*, 3rd ed., John Wiley and Sons, New York, (1989).

[11] L.D. Noordam and R.R. Jones, *J. Mod. Opt.* **44**, 2515 (1997).

[12] D.W. Schumacher, D.I. Duncan, R.R. Jones, and T.F. Gallagher, *J. Phys. B* **29**, L397 (1996); L.D. Noordam, D.I. Duncan, and T.F. Gallagher, *Phys. Rev. A* **45**, 4734 (1992); R.R. Jones, D.W. Schumacher, T.F. Gallagher, and P.H. Bucksbaum, *J. Phys. B* **28**, L405 (1995); R.R. Jones, C.S. Raman, D.W. Schumacher, and P.H. Bucksbaum, *Phys. Rev. Lett.* **71**, 2575 (1993).

[13] R.R. Jones, *Phys. Rev. Lett.* **76**, 3927 (1996).

[14] C.S. Raman, C.W.S. Conover, C.I. Sukenik, and P.H. Bucksbaum, *Phys. Rev. Lett.* **76**, 2436 (1996); C.O. Reinhold, J. Burgdörfer, M.T. Frey, and F.B. Dunning, *Phys. Rev. A* **54**, R33 (1996).

[15] G.M. Lankhuijzen and L.D. Noordam, *Opt. Comm.* **129**, 361 (1996); G.M. Lankhuijzen and L.D. Noordam, *Phys. Rev. Lett.* **76**, 1784 (1996).

[16] M.B. Campbell, T.J. Bensky, and R.R. Jones, *Opt. Express* **1**, 197 (1997).

[17] Kimball Physics, Inc., *Phosphor Screen Data Sheets.*

[18] S.L. Jaiswal, *Evolution of Stark Spectra in Barium and Scaled Energy Spectroscopy of Two Electron Atoms*, M.S. Thesis, University of Virginia, (2000).

Chapter 3

Half Cycle Pulses (HCPs)

Only when a wavepacket is near the atomic core is it able to absorb light from an optical pulse [1–4]. In contrast, HCPs are used to give the entire wavefunction a 'kick' in one direction regardless of the position distribution. HCPs have been used to measure the exact quantum state of wavepackets [5] as well as to determine momentum space distributions [4]. When used to manipulate electron dynamics, HCPs have been used to ionize both wavepackets and eigenstates [1–3, 6], to cause transitions between states [7], and to recombine electrons that have ionized to again form bound systems [8, 9]. Together, the combination of short optical pulses and HCPs provide two essential tools for manipulating and probing wavepacket dynamics.

The method used for generating the HCP fields used in this thesis is discussed in the next section. Calibration of HCP fields is then discussed in section 3.2. The Impulse

Momentum Retrieval (IMR) method is used to determine the momentum distribution of a wavepacket through HCP interaction. The details of IMR are introduced in section 3.3. Finally, a new variation on the IMR method known as lock-in IMR is introduced. Sample results from lock-in IMR are compared to previous results to demonstrate the effectiveness of the new method.

3.1 Half Cycle Pulse Generation

HCPs are generated by illuminating a wafer of biased gallium-arsenide (GaAs) semiconductor with a short pulse of ∼780 nm Ti:Sapphire light. The GaAs wafer is photoconductive with a band gap of approximately 1.4 eV. Light with wavelengths less than approximately 880 nm will promote the semiconductor to the conduction band. Only approximately 40 μJ/cm^2 is necessary to saturate conduction within the GaAs wafer [1]. Therefore, much of the Ti:Sapphire laser light is attenuated prior to hitting the GaAs wafer. Each wafer is 0.5 mm thick and has an internal resistance of 10^9 Ω/cm [10]. While in the insulating band, each GaAs wafer can hold off several kilovolts across 1 cm without breaking down.

A schematic of the HCP production process is shown in figure 3.1. When the Ti:Sapphire laser pulse hits the wafer, electrons within the wafer quickly accelerate due to the bias field. The accelerating electrons radiate a short, nearly uni-polar pulsed field which propagates away from the wafer. The radiated field is polarized along the

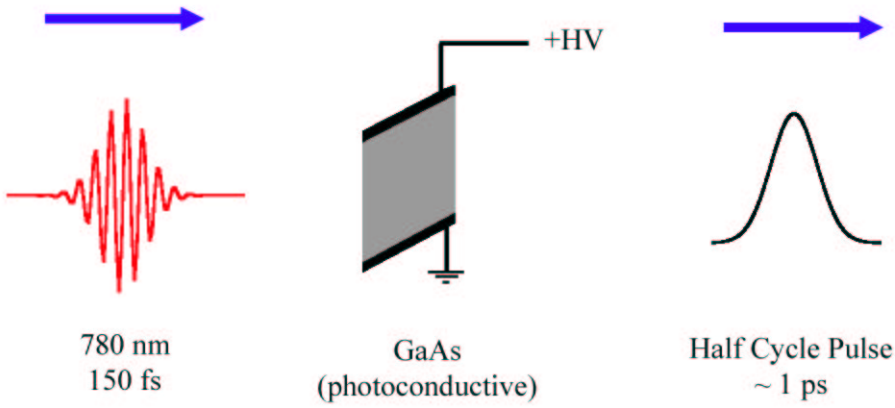

Figure 3.1: Diagram of the method used to produce a HCP field.

axis defined by the +HV lead and ground. The radiated field strength is linearly proportional to the strength of the bias field. The rise time of the radiated field is approximately 0.5 ps.

After the Ti:Sapphire laser pulse has past, the wafer returns to the insulating state. This transition is much slower than the conduction band transition. Electrons decelerate over a period of hundreds of picoseconds. The deceleration produces a field in the opposite direction to that of the initial field, however the maximum strength of the 'recoil' field is typically a factor of 5-10 smaller than the initial pulse height. This negative tail reduces the total time averaged force produced by the total radiated field, although the net force is still nonzero. A graphical representation of a typical HCP temporal profile is shown in figure 3.2.

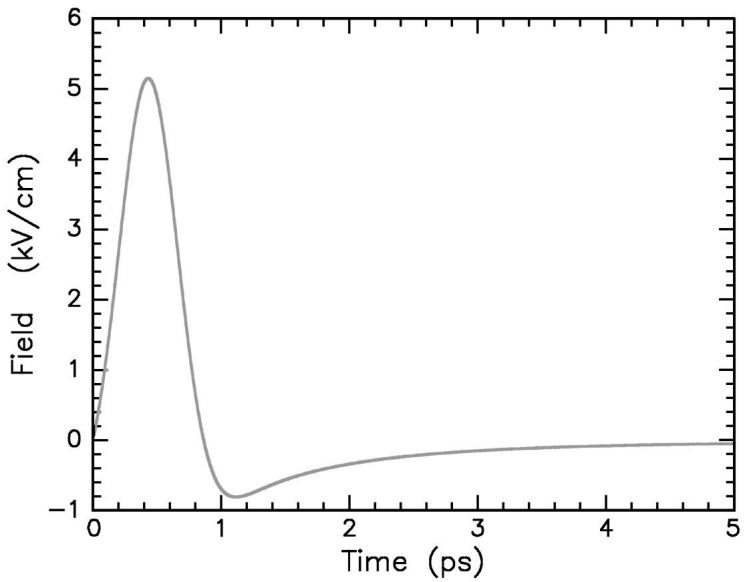

Figure 3.2: Schematic of a typical pulse shape of a HCP field [11]. The initial positive pulse is approximately 1 ps in duration. The negative tail of the HCP persists for hundreds of picoseconds.

The HCP field produced by the GaAs wafer scales linearly with the area of the wafer up to an area of approximately 1 cm^2. The GaAs wafers which are used in this thesis are initially roughly circular and approximately 5 cm in diameter. Each large wafer can be cut into approximately 4 smaller rectangles, each approximately 1.5 cm on a side. Uniform, thin voltage leads approximately 1 mm wide are applied to the top and bottom of one of the wafer pieces with silvered conducting paint. The painted voltage leads must be smooth and uniform as any sharp features in the leads will result in large field gradients and breakdown of the wafer. A wire is connected to the upper lead, while the lower lead is grounded and mounted to the vacuum chamber on a piece of

aluminum. The wire connected to the upper lead is attached to an insulated metal rod on a voltage feedthrough. A bias voltage of up to 10 kV is applied to the rod outside the vacuum chamber. The applied voltage is monitored with a high voltage probe.

The Ti:Sapphire laser pulse used to promote the wafer to the conduction band is expanded in a telescope so that it covers the entire area of the wafer. Any portion of the wafer shielded from the Ti:Sapphire light will not conduct and breakdown may occur within the wafer as electrons are forced to find ways around the shaded area. Once a breakdown of the semiconducting material has occurred in any part of the wafer, the effective area which produces HCP fields is significantly reduced and the wafer must be replaced. An IR card is used to check the size and alignment of the laser pulse by looking at the shadow created by the wafer in the laser pulse while the chamber is open.

The bias field to the GaAs wafer is created in a HV transformer pulse box. A small input voltage (0 V - 60 V) is applied to a transformer. When triggered, the pulse box outputs a 500 μs long voltage pulse with a 50 μs rise time. The maximum output voltage is approximately 100 times the input voltage. The polarity of the HV pulse is selected by a switch. The HV bias field polarity determines the polarity of the HCP field. The trigger for the HV pulse arrives approximately 60 μs before the main laser trigger so that the point of highest voltage of the HV bias field corresponds to the arrival of the Ti:Sapphire laser pulse.

3.2 HCP Calibration

One difficulty with using HCPs is the need to obtain a calibration of the impulse strength of a given HCP field. As discussed in section 2.5, pulses shorter than 1 ns can not be effectively measured by electronic means. A method of measuring the amount of momentum imparted to an electron by a given HCP field is needed. A calibration procedure was developed by Jones *et al.* which measures the nonzero time integrated component of a HCP field by analyzing HCP interaction with specific, known states [1]. They use HCP ionization of Rydberg eigenstates to perform the calibration and this method will be employed to calibrate the HCP fields used in this work.

The nature of the interaction of HCPs with Rydberg states and Rydberg wavepackets is determined by the orbit time of the Rydberg electron. HCPs generated by the procedure discussed in section 3.1 are typically around $\tau_{HCP} = 1$ ps in duration. The Kepler period of a Rydberg eigenstate with principle quantum number n is given by $\tau_K = 2\pi n^3$. If τ_K is much greater than τ_{HCP}, the the HCP - electron interaction can be treated impulsively. The HCP field can be approximated by a delta function impulsive kick. However, if $\tau_K \ll \tau_{HCP}$, then the HCP field must be treated like a slowly varying field. In this thesis, we work entirely in the impulsive regime. For a 1 ps FWHM HCP field, to be safely in the impulsive limit we restrict our analysis to $n > 17$ [12].

For the purpose of this analysis, we consider a Rydberg electron to be a classical entity with momentum $\vec{p}_0$. In the impulsive HCP limit, its momentum after interacting

with a HCP field is $\vec{p} = \vec{p}_0 + \vec{A}$. Here $\vec{A}$ is defined as the impulse transferred to the electron by the HCP. $\vec{A}$ is determined from the time integral of the HCP field and is given by

$$\vec{A} \;=\; -\int \vec{F}_{HCP}(t)dt \;. \tag{3.1}$$

Only for a half cycle pulse is the value of $\vec{A}$ significantly different from zero.

Prior to HCP interaction, an electron moving with momentum $\vec{p}_0$ has energy

$$E_0 \;=\; \frac{p_0^2}{2} \;+\; V(\vec{r}) \tag{3.2}$$

where $V(\vec{r})$ is the potential energy of the electron. By substituting the momentum after HCP interaction, an expression for the final energy of the electron is obtained,

$$E_f \;=\; \frac{1}{2}|\vec{p}_0|^2 \;+\; V(\vec{r}) \;+\; \vec{p}_0 \cdot \vec{A} \;+\; \frac{1}{2}|\vec{A}|^2 \;, \tag{3.3}$$

where we have made the assumption that the electron's motion during the HCP is negligible. The shift in energy, ΔE, due to HCP interaction is therefore given by:

$$\Delta E \;=\; E_f - E_0 \;=\; \vec{p}_0 \cdot \vec{A} \;+\; \frac{1}{2}|\vec{A}|^2 \;. \tag{3.4}$$

The energy gained or lost by the electron due to HCP interaction depends only on its initial momentum (and direction) and the time integrated field of the HCP.

For a HCP field to ionize a Rydberg eigenstate, the change in energy given by equation 3.4 must be greater than the electron's binding energy. The binding energy of a Rydberg electron with principle quantum number n in the absence of any static

fields, is given by

$$E_n = -\frac{Z^2}{2n^2}\ , \tag{3.5}$$

where Z is the effective charge of the atomic core. Combining equations 3.4 and 3.5 and solving for the momentum yields

$$p_c \equiv \frac{Z^2}{2n^2 A} - \frac{A}{2}\ . \tag{3.6}$$

A HCP impulse of strength A will ionize a Rydberg state with principle quantum number n if the momentum of the electron along the direction of the HCP is greater than or equal to p_c.

The calibration procedure is performed in the following manner. First, a population of Rydberg eigenstates with identical principle quantum number n is prepared in a given atomic sample. The amount of HCP ionization of the sample is then measured as a function of HCP field for several values of n. The HCP field strength is controlled by the DC410 data acquisition software which slowly increments a stepper motor controlling the input voltage to the HV transformer. Weak HCP fields do not ionize any of the Rydberg population. Very strong HCP fields ionize all of the Rydberg population, regardless of the momentum of each electron in the ensemble. Due to the symmetry of the eigenstates, equal fractions of the wavepacket have $p_0 > 0$ and $p_0 < 0$. When $p_c = 0$ in equation 3.6, 50% of the initial Rydberg population has been ionized. [1–3].

Figure 3.3 shows HCP ionization of four different Ca Rydberg states as a function of input voltage to the HV transformer. The solid lines are ionization scans taken

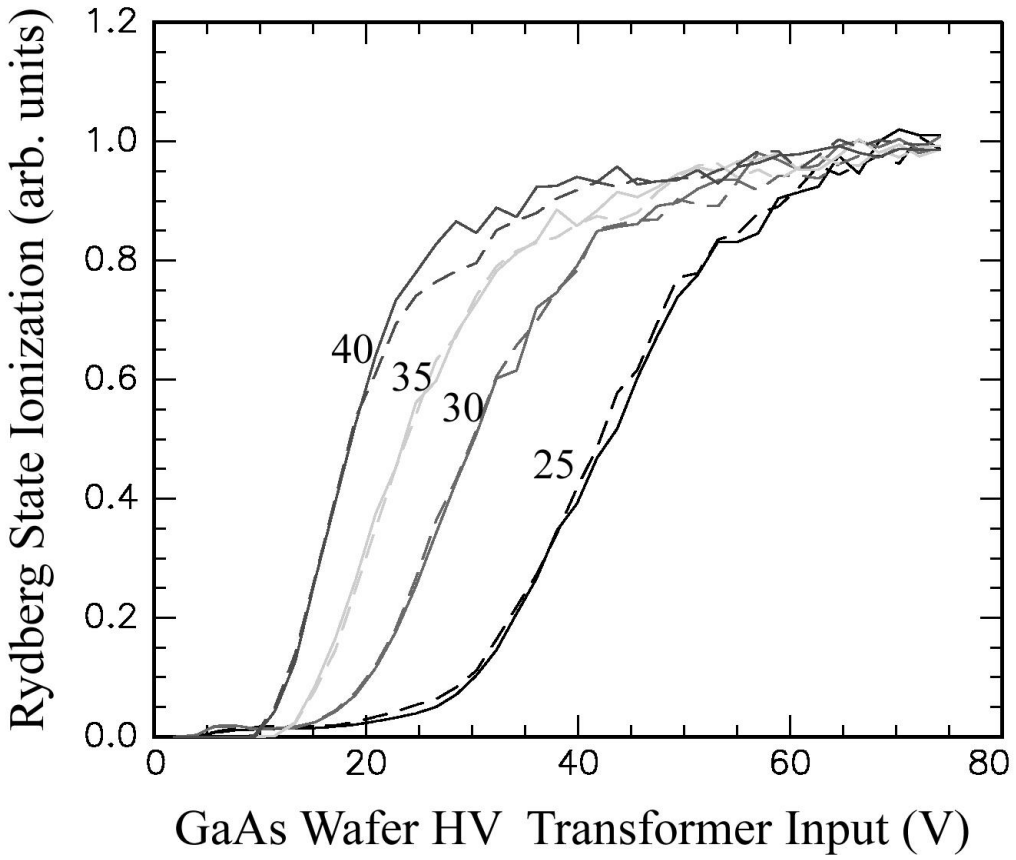

Figure 3.3: Measured ionization probabilities for the $40d$, $35d$, $30d$, and $25d$ eigenstates of calcium as a input voltage to the HV transformer which generates the HV bias on the GaAs wafer. The solid (dashed) curves are for a positive (negative) bias field.

at positive bias voltages. The dashed lines are ionization scans taken at negative bias fields. The polarity of the bias voltage determines the polarity of the HCP field. Higher n states are completely ionized at lower HCP fields than lower n states. The maximum amount of observed ionization for each n state is normalized to unity. Input voltages resulting in 10% and 50% ionization are then recorded. Uncertainty in the measured ion yield corresponding to 100% ionization introduces an error of $\sim$5% in the input voltage of the 50% ionization point. The HCP field is calibrated in atomic units by setting the value of the HCP impulse that results in 50% ionization to the value $A = \frac{1}{n}$ (i.e. $p_c = 0$). These values are compared to calibrated values to recover the HCP field in V/cm [1–4, 13].

HCP ionization data similar to figure 3.3 are measured at the beginning and end of each day, as well as after any major change in the alignment of the laser system. Any significant deviation in the location of the 50% ionization point signals a problem with either the laser alignment, GaAs wafer integrity, or both. The average value of the 50% ionization point for each n state is calculated from an average of all HCP ionization scans taken on a given day. These values are used to calibrate all HCP field measurements taken that day.

Classical calculations of HCP ionization of Rydberg states have been done by several people [1–4, 13, 14]. The classical calculations are performed by numerically integrating the equations of motion for an electron bound to an atomic core by the Coulomb

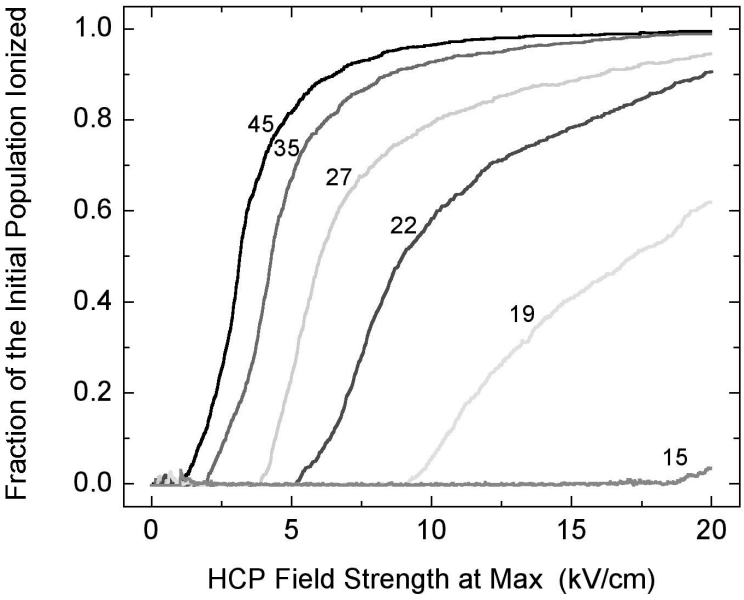

Figure 3.4: Classical calculation of HCP induced ionization of a Rydberg eigenstate. Shown for d state eigenstates of n = 45,35,27,22,19, and 15.

potential. A complete description of the classical calculations performed for this thesis can be found in appendix B. Calculated HCP ionization curves for six values of n are presented in figure 3.4. The overall shape of the HCP ionization curves is reproduced well by the calculations. The relative magnitudes of HCP ionization for successive n values is also consistent with measured data.

3.3 Impulse Momentum Retrieval

As discussed in section 1.4, an electron may gain or lose energy due to HCP interaction regardless of its position. From equation 3.6, we know that a HCP field will ionize an

electron with momentum p along the HCP axis when $p \geq p_c$. Therefore, it is possible to recover information about the average momentum distribution of an ensemble of electrons by applying a HCP field. The technique used to recover the momentum distribution is known as impulse momentum retrieval or IMR. IMR relies on the fact that the total HCP ionization signal is the integral of the momentum distribution in scaled units. Therefore, recovering a derivative of the HCP ionization data yields a momentum distribution along the direction of the HCP polarization axis.

3.3.1 Normal IMR

Experimentally, the amount of HCP induced ionization of a given Rydberg eigenstate or electronic wavepacket is measured as a function of HCP field. The ionization curves are then calibrated in atomic units of HCP impulse. A spline fit to the ionization curves is performed. The derivative of the ionization curves, $\frac{dI}{dA}$ is recovered through the spline fitting routine. Here, I represents the measured ionization probability. It is this quantity that is measured. After we measure I as a function of A, we then compute $\frac{dP}{dA}$, where P is the probability that system has ionized due to a HCP of strength A with field polarized along $\hat{n}$. We want to determine $\frac{dP}{dp_n}$. From the chain rule we have

$$\frac{dP}{dp_n} = \left(\frac{dP}{dA}\right)\left(\frac{dA}{dp_n}\right), \tag{3.7}$$

The resulting graph is the normalized momentum distribution of the system along the direction of HCP polarization. An example of IMR for an eigenstate is shown in figure

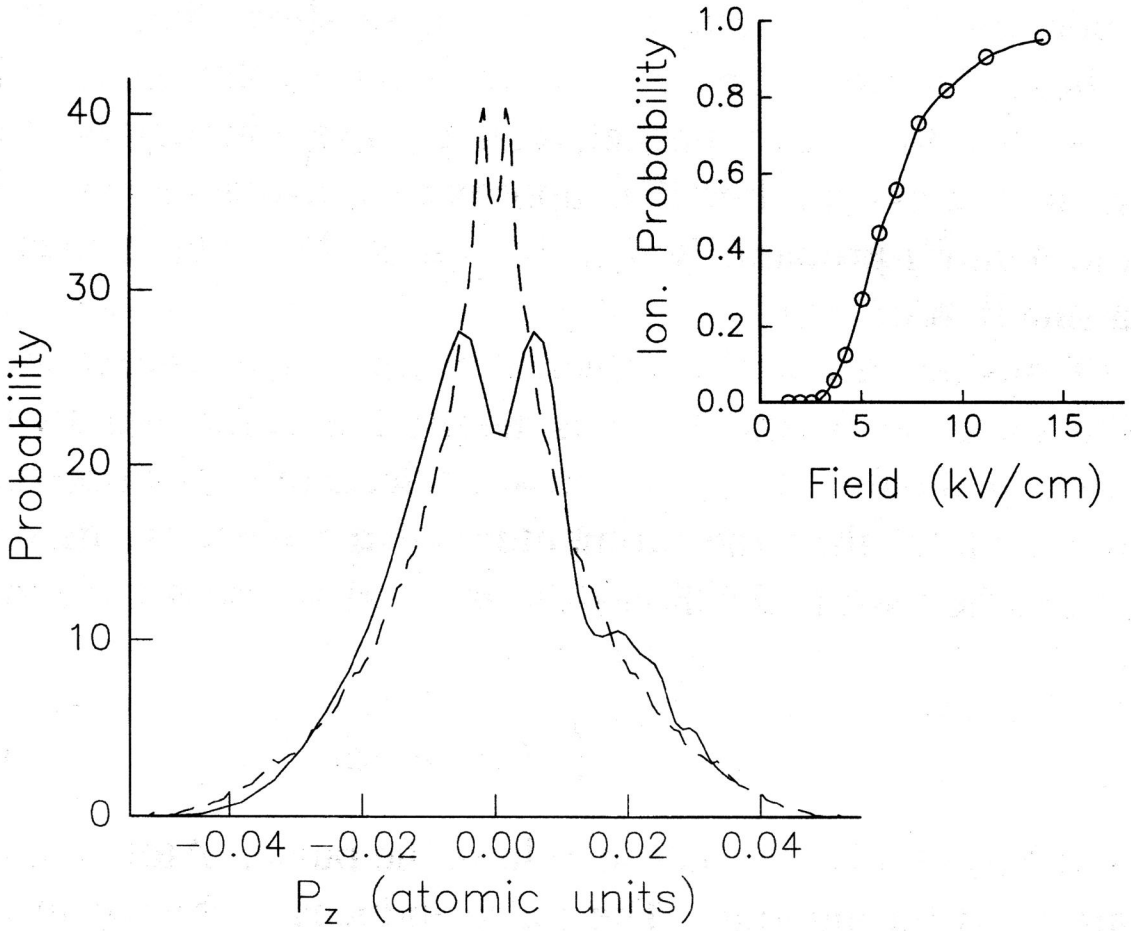

Figure 3.5: Measured probability distribution for p_{0_z} for the Na $25d$ state obtained using the IMR technique (solid curve). Shown also is a theoretical momentum distribution for comparison. Inset: The ionization probability used to generate the experimental momentum distribution. Actual data points are shown with circles and the spline fit to the data is shown in the solid line [4].

3.5 [4].

3.3.2 Lock-In IMR

Previous applications of IMR have directly measured the amount of wavepacket ionization as a function of HCP field strength. Suppose we have a wavepacket with average energy E_{wp}. Any portions of the wavepacket with momentum p_0 along the HCP field polarization axis with

$$p_0 \geq \frac{E_{wp}}{A} - \frac{A}{2} \tag{3.8}$$

will be ionized by a HCP field of strength A. The probability the wavepacket has momentum equal to p_0 is proportional to the derivative of the HCP ionization curve. Unlike the previous IMR work [4, 16], lock-in IMR measures the derivative of the HCP induced ionization directly instead of measuring the fraction of the wavepacket ionized and then calculating its derivative.

In lock-in IMR, the ramped voltage applied to the GaAs wafer which creates the HCP field has the form

$$F(t) = F_0 \left(\frac{t}{T}\right) + \Delta F \cdot cos\Big(2\pi f t\Big) \ . \tag{3.9}$$

F_0 is the maximum voltage applied to the GaAs wafer, T is the total length of the scan, and f and ΔF are the frequency and magnitude of a small applied sinusoidal voltage variation. Figure 3.6 shows a plot of measured HCP ionization signal of an $n = 35$ Rydberg eigenstate. The ionization signal oscillates at the same frequency as

the HCP bias voltage. For the data shown in figure 3.6, $f = 0.02$. The magnitude of the oscillation in the ionization signal is proportional to the derivative of the ionization signal.

A small window of the data is created by multiplying the oscillating "dithered" signal by a Gaussian envelope. An example of the resulting data window is shown in figure 3.6(b). One window is created for each value of HCP field strength, $F_0(t/T)$. Each window is then Fourier transformed, yielding a frequency spectrum for each field strength. Multiplication of the each data window by a Gaussian envelope removes all artificial hard edges created in each data window before Fourier transforming. This eliminates a source of artificial noise in the Fourier spectrum. The spectral power at the frequency f for each data window is recovered by integrating an area around f in the Fourier spectrum. This power is proportional to the amount of variation in the ion signal and is labeled S_{AC}. Similarly, the zero frequency component of the Fourier transform yields the DC component of each data window (labeled S_{DC}). S_{DC} is equal to the previous direct measurements of HCP ionization [4]. The Fourier spectrum for a typical data window is shown in figure 3.7. The sections of the frequency distribution which are integrated to yield S_{AC} and S_{DC} are shaded. For this technique to be meaningful, it is required that $\Delta F \ll F_0$ and $1/f \ll T$. These conditions ensure that the number of oscillation cycles over any small range of F_0 is large and that $\frac{\Delta S}{\Delta F}$ approximates $\frac{dS}{dF}$.

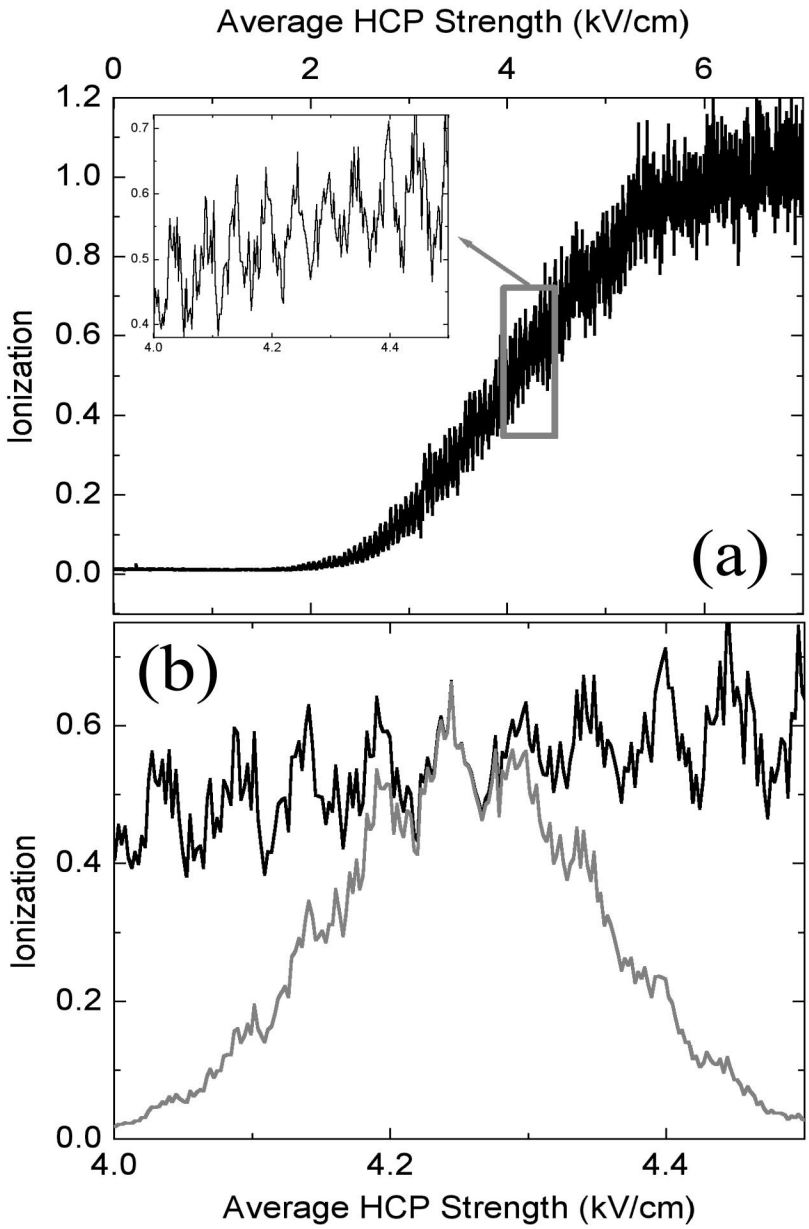

Figure 3.6: (a) HCP ionization scan of a Rydberg eigenstate with a dithered HCP input voltage. Modulations in the ionization signal due to the HCP voltage dither are visible in the inset. (b) The black curve is the HCP ionization signal which was shown in the inset in (a). The red curve is the ionization signal multiplied by a Gaussian envelope function centered at 4.25 kV/cm. A Fourier transform of the red curve yields the values of S_{AC} and S_{DC} at 4.25 kV/cm.

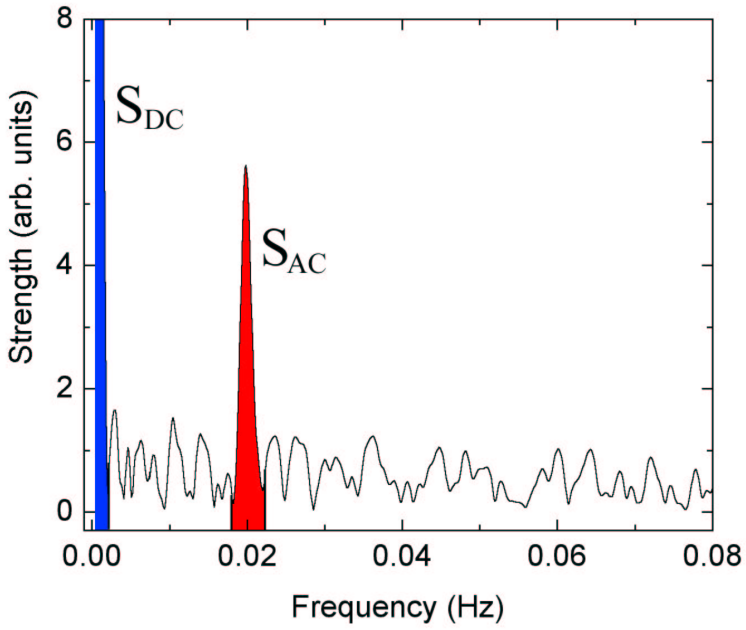

Figure 3.7: The black curve is a Fourier transform of a single Gaussian window of a sample lock-in IMR data scan. This frequency spectrum is the Fourier transform of the red curve in figure 3.6. A large peak in the frequency spectrum occurs at zero frequency due to the DC offset of the data. A smaller peak occurs at the dither frequency f. A small region (sampling window) around each peak is integrated to determine the values of S_{AC} and S_{DC} for the HCP field strength at the center of the Gaussian envelope.

Due to the redundancy introduced by simultaneously measuring an ionization signal (S_{DC}), and its derivative (S_{AC}), additional DC noise reduction is possible. The measured value of S_{DC} can be written as

$$S_{DC}(F) \;=\; S(F) \cdot N(F)\;, \tag{3.10}$$

where $S(F)$ is a reduced noise signal as a function of HCP field and $N(F)$ is a function which represents the noise common to both the "AC" and "DC" signals. $N(F)$ is composed of amplitude noise which varies over time scales longer than the sampling

window. This may arise from fluctuations in the laser power or atom density. In a similar manner, the measured value of S_{AC} can be written as

$$S_{AC}(F) \;=\; \frac{dS(F)}{dF} \cdot N(F) \cdot \Delta F \;, \tag{3.11}$$

where $\frac{dS(F)}{dF}$ is the noise reduced derivative signal as a function of HCP field and ΔF is the constant magnitude of the applied sinusoidal oscillation. The noise function $N(F)$ is identical for both $S_{DC}(F)$ and $S_{AC}(F)$. Solving this system of differential equations for $N(F)$ yields

$$N(F) \;=\; \left(\frac{N(0)}{S_{DC}(0)}\right) S_{DC}(F)\; exp\Big[-\int_0^F \left(\frac{S_{AC}(F')}{S_{DC}(F')}\right)\left(\frac{1}{\Delta F}\right) dF'\Big] \;. \tag{3.12}$$

Therefore, $\frac{dS(F)}{dF}$ can be obtained by dividing $S_{AC}(F)$ by $N(F)$ and ΔF. The normalization function $N(F)$ typically varies by at most 20% across all field values. To get the momentum distribution from $\frac{dS(F)}{dF}$, a simple chain rule yields

$$\frac{dS(F)}{dp} \;=\; \left(\frac{dS(F)}{dF}\right)\left(\frac{dF}{dA}\right)\left(\frac{dA}{dp}\right) \;. \tag{3.13}$$

Equations 3.1 and 3.8 are then used to convert $S(F)$ to $S(p)$.

In principle, a single scan of HCP field strength can be used to recover the entire momentum distribution of a given wavepacket along a given axis. In practice however, it is experimentally difficult to accurately map the portion of the distribution which requires very strong HCP field strengths. To correct for this, two separate scans are typically taken with opposite HCP polarities (for example along $+\hat{z}$ and -$\hat{z}$) to create

a single momentum distribution. For example, a HCP field polarized along $-\hat{z}$ is used to measure momentum values $-\infty < p_z < .015$. Then a HCP polarized along $+\hat{z}$ measures the fraction of the wavepacket with $-.015 < p_z < \infty$. In the region of overlap a difference function is created such that

$$\delta \;=\; p_z^+ - a \cdot p_z^- \;. \tag{3.14}$$

The value of a is chosen which minimizes the parameter δ and a final, combined momentum distribution is obtained. Typically, $0.9 \leq a \leq 1.1$. Once a value for a has been determined then the momentum distributions are combined into a single distribution. A weighted linear interpolation between the two halves is performed in the region of overlap. For example, at precisely $p = 0$ the final momentum distribution is determined by adding $0.5 \times p_z^+$ and $0.5 \times a \cdot p_z^-$.

3.3.3 Momentum of a Radial Wavepacket

To test the effectiveness of the lock-in IMR technique, the momentum distribution of a radial Rydberg wavepacket is recovered and compared to a similar result using normal IMR. First, a wavepacket is created by exciting Ca atoms through an intermediate $4s4s$ state to a $4snd$ radial wavepacket. The wavepacket is created with a 15 cm^{-1}, 1 ps laser pulse and contains approximately seven n states centered around $n = 36$. A state selective field ionization scan of the wavepacket is shown in figure 3.8 [15]. HCP ionization scans of the wavepacket are taken for HCP fields aligned along both $+\hat{x}$ and

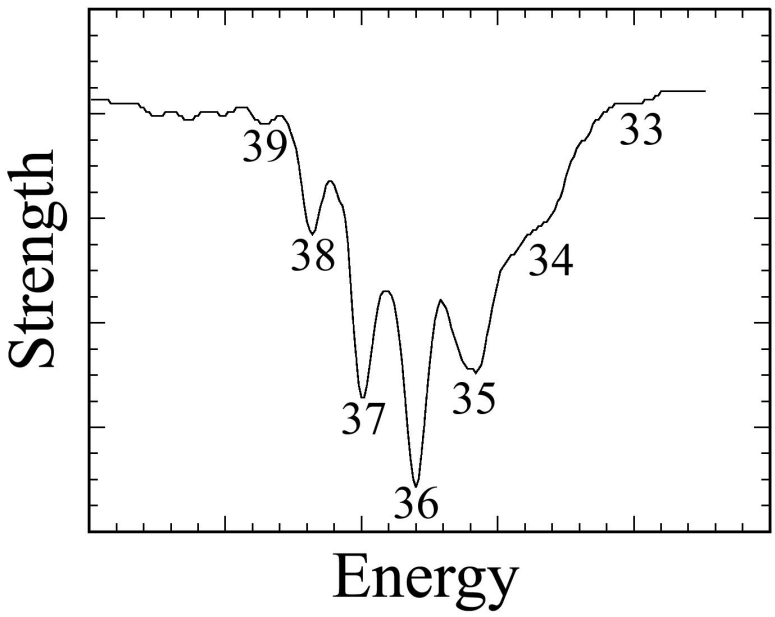

Figure 3.8: State selective field ionization (SSFI) scan of the radial Rydberg wavepacket used to test the lock-in IMR technique. The packet is centered around $n = 36$ and contains approximately seven n states. Each n value is shown on the plot.

$-\hat{x}$ with the lock-in IMR technique. The two scans are then combined through the method described in equation 3.14. The resulting momentum distribution is shown in figure 3.9.

Momentum distributions of radial wavepackets taken with the normal IMR technique can be found in reference [16], however that work did not combine two antiparallel scans to produce a final distribution. (For comparison, momentum distributions of a Stark wavepacket obtained through normal IMR can be found in [17] which are created by combining two antiparallel HCP ionization scans.) A quantum mechanical calculation of the $\hat{x}$ momentum distribution of a radial Rydberg wavepacket is shown in figure

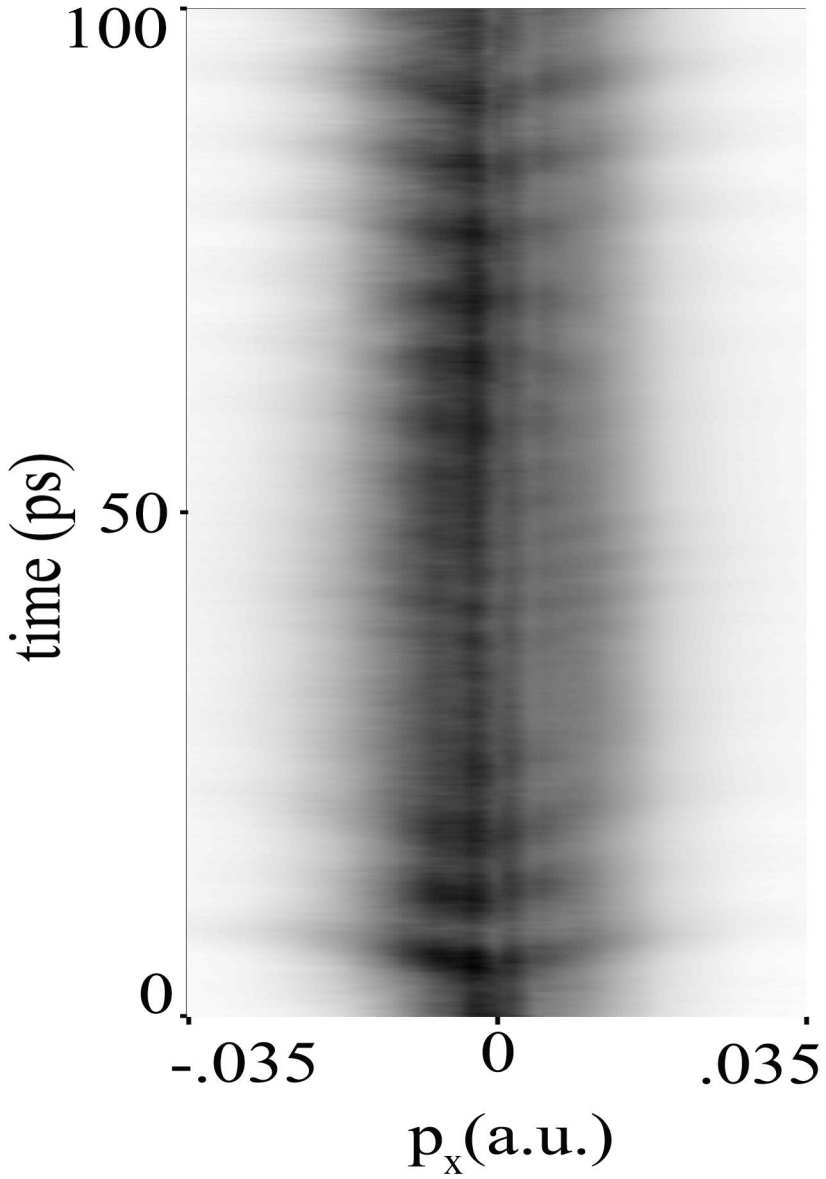

Figure 3.9: Recovered momentum distribution of a radial Rydberg wavepacket using the lock-in IMR method. The time axis shows the time between the creation of the wavepacket and the probe.

3.10 [16, 18]. Both full and fractional revivals of the radial wavepacket can be seen in both the lock-in IMR obtained momentum distribution and the quantum calculations. The fractional revivals are not observed in [16]. In general, the signal to noise ratio achieved through lock-in IMR is up to a factor of two better than the original IMR method. However, small features such as the fractional revival structure are visible with the lock-in IMR method which are not seen in the regular IMR method.

The main advantage to the lock-in IMR technique is the reduced sensitivity to noise. A high signal to noise ratio is possible in the experimental investigation of the radial Rydberg wavepacket. Therefore, the normal IMR method can be applied to recover momentum distribution information. In this case, the lock-in IMR method is used to improve the detail which can be measured in the momentum distribution. However, when trying to study more complex wavepackets (such as the recombined electronic wavepacket in chapter 6) the signal to noise ratio is frequently low. A low signal to noise ratio renders the normal IMR method ineffective. In these cases, the only possible way to recover the momentum distribution of the wavepacket is through lock-in IMR.

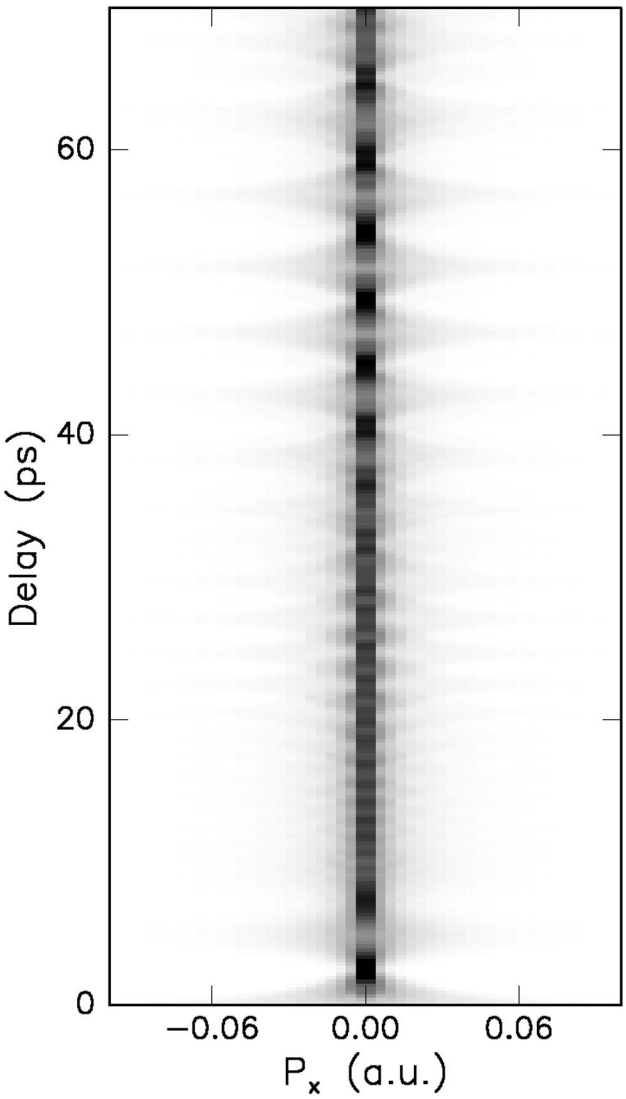

Figure 3.10: Quantum mechanical calculation of the momentum distribution of a radial Rydberg wavepacket [18].

Bibliography

[1] R.R. Jones, D. You, and P.H. Bucksbaum, *Phys. Rev. Lett.* **70**, 1236 (1993).

[2] C.O. Reinhold, M. Melies, H. Shao, and J. Burgdörfer, *J. Phys. B* **26**, L659 (1993).

[3] R.R. Jones, N.E. Tielking, D. You, C. Raman, and P.H. Bucksbaum, *Phys. Rev. A* **51**, R2687 (1995).

[4] R.R. Jones, *Phys. Rev. Lett.* **76**, 3927 (1996).

[5] R.R. Jones and M.B. Campbell, *Phys. Rev. A* **61**, 013403 (1999).

[6] O. Zobay and G. Alber *Phys. Rev. A* **60**, 1314 (1999).

[7] N.E. Tielking and R.R. Jones, *Phys. Rev. A* **52**, 1371 (1995).

[8] T.J. Bensky, M.B. Campbell, and R.R. Jones, *Phys. Rev. Lett.* **81**, 3112 (1998).

[9] J.G. Zeibel and R.R. Jones, *Phys. Rev. Lett.* **89**, 093204 (2002).

[10] American Xtals, Inc., *GaAs Data Sheet.*

[11] P. Uhd Jepsen, R.H. Jacobsen, and S.R. Keiding, *J. Opt. Soc. Am. B* **13**, 2424 (1996); P. Kužel, M.A. Khazan, and J. Kroupa, *ibid.* **16**, 1795 (1999); A. Gürtler, C. Winnewisser, H. Helm, and P. Uhd Jepsen, *J. Opt. Soc. Am. A* **17**, 74 (2000).

[12] T.J. Bensky, G. Haeffler, and R.R. Jones, *Phys. Rev. Lett.* **79**, 2018 (1997).

[13] C.O. Reinhold, H. Shao, and J. Burgdörfer, *J. Phys. B* **27**, L469 (1994); C.O. Reinhold, M. Melles, H. Shao, and J. Burgdörfer, *ibid.* **26**, L659 (1993); M.T. Frey, F.B. Dunning, C.O. Reinhold, and J. Burgdörfer, *Phys. Rev. A* **53**, R2929 (1996); C.O. Reinhold, J. Burgdörfer, M.T. Frey, and F.B. Dunning, *ibid.* **54**, R33 (1996).

[14] N.E. Tielking, T.J. Bensky, and R.R. Jones, *Phys. Rev. A* **51**, 3370 (1995).

[15] T.F. Gallagher, *Rydberg Atoms*, Cambridge University Press, Cambridge, (1994).

[16] R.R. Jones, *Phys. Rev. A* **57**, 446 (1998); M.B. Campbell, T.J. Bensky, and R.R. Jones, *ibid* **58**, 514 (1998).

[17] M.B. Campbell, T.J. Bensky, and R.R. Jones, *Phys. Rev. A* **59**, R4117 (1999).

[18] M.B. Campbell, *Rydberg Wavepacket Dynamics*, Ph.D. Thesis, University of Virginia, (2000).

Chapter 4

Manipulating Wavepacket Dynamics Part 1: Centrifugal Electron - Ion Recombination

4.1 Introduction

Very well described in chapter 3 is one type of novel electromagnetic interaction (the HCP field) which we use to change the electron's environment. In this chapter, we use HCPs to affect the dynamics of atoms which have "fallen apart". That is, we apply HCP fields to a system of an electron and a nearby ion and monitor how the electron - ion system responds. The work presented in this chapter has been published in [1].

The formation of a neutral atom from the combination of an ion and a free electron is a complicated process which has been the subject of considerable study [2, 10]. Typically, recombination is facilitated by a third body which extracts energy from a continuum electron while it is in the vicinity of an ion. In radiative recombination (RR), the third body is a photon that is produced, via spontaneous or stimulated emission, during an electron-ion collision. In three-body recombination (TBR), the primary electron-ion collision takes place in the field of a passing charged particle which carries off the excess energy and momentum. Dielectronic recombination (DR) is a two-step process that proceeds via resonant collisional energy transfer from the free electron to a bound electron on the participating ion. The continuum electron is captured into an autoionizing state which is stabilized via spontaneous or stimulated photon emission.

While each of these recombination mechanisms is conceptually simple, calculating accurate recombination rates is difficult in practice. In any plasma, the net recombination rate and the relative importance of the various recombination mechanisms depends on a number of parameters including the density, temperature, and electronic structure of the constituent ionic and neutral species [2–6]. Nevertheless, detailed knowledge of recombination rates is critical to studies in diverse areas such as the stability of fusion or interstellar plasmas [2, 7], the behavior of ultra-cold Rydberg gases [8], and the formation of antihydrogen from trapped positrons and antiprotons [9].

One method of experimentally investigating recombination events was developed by

Bensky *et al.* [11]. In their method, HCPs (such as those introduced in chapter 3) have been successfully used to mimic the time dependent collision fields responsible for TBR. In this chapter, experiments are described which investigate a new method of studying the effects of static fields on electron - ion recombination based on the techniques developed by Bensky [11, 12]. The role of the collision angle, θ, between an applied static field and the direction of motion of a passing charged particle is investigated. The angle θ is measured in radians from the polarization axis of the static field. We have measured up to a factor of three increase in TBR probability compared to the previous work [11] for certain values of θ. In Bensky's work, the motion of the third body, and therefore the collisional field, is colinear with the direction of polarization of an external static field ($\theta = 0, \pi$). They studied only two limiting cases of collision angles in TBR. We extend this work by investigating electron - ion recombination probability for a range of θ values. The inherent cylindrical symmetry involved in the problem implies that the results can be extended to any field orientation.

Three individual cases are considered experimentally. In the first case, the HCP field mimics that of a charged particle passing a free electron and a nearby ion along the same direction as the static field polarization axis. This case is called the "parallel" case (θ=0). In this case, the atom experiences a kick along the static field polarization axis. In the second case, ($\theta = \pi$), the system feels a kick in a direction opposite, or antiparallel to the static field polarization axis. This is called the "antiparallel" case.

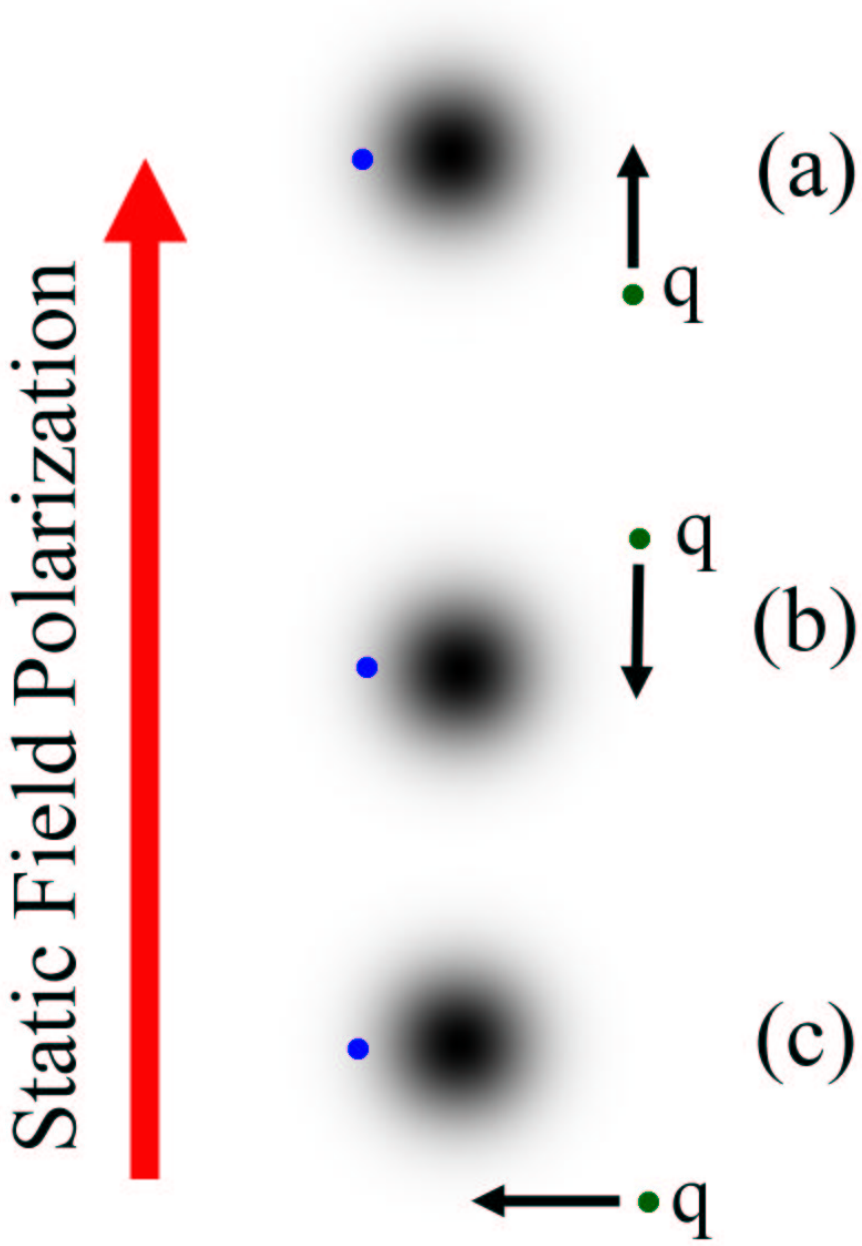

Figure 4.1: A schematic diagram of the three orientations of three body recombination studied in this chapter. The (a) "parallel" (θ=0), (b) "antiparallel" ($\theta = \pi$), and (c) "orthogonal" ($\theta = \pi/2$) cases are shown. The passing charge q is shown in green. The electron is shown in blue next to a nearby ion.

Finally, in the third case the system feels a kick orthogonal to the static field axis ($\theta = \pi/2$). This is analogous to a charged particle moving past the system orthogonal to the static field axis. This will be known as the "orthogonal" case. A schematic of the corresponding three body recombination collision angles in shown in figure 4.1. A schematic of the combined Stark and Coulomb potentials is shown in figure 4.2(a). The saddle point is the $-z$ location of the local maximum in the potential. Shown in figures 4.2(b) and 4.2(c) are "top views" of two of the three field orientations studied in this work. Recombination probability is also measured for values of θ aside from the three main cases (parallel, antiparallel, and orthogonal). The results show a simple linear superposition of the three main cases. Therefore, only results from the three main cases will be presented.

As stated previously, our primary interest is the effect of static electric fields on the recombination process to better understand actual recombination rates in plasma environments. Therefore, Ca atoms are photoionized and recombined in the presence of a uniform static field, and we record the number of Rydberg atoms produced as a function of (i) the delay between the photoionizing laser and recombining HCP (Δt_{HCP}); (ii) the initial energy of the continuum electron; (iii) the HCP field strength; and (iv) the relative orientation of the HCP and static fields. For relatively weak kicks, we find that the recombination probability is significantly higher for orthogonal, as opposed to parallel or antiparallel, HCP and static fields. The enhanced recombination is due to

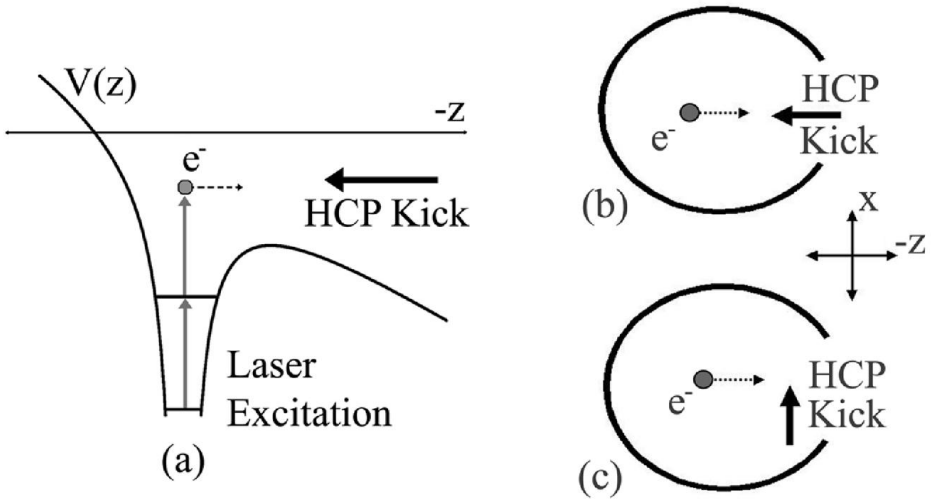

Figure 4.2: Shown in (a) is a schematic "side view" of the laser excitation and HCP ionization scheme in the presence of a static electric field. In (a), the "antiparallel" orientation of the HCP field and static field is illustrated. Figure (b) shows a "top view" of the Coulomb and Stark potentials for the "antiparallel" field orientation. The solid line represents a potential barrier which prevents the electron from exiting the system. The electron's motion in the figure is towards the hole in the potential. Figure (c) shows a similar situation to (b) except with the "orthogonal" field orientation.

a centrifugal effect in which the free electron is dynamically stabilized due to a change in its angular momentum rather than a decrease in its energy.

4.2 Experimental Methods

In the experiment, a 5 ns dye laser promotes Ca atoms in a thermal atomic beam from the $4s4s$ ground state to an intermediate $4s4p$ level. The excitation takes place in a static field which does not appreciably effect the ground or intermediate state

of the calcium atoms. Each laser pulse is polarized along the direction of the static field polarization axis. The ensemble of atoms is then exposed to a 1 ps laser pulse which transfers population from the $4s4p$ state to a coherent superposition of $4s\epsilon k$ continuum Stark states. The newly created $4s\epsilon k$ continuum wavepacket then moves radially outward. Without further interaction, each portion of the wavepacket that moves towards the saddle point in the Stark potential will escape to infinity since its energy is greater than the saddle point energy, $E_c = -2\sqrt{F_s}$. The time that it takes for the wavefunction to be completely ionized depends on the average energy and bandwidth of the laser pulse that excites the wavepacket, and the strength of the applied field. For a wavepacket with an average energy $E_0 > E_c$, a significant portion ($\geq$90%) of the wavefunction will ionize after a few multiples of the Kepler period ($\tau_K = 2\pi n^3$), where n is the principal quantum number of the central state of the wavepacket. Eventually, all the wavepacket ionizes, independent of the launch direction due to the coupling between the "uphill" and "downhill" Stark states in the non-hydrogenic potential. Obviously, no recombination occurs in this case since there is no passing charge in the system. The role of the non-hydrogenic potential is critical to understanding the observed recombination and will be discussed in detail in the following section. Furthermore, appendix D presents a full description of Stark states and non-hydrogenic state coupling for completeness.

The effect of a passing charged particle in a plasma is simulated by a HCP whose

duration is small compared to the time scale of τ_K. The HCP field arrives at a variable time delay Δt_{HCP} after the creation of the Stark continuum wavepacket. The short HCP duration allows treatment of the system in the impulsive regime. The probability for successful electron - ion recombination is a function of Δt_{HCP} as well as the direction and magnitude of the impulse delivered by the HCP field. Similarly, the probability of observed recombination is dependent upon the relative positions of an ion and a nearby free electron as well as the strength of the field generated by a passing charge and the impact parameter. An impulse incident upon the electron - ion system will recombine only the part of the electron's wavefunction that is both radially inside the saddle point and, after HCP interaction, has total energy less than the effective m - dependent saddle point energy.

Figure 2.9 shows a schematic of the interaction region and detector assembly used in this experiment. A constant voltage is applied to the upper field plate to create the static field which is oriented in the $\hat{z}$ direction. $4s4p$ calcium atoms are transferred into the field induced continuum by a picosecond laser pulse with a wavelength of approximately 391 nm. The laser pulse has a bandwidth of approximately 20 cm^{-1} and is therefore resonant with a band of zero field Rydberg levels. The HCP "collision field" is generated through the method described in chapter 3. The HCP only simulates the component of the true collision field seen by an atomic system transverse to the motion of the passing charge. Since the time integrated impulse generated by the longitudinal

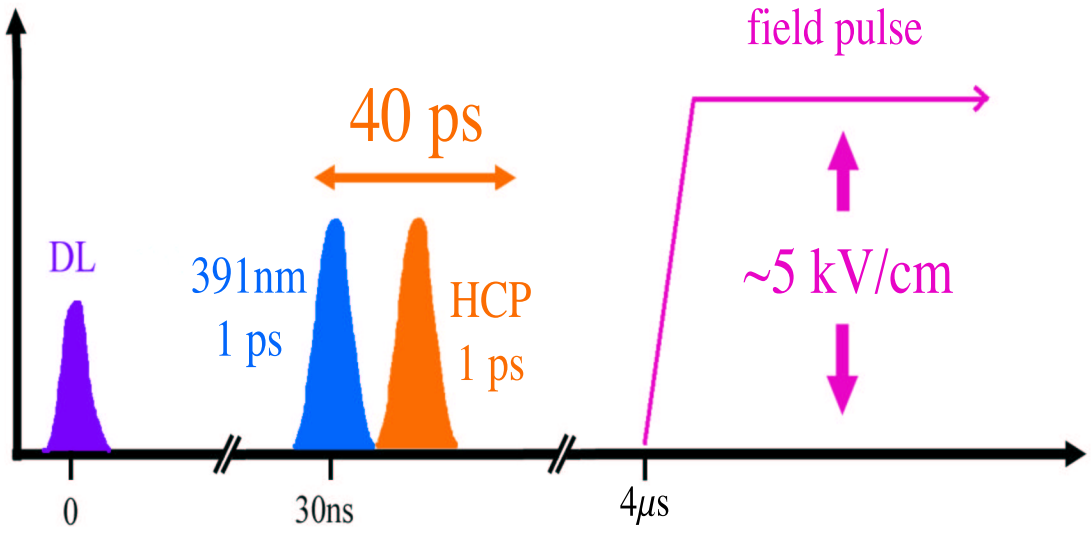

Figure 4.3: Timing diagram of the experiment.

component of the collision field is zero, simulating only the transverse component is still a reasonable method of performing "artificial collisions." The GaAs wafer which generates the HCP field is mounted on a rotation stage so that the angle between the HCP polarization axis and the static field may be varied continuously. This angle is the TBR collision angle, θ, and can be varied from 0 to π.

Interaction with the HCP causes a portion of each atom's wavefunction to be recombined. The recombined fraction is bound and experiences no acceleration due to the static field. The remaining fraction of each wavepacket completely ionizes, resulting in both an ion and a free electron. The ions are accelerated towards the lower field plate due to the presence of the static field. The free electrons are similarly removed to the upper field plate. In approximately 3 μs all charged species are cleared from

the interaction region, leaving only neutral atoms. *Unless the HCP field is present, no neutral Rydberg atoms are formed.* Following the 3 μs delay, a strong ($\sim$ 5 kV/cm) field pulse is applied to ionize any Rydberg atoms in the interaction region. The Rydberg atoms move less than 1 mm during the 3 μs delay. A schematic of the experimental timings of the various laser pulses and electrical pulses is shown in figure 4.3. Since the 391 nm laser pulse and HCP field counterpropagate, a continuous range of pump - probe time delays is measured in a single laser shot with a resolution of approximately 1 ps [17]. In this manner, the probability of recombination as a function of Δt_{HCP} is directly related to the amount of observed field ionization as a function of linear position along the slit in the upper field plate. Data is taken for peak HCP collision field strengths ranging from $0 \rightarrow 6$ kV/cm.

4.3 Results

Consider a continuum wavepacket created at $t = 0$, with a central n of $n = 35$ in an electric field of 450 V/cm. After $t = \Delta t_{HCP}$, a HCP is incident upon the continuum wavepacket. This HCP field recombines a fraction of the wavepacket with its parent ion. Figure 4.4 shows density plots of the recombined fraction as a function of HCP field strength and Δt_{HCP} for the antiparallel (a) and parallel (b) cases. Dark represents greater probability for recombination. HCP field strength is plotted on the vertical axis and Δt_{HCP} is shown on the horizontal axis. The data agree well with previous

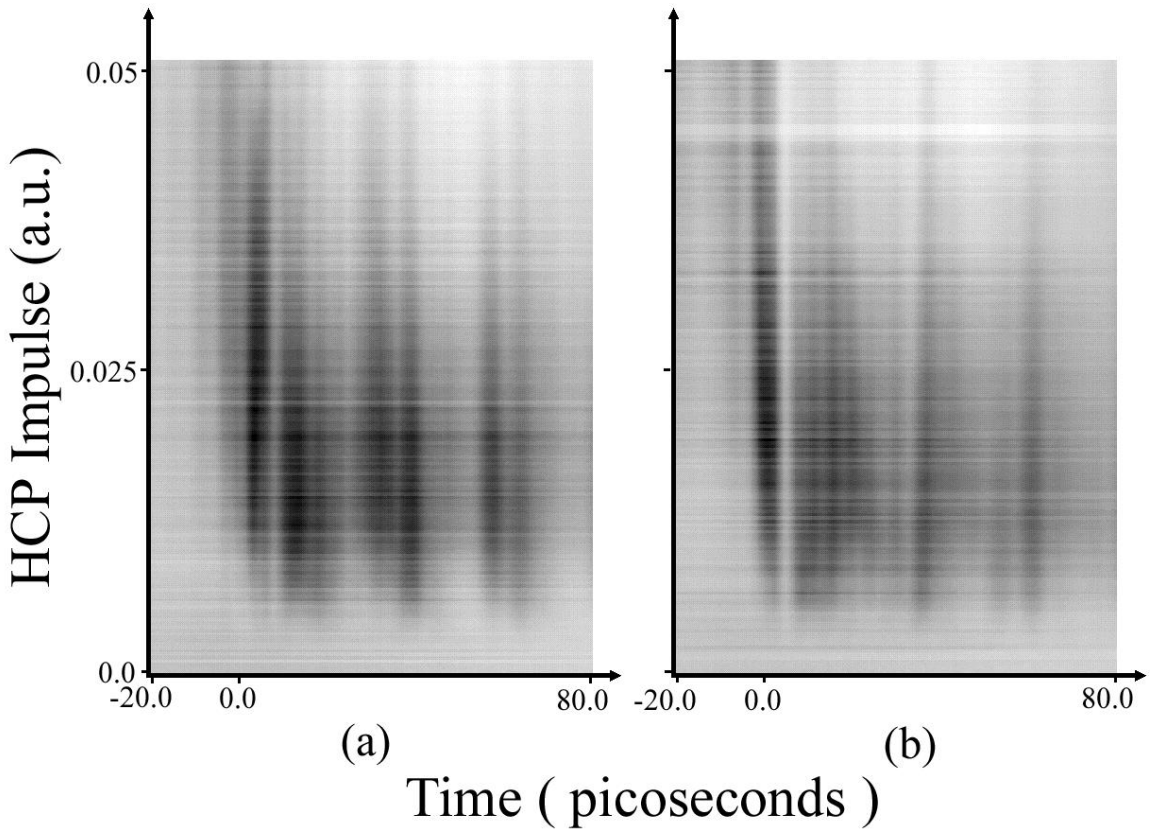

Figure 4.4: Density plot of recombination probability as a function of HCP field strength (vertical axis) and time delay between the wavepacket creation and HCP interaction, Δt_{HCP} (horizontal axis) for (a) parallel fields and (b) antiparallel fields. Dark represents areas of greater recombination probability. The Δt_{HCP} bin size is approximately 1 ps. Horizontal modulations in the data are an artifact of shot to shot laser fluctuations.

observations of TBR for both field orientations [11]. The previous work however only measured recombination probability for a single value of HCP field strength.

Figure 4.5 shows a density plot of the recombination probability as a function of HCP kick strength (vertical axis) and Δt_{HCP} (horizontal axis) for the orthogonal field orientation. Again, dark represents greater recombination probability. All the experimental conditions are the same in figures 4.4 and 4.5 with the exception of the collision angle θ. For early times ($0 \leq t \leq 10$ps) in both the parallel and antiparallel cases, a maximum in recombination probability is observed for a HCP impulse of approximately $A = 0.025$. For longer times ($t > 10$ps) the location of the maximum shifts to weaker values of HCP strength. In the orthogonal case however, the maximum in recombination probability occurs at roughly the same value of HCP strength for all times, $A = 0.018$.

Horizontal slices through the data in figures 4.4 and 4.5 are shown in figure 4.6 for a HCP impulse of $A = 0.021$. In both the parallel and antiparallel cases, the recombination signal shows two sets of pronounced modulations as a function of time. A fast modulation with a period of $\sim$10 ps is superimposed over a slower modulation with a period of $\sim$20 ps. The fast modulation is consistent with the classical Kepler period $\tau_K = 2\pi n^3$ ($\tau_K = 9.7$ ps for $n = 40$). The slow modulation is consistent with the angular momentum precession or Stark period $\tau_S = 2\pi/3Fn$ ($\tau_S = 19$ ps for the conditions in figure 4.4). The phase of the Stark oscillation changes for the parallel

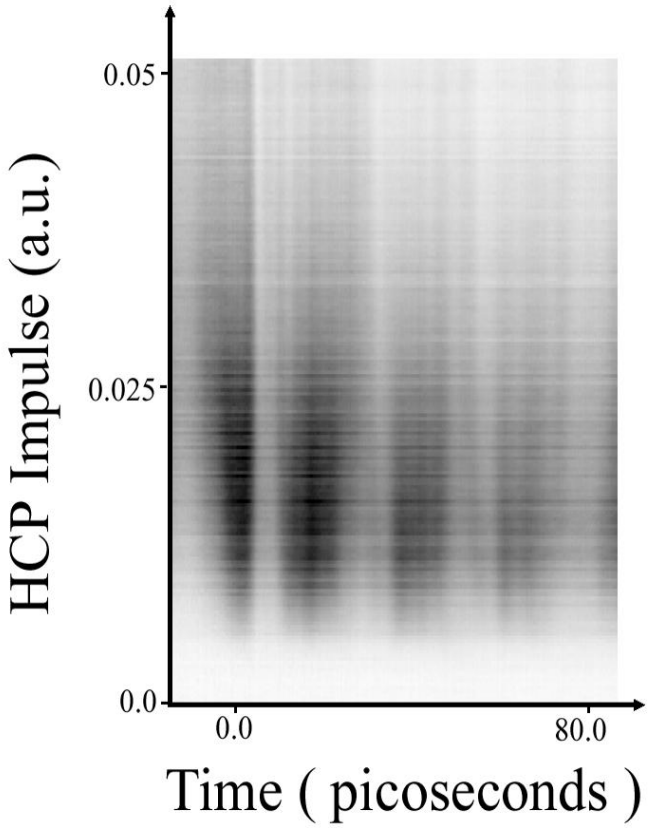

Figure 4.5: Density plot of recombination probability as a function of HCP field strength (vertical axis) and time delay between the wavepacket creation and HCP interaction, Δt_{HCP} (horizontal axis) for the orthogonal field orientation. Dark represents areas of greater recombination probability.

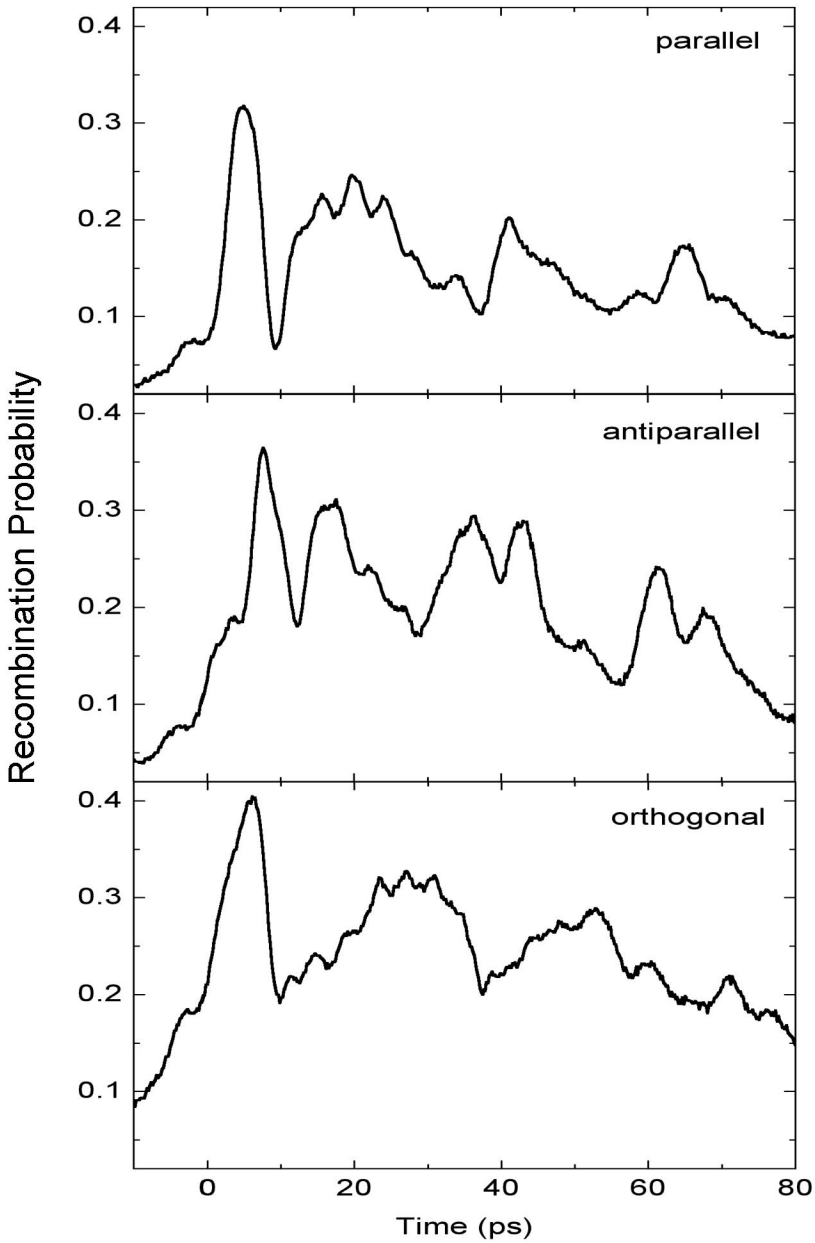

Figure 4.6: Recombination probability as a function of time for the three cases of collision angle. In each case the HCP impulse is $A = 0.021$. Each line is a single horizontal slice through the data shown in figures 4.4 and 4.5. Modulations are seen which are consistent with both the Kepler and Stark oscillation frequencies.

and antiparallel cases [11]. For the orthogonal case, the Kepler modulations are not as obvious, however the Stark oscillations are seen clearly. In the rest of this chapter, we will focus mainly on early times, or approximately the time duration of the first Kepler oscillation of the wavefunction.

We turn our attention to how the recombination probability changes as a function of HCP strength (vertical slices through the recombination probabilities in figures 4.4 and 4.5. At early times, a maximum in recombination probability as a function of HCP strength occurs at much weaker HCP fields (around A=0.018) in the orthogonal case than in the parallel or antiparallel cases. Furthermore, the amount of recombination signal observed for weak collision fields is greater for the orthogonal case than in the other two cases for all values of Δt_{HCP}. This is the main experimental result of this chapter. *In the orthogonal case, recombination probability is enhanced for weak collision fields due to dynamical stabilization of the continuum electron rather than energy extraction.* This effect will be described in detail in the next section.

Figure 4.7 shows the measured amount of recombination as a function of HCP strength for selected values of time delay, Δt_{HCP}. These curves are vertical slices through data similar to that presented in figures 4.4 and 4.5. Note the enhancement of recombination probability for weak HCP fields for the orthogonal field orientation when compared with the parallel and opposite field orientations. For $\Delta t_{HCP} = 3.0$ ps, we see the greatest relative enhancement of recombination probability, approximately

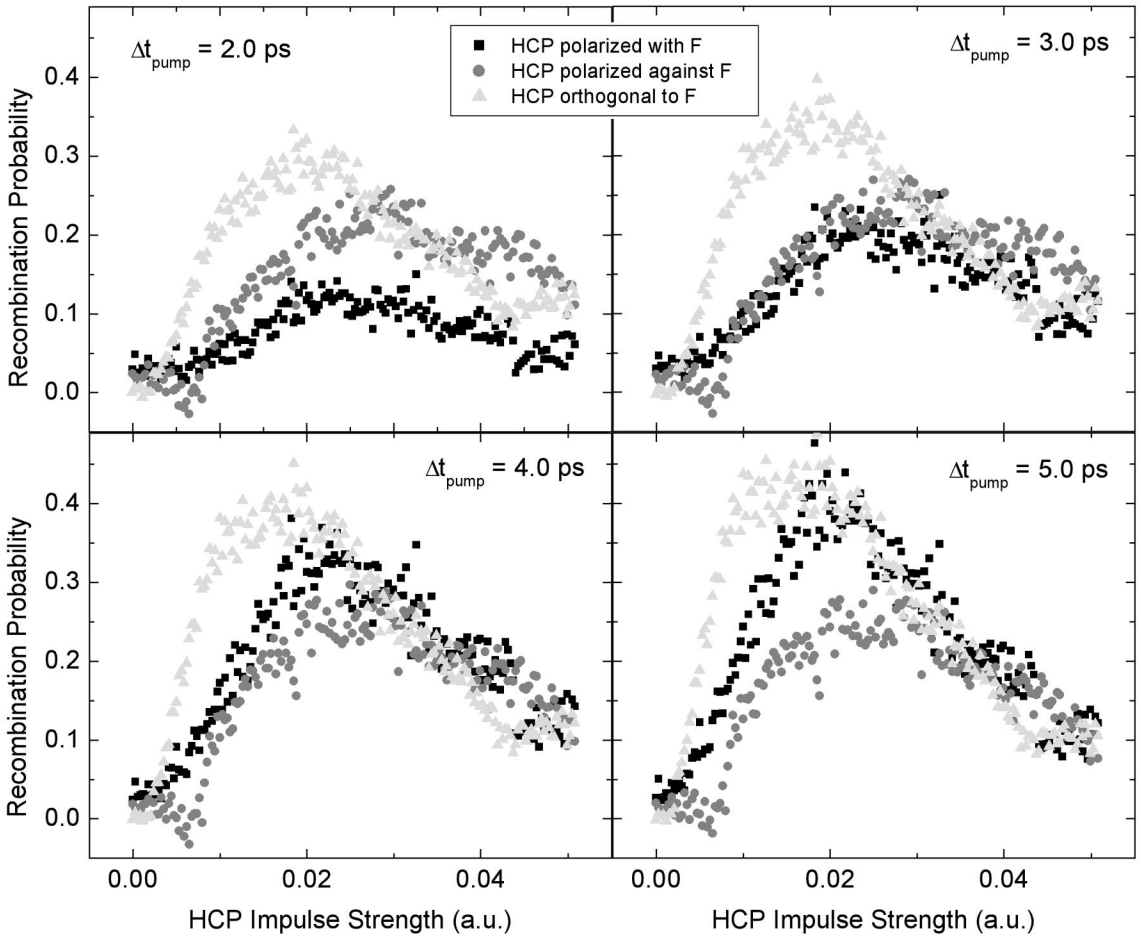

Figure 4.7: Experimentally measured recombination probability as a function of HCP field strength for selected values of Δt_{HCP}. Data from the parallel (□), antiparallel (◯), and orthogonal (△) field orientations are shown for each value of Δt_{HCP}. Note that at short times, greater recombination probability exists for weaker kick strengths. Noise in the signal is due primarily to shot to shot laser fluctuations.

a factor of 3 for $A_{HCP} = 0.015$. Even though modulations in recombination probability are observed at $\Delta t_{HCP} = \tau_K$ and $\Delta t_{HCP} = \tau_S$, the weak orthogonal HCP field recombination enhancement persists throughout. For example, at $\Delta t_{HCP} = 2$ ps, the antiparallel case shows a greater recombination probability than the parallel case. At $\Delta t_{HCP} = 5$ ps, the situation has reversed. At both $\Delta t_{HCP} = 2$ ps and $\Delta t_{HCP} = 5$ ps however, the orthogonal case is enhanced relative to either the parallel or antiparallel cases for weak HCP fields.

4.4 Discussion

To understand the variation in recombination probability as a function of the relative field orientation, the role of the parabolic quantum number m in the Stark effect must be understood. Appendix D provides a general overview of the Stark effect as well as parabolic coordinates. The concepts introduced there are extended in this chapter to deal with field ionization. The effective energy of the saddle point in the Stark potential has a dependence on m due to the eccentricity of the electron's motion. In the hydrogenic case, an electron in a given m state is bound if its energy is lower than the critical energy given by [18]

$$E_c(m) = -\frac{F_s}{2}\eta_c - \frac{2Z_2}{\eta_c} + \frac{m^2 - 1}{2\eta_c^2} \ . \tag{4.1}$$

In equation 4.1, $\eta_c = r - z$ is the η position of the saddle point in parabolic coordinates, F_s is the static field, and Z_2 is the parabolic separation constant. The location of the η minimum in the potential (labelled η_c) is found by locating the zero of the derivative of equation 4.1 with respect to η. Care must be taken when applying the result as the separation constant Z_2 is determined by the orientation of the electron's orbit.

If the energy E_0 of the electron is greater than $E_c(m)$, then the potential surface is open and a hole exists on the $-\hat{z}$ or "downhill" side of the potential. The spatial extent of the hole grows with increasing values of E_0. The $\hat{z}$ projection of the electron's angular momentum and time-averaged dipole moment determine if and when a particular orbital trajectory will intersect the hole [19]. In hydrogen, the orientation of a given electron orbit is defined by the Runga-Lenz vector $\vec{M}$, given by [20–22]

$$\vec{M} = \vec{p} \times \vec{L} - Z\hat{r} + \frac{1}{2}(\vec{r} \times \vec{F}) \times \vec{r} \, . \tag{4.2}$$

The $\hat{z}$ component of $\vec{M}$, given by M_z, is proportional to the time-averaged projection of the electron's dipole moment on the $\hat{z}$ axis. M_z is a constant of the motion and takes on values from $-1 \leq M_z \leq 1$. In this case, the separation constant Z_2 is best determined by the orientation of the electron's orbit and can be written in terms of M_z,

$$Z_2 = \frac{1}{2}(Z - < M_z >) \, . \tag{4.3}$$

An electron moving along the $-\hat{z}$ axis has $M_z = -1$ and passes directly through the hole in the potential. However, orbital orientations which have $M_z > -1$ do not sample

the potential at large values of $-z$ and may remain bound even if $E > E_c(m)$. Also, for trajectories with large values of $|m|$, the electron may temporarily encounter the hole in the potential, however the large angular velocity at its outer turning point ensures its return unless $E \gg E_c(m)$ [23]. For each combination of m and M_z, there exists a critical energy $E_c(m, M_z) \geq E_c(m)$, above which, the electron will ionize [20]. As either m or M_z increases, so does $E_c(m, M_z)$.

The ionization mechanism proceeds quite differently in non-hydrogenic atoms. Due to the penetration of the atomic core, the potential is non-Coulombic at small values of r. Therefore, no true "uphill" or "downhill" orbits exist and M_z is no longer conserved. Uphill (downhill) orbits are defined as orbits where the net dipole moment of the electron distribution is parallel (antiparallel) to the static field polarization axis. In non-hydrogenic atoms (such as in the case of calcium studied here), uphill orbits precess into downhill orbits and vice versa as time evolves. Consequently, all classical electron trajectories for a given value of $|m|$ ionize at the same critical energy, $E_c(m)$, irrespective of their initial orientations [18, 19, 24]. $E_c(m)$ is determined by equation 4.1 by considering the value of Z_2 corresponding to the most downhill hydrogenic trajectory. For low m Rydberg orbits, Z_2 can be given to lowest order in terms of n, m, and the parabolic quantum number n_2 as

$$Z_2(m, n_2) = \frac{1}{n}\left(n_2 + \frac{|m|+1}{2}\right) \ . \tag{4.4}$$

In the case of the most downhill trajectory, n_2 takes on the value $n - m - 1$ and Z_2 is

given to lowest order by

$$Z_2(m) = 1 - \frac{|m| + 1}{2n} \ . \tag{4.5}$$

In the $\theta = \pi/2$ field orientation, HCP interaction transfers electron population to states with high m values. Electrons in higher m states, experience a more hydrogenic potential since the non-Coulombic portion of the binding potential is forbidden. We define m_c to be the critical value of m above which the electron behaves hydrogenically. Consequently, for $|m| > m_c$, E_c is orientation dependent as in the purely hydrogenic case. Therefore, recombination can occur via angular momentum transfer rather than by energy extraction. It is even possible for a HCP field to increase the total energy of an electron and still recombine it, if $E_c(m, M_z) > E_0$.

A full quantum simulation of electron - ion recombination is beyond the scope of this work, however significant theoretical advances have been made along these lines [25]. Instead, to obtain an approximation of the dynamics involved we numerically integrate the classical equations of motion [26]. In the classical simulation, an ensemble of electrons is launched from the inner turning point of the hydrogenic $\ell = 2$, $m_\ell = 0$ orbit. The orientation of each electron's orbit is randomly chosen. The exact time when an electron is launched in the simulation is determined by randomly sampling a Gaussian distribution centered at $t = 0$ with a 1 ps FWHM. Each electron is allowed to evolve in the presence of a constant static field until acted upon by a Gaussian shaped HCP with a 0.75 ps FWHM. This field pulse is the analog of the field of a passing

charged particle. The angle of incidence, θ, between the static field and the HCP may be varied for each calculation. After interaction with the HCP, each electron evolves for a long time relative to any other time scales in the problem ($\gg 100$ ps). To determine if a given electron has been recombined, first its final η position is determined. If the electron has a final value of $\eta > \eta_c$, then it is located outside the saddle point and was not recombined. For the remaining events, the m value and final energy E_f of each electron are determined. For an electron which has a final m value $|m| \leq m_c$, if $E_f < E_c(m)$ then the electron is counted as recombined. Similarly, if an electron has $|m| > m_c$, and $E_f < E_c(m, M_z)$ then it is also considered recombined. All other events are considered ionized.

The degree of hydrogenic character of the high m states is determined from a calculation of the avoided crossings in a calcium Stark map. Stark maps are created for each value of m by the methods introduced in appendix D. The size of a typical avoided crossing is determined for each m value. The lifetime of each state is inversely proportional to the size of the avoided crossing. For a state to be considered hydrogenic, its lifetime should be comparable to the 4 μs delay between HCP interaction and the HV field pulse. The average avoided crossing energy separation is approximately 10 MHz for $m = 4$ and 200 kHz for $m = 8$. The value $m_c = 4$ is chosen for the calculations presented here to match the calculations and the data. The effect of making different choices for the value of m_c on the calculated recombination probability will be

investigated later in this section.

The calculated amount of recombination is plotted as a function of HCP field strength for the parallel, opposite, and orthogonal cases in figure 4.8 for selected values of Δt_{HCP}. These results can be directly compared with the experimentally observed recombination probabilities in figure 4.7. Qualitative agreement exists between the experimental data and the classical simulations. An overall reduction in the total amount of calculated recombination is seen for increasing values of Δt_{HCP}. This is not directly seen in the experimental data over the small time scales shown in figures 4.7 and 4.8. However, the average amount of observed recombination does decrease after each Kepler period. The main result of this chapter is however reproduced by the calculations: *An enhancement in recombination probability exists for orthogonally oriented collision fields when compared to either the parallel or antiparallel orientations.*

Figure 4.9 shows results from five different classical calculations. Shown are the $m = 0$ calculations for the parallel and opposite field orientations, as well as three different orthogonal case calculations. Each of the different orthogonal calculations illustrates a different method of treating the m dependence of E_c in the calculation. In the thin black solid line, all dynamical effects have been ignored. Recombination occurs only if the electron has energy less than that of the reddest Stark state for $m = 0$ ($E < -2\sqrt{F_s}$). In the thin black dashed line, the m dependence of the saddle point energy is considered, but not the hydrogenic nature of the high m states. Neither of

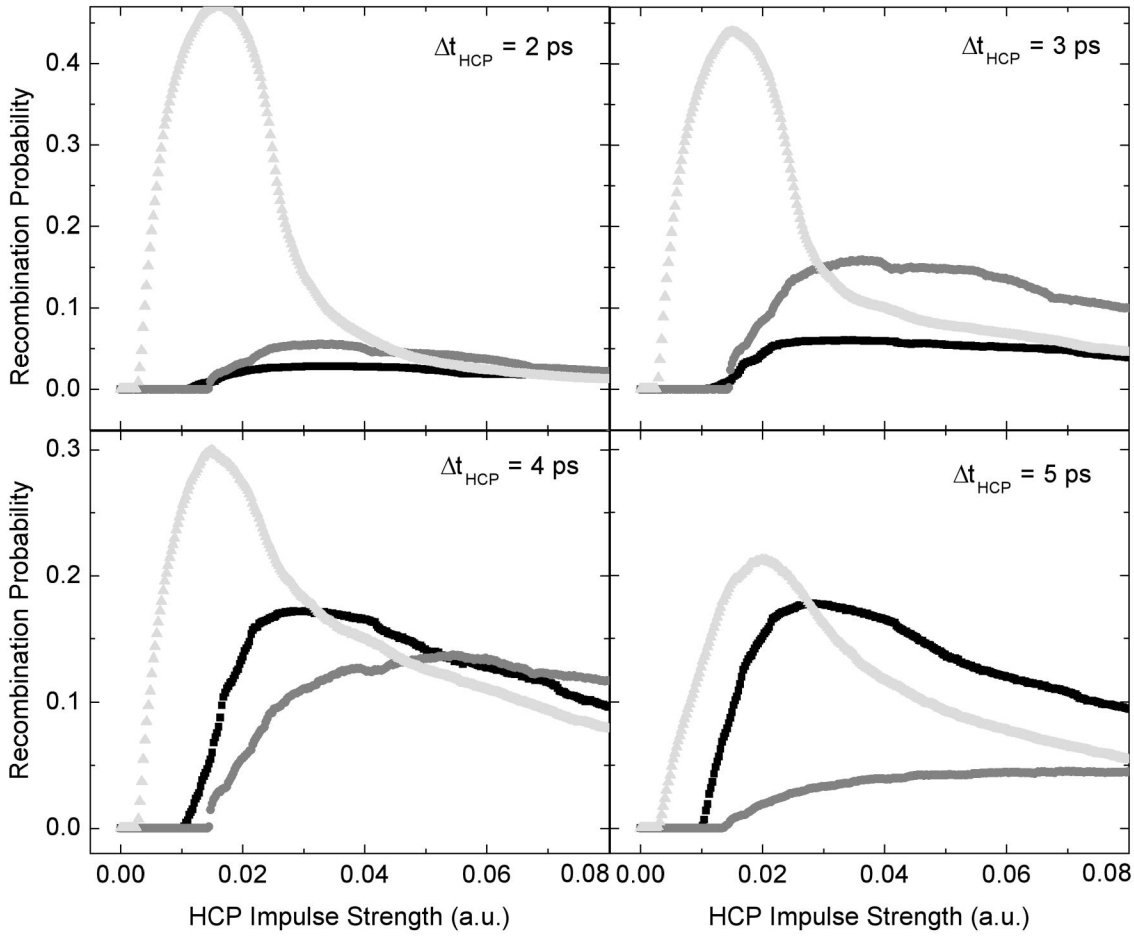

Figure 4.8: Classical calculations of recombination probability as a function of HCP field strength for selected time delays, Δt_{HCP} between continuum wavepacket creation and HCP interaction. Black boxes are calculations of the parallel case, dark grey circles are calculations of the opposite case, and light grey triangles are calculations of the orthogonal case.

these curves reproduces the significant recombination enhancement seen in the data. Only when the orientation dependence of the hydrogenic high m states is added to the calculations does the weak field enhancement appear in the calculations. This case is shown by the light grey triangles. *The significant enhancement of the calculated recombination rate is mainly due to the production of high m states by the HCP.*

In figure 4.10, we examine the effect that different choices of m_c have on the recombination probability. Shown is the recombination probability at $\Delta t_{HCP} = 4$ ps for the orthogonal field orientation. For the calculated recombination probabilities in the orthogonal configuration presented thus far, we have used $m_c = 4$. Figure 4.10 shows recombination probabilities for many choices of m_c ($m_c = 4, 6, 10, 20$, and ∞). The calculated recombination probability for $m_c = \infty$ represents the calculated recombination probability when no hydrogenic high m state behavior is considered. The amount of recombination enhancement does depend on the value chosen for m_c, but for all $m_c \leq 20$, some enhancement is seen over the parallel and antiparallel orientations. Therefore, the existence of the recombination enhancement for orthogonally oriented collision fields is not critically tied to our choice of m_c. As long as the hydrogenic nature of the high m states is considered at some level ($m_c \leq 20$), then recombination enhancement is seen in the simulations.

The m distribution of the recombined electrons in the classical simulation is also recovered and shown in figure 4.11. Only electrons recombined in the orthogonal field

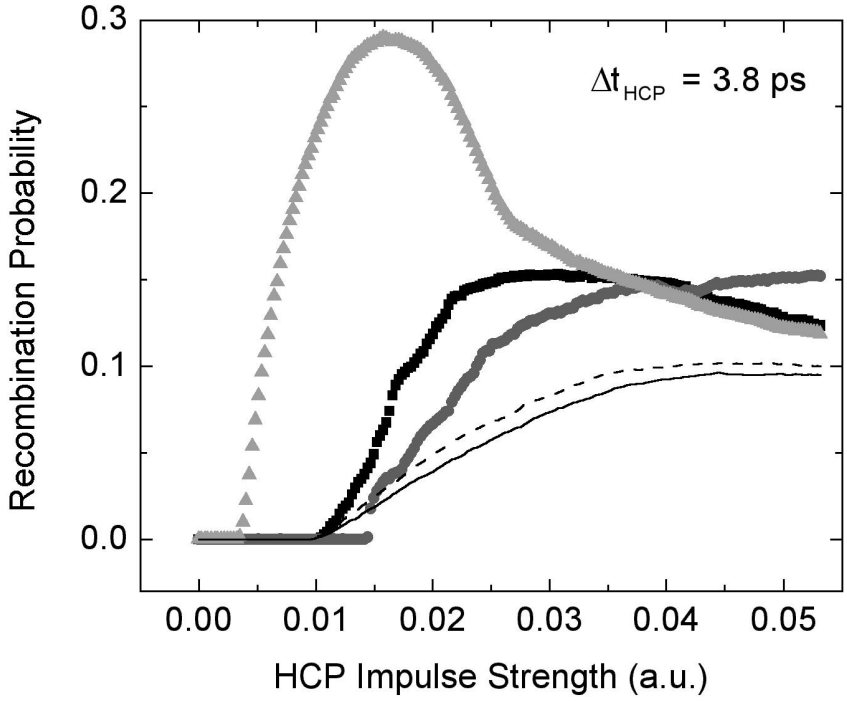

Figure 4.9: Classical calculations of recombination probability as a function of HCP field strength for a time delay of $\Delta t_{HCP} = 3.8$ ps. The black squares and dark grey circles are calculations of recombination probability for the parallel and antiparallel field orientations respectively. The light grey triangles show recombination probability for the orthogonal case when both the m dependence of the saddle point energy and the hydrogenic nature of the high m population are considered. The dashed black curve shows the calculated recombination probability for the orthogonal field geometry if only the m dependence of E_c is considered. The solid black curve shows the calculated recombination probability in the orthogonal case if all dynamical effects are ignored.

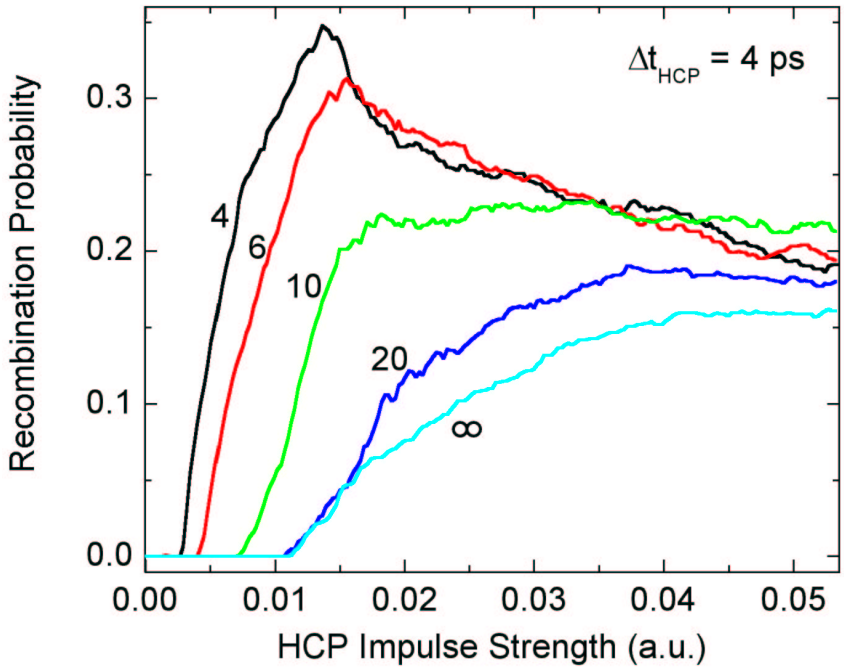

Figure 4.10: Classical calculations of recombination probability as a function of HCP field strength for a time delay of $\Delta t_{HCP} = 4$ ps for several values of m_c. The enhancement of recombination probability decreases for increasing values of m_c. The value $m_c = 4$ most closely matches the experimental data and therefore is used in the calculations of recombination probability in the orthogonal case.

orientation have nonzero m distributions. For a HCP field of 4 kV/cm, and $\Delta t_{HCP} =$ 1.0 ps, the mean m value of a recombined electron is approximately $m = 17$. Such high average m values indicate that the majority of the electrons that undergo recombination do so due to promotion to very high m states. Quantum calculations indicate the high m transfer is possible due to the large static field present in the experiment and the orientation of the HCP field. This will be discussed in detail in chapter 5. In a field free environment however, transfer to very high m values can not be done with a single linearly polarized HCP field. This too is discussed in chapter 5.

4.5 Conclusions

We have used HCPs to examine electron - ion recombination in the presence of a static field. We find a significant enhancement of the recombination yield when the static and HCP fields are orthogonally polarized. The enhancement is due to a dynamical effect associated with the excitation of high-$|m|$ states during the HCP. This mechanism is analogous to the collisional and static field induced ℓ and m mixing which enables zero electron kinetic energy (ZEKE) spectroscopy by suppressing autoionization of highly excited Rydberg molecules [27]. Moreover, centrifugal recombination should play a role in TBR or pulsed-field recombination in any plasma where static micro- or containment fields are present.

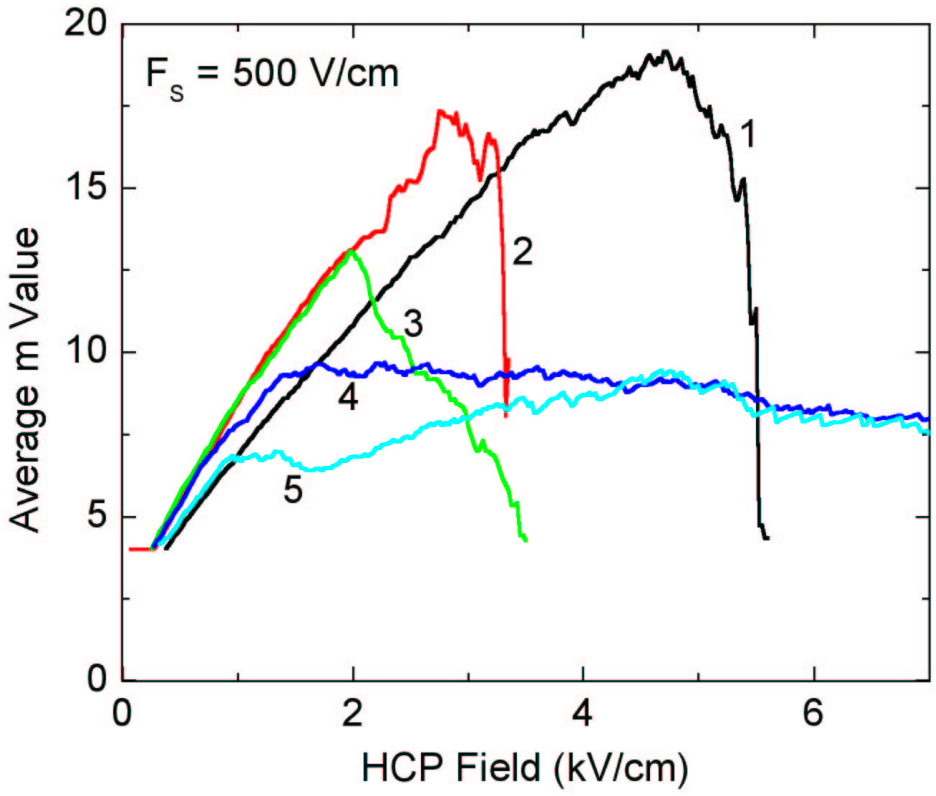

Figure 4.11: Average m value of the recombined electrons in a classical simulation for Δt_{HCP} = 1,2,3,4, and 5 ps in the orthogonal field orientation. The static field present in the simulation is F_S = 500 V/cm. For small values of Δt_{HCP}, the majority of the recombined electrons have high m values.

Bibliography

[1] J.G. Zeibel and R.R. Jones, *Phys. Rev. Lett.* **89**, 093204 (2002).

[2] Y. Hahn, *Rep. Prog. Phys.* **60**, 691 (1997), and references therein.

[3] J. Stevefelt, J. Boulmer, and J-F. Delpech, *Phys. Rev. A* **12**, 1246 (1975).

[4] P.O. Fedichev, M.W. Reynolds, and G.V. Shlyapnikov, *Phys. Rev. Lett.* **77**, 2921 (1996).

[5] Y. Hahn, *Phys. Lett. A* **231**, 82 (1997).

[6] Y. Hahn, *Phys. Lett. A* **264**, 465 (2000).

[7] A. Burgess, *Astrophys. J.* **139**, 776 (1964).

[8] T.C. Killian *et al.*, *Phys. Rev. Lett.* **86**, 3759 (2001).

[9] G. Gabrielse *et al.*, *Phys. Lett. B* **455**, 311 (1999); C. Wesdorp, F. Robicheaux, and L.D. Noordam, *Phys. Rev. A* **64**, 033414 (2001).

[10] W. Graham *et. al.*, eds., NATO ASI Series B: Physics, Vol. 296. *Recombination of Atomic Ions*, Plenum, New York, (1992).

[11] T.J. Bensky, M.B. Campbell, and R.R. Jones, *Phys. Rev. Lett.* **81**, 3112 (1998).

[12] R.R. Jones, D. You, and P.H. Bucksbaum, *Phys. Rev. Lett.* **70**, 1236 (1993).

[13] V. L. Jacobs and J. Davis, *Phys. Rev. A* **19**, 776 (1979).

[14] R.R. Jones, *Phys. Rev. Lett.* **76**, 3927 (1996).

[15] D. You *et al.*, *Opt. Lett.* **18**, 290 (1993).

[16] N.E. Tielking, T.J. Bensky, and R.R. Jones, *Phys. Rev. A* **51**, 3370 (1995).

[17] M.B. Campbell, T.J. Bensky, and R.R. Jones, *Opt. Express* **1**, 197 (1997).

[18] T.F. Gallagher, *Rydberg Atoms*, 1st ed., Cambridge University Press, Cambridge, (1994).

[19] J.G. Zeibel and R.R. Jones, . *Phys. Rev. Lett.* **89**, 093204 (2002).

[20] E. Luc-Koenig and A. Bachelier, *J. Phys. B* **13**, 1743 (1980).

[21] T.P. Hezel, C.E. Burkhardt, M. Ciocca, and J.J. Leventhal, *Am. J. Phys.* **60**, 324 (1992).

[22] L.D. Landau and E.M. Lifshitz, *Quantum Mechanics (Non Relativistic Theory)*, 3rd ed., Pergamon Press, Oxford, (1976).

[23] G.M. Lankhuijzen and L.D. Noordam, *Phys. Rev. Lett.* **76**, 1784 (1996).

[24] M.G. Littman, M.M. Kash, and D. Kleppner, *Phys. Rev. Lett.* **41**, 103 (1978).

[25] F. Robicheaux and J. Shaw, *Phys. Rev. Lett.* **77**, 4154, (1996).

[26] For details regarding the classical calculations performed for this experiment, see appendix B.

[27] W.E. Chupka, J. Chem. Phys **98**, 4520 (1993); S.T. Pratt, *ibid* **98**, 9241 (1993); F. Merkt and R.N. Zare, *ibid* **101**, 3495 (1994); M.J.J. Vrakking and Y.T. Lee, *ibid* **102**, 8818 (1995); M.J.J. Vrakking, I. Fischer, D.M. Villeneuve, and A. Stolow, *ibid* **103**, 4538 (1995).

Chapter 5

Manipulating Wavepacket Dynamics Part 2: Suppression of Autoionization

5.1 Introduction

Electrons which have been ionized and subsequently subjected to HCP fields were studied in chapter 4. In this chapter however, we look at the effect of applying HCP fields to a *bound* system with total energy above the first ionization limit. In other words, instead of looking at the response of a system which has already ionized, we look at the response of a system which has yet to ionize. The experiment presented in

this chapter is being published here [1].

Autoionization (AI) is a process by which a doubly excited neutral atom ionizes via resonant collisional energy transfer from one excited electron to another. AI is the dominant stabilization mechanism for multiply excited atoms with low angular momentum. Both theory and experiment suggest AI probability can be influenced by the presence of electric fields [2–11]. AI in the presence of electric fields has been studied under many conditions [6,7,12], however to our knowledge no studies have been performed which investigate the effect of transient electric field pulses on AI probability. In this chapter, we study the effect of transient, half-cycle electric field pulses (HCPs) on AI, where the duration of the HCP field is significantly shorter than τ_K . The process of field ionization due to impulsive electric fields has been shown to be dramatically different than for slowly varying or adiabatic fields [13]. Therefore, we test whether AI is different in the two regimes as well.

AI is an important process in astrophysical plasmas [6, 7, 14] and Zero Electron Kinetic Energy (ZEKE) spectroscopy [15–23]. AI is the inverse process of dielectronic recombination (DR) and therefore one can gain information on DR by studying AI [2–5, 12, 24–28]. Our measurements have implications for DR in plasmas due to the similarities of the HCPs used here with the field of a passing charge [29]. We can mimic these fields experimentally and directly measure their effects on AI probability.

Another interesting effect of HCP interaction with an autoionizing system is the

possibility of effectively "turning off" AI through the application of a specific set of impulsive fields. If it is possible to turn off AI with HCP field interactions, then HCPs can be used to probe the time dependent population transfer among AI states. In this case, a HCP field would be used to turn off AI at specific times to measure the remaining population as a function of time.

For constant ℓ, the probability for finding the Rydberg electron in the vicinity of the ion core scales as n^{-3}, in inverse proportion to the electron's classical Kepler period, $\tau_K = 2\pi n^3$. For constant n there is no simple ℓ scaling formula. The electron/ion core overlap is relatively constant for low-ℓ states due to the finite size of the ion core. However, the overlap decreases extremely rapidly with increasing ℓ due to the centrifugal barrier at small electron radius. Typically, for $\ell \gtrsim 3$, the ion core is localized well within the radial volume, $r \lesssim \ell(\ell+1)/2$, that is classically forbidden to the Rydberg electron [30, 31]. Consequently, for these high-ℓ states the AI rate drops precipitously with increasing ℓ, and is considerably smaller than the corresponding rate of the low-ℓ ($\lesssim 3$) states [26–28, 32].

We define the AI rate and radiative rate of a given atom as $\Gamma_{AI}(\ell)$ and Γ_R respectively. For doubly-excited Rydberg states, Γ_R is often dominated by emission from the core and, therefore, is ℓ independent. $\Gamma_{AI}(\ell)$ however depends critically on the overlap of the Rydberg wavefunction with the small atomic core. This overlap decreases with increasing values of principal and angular momentum quantum numbers, n and ℓ, for

the Rydberg electron [30].

In the presence of a static or adiabatically varying field, the potential that binds the Rydberg electron no longer possesses (near) spherical symmetry and, therefore, electronic angular momentum is no longer a conserved quantity. However, m, the quantum number corresponding to the projection of the electron's angular momentum on the field axis, remains good in the field [18,22]. For each principal quantum number n and angular momentum projection m, there are $n-m$ Stark states which are linear combinations of the available $n-m$ angular momentum eigenstates [33]. To a rough approximation, all of the states corresponding to a specific Stark manifold share a single average AI rate, Γ_{AI_S} [34–37] where

$$\Gamma_{AI_S} = \left(\frac{1}{n-m}\right) \sum_{\ell=m}^{n} \Gamma_{AI}(\ell) \; > \; \Gamma_R \; . \tag{5.1}$$

Because the large core-scattering rates for the lower ℓ states dominate the average, in low m ($\lesssim 4$) manifolds Γ_{AI_S} is a factor of order of $1/n$ smaller than the corresponding rate for a pure $\ell \sim m$ level. By the same reasoning however, Γ_{AI_S} can be many orders of magnitude greater than the zero field rate for a pure high ℓ ($\ell \sim n$) level [34–37].

In this chapter, we test for AI suppression in the transient impulsive field regime. In the case of a slowly varying field, the angular momentum states are mixed by the field, producing a mixture of Stark states. In the case of a transient pulse however, the single transient field pulse transfers population from some initial level (or levels) and produces a linear superposition of different *pure* angular momentum states [38]. The

angular momentum of the superposition state is not continuously mixed in the absence of the field. The evolution of this coherent wavepacket can be very different from that of a mixed angular momentum state. For example, if a transient field creates a linear superposition of high and low ℓ states, only the low $\ell < \ell_c$ part of the wavefunction will participate in AI. Here ℓ_c is defined as the the critical value of ℓ where $\Gamma_{AI}(\ell) = \Gamma_R$. The remaining high ℓ components eventually stabilize, via spontaneous emission or another relaxation process. While a static or long lived oscillatory field can alter AI rates through angular momentum mixing, transient fields might eliminate possible decay channels by angular momentum *transfer*.

5.2 Experimental Methods

Figure 2.9 shows a schematic of the interaction region and detector assembly. A thermal beam of Ca atoms enters the interaction region along $+\hat{x}$. A 432 nm, 5 ns dye laser enters in the interaction region along $+\hat{y}$. This pulse promotes Ca atoms from the $4s4s$ ground state to an intermediate $4s4p$ level. A second 5 ns dye laser pulse also enters the interaction region along $+\hat{y}$ and creates a $4snd$ Rydberg eigenstate. The second pulse is tunable from 389 nm to 393 nm and can excite any eigenstate from $17 \leq n \leq \infty$. Typically, we excite initial n states in the region $17 \leq n \leq 30$. A 1 ps FWHM HCP field is generated by the method discussed in chapter 3. The HCP is linearly polarized along the bias field axis and is directed into the interaction region by a parabolic mirror [39].

The HCP field performs transitions from the $4snd$ eigenstate to a range of $4sn'\ell$ and $4s\epsilon\ell$ states. The actual final state distribution depends on the strength and orientation of the HCP and the initial state distribution.

At approximately the same time as the interaction with the HCP field, atoms in the interaction region undergo an isolated core excitation (ICE) to an autoionizing state [40]. The ICE is performed by exciting the core $4s^+$ Ca electron to the $4p^+$ state with a 393 nm, 1 ps FWHM laser pulse. The 393 nm pulse is created by frequency doubling the 120 fs, 782 nm output from the Ti:Sapphire laser system in a 3 cm long KDP crystal [41]. The resulting laser pulse has a bandwidth of approximately 20 cm^{-1}. The ICE occurs at a variable time delay Δt_{ICE} after the arrival of the HCP field. When the HCP field arrives before the ICE pulse, $\Delta t_{ICE} > 0$. The complete laser excitation process is summarized in figure 5.1.

The system evolves for 100 ns after the HCP and ICE pulse interactions. During this time, either autoionization will occur, or the inner electron will spontaneously decay [42–44]. If the system spontaneously decays, a singly excited neutral Rydberg atom remains. Otherwise, an ion and free electron are formed. After 100 ns, a -60 V clearing pulse is applied to the lower field plate. Ions present in the interaction region are accelerated towards a slit in the upper field plate by the clearing pulse. The magnitude of the clearing pulse is strong enough to ionize neutral atoms with $n > 50$. Any neutral Rydberg atoms with $n > 50$ present in the interaction region are therefore

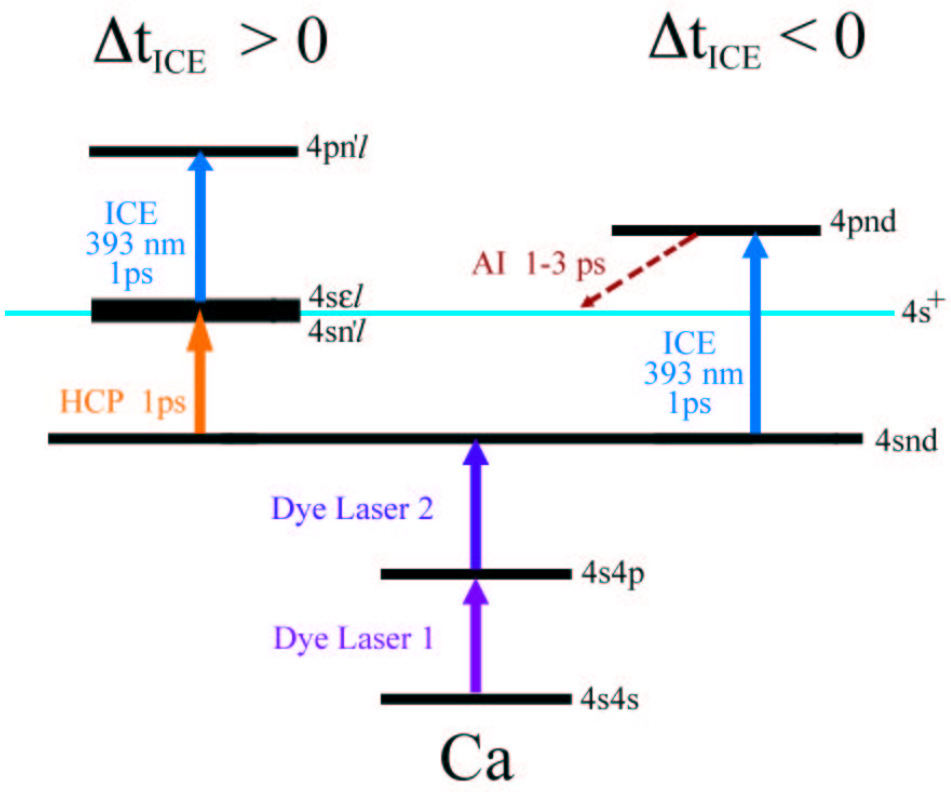

Figure 5.1: Laser excitation schematic for the experiment. Two dye lasers create a $4snd$ Rydberg eigenstate in calcium. If $\Delta t_{ICE} > 0$, a HCP field interacts with the Rydberg eigenstate creating a $4sn'\ell'$ wavepacket. A 1 ps, 393 nm pulse then performs an ICE on the $4sn'\ell'$ wavepacket, creating a $4pn'\ell'$ autoionizing wavepacket. For $\Delta t_{ICE} < 0$, the ICE is performed on the $4snd$ Rydberg eigenstate creating a $4pnd$ autoionizing state with a lifetime of approximately 3 ps.

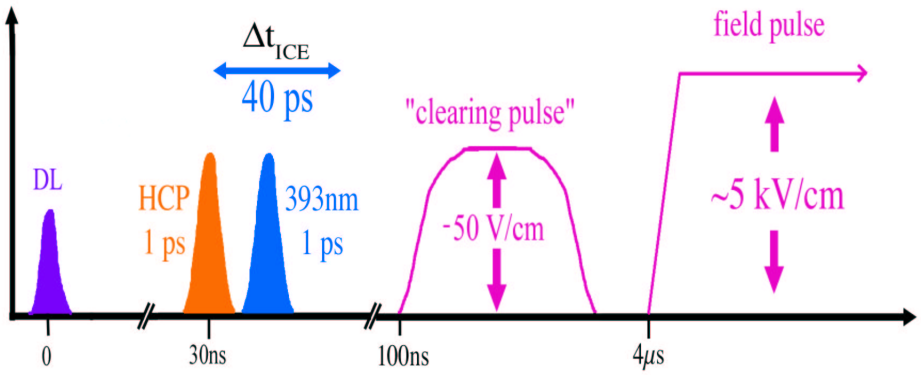

Figure 5.2: A schematic diagram of the experimental timings used in this experiment. All relevant laser pulses and electrical pulses are shown.

indistinguishable from autoionization events. The ions pass through a narrow slit in the upper field plate and are incident upon the single shot detector. AI probability is directly proportional to the measured ion yield. Approximately 100 ps of Δt_{ICE} information is recovered by the detector in each laser shot with 1 ps resolution [45, 46]. Either the HCP field strength or the ICE laser excitation frequency is varied after each laser shot while taking data. In this way, ion yield is recovered as a function of either Δt_{ICE} and HCP field strength or Δt_{ICE} and ICE laser frequency. A schematic diagram of the relative timings of the laser pulses and electric fields used in data collection is shown in figure 5.2 for reference.

5.3 Results

AI probability is measured in three different electric field configurations. First, the effect of a single HCP field incident upon an autoionizing atom is studied. In this case, both laser pulses are polarized in the same direction as the HCP field, creating an $m = 0$ initial state. In the absence of other fields, the HCP polarization axis becomes the good axis in the problem and the azimuthal quantum number m along this axis is a good quantum number. Therefore, the initial $m = 0$ state will remain so during the interaction with the HCP field. In a second experiment, AI probability is measured in the presence of two orthogonally polarized HCP fields separated in time by Δt_{HCP}. This pulse combination closely resembles the fields experienced in a true collision event [29]. In the two pulse case, $\Delta m \neq 0$ transitions are allowed. In a third case, the effect of a HCP field interacting with an autoionizing state in the presence of an orthogonally applied static electric field is investigated. In this configuration $\Delta m \neq 0$ transitions are also allowed.

For the three field configurations, the ion yield vs. Δt_{ICE} data are essentially bi-level curves for all values of HCP field strength (F_{HCP}) and ICE laser frequency. Within our signal to noise, the ion yield vs. Δt_{ICE} has constant values for negative and positive Δt_{ICE}, respectively. The delay independence of the ion signal is expected at negative delays of more than a few picoseconds. In this case, all of the atoms excited to $4pnd$ states have autoionized before the arrival of the HCP, so the HCP has no

effect on the ion yield or AI rate. Therefore, the $\Delta t_{ICE} < 0$ curves are a measure of the ion yield in the absence of the HCP field. For $\Delta t_{ICE} > 0$, the HCP arrives before the ICE and interacts with singly excited $4snd$ atoms. For all positive values of the Δt_{ICE}, the amount of ion yield observed is approximately constant. Therefore, for simplicity the $\Delta t_{ICE} > 0$ and $\Delta t_{ICE} < 0$ data are referred to as "in-field" and "zero-field" respectively. The fact that the ion yield is roughly constant in the in-field case is somewhat surprising. Complex, time dependent wavepacket behavior has been observed in similar cases, such as a $4snd$ radial wavepacket [47, 48] and a Stark wavepacket [49]. However in this situation, it is possible that the number of different states excited by the HCP is too great to observe any coherent time dependent features.

5.3.1 Single HCP Measurements

In the first experiment, ion yield is measured as a function of detuning of the ICE laser from the $4s^+ \rightarrow 4p^+$ ionic transition and time delay Δt_{ICE}. The ion yield is directly proportional to the excitation and autoionization probability. The atoms are initially prepared in a $4s19d$ eigenstate. For the in-field case ($\Delta t_{ICE} > 0$), a HCP field (≈ 3 kV/cm) promotes the $4s19d$ eigenstate to a $4sn'\ell$ wavepacket. An ICE is performed on the inner $4s^+$ electron resulting in an autoionizing $4pn'\ell$ wavepacket. The measured autoionization probability of the $4pn'\ell$ wavepacket is shown in the solid curve in figure 5.3(a). In contrast, for the zero-field case ($\Delta t_{ICE} < 0$), the $4s19d$ eigenstate undergoes

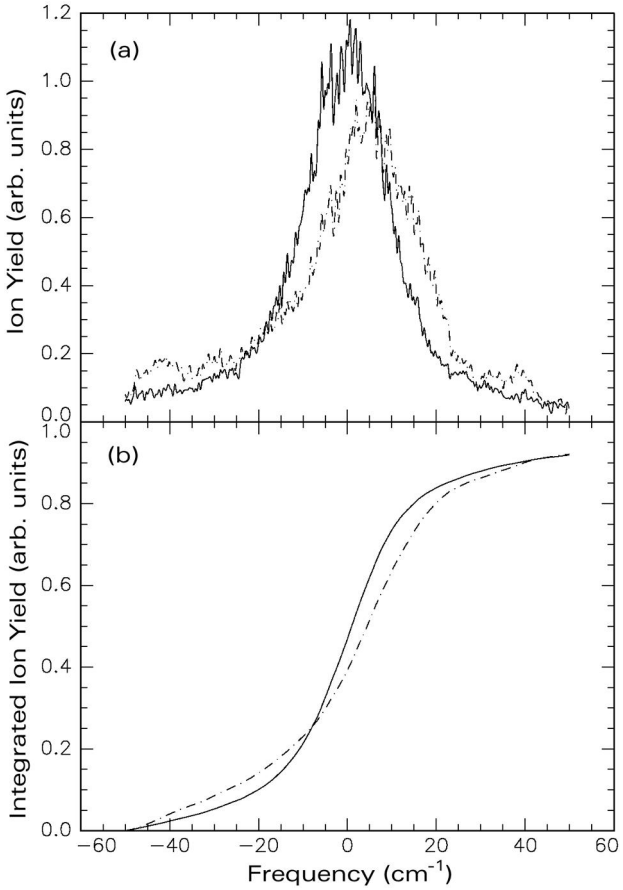

Figure 5.3: (a). Observed ion yield plotted as a function of the detuning of the ICE laser from $4s^+ \rightarrow 4p^+$ transition. The solid curve represents the in-field case ($\Delta t_{ICE} > 0$), while the dashed curve corresponds to the zero-field case ($\Delta t_{ICE} < 0$). The initial state is $4s19d$ and the maximum HCP field is 2.5 kV/cm. (b). Integrated ion yield as a function of frequency. Note that the integrated ion yield is the same for $\Delta t_{ICE} > 0$ and $\Delta t_{ICE} < 0$. The linewidth of the ICE laser is approximately 15 cm^{-1} and the curves in (a) are obtained by scanning the frequency of the ICE laser.

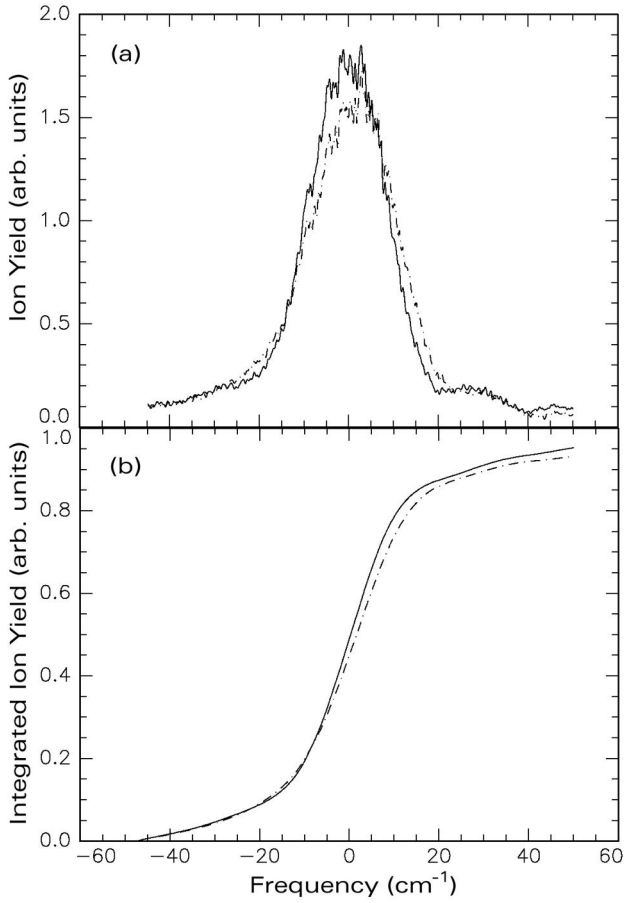

Figure 5.4: (a). Observed ion yield as a function of the detuning of the ICE laser from $4s^+ \rightarrow 4p^+$ transition for an initial $4s27d$ state. The solid curve represents the in-field case ($\Delta t_{ICE} > 0$), while the dashed curve corresponds to the zero-field case ($\Delta t_{ICE} < 0$). The maximum HCP field is 2.5 kV/cm. Integrated ion yield is shown in (b). As in Figure 5.3, no suppression of AI is observed.

ICE to a $4p19d$ state which quickly autoionizes prior to HCP interaction. The AI probability for the zero-field case is shown with the dashed line in figure 5.3(a). The integrated AI probability as a function of ICE laser frequency is shown in figure 5.3(b) for both the in-field (solid curve) and zero-field (dashed curve) configurations.

At some frequencies, fewer ions are produced in the in-field configuration. This was the expected result if the influence of the HCP has stabilized the atoms against ICE. However, at other frequencies, the opposite effect is observed. In fact, a noticeable shift in the centroid of the AI resonance is observed for the in-field case. To explain this phenomenon, we consider the quantum defects of the states involved. The difference between the quantum defects of the $4s19d$ and $4p19d$ states results in an ICE resonance which is detuned from the $4s^+ \rightarrow 4p^+$ ionic transition. The quantum defects are $\delta_{4s19d} = 0.975$ and $\delta_{4p19d} = 0.85$ [50, 51], leading to an energy shift of approximately 4.6 cm^{-1}. However, in the in-field case, the HCP populates high ℓ states which have negligible quantum defects in both the $4s$ and $4p$ configurations. Therefore, the in-field resonance appears at the ionic transition frequency [40]. For comparison, we show the AI probability for a $4s27d$ initial state in figure 5.4. The shift in energy of the AI resonance between the zero-field (solid curve) and in-field (dashed curve) cases observed in figure 5.4(a) is less than in figure 5.3(a). In this case, $\delta_{4s27d} = 1.150$ and $\delta_{4p27d} = 0.98$ [50, 51]. Even through the difference in quantum defects is larger, the resulting energy difference is less due to the smaller energy spacing between n states.

Therefore, the zero-field resonance is shifted by only 2.1 cm^{-1}.

The extremely low AI rate from the high ℓ states should also result in an extremely narrow in-field ICE resonance. Since the 1 ps ICE laser pulse has a large bandwidth, the ICE resonance is instrument limited to approximately 20 cm^{-1}. From this analysis, it appears that the HCP is creating high ℓ states, however we still need to determine whether any stabilization occurs.

To determine the amount of stabilization (if any) in the data, we take advantage of the fact that the integratd strength of the ICE resonance must be independent of the initial Rydberg state, and therefore must be identical for both the in-field and zero-field measurements. Since (in the absence of HCP ionization) the number of singly-excited Rydberg atoms is the same before and after the HCP, any difference in the frequency integrated ion yield for the two cases indicates a difference in the AI probability following the ICE. The total integrated ion yields in both figures 5.3(b) and 5.4(b) are identical within experimental error, indicating no HCP induced stabilization against autoionization. Similar results are obtained for all initial Rydberg configurations. There are two possible explanations for the lack of AI suppression. Either the population is not being transferred into bound states with high enough ℓ values to significantly reduce the AI rate, or the population is not remaining in these high ℓ states once it is initially transferred there.

5.3.2 Measurements with Two Orthogonal HCPs

In the second experiment, AI probability is measured when an atom in an autoionizing state interacts with two separate, orthogonal HCP fields. This combination of two orthogonal HCPs closely resembles the full collision fields in a plasma [29]. Each pulse enters the interaction region at a small angle to the $\hat{x}$ axis and approximately perpendicular to the ICE pulse (see figure 5.5). With this geometry, AI probability is measured for a range of time delays Δt_{HCP} in a single laser shot. The combination of two orthogonal HCP fields transfers population from the initial Rydberg eigenstate to a wavepacket of various n, ℓ, m states. An ICE laser pulse propagates collinear with the slit in the upper field plate ($+\hat{y}$) a time delay Δt_{ICE} after the HCP pulses pass through the interaction region.

AI probability as a function of ICE laser detuning is shown in figure 5.6. These curves are completely analogous to figures 5.3 and 5.4. The dashed curve in figure 5.6 (a) corresponds to the zero-field case ($\Delta t_{ICE} < 0$). In this case the ICE is performed prior to the HCP interactions. The solid curve in figure 5.6(a) shows in-field AI probability ($\Delta t_{ICE} > 0$). For the in-field case, the initial Rydberg eigenstate is exposed to two orthogonal HCP fields prior to ICE. As in the single pulse case, the center of the AI resonance is shifted slightly in the zero-field case due to the difference in the quantum defects of the $4s20d$ and $4p20d$ states. A slight suppression ($\approx 10\%$) of the total integrated AI probability is observed for the in-field scenario.

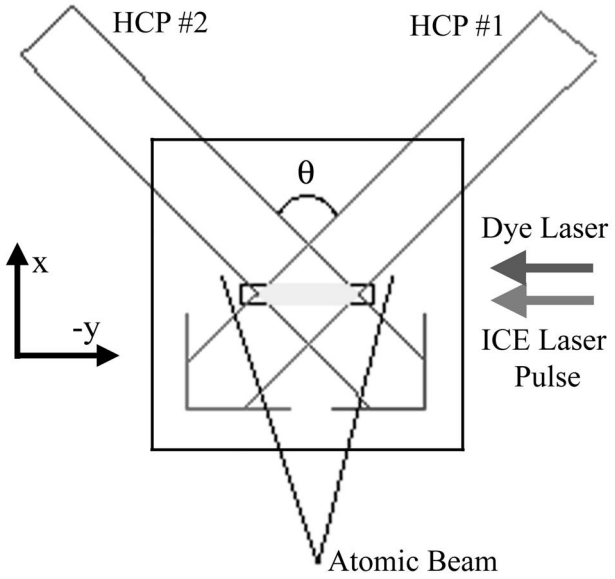

Figure 5.5: A schematic diagram of the experimental approach used to measure AI suppression due to two orthogonal HCP fields. HCP1 is polarized along $+\hat{z}$ moves through the interaction region at some small angle $\theta/2$ to the $-\hat{x}$ direction. HCP2 is approximately polarized along $+\hat{y}$ and moves through the interaction region at an angle $-\theta/2$ to $-\hat{x}$. A spatially dependent time delay Δt_{HCP} exists between the two HCP fields. The point in the interaction region where the two pulses arrive simultaneously ($\Delta t_{HCP} = 0$) is defined to be $y = 0$. Typically $\theta < 10^{\circ}$ and we can study a range of -20 ps $< \Delta t_{HCP} <$ 20 ps.

We also examine the effect of varying the relative time delay between the two HCP fields on the ion yield. Figure 5.7 shows the frequency integrated ion signal as a function of the delay Δt_{HCP} between the two HCPs. For this data scan, the ICE pulse delay is set so that $\Delta t_{ICE} = 0$ when $\Delta t_{HCP} = 0$ at the center of the extraction slit. Therefore, the zero-field data appears at negative values of Δt_{HCP} and the in-field measurement is shown at positive Δt_{HCP}. Of course, from symmetry, the in-field signal is symmetric about $\Delta t_{HCP} = 0$. This symmetry is not obvious in figure

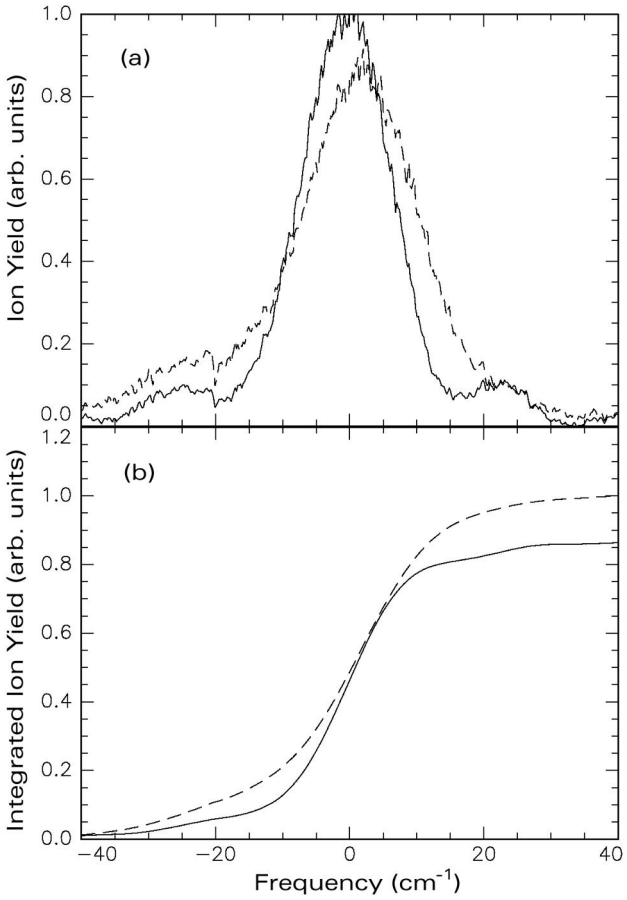

Figure 5.6: (a). Observed ion yield as a function of the detuning of the ICE laser from $4s^+ \rightarrow 4p^+$ transition. The solid curve is the in-field case ($\Delta t_{ICE} > 0$), and the dashed curve is the zero-field case ($\Delta t_{ICE} < 0$). The initial eigenstate is $4s20d$ and each HCP field has a maximum field of ≈ 3 kV/cm with, $\Delta t_{HCP} \approx 5$ ps. Integrated ion yield is plotted in (b) analogous to Figs. 5.3,5.4. A small amount of AI suppression ($\approx 10\%$) is observed.

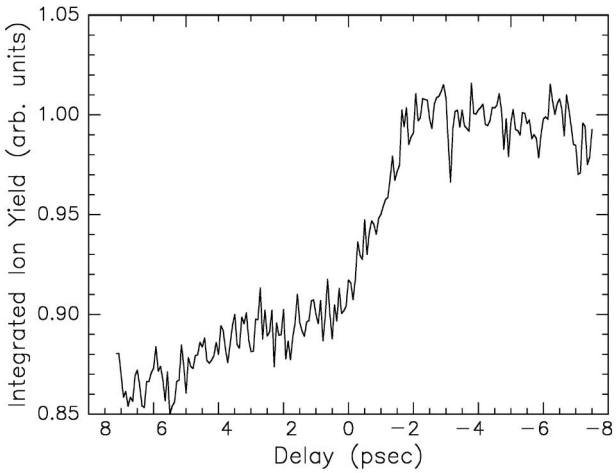

Figure 5.7: Frequency integrated ion yield as a function of relative HCP delay, Δt_{HCP}. $\Delta t_{ICE} = 0$ at the same point as $\Delta t_{HCP} = 0$. Therefore, negative values of Δt_{HCP} correspond to the zero-field case, as described in the text.

5.7 due to the positioning of $\Delta t_{ICE} = 0$ at $\Delta t_{HCP} = 0$. The data is displayed in this way to highlight the small, but significant, AI stabilization that is induced by the HCP fields. Our measurements indicate that the stabilization effect is relatively insensitive to the delay between the two HCPs. Clearly, the stabilization observed with the two HCPs is facilitated by population transfer to high-m, high-ℓ levels. This is in contrast to the single HCP measurements where low-m, high-ℓ states are populated and no stabilization is observed. Simulations will be presented in section 5.4.2 which investigate the relationship between Δt_{HCP} and the final state m distribution.

5.3.3 Measurements with Orthogonal HCP and Static Electric Fields

Finally, in the third experiment, a static field is applied along the $\hat{z}$ axis and an impulsive field kick is applied along $\hat{x}$. A constant voltage is applied to the upper field plate, creating a static field in the interaction region in the $\hat{z}$ direction. A two step laser excitation promotes ground state Ca atoms into an $m = 0$ Stark manifold. The frequency of the second laser is tuned to either the location of the d state in zero field or the reddest state of the high ℓ part of the Stark manifold. The static field is along $\hat{z}$ and mixes the ℓ states into $n - 1$ Stark states, all with $m = 0$. The magnitude of F is less than the the Inglis - Teller limit, the field where adjacent Stark manifolds intersect. After the laser excitation, a HCP field polarized along $+\hat{x}$ is incident upon the system. The HCP field transfers population from the initial Stark state to a distribution of n, ℓ, m final states. Any high m states in the resulting distribution are forbidden from having any low ℓ character. AI probability is measured as a function of ICE laser frequency for a number of different static field and HCP field values. Typical experimental results are shown in figure 5.8. The integrated AI probability is shown as a function of ICE laser frequency for a $n = 22$ manifold in a field of 50 V/cm. Total AI probability is suppressed approximately 8% for the in-field case ($\Delta t_{ICE} > 0$). Even though the evolution of the Rydberg electron is very different in the cases of (i) two orthogonal HCPs and (ii) a HCP and an orthogonal static field, similar stabilization probabilities

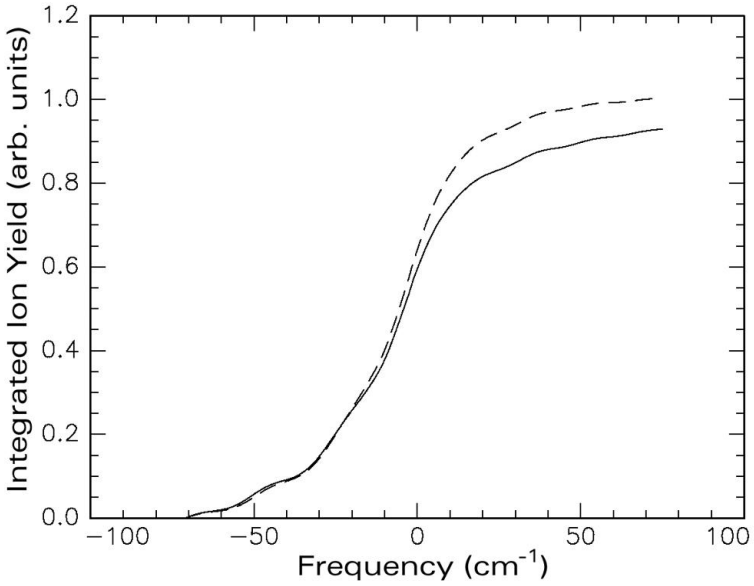

Figure 5.8: Integrated ion yield as a function of detuning from the ionic $4s^+ \rightarrow 4p^+$ transition. The initial state is a distribution of $4s22k$ Stark states in a 50 V/cm static field. The solid curve shows the in-field case ($\Delta t_{ICE} > 0$) and the dashed curve is the zero field case. The same static field is present in both cases. The HCP has a peak field of ~ 3 kV/cm and is polarized orthogonal to the static field. As in the case of two orthogonally polarized HCPs, a small amount of AI suppression is observed.

are observed. Clearly, the key to AI suppression is the transfer of population to high-m states.

5.4 Discussion and Numerical Analysis

Stabilization of an autoionizing system occurs when an excited inner electron decays to its ground state by spontaneously emitting a photon, rather than scattering off another excited electron. AI can only occur while the inner electron is in an excited

state. Therefore, the lifetime of that state determines the maximum amount of time during which AI can occur. The lifetime of the Ca inner $4p$ state studied in this work is approximately 3 ns [53]. An electron in a $22d$ state performs approximately 1850 Kepler orbits during 3 ns. The lifetime of the $4p22d$ state is approximately 4.2 ps [51]. Therefore, each time an electron in a $22d$ state returns to the $4p$ atomic core (every 1.6 ps), it has roughly a 32% chance of being autoionized. Due to the large number of Kepler oscillations, the probability that a $4p22d$ state does not autoionize during the 3 ns lifetime of the $4p$ inner electron state is practically zero. Instead, measurable suppression of AI is expected only if the outer electron remains in a high ℓ state with a small autoionization probability during the entire lifetime of the inner excited state [36].

5.4.1 Single HCP Calculations

In the first experiment presented, a single HCP field transfers population to several final ℓ states. The shift in the position of the resonance in figure 5.3(a) indicates that the HCP is populating states with high ℓ. Since no suppression of AI is observed in this experiment however, no stabilization occurs. One possibility for this is that the HCP could be directly ionizing the Rydberg electron. A HCP, which has sufficient strength to transfer a substantial fraction of the Rydberg population to high ℓ states also increases the energy of the electron. The change in energy can be great enough so that the electron is ionized (or has $n \geq 50$). Another possibility is that any high ℓ population

resulting from HCP interaction samples low ℓ character prior to stabilization. Since the low ℓ states have a large AI probability, if the high ℓ states sample any low ℓ character, AI occurs.

A numerical integration of the time dependent Schrödinger equation for a doubly excited calcium atom under the influence of an electric field is performed. Details of this calculation can be found in appendix C. Matrix elements are calculated for all possible dipole transitions in a range of $10 < n < 90$. For a single HCP, only $\Delta m = 0$ transitions are considered. At $t = 0$, the population in a specified Rydberg eigenstate is set to 1. The system evolves for 3 ns (approximately the lifetime of the $4p^+$ inner excited state). After $t = \Delta t_{ICE}$, population is removed from each state in the system according to the autoionization rates calculated in section C.4.2. Any population reaching the highest n state in the simulation is considered ionized and removed. The magnitude of the clearing pulse used to accelerate ions toward the microchannel plates is sufficient to ionize $n > 50$ Rydberg states.

The temporal profile of the HCP fields used in this work are not completely described by a "half - cycle". The true temporal shape of the HCPs is approximated by a 1 ps FWHM Gaussian pulse convoluted with a 5 ns to 10 ns long, low amplitude negative tail, such as shown in figure 3.2 [54]. The long time negative tail brings the total integrated field of the HCP closer to zero, even though the short term impulsive part of the HCP field is nonzero. The electric field profile used in the calculations closely

matches the HCP field in figure 3.2. Typical numerical results are shown in figures 5.9 and 5.10 for an initial state of $n = 22, \ell = 2, m = 0$, with $\Delta t_{ICE} = 1.5$ ps. A maximum HCP field of 5 kV/cm is applied. Even though higher HCP fields yield larger amounts of ℓ transfer, they also lead to a non-negligible probability of direct HCP ionization. For HCP fields greater than 5 kV/cm, a significant portion of the initial population reaches the edges of the basis set of the simulation and is counted as ionized. Figure 5.9 shows remaining population as a function of time for the first 3 ps after HCP interaction. Over 50% of the initial population is located in high ℓ states at $t = \Delta t_{ICE}$, however, after 3 ns (shown in figure 5.10) less than 1% of the initial population remains unionized. Even though population is transferred to high ℓ states by the impulsive part of the HCP field, no stabilization occurs.

The "stair-step" decrease in Rydberg population that is shown in figure 5.10 is due to the coherent evolution of angular momentum in the tail of the HCP field. Immediately after autoionization commences, the fraction of the Rydberg population that has low-ℓ character rapidly ionizes. At this time, all of the surviving bound population resides in high-ℓ states. However, the small static field causes a precession of the angular momentum in the "Stark wavepacket" from high- into low-ℓ [49, 55, 56]. After one "Stark period," $\tau_S = 2\pi/(3F_{tail}n)$, a significant fraction of the bound population again has low-ℓ character [49, 55, 56]. Autoionization of the low-ℓ part of the wavepacket results in another rapid decrease in the Rydberg population. The cycle repeats until the

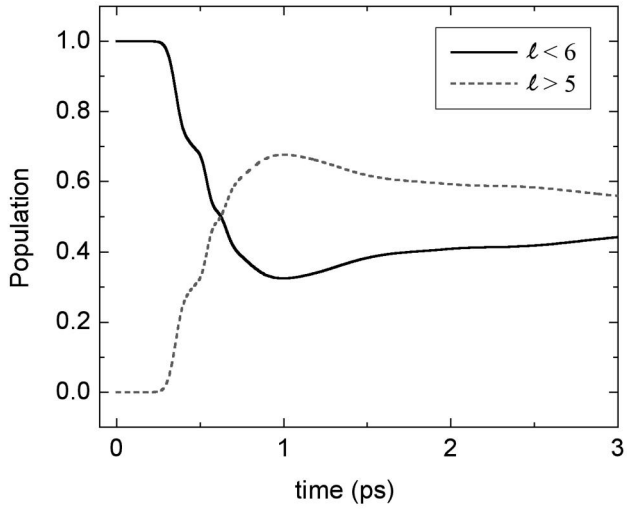

Figure 5.9: Quantum mechanical simulation of the interaction of a single HCP with an autoionizing state as discussed in the text. The initial Rydberg state has $n = 22$, $\ell = 2$, and $m = 0$. The HCP has a peak field of 5 kV/cm and a static negative tail of 10 V/cm. The solid curve shows the population in low ℓ states ($\ell < 6$), while the dashed curve shows the population in high ℓ.

atom has completely ionized. In the best case (i.e. the greatest survival probability), the simulation predicts less than 10% surviving Rydberg population after 1 ns and less than 1% remaining after the 3 ns $4p$ core lifetime. The effective autoionization rate is proportional to the magnitude of the static field. Choosing a HCP tail field of 20 V/cm would result in an autoionization lifetime that is half of that indicated in Figure 5.10. Therefore, even though the HCP induces angular momentum *transfer* that should stabilize some fraction of the atoms from AI, the quasi-static tail field *mixes* low ℓ character back into the Rydberg wavefunction.

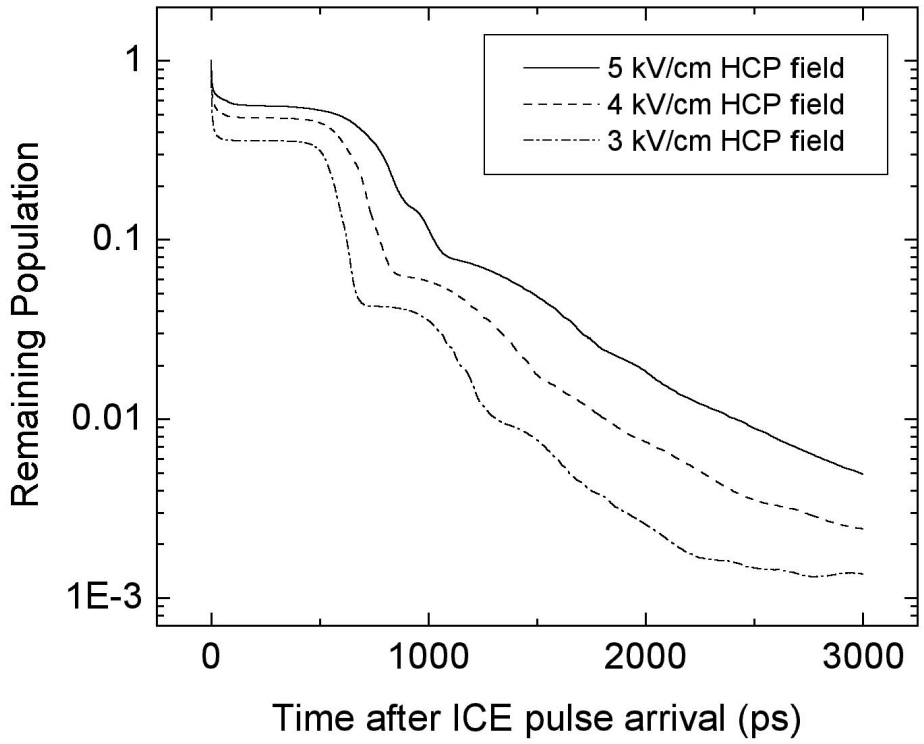

Figure 5.10: Surviving Rydberg population as a function of time calculated under the same conditions as in Figure 5.9. The system is allowed to autoionize after a time $\Delta t_{ICE} = 1.5$ ps according to calculated AI rates for calcium. Calculated surviving population is shown as a function of time for three values of HCP field strength. Less than 1% of the initial population remains after 3 ns.

5.4.2 Calculations with Two Orthogonal HCPs

To simulate two orthogonal fields interacting with the system, all m states for each allowed ℓ value must be included in the simulation. In this case, the density of available states grows rapidly with increasing n (as n^2 instead of as n in the previous case). Therefore, the simulation must be restricted to $10 < n < 45$ due to computational limitations. At $t = 0$, all the population resides in a specified n, ℓ, m Rydberg eigenstate. Two orthogonal HCP fields separated in time by Δt_{HCP} interact with the system. The orthogonal fields transfer population from the initial state to many n, ℓ, and m final states. After the main impulse of each HCP field interacts with the system, any remaining field is effectively constant and polarized along some axis. This resultant field direction is now the good axis of the problem. The m distribution of the system along this resultant field axis is examined as a function of HCP field strength and Δt_{HCP}. In the constant residual field, m is a good quantum number, so the angular momentum may mix only between $\ell = m$ and $\ell = n - 1$. Any fraction of the initial population that has been transferred to high m is then forbidden from sampling low ℓ states with $\ell < m$.

As a check of the two pulse simulation, the time between the two HCPs (Δt_{HCP}) is set to zero, and the strength of the two HCP fields is set equal. The final m distribution is calculated for every possible orientation angle in the $\hat{xz}$ plane. The resulting dynamics should be identical to that of a single HCP with strength $\sqrt{2}$ times that of

either individual pulse interacting with the same initial state. In this case, no high m transfer along the line $z = x$ is expected. Figure 5.11 shows the m distribution for two orthogonal HCPs with maximum field strengths of 3 kV/cm along $+\hat{x}$ and $+\hat{z}$ with an initial state of $|22, 2, 0>$. Since the initial state is an $\ell = 2$ state as measured along $\hat{z}$, the m distribution along $\frac{1}{\sqrt{2}}(\hat{x} + \hat{z})$ may have $|m| = 0, 1, 2$ character, but is forbidden from having any higher m components (see section C.5 for further explanation).

Figure 5.12 shows the calculated m distribution after the passage of two orthogonal HCP fields with a relative delay of $\Delta t_{HCP} = 0.8$ ps. The first HCP is polarized along $\hat{x}$ and the second along $\hat{z}$. Along $\frac{1}{\sqrt{2}}(\hat{x} + \hat{z})$, less than 10% of the population is actually transferred to states with $m > \ell_c$. All population with $m \leq \ell_c$ is considered autoionized due to the ℓ state mixing. Similar calculations are performed for a variety of values of Δt_{HCP}, with similar results. Increasing the peak field of the two HCPs to greater than 3 kV/cm leads to direct HCP ionization. Approximately 10% of the final Rydberg population resides in states with $m > \ell_c$, and therefore, is stable against autoionization. This value is in good agreement with our experimental observation of $\approx 10\%$ stabilization probability for two crossed polarized HCPs.

5.4.3 Calculations with Orthogonal HCP and Static Fields

Finally, the effect of applying an orthogonal HCP field on an autoionizing system in the presence of a static field is calculated. The static field is applied along the $\hat{z}$

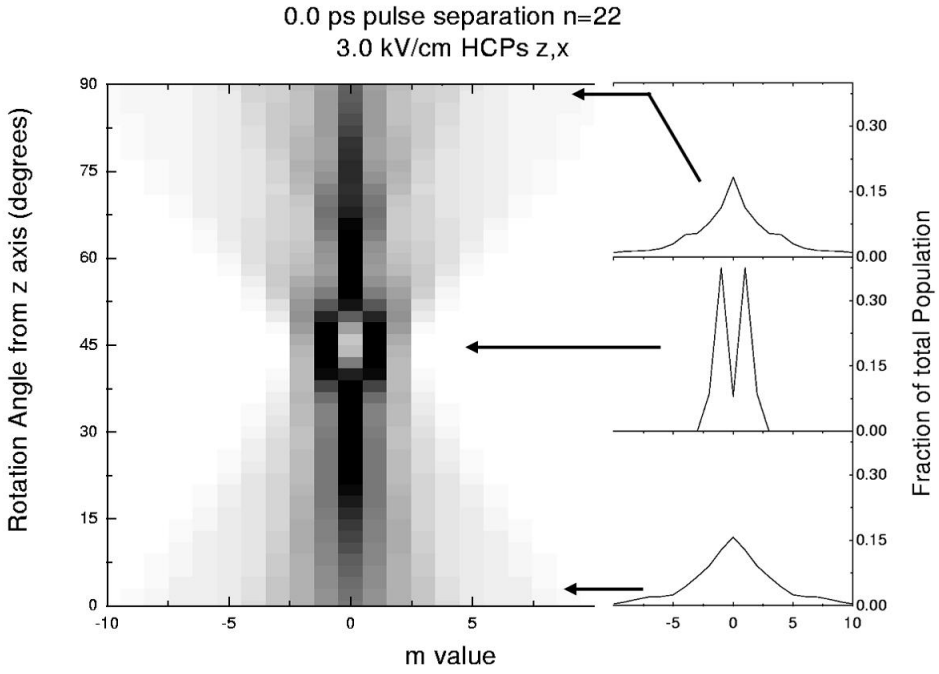

Figure 5.11: Quantum mechanical calculation of the interaction of two orthogonal HCP fields with an autoionizing state as discussed in the text. The initial Rydberg eigenstate has $n = 22$, $\ell = 2$, and $m = 0$ when measured along $\hat{z}$. Both HCP fields have peak fields of 3 kV/cm (first HCP along $\hat{z}$ and second HCP along $\hat{x}$) and static negative tails of 10 V/cm. The time delay between the two pulses is $\Delta t_{HCP} = 0.0$. The m distribution is shown 2 ps after the HCP interaction as measured along any axis from $\hat{z}$ to $\hat{x}$. Dark represents m values with a greater population. The m distribution along a 45 degree axis, contains only $|m| = 0, 1, 2$ since this is the resultant field axis.

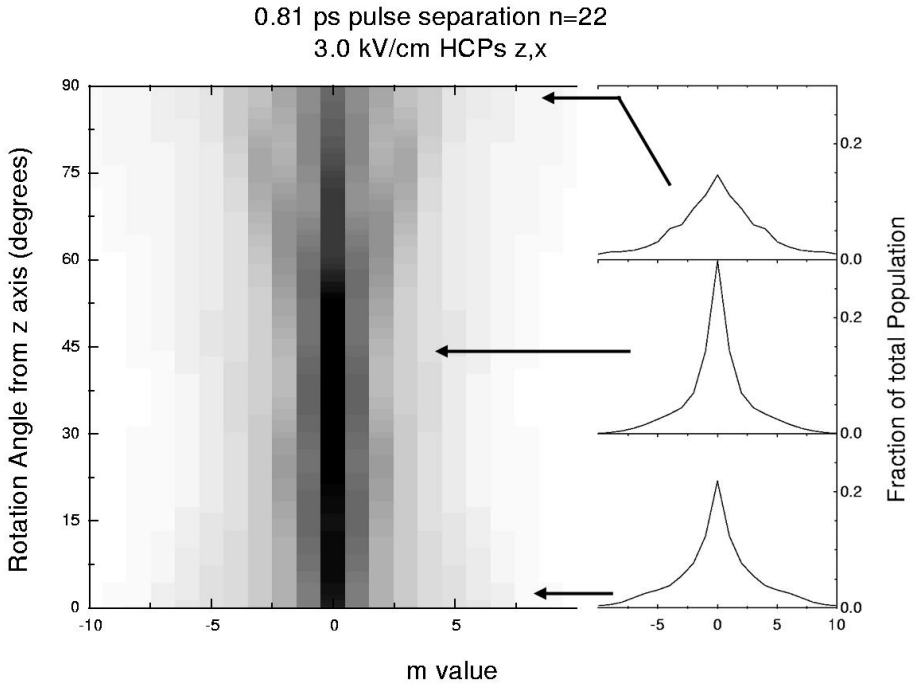

Figure 5.12: Quantum mechanical calculation of the interaction of two orthogonal HCP fields with an autoionizing state as discussed in the text. The initial Rydberg eigenstate has $n = 22$, $\ell = 2$, and $m = 0$ measured along $\hat{z}$. Both HCP fields have peak fields of 3 kV/cm (first HCP along $\hat{z}$ and second HCP along $\hat{x}$) and static negative tails of 10 V/cm. The time delay between the two pulses is $\Delta t_{HCP} = 0.8$ ps. The m distribution is shown 2 ps after the HCP interaction as measured along any axis from $\hat{z}$ to $\hat{x}$. Dark represents m values with a greater population. The m distribution along $\frac{1}{\sqrt{2}}(\hat{x} + \hat{z})$ only contains less than 10% of the population in $m > \ell_c$.

axis. A HCP field polarized along $\hat{x}$ interacts with the system. The Stark states in calcium within a Gaussian window centered at the zero field energy of the $4s22d$ state are populated at $t = 0$. The window has a bandwidth of 0.5 cm^{-1}. The initial state is chosen to resemble the initial state in the experiment in section 5.3.3. The exact energy levels and oscillator strengths for calcium are calculated as a function of F from a diagonalization of the non-hydrogenic $|n, \ell, m >$ basis. The details of this diagonalization can be found in section D.2.3. The system evolves according to the time dependent Schrödinger equation in the presence of both the static field (along $\hat{z}$) and the HCP field (along $\hat{x}$). The calculation includes all allowed n, ℓ, and m states in the range $10 < n < 45$. Following the impulsive part of the HCP interaction, the final m state distribution along $\hat{z}$ is recovered. Figure 5.13 shows the final state m distribution for a static field of 200 V/cm and a maximum HCP field of 3 kV/cm. Less than 10% of the total population arrives in high m states ($m > \ell_c$). Increasing the maximum field strength of the HCP much above 3 kV/cm in a field of 200 V/cm again results in a breakdown of the simulation as population begins moving to the highest n values. This is analogous to direct ionization of the system due to interaction with the HCP and static fields. All population with $m \leq \ell_c$ is again considered autoionized. The calculated amount of AI in the presence of a combination of static field and orthogonal HCP field differs from the zero field amount by ≈10%.

The final state m distribution is also calculated if all the k states in the $n =$

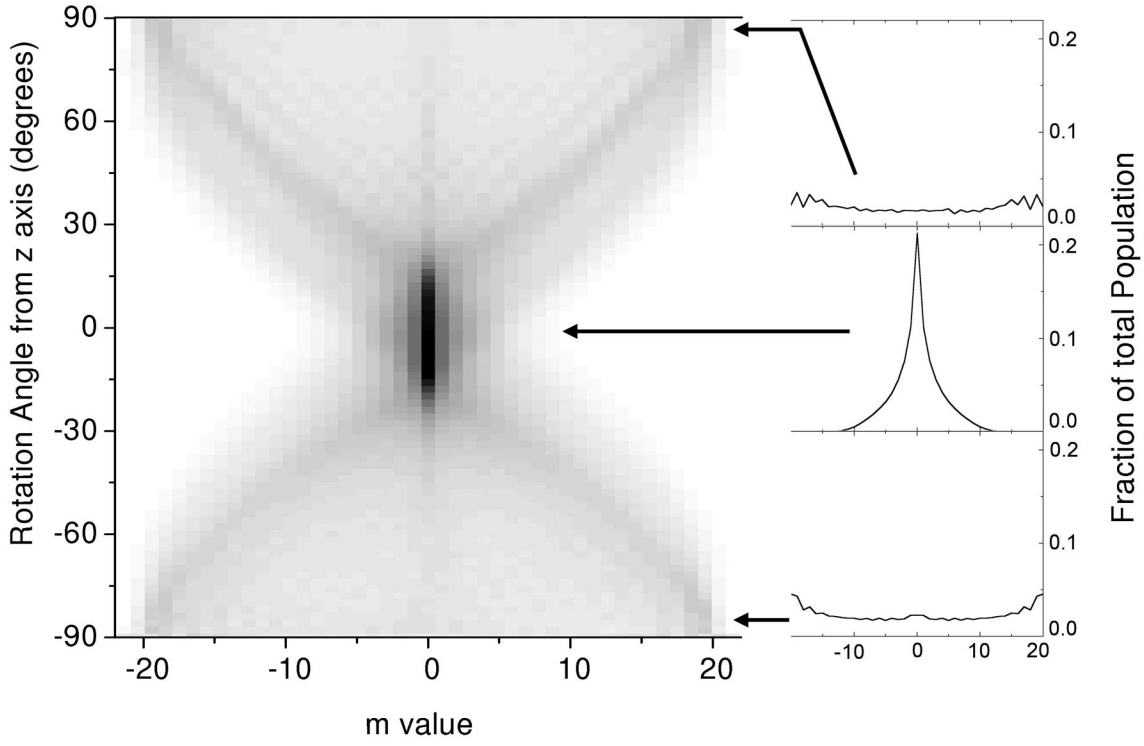

Figure 5.13: Quantum mechanical calculation of the interaction of a HCP and an orthogonal applied static field as discussed in the text. Initially, an ensemble of $4s22k$ states is excited in a 200 V/cm static field. The initial state energy distribution is centered around the zero field location of the $4s22d$ state. The static field is oriented along the $\hat{z}$ axis. The HCP is polarized in the $\hat{x}$ direction and has a peak field of 3 kV/cm with a 10 kV/cm static field tail. The m distribution is shown 2 ps after the HCP interaction as measured along any axis from $-\hat{z}$ to $+\hat{z}$. Dark represents m values with a greater population. Less than 10% of the population has $m > \ell_c$ after HCP interaction.

22 manifold are excited equally. This is the experimental analog of using a broad bandwidth laser to excite the entire Stark manifold. The results do not significantly differ from those of the previous cases.

5.5 Conclusions

We have extended the study of an autoionizing system in the presence of electric fields from the adiabatic field regime into the impulsive field limit. We have examined, experimentally and theoretically, transient electric field induced stabilization of Rydberg atoms against AI for three different transient/static field configurations. These time dependent field configurations mimic the micro-fields experienced by atoms, molecules, and ions embedded in neutral plasmas or space-charge distributions. We have found that impulsive transients, oriented parallel to relatively weak static electric fields, are totally ineffective in stabilizing atoms against autoionization due to angular momentum mixing in the static field. We predict and observe the stabilization of autoionizing atoms for field configurations where high-m states are populated. These states are stable against autoionization and, in contrast to low-m states, are immune to angular momentum mixing with rapidly autoionizing low-ℓ levels. However, the fraction of atoms that is stabilized is small ($\approx 10\%$ or less) due to the relatively low probability for populating high-m states during a field impulse. Ultimately, impulsive field ionization of the Rydberg electron limits the strength of the transient field that can effectively

stabilize the atom against AI.

Bibliography

[1] J.G. Zeibel, S.N. Pisharody, and R.R. Jones, *Phys. Rev. A*, accepted for publication, (2002).

[2] K. LaGattuta, I. Nasser, and Y. Hahn, *J. Phys. B* **20**, 1565 (1987).

[3] I. Nasser and Y. Hahn, *Phys. Rev. A* **36**, 4704 (1987).

[4] F. Robicheaux and M.S. Pindzola, *Phys. Rev. Lett.* **79**, 2237 (1997).

[5] A. Muller *et. al.*, *Phys. Rev. A* **36**, 599 (1987).

[6] Y. Hahn, *Rep. Prog. Phys.* **60**, 691 (1997), and references therein.

[7] W. Graham *et. al.*, eds., NATO ASI Series B: Physics, Vol. 296. *Recombination of Atomic Ions*, Plenum, New York, (1992).

[8] J.G. Story, B.J. Lyons, and T.F. Gallagher, *Phys. Rev. A* **51**, 2156 (1995).

[9] Lung Ko, V. Klimenko, and T.F. Gallagher, *Phys. Rev. A* **59**, 2126 (1999).

[10] V. Klimenko, Lung Ko, and T.F. Gallagher, *Phys. Rev. Lett.* **83**, 3808 (1999).

[11] V. Klimenko and T.F. Gallagher, *Phys. Rev. Lett.* **85**, 3357 (2000).

[12] J. Stevefelt, J. Boulmer, and J-F. Delpech, *Phys. Rev. A* **12**, 1246 (1975).

[13] D. You et al., *Opt. Lett.* **18**, 290 (1993).

[14] A. Burgess, *Astrophys. J.* **139**, 776 (1964).

[15] E.W. Schlag *ZEKE Spectroscopy*, (Cambridge University Press, Cambridge, 1998) and references therein.

[16] F. Merkt and R.N. Zare, J. Chem. Phys. **101**, 3495 (1994).

[17] M.J.J. Vrakking and Y.T. Lee, J. Chem. Phys. **102**, 8818 (1995).

[18] M.J.J. Vrakking and Y.T. Lee, J. Chem. Phys. **102**, 8833 (1995).

[19] M.J.J. Vrakking, I. Fischer, D.M. Villeneuve, and A. Stolow, J. Chem. Phys. **103**, 4538 (1995).

[20] M.J.J. Vrakking, D.M. Villeneuve, and A. Stolow, Phys. Rev. A **54**, R37 (1996).

[21] P. Bellomo, D. Farrelly, and T. Uzer, J. Chem. Phys. **107**, 2499 (1997).

[22] P. Bellomo, D. Farrelly, and T. Uzer, J. Chem. Phys. **108**, 5295 (1998).

[23] S.R. Proctor, M.J. Webb, and T.P. Softley, Faraday Discuss. **115**, 277 (2000).

[24] Y. Hahn and K.J. LaGattuta, *Phys. Rep.* **166**, 195 (1987).

[25] K. LaGattuta, I. Nasser, and Y. Hahn, *Phys. Rev. A* **33**, 2782 (1986).

[26] D. S. Belic *et. al.*, *Phys. Rev. Lett.* **50**, 339 (1983).

[27] I. Nasser and Y. Hahn, *Phys. Rev. A* **30**, 1558 (1984).

[28] H. Gao *et. al.*, *Phys. Rev. Lett.* **75**, 4381 (1995).

[29] T.J. Bensky, G. Haeffler, and R.R. Jones, *Phys. Rev. Lett.* **97**, 2018 (1997).

[30] T.F. Gallagher, *Rydberg Atoms*, 1st ed., Cambridge University Press, Cambridge, (1994).

[31] L.D. Landau and E.M. Lifshitz, *Quantum Mechanics (Non Relativistic Theory)*, 3rd ed. (Pergamon Press, Oxford, 1976).

[32] R.R. Jones and T.F. Gallagher, Phys. Rev. A **38**, 2846 (1988).

[33] H.A. Bethe and E.E. Salpeter, *Quantum Mechanics of One and Two Electron Atoms*, (Springer-Verlag, New York, 1977).

[34] R.R. Jones and T.F. Gallagher, Phys. Rev. A **39**, 4583 (1989).

[35] W. Sandner, K.A. Safinya, and T.F. Gallagher, Phys. Rev. A **33**, 1008 (1986).

[36] V.L. Jacobs and J. Davis, *Phys. Rev. A* **19**, 776 (1979).

[37] V.L. Jacobs *et al.* Phys. Rev. Lett. **37**, 1390 (1976).

[38] N.E. Tielking and R.R. Jones, Phys. Rev. A **52**, 1371 (1995).

[39] R.R. Jones, D. You, and P.H. Bucksbaum, *Phys. Rev. Lett.* **70**, 1236 (1993).

[40] W.E. Cooke, T.F. Gallagher, S.A. Edelstein, and R.M. Hill, *Phys. Rev. Lett.* **40**, 178 (1978).

[41] R.R. Jones, *Phys. Rev. A* **58**, 2608 (1998).

[42] J.G. Story, D.I. Duncan, and T.F. Gallagher, Phys. Rev. Lett. **70**, 3012 (1993).

[43] J.E. Thoma and R.R. Jones, Phys. Rev. Lett **83**, 516 (1999).

[44] S.N. Pisharody and R.R. Jones, *Phys. Rev. A* **65**, 033418 (2002).

[45] M.B. Campbell, T.J. Bensky, and R.R. Jones, *Opt. Express* **1**, 197 (1997).

[46] For a full description of the single shot detector and how a counterpropagating beam geometry recovers a range of pump - probe time delays, see chapter 2.

[47] R.R. Jones, *Phys. Rev. Lett* **76**, 3927 (1996).

[48] J.G. Zeibel and R.R. Jones, *J. Phys. B* **34**, 1213 (2001); See also appendix A.

[49] M.B. Campbell, T.J. Bensky, and R.R. Jones, *Phys. Rev. A* **59**, R4117 (1999).

[50] J.A. Armstrong, P. Esherick, and J.J. Wynne, *Phys. Rev. A* **15**, 180 (1977).

[51] R.R. Jones, *Phys. Rev. A* **58**, 2608 (1998).

[52] Complete details of how a HCP field transfers momentum to an electron are presented in chapter 3.

[53] A. Lindgard and S.E. Nielsen, *At. Data Nucl. Data Tables* **19**, 597 (1977).

[54] N.E. Tielking, T.J. Bensky, and R.R. Jones, Phys. Rev. A **51**, 3370 (1995).

[55] A. ten Wolde *et al.*, Phys. Rev. A **40**, 485 (1989).

[56] L.D. Noordam *et al.*, Phys. Rev. A **40**, 6999 (1989).

Chapter 6

Manipulating Wavepacket Dynamics Part 3: The Dynamics of a Recombined Wavepacket

6.1 Introduction

An investigation of the effects that HCP fields have on the system of an ion and a free electron in a static field was presented in chapter 4. We were able to determine the probability that the HCP caused the electron and ion to recombine to form a bound atom. Recombination probability was investigated as a function of a number of parameters. However, no information was recovered about the subsequent motion of

the newly recombined atom [1]. In this chapter, we again look at the response of an electron - ion system to a HCP field. However, this time we investigate the system in a field free environment. In addition, we try to recover information about the motion of the recombined system following HCP assisted recombination.

Furthermore, recent work has suggested that the dynamics of a recombined atomic system may exhibit interesting properties [2–4]. Both classical and fully quantum simulations indicate it is possible to localize a recombined electron far from the atomic core under certain experimental conditions. This spatial localization can recur periodically for long times [2,3]. To our knowledge however, this effect has yet to be observed experimentally. In this chapter, we attempt to: (i) recover the momentum distribution of a recombined wavepacket as a function of time after recombination occurs and, (ii) investigate the phenomenon of electron localization within a recombined wavepacket.

6.2 Experimental Setup

In this experiment, a 1 ps laser pulse photoionizes Ca atoms from a thermal beam, producing a low density, $\rho \sim 10^7$ cm^{-3}, non-equilibrium plasma. The frequency of the laser pulse is tuned just above the field free ionization threshold. Immediately following the laser pulse, each photoionized electron moves slowly away from its parent ion in the form of a radially localized continuum wavepacket. After a short time delay τ, the plasma is exposed to a sub-picosecond half cycle pulse of THz radiation [5]. The HCP

stimulates the recombination of a fraction of the outgoing electrons with their parent ions, forming highly-excited Rydberg atoms [2]. A second HCP is then used to probe the resulting recombined wavepacket. The momentum distribution of the wavepacket is recovered through the lock-in IMR technique introduced in chapter 3 [7].

Technically, the recombination induced by the HCP can be classified as stimulated RR. However, the electric field in our pulse is not oscillatory. In fact, the temporal profile of the HCP (shown in figure 3.2) is essentially identical to the transverse field that an electron-ion pair experiences during a fast, long-range collision with a third charged particle. Therefore, rather than describe HCP assisted recombination in terms of stimulated emission and absorption of multiple photons, it is more intuitive to consider the process as artificial TBR with the HCP replacing the collision field [2]. In classical terms, the HCP field gives an electron an impulse or kick of strength $\vec{A}$ [9,10]. If the kick opposes the motion of the electron, sufficient momentum and energy may be extracted to recombine the electron with its parent ion. Quantum mechanically, this momentum and energy transfer is manifest in the redistribution of electron amplitude from the outgoing wavepacket into a coherent superposition of bound and continuum states [2,3]. The recombination probability per atom is equal to the bound-state population in this final superposition state.

The goal of this chapter is to recover information about the evolution of the recombined wavepacket. To this end, atoms are photoionized and recombined, and then

probed with a second HCP field. The number of Rydberg atoms remaining after the final HCP probe is recorded as a function of (i) the delay between the recombining HCP and the probe HCP (Δt_{probe}); (ii) the initial energy of the recombined electron; (iii) the HCP probe field strength; and (iv) the relative orientation of the two HCP fields.

A schematic diagram of the detector used in this work is shown in figure 2.9. Initially, ground state Ca $4s4s$ atoms are excited to a $4s4p$ level by a a 5 ns, 423 nm, dye laser pulse. A 1 ps, 389 nm laser pulse then photoionizes the $4s4p$ atoms, producing a continuum wavepacket with a mean energy, $E_{wp} \sim 15\text{cm}^{-1}$. The wavepacket has an energy spread of approximately 15 cm^{-1} due to the bandwidth of the 389 nm laser pulse. The two laser beams are linearly polarized perpendicular to the plane of the field plates, and the photoionized electrons have azimuthal quantum number, $m = 0$.

After a delay, $\tau < 10$ ps, the plasma and neutral atoms in the interaction region are exposed to a 1 ps HCP. The HCP is generated from a GaAs wafer by the method introduced in chapter 3. The HCP field is linearly polarized parallel to the bias field on the GaAs wafer, and proportional to the bias voltage [5]. The HCP field amplitude, $F_{HCP} < 20$ kV/cm is insufficient to affect the neutral $4s4s$ or $4s4p$ Ca atoms. However, depending on the HCP strength and delay τ, the HCP can recombine a small fraction ($\sim 20\%$) of the continuum electrons with their parent ions [2].

After a further delay, $\Delta t_{probe} < 100$ ps, the plasma and recombined atoms in the

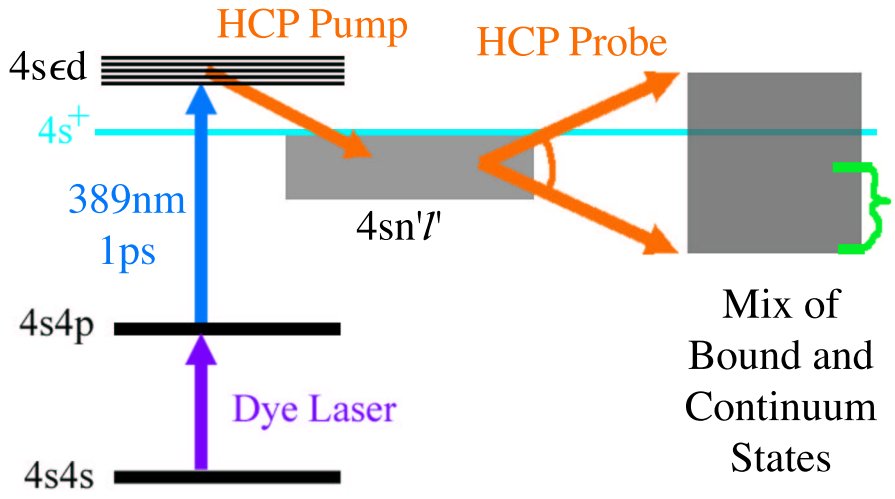

Figure 6.1: A schematic diagram of the relevant energy levels in this experiment. The actual measurement performed determines the fraction of the final states still bound after the HCP probe. This is shown graphically by the states indicated by green bracket on the right.

interaction region are exposed to a second, 1 ps HCP. This second (probe) HCP is generated from another GaAs wafer which is mounted on a rotation stage so that the angle between the first HCP (pump) and the second HCP (probe) can be continuously varied. The pump and probe HCPs counterpropagate through the interaction region. The probe HCP ionizes a fraction of the neutral atoms created by the HCP pump pulse. The fraction of recombined atoms which are ionized depends on the strength and relative delay of the HCP probe, as well as the relative orientation between the pump and probe pulses. An energy level diagram for this experiment is shown in figure 6.1.

Approximately 20 ns following the HCP probe pulse, a 30 V, 4 μs long field pulse

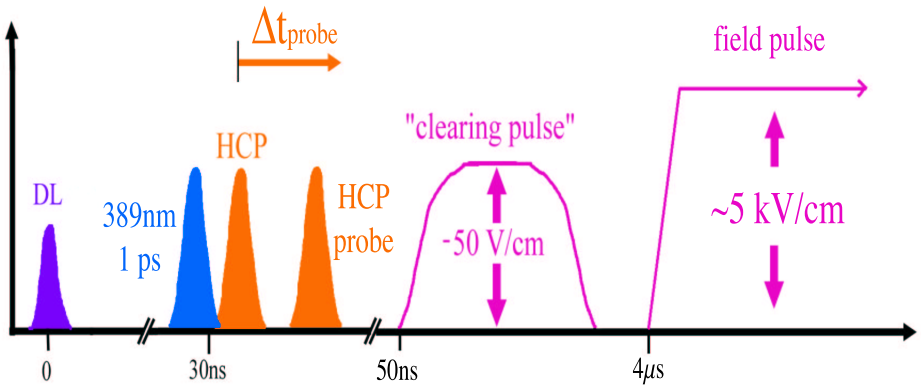

Figure 6.2: A timing diagram of the experiment.

is applied to the upper field plate creating a pulsed field of 25 V/cm in the interaction region. Any ions present in the interaction region are accelerated toward the lower field plate due to their interaction with this "clearing pulse". Loosely bound ($n > 60$) Rydberg atoms are also ionized by the clearing pulse and are therefore indistinguishable from ionization events. Following the clearing pulse, a high voltage pulse ($\sim$7 kV) is applied to the lower field plate. This HV pulse field ionizes any neutral Rydberg atoms remaining in the interaction region. Ions that are produced via SSFI travel through a slit in the upper field plate and are collected by the single shot detector (see section 2.6). Ion signal measured by the detector is proportional to the number of recombined atoms which are not ionized by the HCP probe. A timing diagram for this experiment in shown in figure 6.2.

Before the dynamics of a recombined wavepacket can be investigated, a recombined wavepacket must be created. We want to create a wavepacket which contains the largest

amount of the initial electron population possible for a given set of initial conditions. Consider a HCP impulse of strength $\vec{A} = -A\hat{n}$ incident upon a classical continuum electron with energy E_0 at time $t = \tau$. The HCP field causes a change in the energy of the electron

$$\Delta E = \vec{p}(\tau) \cdot \vec{A} + \frac{|\vec{A}|^2}{2} \ . \tag{6.1}$$

The continuum electron will recombine if

$$E_0 \ + \ \Delta E \ > \ 0 \ . \tag{6.2}$$

This condition is satisfied when

$$p_n(\tau) \ \equiv \ \vec{p}(\tau) \cdot \hat{n} \ \geq \ \frac{E_0}{A} + \frac{A}{2} \ . \tag{6.3}$$

Therefore, we define a critical momentum $p_c \equiv \frac{E_0}{A} + \frac{A}{2}$, such that the recombination probability of a continuum wavepacket is equal to the probability that the electron has $p_n \geq p_c$.

Figure 6.3 shows the momentum distribution of a continuum wavepacket at two different times. In (a), the distribution is broad and a relatively large portion of the wavepacket has $p_n \geq p_c$. Therefore, in (a) the recombination probability is large. However, in (b) the momentum distribution is narrow and only a small portion of the wavepacket has $p_n \geq p_c$, resulting in a low recombination probability. Therefore, by measuring the recombination signal as a function of time delay and HCP field, one can recover a portion of the wavepacket's time dependent momentum space probability

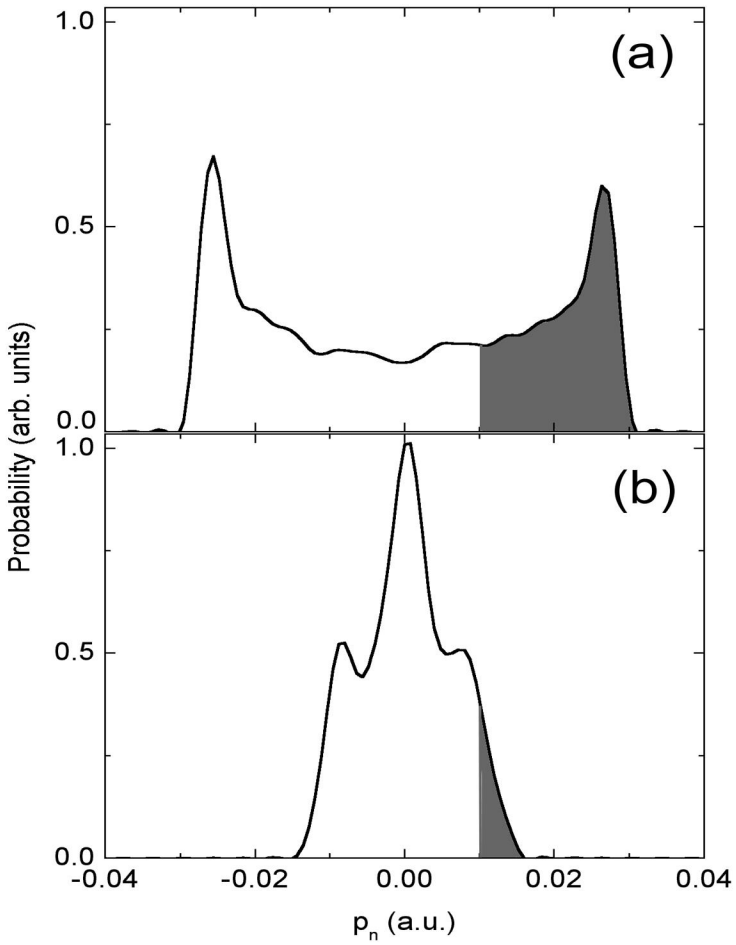

Figure 6.3: A schematic representation of the fraction of the wavepacket which is recombined. Here, $p_c = 0.01$. In (a), a large fraction of the wavepacket has $p_n \geq p_c$. This situation will lead to a larger recombined fraction than in (b), where only a small fraction of the initial wavepacket has $p_n \geq p_c$.

distribution [2].

To obtain the largest possible amount of recombination, p_c must be as small as possible. This occurs for an optimum kick strength A_{opt} such that $A_{opt} = \sqrt{2E_0}$. However, interesting behavior of the recombined wavepacket is predicted not for $A = A_{opt}$, but rather when $A = p_n(\tau)$. In this case, $\Delta E = -\frac{1}{2}p(\tau)^2$ and the HCP field removes all the kinetic energy from the outgoing electron. Simulations of the motion of the recombined wavepacket for various values of A will be presented in section 7.3

In this work, A is determined experimentally by fixing a value of τ and a value of HCP probe field strength, then scanning the HCP pump field strength. The pump field strength which results in long term modulations in the HCP probe ionization signal is chosen as the appropriate HCP pump field strength. The recombined wavepacket created with these parameters is then studied with the lock-in IMR technique.

6.3 Results

Figure 6.4 shows the survival probability of a recombined wavepacket as a function of HCP pump strength A_1 and HCP probe time delay, Δt_{probe}. The time delay τ between the initial photoionization and the pump HCP is 3 ps [6]. The pump and probe pulses are both polarized along $+\hat{z}$. The probe pulse has an impulse of $A_2 = 0.021$ and ionizes all portions of the recombined wavepacket with $p_z > p_0$, where p_0 is defined in equation 3.8 in section 3.3.2. Dark regions in figure 6.4 correspond to combinations of Δt_{probe} and

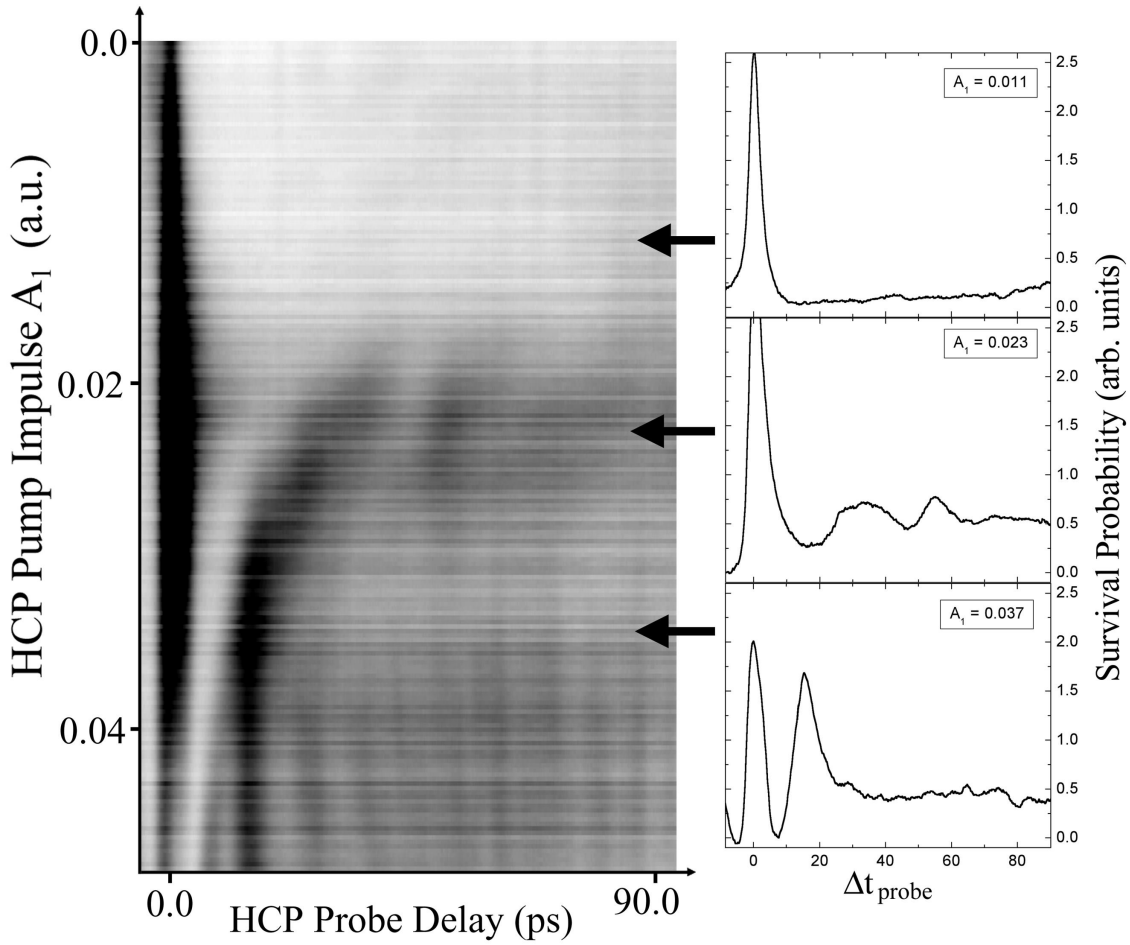

Figure 6.4: Measured survival probability of the recombined wavepacket as a function of HCP pump strength A_1, and HCP probe time delay, Δt_{probe}. The initial time delay τ between launching of the continuum radial wavepacket and recombination is 3 ps. The pump and probe pulses are both polarized along $+\hat{z}$. The probe pulse has a impulse of $A_2 = 0.021$ and will ionize all of the recombined wavepacket with $p_z > 0 > p_0$. Dark regions correspond to combinations of Δt_{probe} and A_1 which result in a high probability of $p_z < p_0$. The pump and probe pulses are both polarized along $+\hat{z}$. Long time oscillations in the momentum distribution are observed around $A_1 = 0.023$. This is shown graphically in the three insets.

A_1 which result in a high fraction of bound electrons following both pump and probe interactions. Long time oscillations in the momentum distribution are seen for HCP pump fields around $A_1 = 0.023$. For the most part, if the magnitude of A_1 is slightly greater or less than 0.023, then no long lived oscillations in the survival probability exist. Some oscillatory features are however observed at $A_1 > 0.045$. The origin of this effect will be discussed in a later section.

A value of HCP pump strength is chosen from the data shown in figure 6.4 which shows the longest lived oscillations in the momentum distribution. The HCP pump strength is then fixed to this value. For the data in figure 6.4 this is $A_1 = 0.023$ and is shown graphically in the middle insert. The strength and direction of the HCP probe is then varied to study the dynamics of the recombined packet. The measured fraction of recombined atoms which remain bound after the probe pulse is shown in figures 6.5 and 6.6 as a function of both A_2 and Δt_{probe}. In figure 6.5(a), both the pump and probe are polarized along $+\hat{z}$, while in figure 6.5(b), the probe is polarized along $-\hat{z}$. When the pump and probe pulses are parallel (opposite), dark areas in the plots represent combinations of A_2 and Δt_{probe} which lead to a net negative (positive) value of p_z in the recombined wavepacket. In figure 6.6, the probe is polarized along $+\hat{x}$, perpendicular to the pump pulse. Very little change in the bound fraction of the recombined wavepacket is seen as a function of Δt_{probe}. This indicates that there is little or no net motion of the recombined wavepacket in the $\hat{x}$ direction after $\Delta t_{probe} = 0$. Therefore, any long

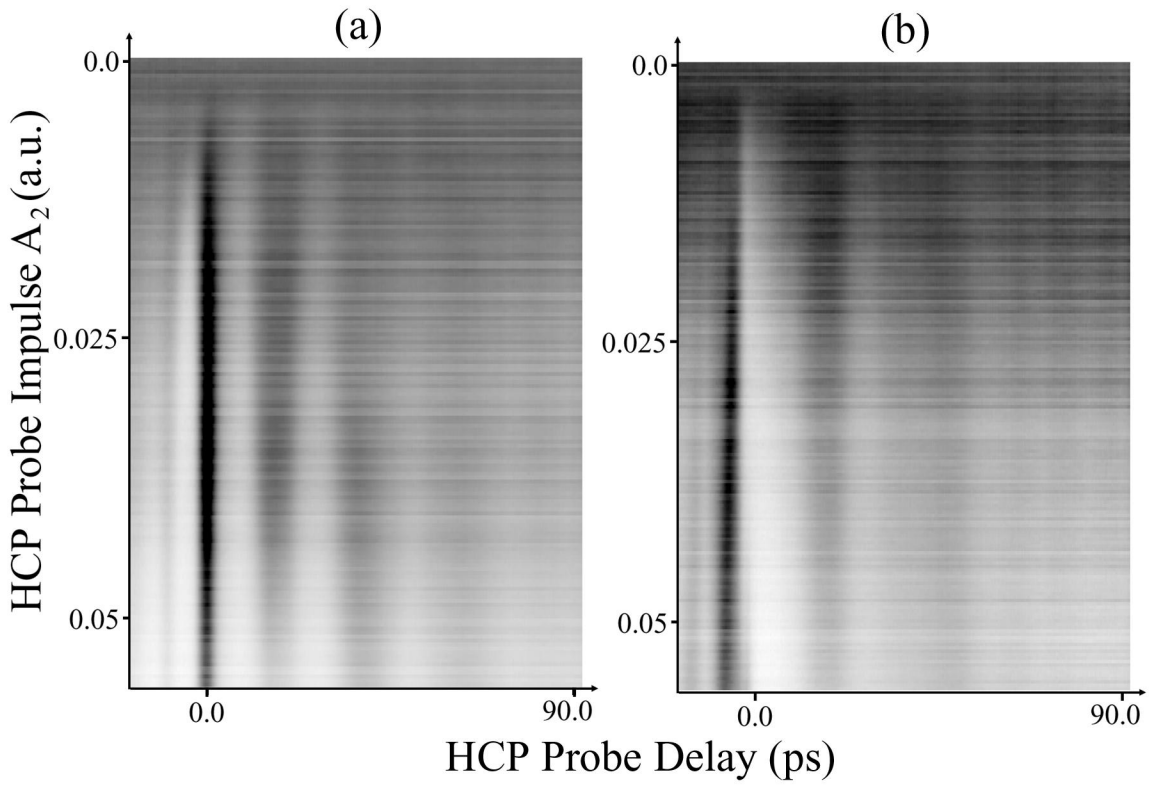

Figure 6.5: Measured fraction of recombined atoms which remain bound after the probe pulse as a function of both probe strength A_2 and Δt_{probe}. In (a), the HCP pump and probe are both polarized along $+\hat{z}$. In (b) however, the pump pulse is polarized along $+\hat{z}$ and the probe is polarized along $-\hat{z}$.

lived net motion of the momentum distribution is primarily confined to the $\hat{z}$ direction.

A vertical slice through the data shown in figure 6.5(a) at a single value of Δt_{probe} yields the bound state probability of the recombined wavepacket as a function of HCP probe strength. One minus this quantity is the amount of HCP ionization of the recombined wavepacket. It is possible to follow the normal IMR technique outlined in chapter 3 and directly recover the momentum distribution of the recombined wavepacket from

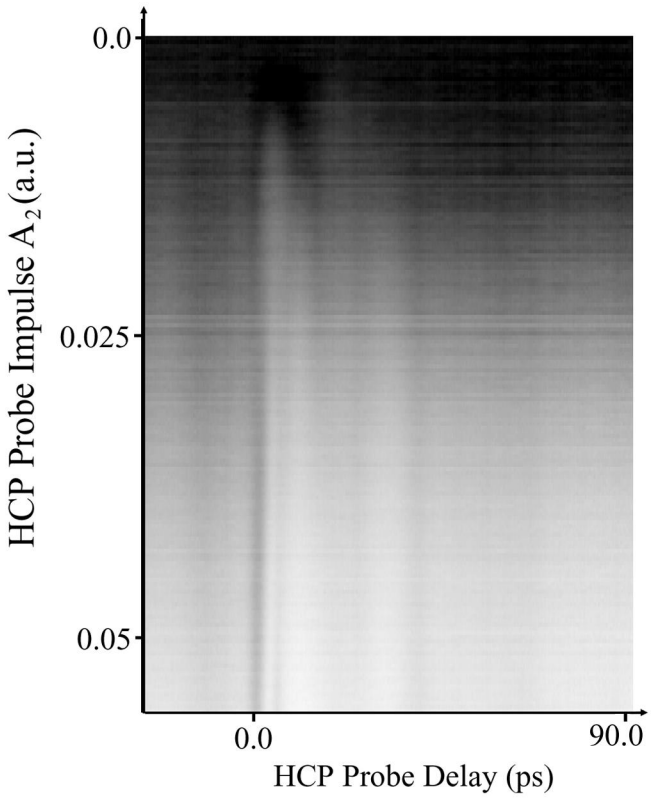

Figure 6.6: Similar to figure 6.5, but the HCP probe is polarized along $+\hat{x}$. For the perpendicular pump - probe geometry shown here, very little change in the number of bound atoms is seen after $\Delta t_{probe} = 0$ for a given value of A_2. Any long lived net motion of the momentum distribution is confined to the $\hat{z}$ direction.

the data in figures 6.5 and 6.6 [7]. However, due to the relatively small signal to noise ratio in the measured ionization curves, direct application of the IMR method yields extremely noisy momentum distributions. Instead, we use a variation on the normal IMR technique known as lock-in IMR to recover the momentum distribution of the recombined wavepacket. The lock-in IMR method is described in detail in section 3.3.2. Briefly, instead of trying to take the derivative of the HCP ionization data to recover the momentum distribution, the derivative signal is measured directly. With lock-in IMR, we can avoid the need to take the derivative of a noisy signal.

Before IMR can be applied to the experimental data however, an average recombined wavepacket energy E_{wp} must be found. To determine E_{wp}, a Fourier transform of a horizontal slice through the data shown in figure 6.5(a) is taken. The resulting frequency spectrum reveals the relative strength present at each frequency component. Each frequency component can be mapped to an energy splitting between two levels in the wavepacket [8]. In this manner, we plot the Fourier spectrum in figure 6.7 as a function of energy. In region (a) of figure 6.7, a peak is seen at an energy corresponding to the splitting of the Rydberg angular momentum states. No $\Delta n = 1$ transitions can be detected in region (a) as states with $n > 60$ are ionized by the clearing pulse and are not present in the recombined wavepacket. In region (b), a large peak is seen at the energy splitting corresponding to the $\Delta n = 1$ transitions for $n \sim 52$. The center of this peak is located at $E = 39$ cm^{-1}. In region (c), any peaks present are from $\Delta n > 1$

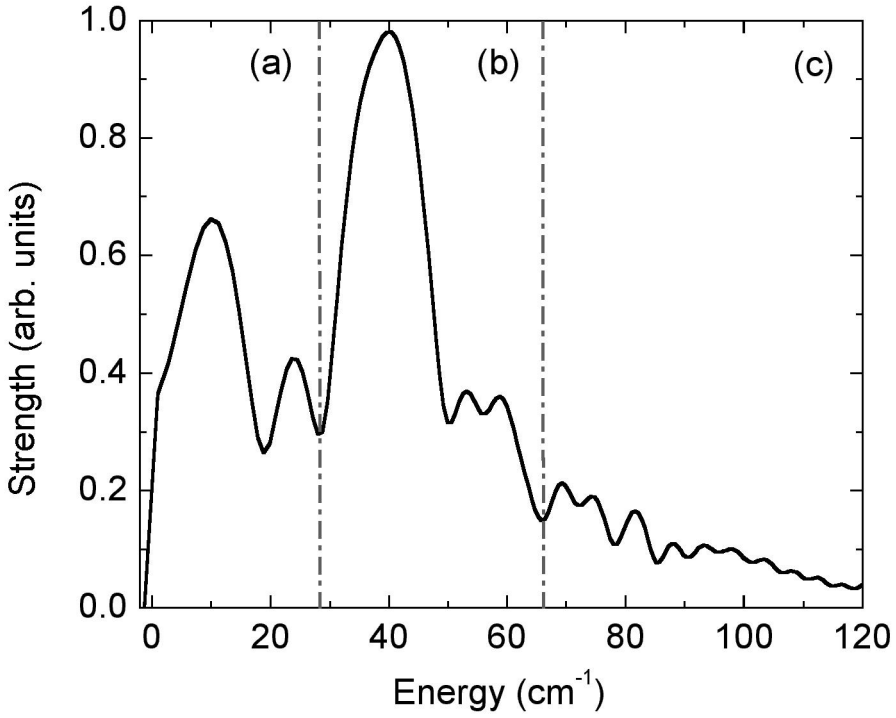

Figure 6.7: To determine the average energy of the recombined wavepacket, a Fourier transform of the data shown in figure 6.5(a) is taken. The measured frequency spectrum is plotted as a function of E as discussed in the text. In region (a), the energy splittings between angular momentum levels gives rise to a peak at low E. Regions (b) and (c) indicate regions with energy splittings between levels with $\Delta n = 1$ and $\Delta n = 2$ respectively [8]. The HCP pump and probe are both polarized along $+\hat{z}$. The value E_{wp} = -39 cm^{-1} is chosen from the large peak in region (b). Since the initial continuum wavepacket is approximately 15 cm^{-1} in the continuum, the average change to the energy of the wavepacket induced by the HCP is ΔE = -54 cm^{-1}.

energy splittings [8].

The central energy of the recombined wavepacket is therefore set to E_{wp} = -39 cm^{-1} based on the data in figure 6.7. Since the initial continuum wavepacket is approximately 15 cm^{-1} in the continuum, the average change to the energy of the wavepacket induced by the HCP is ΔE = -54 cm^{-1}. The distribution of final energies in the recombined wavepacket will be discussed in more detail in the next section.

The classical derivation of IMR assumes that the wavepacket has a well defined energy, E_{wp}. Therefore, optimal IMR conditions exist when the spread in the energy distribution of the wavepacket (ΔE) is much less than E_{wp}. Since the distribution of energies in the recombined wavepacket studied here is continuous from approximately E_{wp} = -60 cm^{-1} to the continuum, the assumptions implicit in IMR are not strictly valid. Nevertheless, we apply the lock-in IMR method to recover some information about the momentum distribution of the recombined wavepacket. By examining the momentum distributions which result from IMR in these less than ideal conditions, information about the robustness of the IMR technique is also determined.

After the value of E_{wp} is determined, the momentum distribution of the recombined wavepacket along the axis of the HCP probe is recovered through lock-in IMR. The angle of the probe pulse can be varied to recover the momentum distribution along any axis. Figure 6.8 shows the experimentally determined momentum distribution along $\hat{z}$ for a range of time delays $0 \leq \Delta t_{probe} \leq 70$ ps. The momentum distribution is recovered

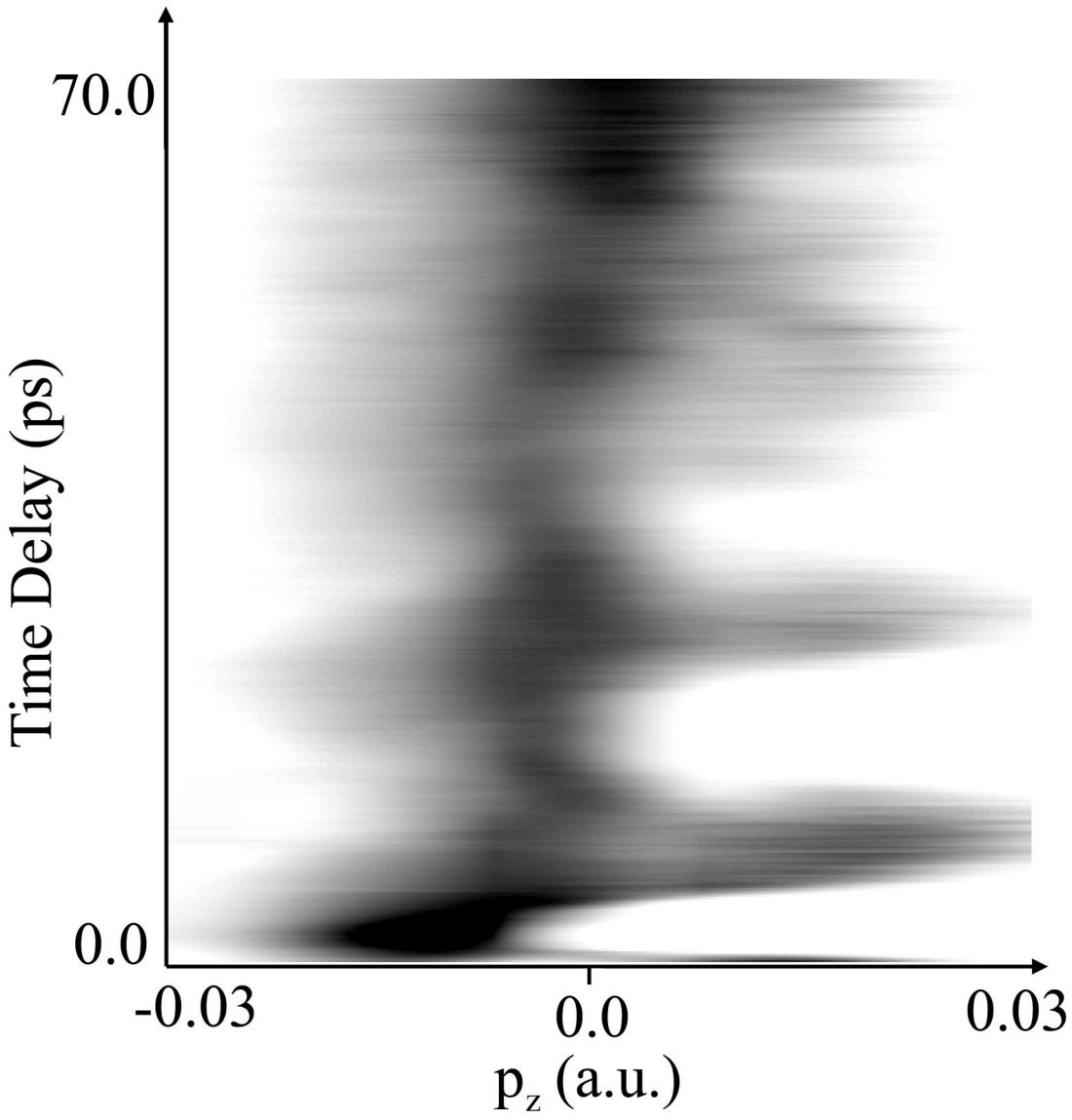

Figure 6.8: Experimentally determined momentum distribution along $\hat{z}$ for a range of time delays $0 \leq \Delta t_{probe} \leq 70$ ps. The distribution is recovered from two separate scans of HCP probe strength A_2 as discussed in the text.

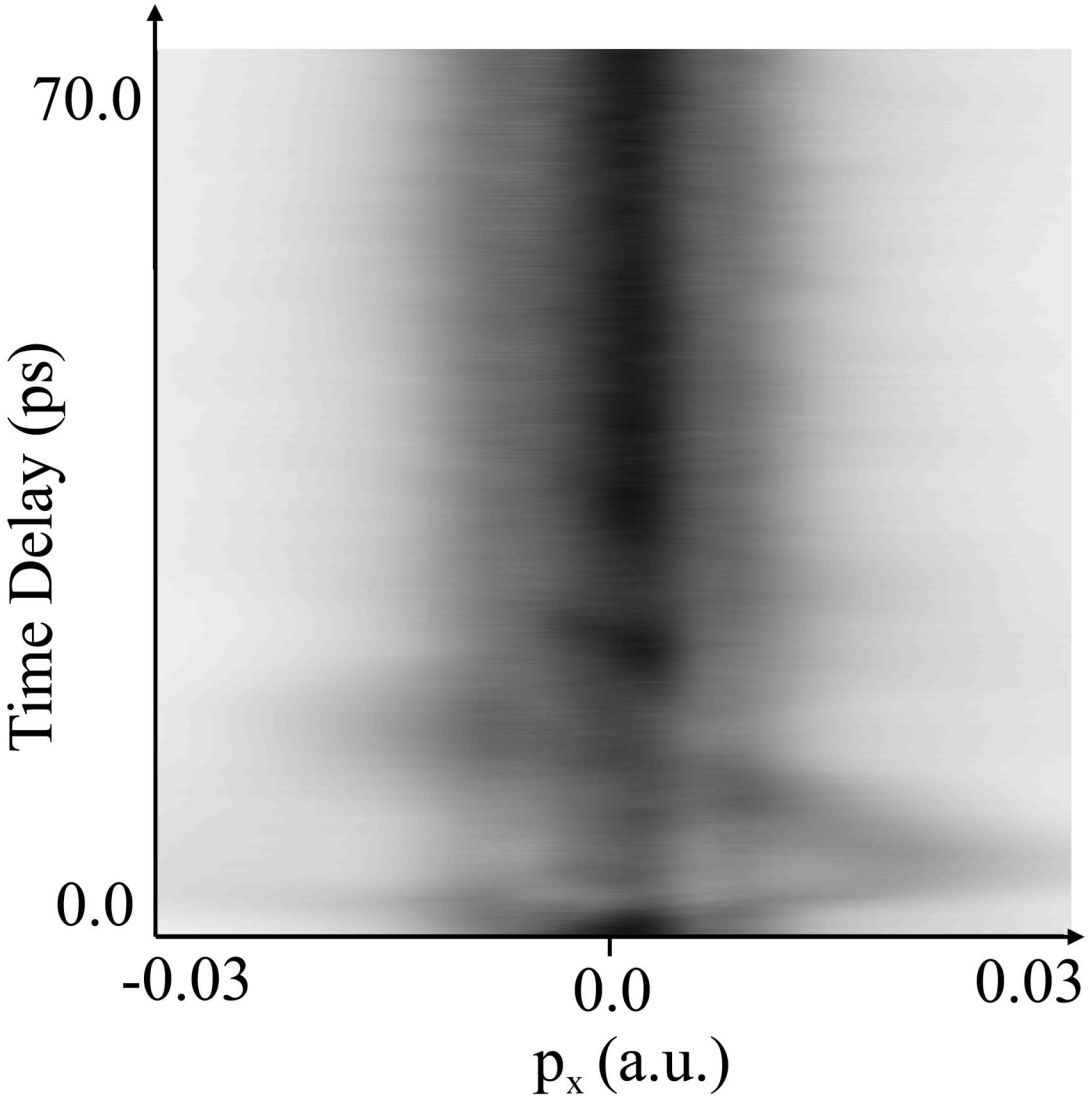

Figure 6.9: Experimentally determined momentum distribution of the recombined wavepacket measured along $\hat{x}$. The distribution is recovered in the same manner as the distribution shown in figure 6.8.

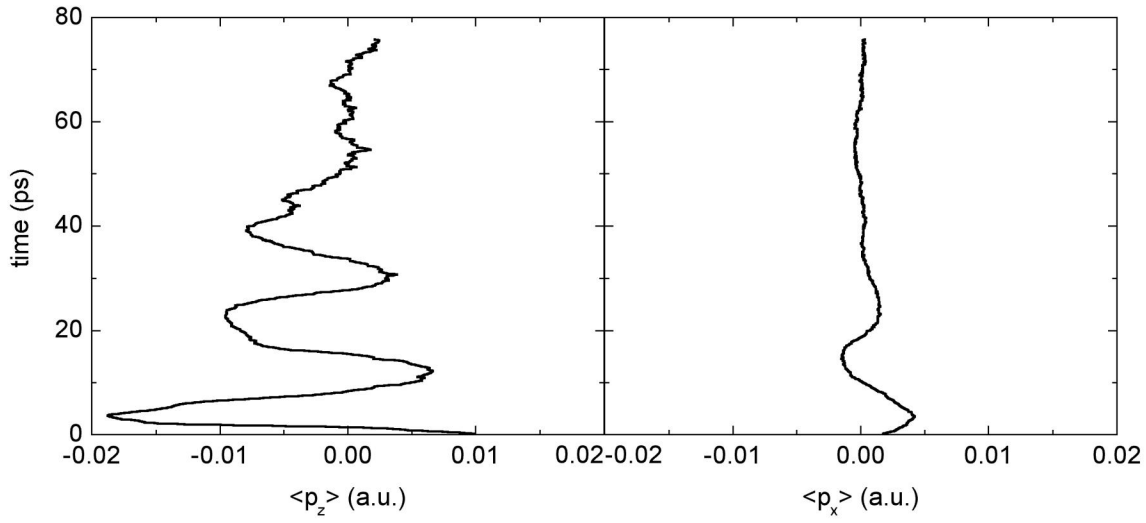

Figure 6.10: Measured expectation values of p_x and p_z from the data presented in figures 6.8 and 6.9. Even though $< p_x >$ is expected to be zero, some oscillation is noted. This is most likely due to slight misalignments between the pump and probe HCPs.

from two separate scans of HCP probe strength (one with the probe polarized along $+\hat{z}$ and one along $-\hat{z}$) as discussed in section 3.3.2. Figure 6.9 shows a similar momentum distribution but measured along $\hat{x}$. Some initial motion along $+\hat{x}$ is seen in the first 10 ps. Following this, no net motion of the recombined wavepacket along $\hat{x}$ is observed. This initial $\hat{x}$ motion is likely due to slight misalignment between the pump and probe HCPs. The average values of p_x and p_z are calculated from the data in figures 6.8 and 6.9 and the results are shown in figure 6.10.

Once the momentum distribution is recovered from the data, it can be used to obtain position space information. At any instant in time, the average value of radial

position is related to the average momentum value through the equation

$$< r > \;=\; \left\langle \frac{1}{\frac{|\vec{p}|^2}{2} - E_{wp}} \right\rangle . \tag{6.4}$$

Due to the inherent symmetry of the problem, the average values of p_x and p_y should be equal. Equation 6.4 then can be written as

$$< r > \;=\; \left\langle \frac{1}{\frac{p_z^2+2p_x^2}{2} - E_{wp}} \right\rangle . \tag{6.5}$$

The wavepacket energy (E_{wp}) is determined from the data in figure 6.7 and the values of p_z and p_x are determined from the distributions shown in figures 6.8 and 6.9 respectively. Some error may be introduced into the calculation of $< r >$ due to the oscillations present in the experimentally determined value of $p_x >$ in figure 6.10.

To obtain a value for $< r >$ at a given time Δt_{probe}, the p_z and p_x distributions are first combined to form a net $|\vec{p}|^2$ distribution. Then, this distribution is summed over all momentum values to determine $< r >$. Since no forces act along $\hat{x}$ or $\hat{y}$, the expectation values $< x >$ and $< y >$ are approximately zero. Therefore, changes in the value of $< r >$ are due primarily to changes in $< z >$. Therefore, the recovered $< r >$ distribution should be approximately proportional to $< z >$. The value of $< r >$ recovered from the momentum distributions in figures 6.8 and 6.9 is shown in figure 6.11 as a function of Δt_{probe}. Within each oscillation in the $< r >$ distribution, some asymmetry is present. The value of $< r >$ increases rapidly to a maximum value and then slowly decreases back to a minimum. For example, at $\Delta t_{probe} = 12$ ps, $< r >$ is a

minimum. From 12 ps to 17 ps, the value of $< r >$ quickly increases to a maximum. Then from 17 ps to 30 ps, $< r >$ decreases back to a minimum value. The origin of this asymmetry will be discussed in the next section.

6.4 Discussion and Numerical Analysis

Classical trajectory Monte-Carlo (CTMC) calculations have been performed to simulate the experiment presented in this chapter. Full details of the calculations can be found in appendix B. In the calculation, an ensemble of approximately 10 000 electrons is launched into a Coulomb potential from the inner turning point of a semi-classical angular distribution of hydrogenic $\ell = 2$, $m = 0$ orbits. Electrons are released at $t = 0$ and have a Gaussian energy distribution (FWHM = 15 cm^{-1}) centered about a mean energy, $E = 15$ cm^{-1}. These initial conditions mimic laser photoionization into the continuum. After a time $t = 3$ ps, each electron is exposed to a 0.80 ps FWHM Gaussian HCP which is polarized along $+\hat{z}$. After the HCP field, the intermediate energy E_1 of each electron is recorded. A variable time Δt_{probe} after the first HCP, each electron is exposed to a second 0.80 ps FWHM Gaussian HCP probe. After the probe HCP interaction, final values of $\vec{r}$, $\vec{p}$, and E_f are recorded for each electron. If an electron has $E_f < -30$ cm^{-1}, then it is counted as bound after the probe pulse. The offset in E_f from zero is due to ionization of loosely bound high Rydberg states by the clearing pulse. Calculations are performed for values of pump strength $0 \leq A_1 \leq 0.05$

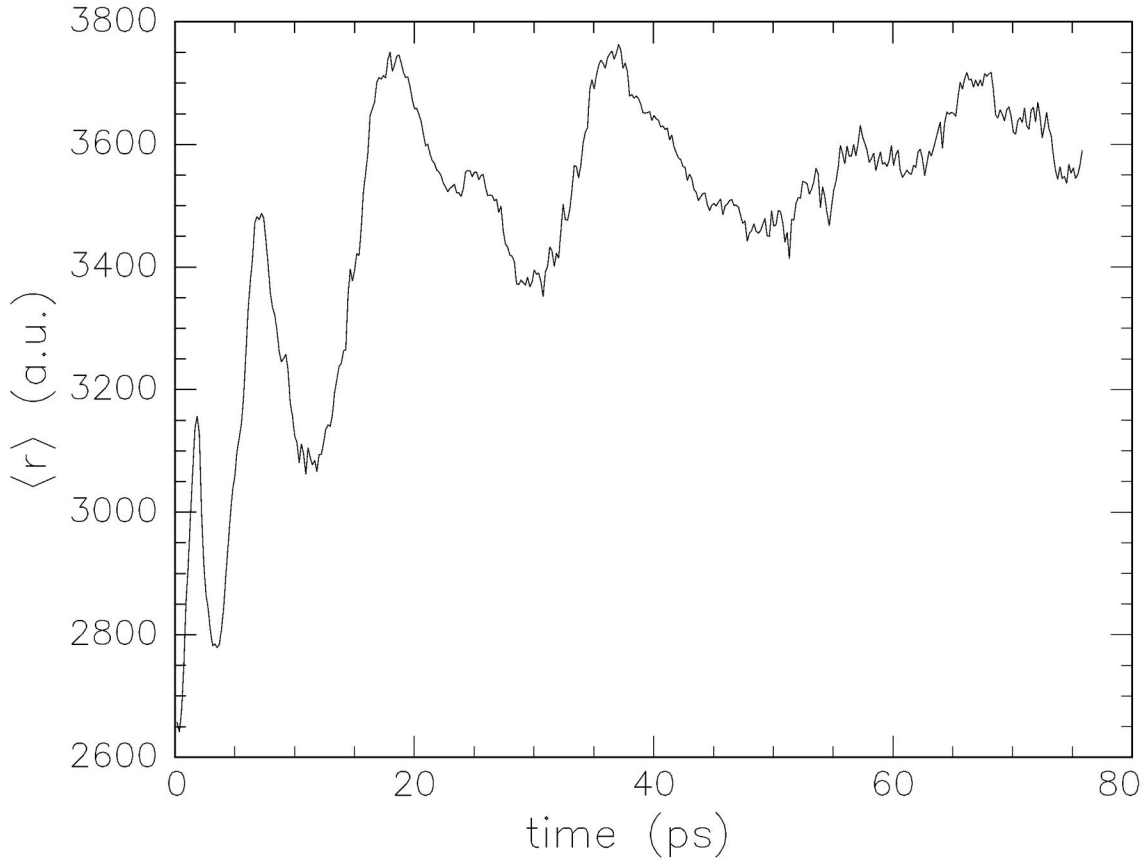

Figure 6.11: The average value of the radial position ($< r >$) as a function of Δt_{probe}. Changes in the value of $< r >$ are due primarily to changes in $< z >$. Within each oscillation in the $< r >$ distribution, some asymmetry is present. The value of $< r >$ increases rapidly to a maximum value and then slowly decreases back to a minimum.

and values of probe time delay, $0 \leq \Delta t_{probe} \leq 50$ ps. Figure 6.12 shows the results of these calculations. Dark areas represent combinations of A_1 and Δt_{probe} which result in a higher probability of having electrons still bound after the HCP probe. For a range of HCP pump field strengths centered around $A_1 = 0.024$, clear oscillations in the number of remaining electrons exists as a function of Δt_{probe}.

The energy distribution of the continuum wavepacket following the HCP pump is shown in figure 6.13 as a function of A_1 for the same initial conditions that are present in figure 6.12. When $A_1 = 0.024$, the oscillations in recombination probability in figure 6.12 are the strongest. The energy distribution of the wavepacket corresponding to this case is sharply peaked at $E_1 = -39$ cm^{-1} (figure 6.13(b)). Approximately 12% of the initial population has $E_1 < -30$ cm^{-1}, which is defined as the continuum limit due to the clearing pulse used in the experiment. Of this recombined population, over 40% has energy between -40 cm^{-1} and -38 cm^{-1}. In other words, 40% of the recombined wavepacket has principal quantum number $n = 52, 53$, or 54 for $A_1 = 0.024$. The narrow peak in the energy distribution broadens for A_1 either greater or less than $A_1 = 0.024$.

Additional CTMC calculations are done to simulate the effect of varying HCP probe strength on recombination probability. Instead of fixing a value for A_2, the magnitude of the HCP pump pulse is set to the value which results in the long lived oscillations in figure 6.12 ($A_1 = 0.024$) and then the probe strength is varied. Sample results are shown in figures 6.14 and 6.15. Dark areas indicate combinations of A_2 and Δt_{probe}

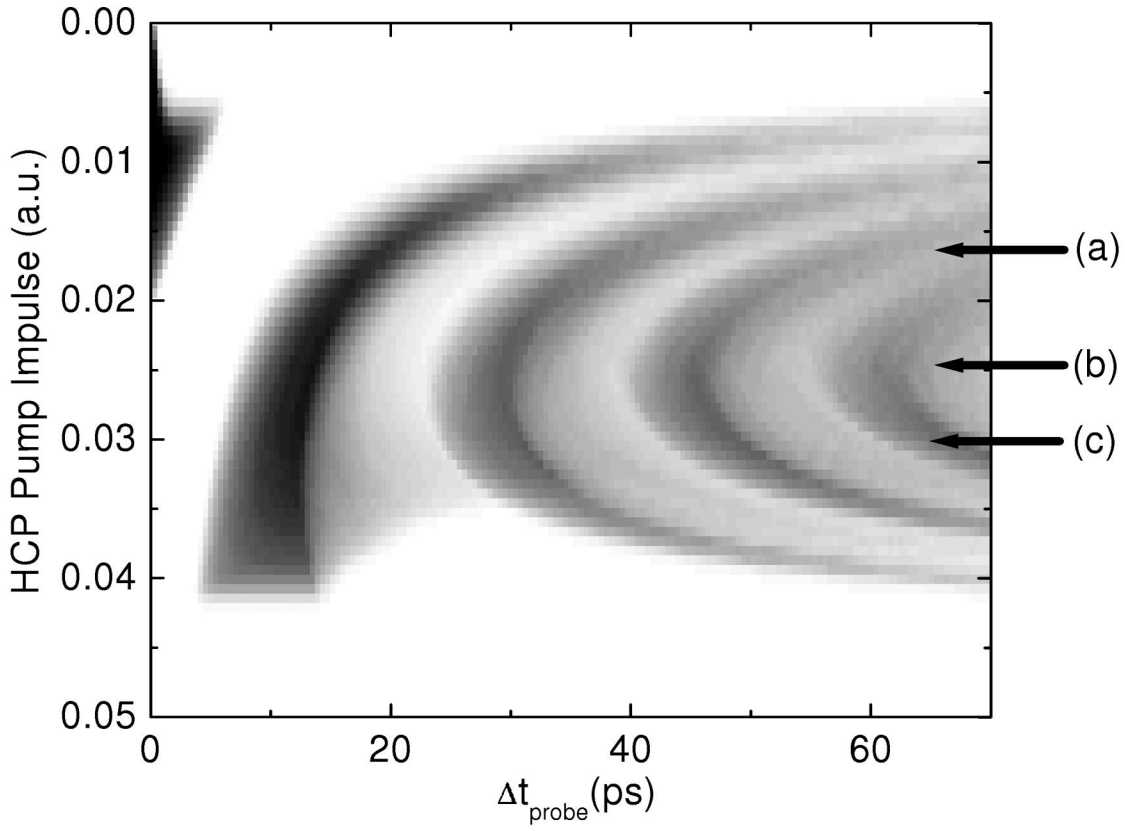

Figure 6.12: Calculated recombination rates as a function of HCP pump impulse (A_1) and the HCP probe delay (Δt_{probe}). Dark areas represent combinations of A_1 and Δt_{probe} which lead to a higher probability of having electrons still bound after the HCP probe interaction. In this figure, $A_2 = 0.016$. For a range of HCP pump field strengths centered around $A_1 = 0.024$, clear oscillations in the number of remaining electrons are observed as a function of Δt_{probe}. This feature is also seen in the experimental data in figure 6.4. Fast oscillations in the fraction of bound electrons that are seen in the experimental data are not reproduced in the calculations. The intermediate energy distribution (E_1) of the wavepacket following the HCP pump is shown in figure 6.13 for three selected values of A_1. These values are shown here by the three arrows.

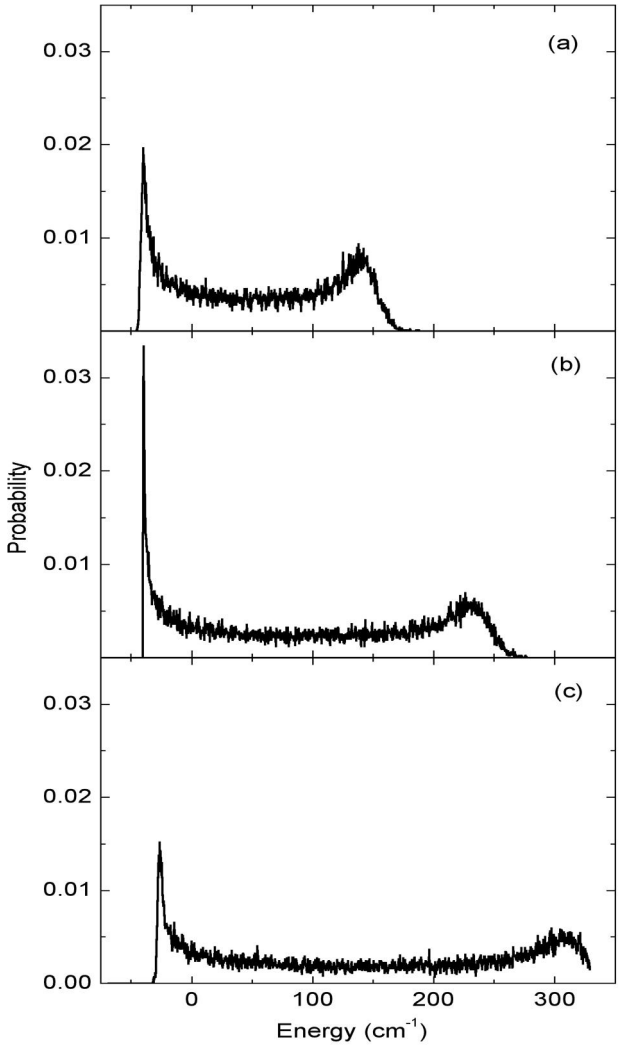

Figure 6.13: Calculated energy distribution of the continuum wavepacket following the HCP pump pulse for three values of A_1: (a) $A_1 = 0.016$, (b) $A_1 = 0.024$, and (c) $A_1 = 0.030$. The initial energy distribution of the continuum wavepacket is a Gaussian envelope centered at $+15$ cm^{-1}, with a 10 cm^{-1} full width at half maximum. The value of A_1 which leads to the strongest oscillations in figure 6.12 has a sharp peak in the energy distribution at $E_1 = -39$ cm^{-1}.

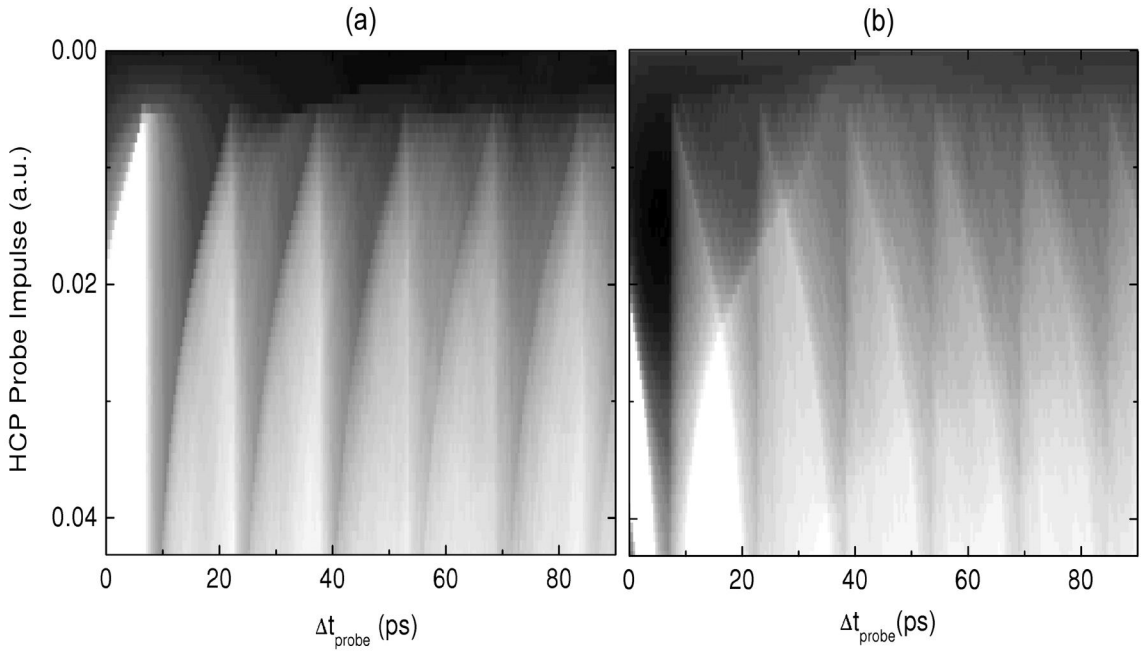

Figure 6.14: Calculation of bound state probability as a function of both HCP probe strength (A_2) and Δt_{probe}. Dark areas on the plot show combinations of A_2 and Δt_{probe} which yield a high probability of a bound electron after both pump and probe interaction. The magnitude of the HCP pump pulse is fixed to $A_1 = 0.024$. The calculations show good agreement with the data shown in figures 6.5 and 6.6. The pump pulse is polarized along $+\hat{z}$. In (a), the calculated amount of recombination is shown for a probe pulse along $+\hat{z}$. In (b), the probe pulse is oriented along $-\hat{z}$.

which result in a high probability of having electrons bound to the core following both the pump and probe pulses. When the probe pulse is aligned along the same axis as the pump (as in figure 6.14), pronounced oscillations are seen in the bound state probability. However, when the pump and probe pulses are orthogonal (figure 6.15), the bound state probability is relatively independent of Δt_{probe}.

The calculations presented in figures 6.14 and 6.15 simulate the measured HCP

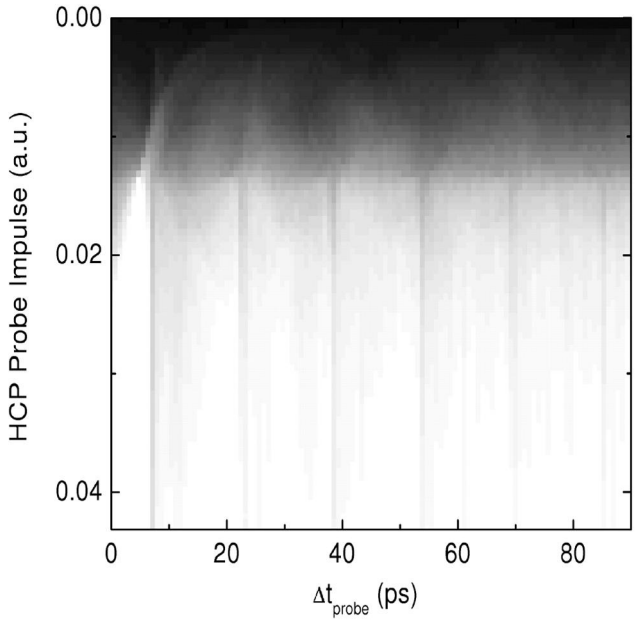

Figure 6.15: Similar to figure 6.14, but for a HCP pump polarized along $+\hat{z}$ and a HCP probe polarized along $+\hat{x}$.

probe scans shown in figures 6.5 and 6.6. The IMR technique is applied to the calculation results to obtain calculated momentum distributions which can be compared to the measured ones. The momentum calculation results are shown in figure 6.16. Each IMR momentum distribution is assembled from two separate calculations of HCP probe strength. For positive (negative) momentum values, a parallel (opposite) pump - probe orientation is used. Some overlap is present when performing IMR and this region is used to match the two halves of the distribution. The details of the matching are described in section 3.3.2.

The momentum distributions obtained from the calculated IMR can then be com-

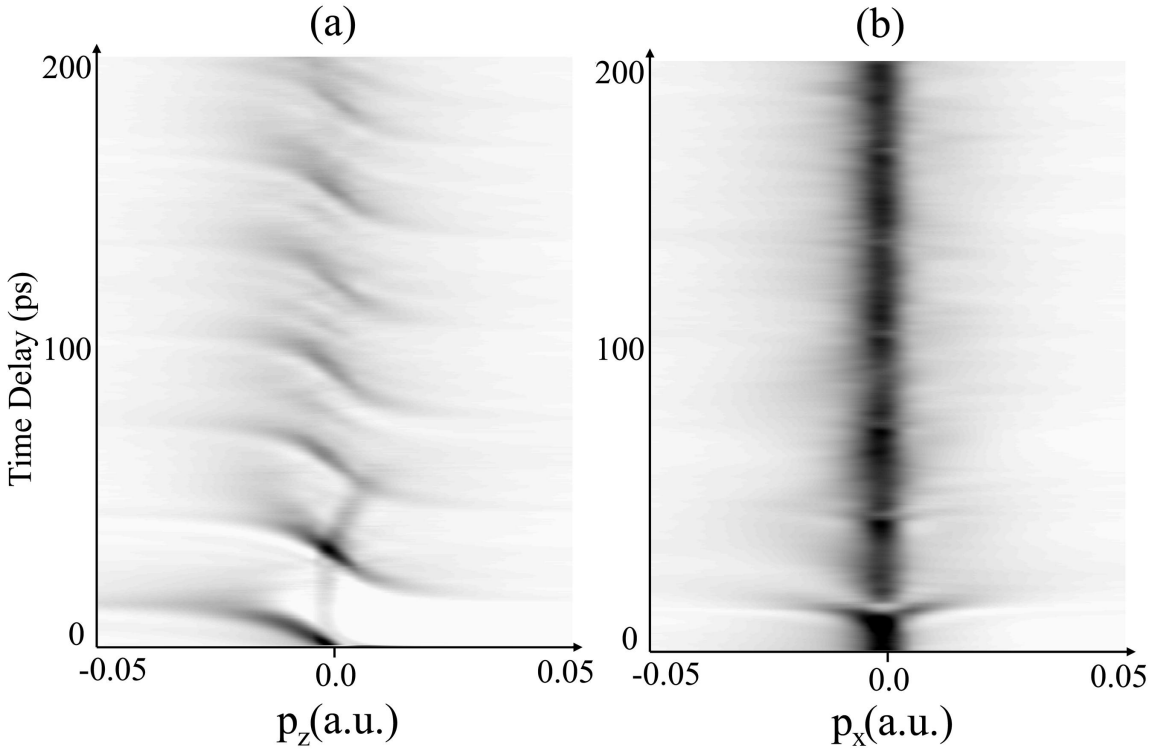

Figure 6.16: Plot of the calculated momentum distribution obtained from IMR of the calculation shown in figures 6.14 and 6.15. In this figure, the momentum distribution is obtained through the same method used to obtain momentum distributions from the experimental data. A couple features are observed in the calculated spectra that do not correspond to the measured momentum distributions, although the overall resemblance is good.

pared to the momentum distributions obtained directly from the CTMC calculations. Instead of simulating IMR, the $\hat{x}$ and $\hat{z}$ momentum of each event in the simulation is recorded for 200 ps. A histogram is then made of the p_z and p_x values for each time step in the simulation. All the histograms are combined in a single greyscale plot and shown in figure 6.17. Shown are the p_z and p_x momentum distributions of a simulated recombined wavepacket with the same initial conditions as in figures 6.14 and 6.15. Qualitative agreement exists between the IMR recovered momentum distributions in figure 6.16 and the direct calculation results in figure 6.17. Even though ideal conditions are not present for IMR, it appears that the IMR method performs acceptably for recovering the momentum distribution of a recombined wavepacket. Additional simulations of the creation and evolution of recombined wavepackets is presented in chapter 7.

The first HCP (the pump pulse) gives an the continuum wavepacket an initial kick in the $-\hat{z}$ direction. Therefore, for the first few picoseconds after interaction with the HCP pump, the momentum of the wavepacket in the $\hat{z}$ direction is almost entirely negative. This is seen in both the measured and calculated momentum distributions (figures 6.8 and 6.16 respectively). Portions of the initial continuum wavepacket which initially were moving along $-\hat{z}$ continue to do so. However, some portions of the initial wavepacket which were moving in the $+\hat{z}$ direction prior to HCP interaction have been recombined and move back along $-\hat{z}$. Once the recombined wavepacket passes the atomic core,

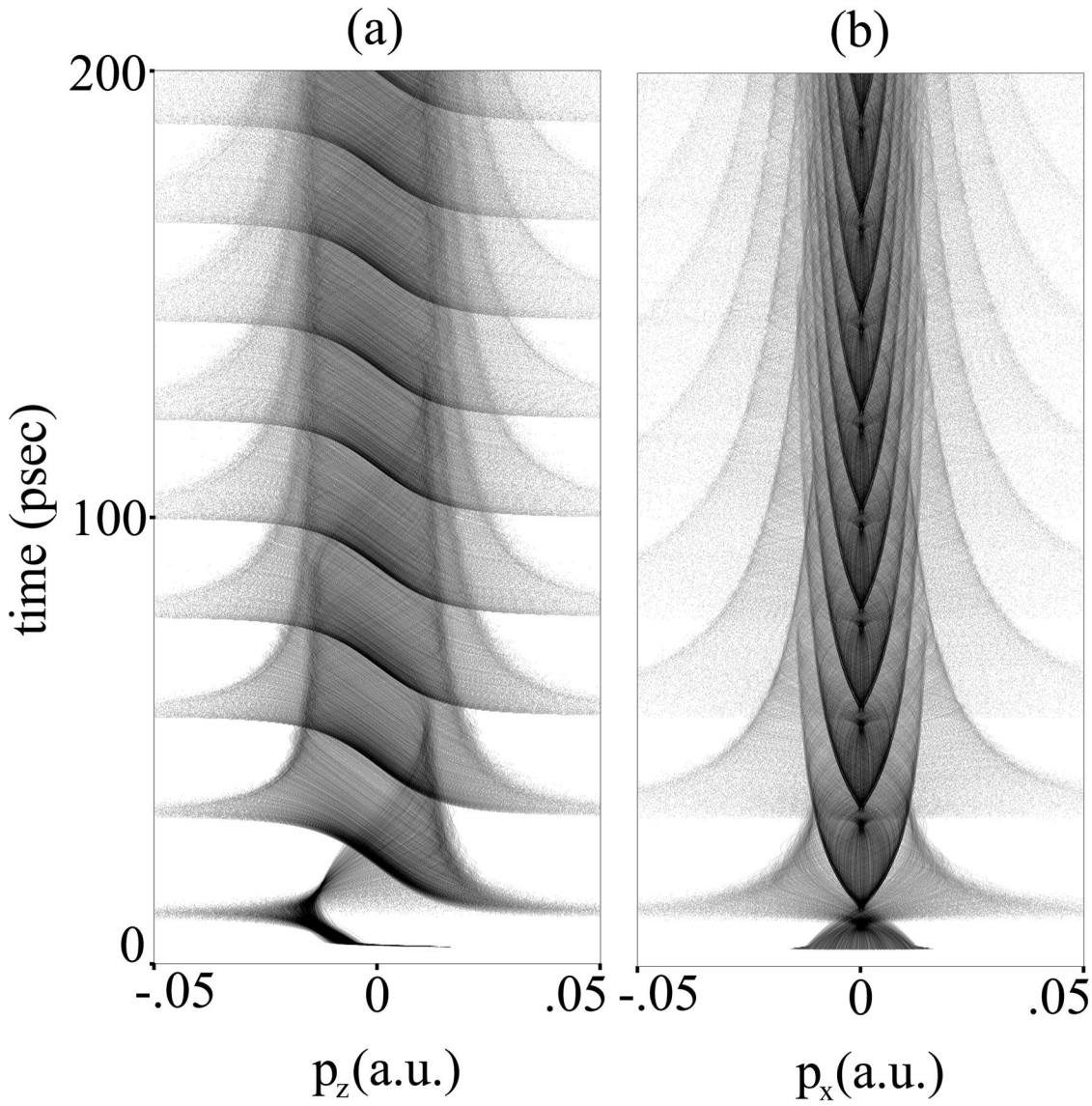

Figure 6.17: Calculated (a) p_z and (b) p_x momentum distributions of a recombined wavepacket.

it then quickly reverses direction and moves back along $+\hat{z}$ again. For the measured momentum distribution in figure 6.8, this transition happens at 7 ps. As the recombined wavepacket evolves in the Coulomb potential, the average value of p_z continues to oscillate between positive and negative values. This oscillation is shown in figures 6.10(a) and 6.18(a) for the measured data and calculations respectively. Dephasing of the measured recombined wavepacket washes out the details of the distribution at large values of Δt_{probe}. A simulation of the evolution of the recombined wavepacket is shown in figure 7.14.

Zeros in the calculated IMR p_z momentum distribution occur at approximately 23 ps intervals. Of particular interest is the characterization of the crossover from positive to negative momentum values when compared to the crossover from negative to positive values. For example, at $\Delta t_{probe} = 14$ ps, the average value of p_z ($< p_z >$) is approximately +0.006. (Calculated values of $< p_z >$ are shown in figure 6.18.) From $\Delta t_{probe} = 14$ ps to $\Delta t_{probe} = 24$ ps, $< p_z >$ decreases slowly (but is still positive). At 24 ps, $< p_z >= 0$. The change from small positive values of $< p_z >$ to small negative values of $< p_z >$ occurs relatively slowly. Then, from $\Delta t_{probe} = 24$ ps to $\Delta t_{probe} = 29$ ps $< p_z >$ decreases to ever more negative values. At approximately $\Delta t_{probe} = 29$ ps, $< p_z >$ switches sign very rapidly, changing from -0.01 at 29 ps to +0.004 at 34 ps. Such evolution is consistent with a large portion of the recombined wavepacket being localized along the $+\hat{z}$ axis. The switch from positive to negative values of $< p_z >$

occurs slowly as electrons reach the outer turning point of their orbit oriented with major axis along $\hat{z}$. Likewise, the switch from negative to positive values of $< p_z >$ must occur quickly as each electron rapidly passes the inner turning point of a Kepler orbit. The asymmetry in the p_z momentum distribution therefore indicates a high degree of localization on one side of the atomic core. This localization phenomenon will be investigated further in chapter 7. This asymmetry is similarly observed in the experimental data (figure 6.10), although the effect washes out after a few oscillations due to the spread of energies present in the recombined wavepacket. Note the lack of similar momentum oscillations in the calculated $< p_x >$ distribution in figure 6.18(b). A small feature is seen at small values of Δt_{probe} in the measured $< p_x >$ distribution in figure 6.10(b). This is likely due to the pump and probe pulses not being completely perpendicular.

Overall, the qualitative features of the measured momentum distribution in figure 6.8 are reproduced in figure 6.16(a). Small details evident in the calculated distribution are not completely reproduced in the data. Similarly, there are some observed features in the experimental data which are not reproduced in the calculations. Fast oscillations in the fraction of bound ions are seen in figure 6.4 for large values of HCP pump strength. No similar feature is observed in the calculations. The time spacing of these oscillations corresponds roughly to the Kepler period for $n = 40$. There are some potential explanations for these oscillations.

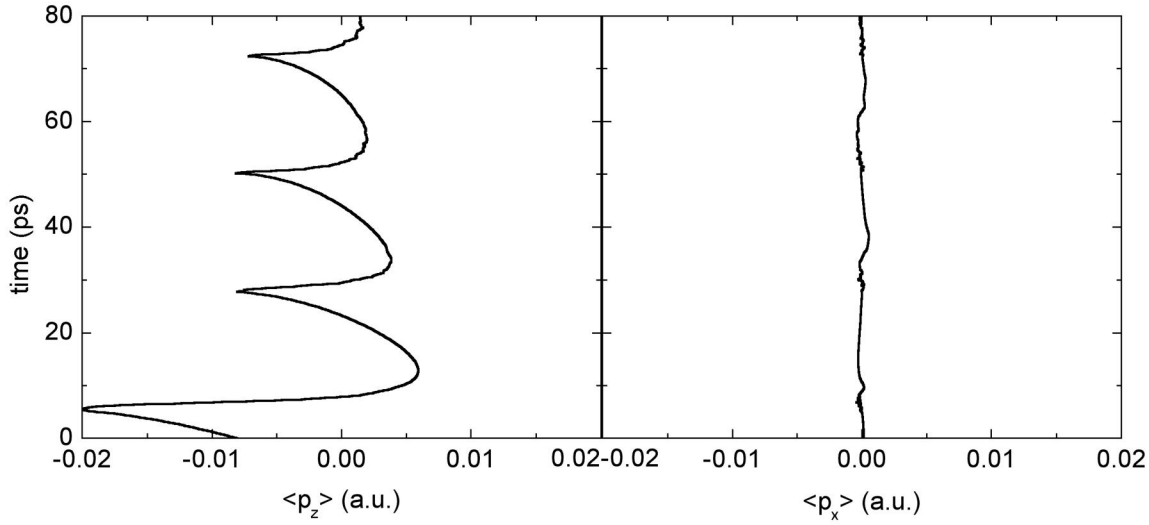

Figure 6.18: Calculated value of $< p_z >$ and $< p_x >$ for a recombined wavepacket for $0 \leq \Delta t_{probe} \leq 80$ ps.

One possible explanation arises from the temporal profile of the HCPs used in this experiment. The analysis provided so far in this chapter assumes that the HCP is approximated by a Gaussian envelope. However, the experiment presented in chapter 5 showed that the HCP profile is probably more closely given by figure 3.2, with a strong impulsive part and a long lasting tail of opposite polarity. Perhaps when a very strong ($A_1 \geq 0.045$) HCP pump performs recombination, the large impulsive part of the HCP sends the portion of the continuum wavepacket with initial motion along $+\hat{z}$ flying back past the atomic core. As the wavepacket passes the core, the negative tail of the HCP slows down the wavepacket and allows it to be captured into a lower n state.

For completeness, HCP probe scans are taken in the region of the fast oscillations

with a pump impulse $A_1 = 0.047$. The lock-in IMR technique is applied to the resulting data and a momentum distribution is recovered. It is shown in figure 6.19.

6.5 Conclusions

Recombined electronic wavepackets have been made in calcium with sub-picosecond unipolar pulses of terahertz radiation (HCPs). The fraction of the wavepacket ionized when exposed to a second "probe" HCP is measured. Subsequently, the momentum distribution of the recombined electronic wavepacket is recovered through a variation of the impulse momentum retrieval method known as lock-in IMR. Experimental results are compared to classical calculations. Acceptable qualitative agreement is achieved. We were able to show that impulse momentum retrieval can be used to recover momentum distributions even when the ideal conditions for IMR are not strictly satisfied. Calculations show that when long lived oscillations occur in the HCP probe ionization signal, then a large fraction of the recombined wavepacket is composed of states within a narrow band of energies. This is likely the reason for the success of the IMR method in recovering the momentum distribution of the recombined wavepacket. We were also able to observe features in the recombination probability which are not predicted by the simulations. An asymmetry is observed in $< p_z >$. This is consistent with a time dependent localization of the electron distribution along $\hat{z}$. This localization will be investigated in detail in chapter 7.

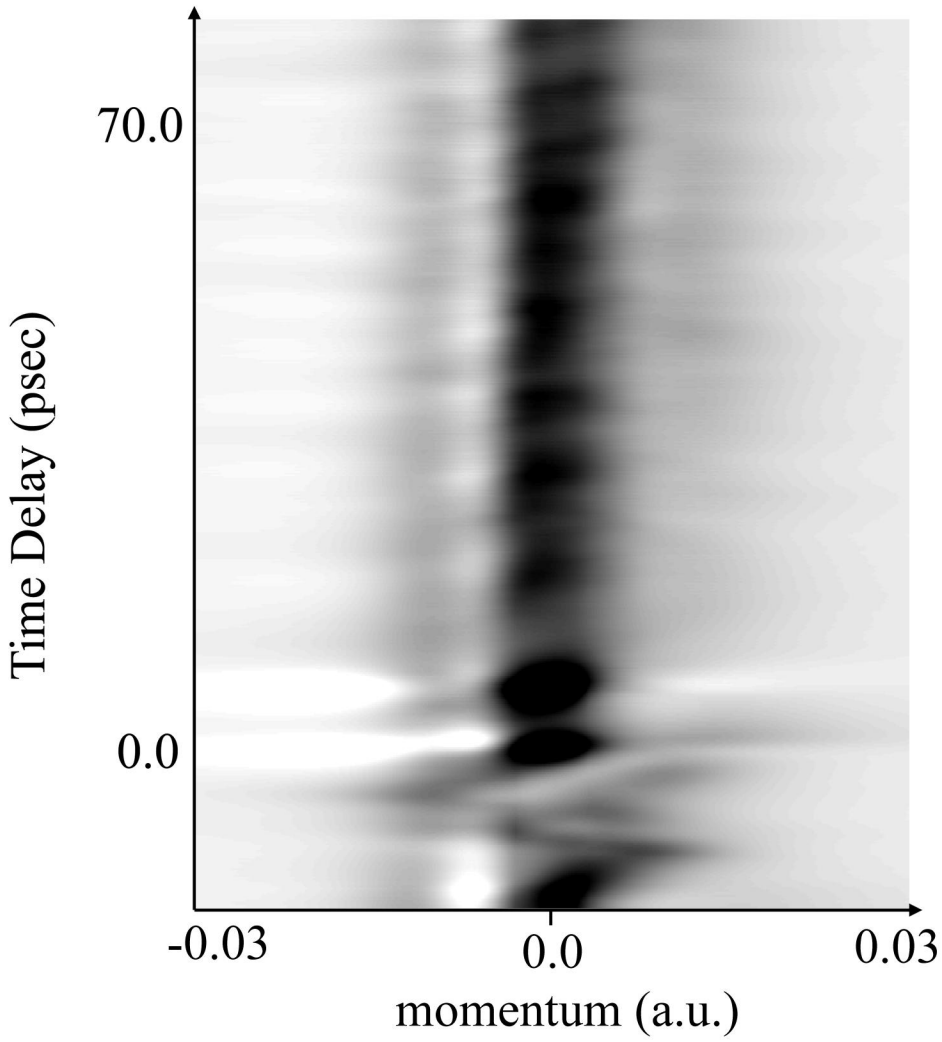

Figure 6.19: HCP probe scans are taken in the region of the fast oscillations with the pump impulse $A_1 = 0.047$. The IMR technique is applied to the resulting data and a momentum distribution is recovered and shown here.

Bibliography

[1] Y. Hahn, Rep. Prog. Phys. **60**, 691 (1997) and references therein; *Recombination of Atomic Ions*, W. Graham *et. al.*, eds., *NATO ASI Series B: Physics*, **296**, Plenum, New York, (1992) and references within.

[2] T.J. Bensky, M.B. Campbell, and R.R. Jones, *Phys. Rev. Lett.* **81**, 3112 (1998).

[3] F. Robicheaux, *Phys. Rev. A* **60**, 431 (1999).

[4] See also the experiment presented in chapter 4

[5] D. You *et al.*, *Opt. Lett.* **18**, 290 (1993).

[6] The 389 nm laser pulse which launches the wavepacket has a FWHM of 1 ps, so the parameter τ is more accurately represented as $\tau = 3 \pm 1$ ps.

[7] R.R. Jones, *Phys. Rev. Lett* **76**, 3927 (1996).

[8] R.R. Jones and M.B. Campbell, *Phys. Rev. A* **61**, 013403 (1999).

[9] See chapter 3 for a full description of the mechanics of how a HCP field imparts a momentum kick to an electron.

[10] R.R. Jones, D. You, and P.H. Bucksbaum, *Phys. Rev. Lett.* **70**, 1236 (1993); R.R. Jones, *ibid* **76**, 3927 (1996); C.O. Reinhold *et al.*, *J. Phys. B* **26**, L659 (1993); C.O. Reinhold *et al.* Phys. Rev. A **54**, R33 (1996); A. Bugacov *et al.*, *ibid* **51**, 1490 (1995).

[11] M.B. Campbell, T.J. Bensky, and R.R. Jones, *Opt. Express* **1**, 197 (1997).

[12] R.R. Jones, *Phys. Rev. A* **57**, 446 (1998); M.B. Campbell, T.J. Bensky, and R.R. Jones, *Phys. Rev. A* **58**, 514 (1998).

[13] T.F. Gallagher, *Rydberg Atoms*, 1st ed., Cambridge University Press, Cambridge, (1994) and references therein.

[14] E. Luc-Koenig and A. Bachelier, *J. Phys. B* **13**, 1743 (1980).

[15] G.M. Lankhuijzen and L.D. Noordam, *Phys. Rev. Lett.* **76**, 1784 (1996).

[16] M.G. Littman, M.M. Kash, and D. Kleppner, *Phys. Rev. Lett.* **41**, 103 (1978).

Chapter 7

Classical Calculations of Electron Localization

7.1 Introduction

Underlying the results from chapter 6 is an intriguing possibility. The main goal of chapter 6 was to investigate the time evolution of a recombined wavepacket. However, the motion of the recombined wavepacket was found to be consistent with the formation of a three dimensionally localized electronic wavepacket. The creation of a 3-D localized wavepacket moving along a classical trajectory has been a goal of atomic physics for a long time [1]. While wavepackets have been created which are localized in either the angular [2] or the radial [3] coordinate, the search for a truly localized 3-D wavepacket

has been elusive. This has been the case despite theoretical work which has proposed possible methods to produce such a packet [4].

While the creation of a 3-D localized wavepacket is an important step in the investigation of quantum - classical correspondence and the classical limit state of highly excited atoms, perhaps a more exciting application is the area of quantum control [5]. Wavepackets can be though of in two separate, yet complimentary ways: (i) as a wave, or (ii) an ensemble of particles. Rydberg atoms lend nicely to the ensemble picture, where a Rydberg wavepacket can be thought of as an ensemble of particles, each in classical motion [6]. The problem of quantum control then is analogous to the control of an ensemble of classical particles. From this point of view it is clear why creating a 3-D localized wavepacket is important to quantum control. If all the particles in the ensemble are localized in a small region of phase space, then a control pulse will affect them similarly. If the ensemble is diffuse however, then each particle in the ensemble will react differently to the same control pulse. Therefore, the creation of a 3-D localized wavepacket is an essential first step into the realm of quantum control experiments. Once this is accomplished, a wide variety of controlling pulses may be used in an attempt to control the subsequent evolution of the system [7, 8].

Recently a 3-D localized wavepacket was created by exciting an extremal Stark state in an externally applied static field [8, 9], however this state only remains localized in the presence of the field. Further manipulation of this localized wavefunction is com-

plicated by the external field. Recently, a technique for the creation of a field-free 3-D localized wavepacket has been postulated through the process of electron-ion recombination [10, 11]. This method was attempted in the experiment presented in chapter 6 and the results are consistent with the creation of a 3-D localized wavepacket. In this chapter, we perform classical calculations and Classical Trajectory Monte Carlo (CTMC) simulations of the electron - ion recombination process performed in chapter 6. The goals of this chapter are (i) to investigate the effect that each experimental parameter (initial energy, kick strength, and kick timing) has on the degree of localization of the recombined wavepacket, and (ii) to determine the parameters which lead to the highest degree of localization.

The localization of an electron may proceed in the manner first described in chapter 6. First a neutral atom is photoionized, creating an outgoing continuum wavepacket. Before the packet has moved from the influence of the atomic core it is subjected to an impulsive electric field. Experimentally, this impulse is delivered by a HCP. Some portion of the continuum wavepacket becomes bound to the atomic core again due to HCP interaction. The bound fraction of the wavepacket may localize at a specific point away from the atomic core under certain conditions. Once a 3-D localized distribution is created, it is predicted to recur repeatedly.

7.2 Analytical Calculations

7.2.1 Introduction

In an attempt to understand the degree of wavepacket localization, we solve the equations of motion of a continuum electron after it experiences a HCP kick. The motivation for this is simple. We desire to show, through analytic means, that electron localization is possible through HCP induced recombination for a wide variety of initial conditions. Furthermore, we attempt to quantify the bounds of initial parameters which lead to the maximum possible localization. We begin with Newton's laws and Kepler's equations and calculate the electron's motion as function of its initial energy, position, velocity, and the magnitude of the linear kick which performs the recombination. Useful quantities are calculated along the way which help describe the orbital dynamics. These include the energy after HCP interaction, angular momentum, and eccentricity of the electron's orbit.

In this section, the HCP impulse is assumed to be instantaneous, affecting only one component of the momentum at one specified time. In contrast, a classical numerical simulation of the dynamics of a localized wavepacket will be presented in section 7.3 which studies the effect of non-instantaneous impulsive fields along various axes. In both sections, the effect of the timing and strength of a linear impulse on the localized wavepacket dynamics is investigated.

7.2.2 Initial Conditions

A continuum electron is excited at $t = 0$ and moves radially away from its parent ion. The electron is initially in $m = 0$ and $\ell = 0$ and moves under the influence of the Coulomb potential $V(r) = -\frac{1}{|\vec{r}|}$. (See figure 7.1 for a diagram of the initial system.) The electron is released from the origin of the coordinate system. Technically, the equations of motion are singular at the origin, so the electron should be though of as having been released at a distance $r = \epsilon$ at a time $t = \delta t$. The initial motion of the electron is purely radial. Its position and velocity are given by $\vec{r}(t)$ and $\dot{\vec{r}}(t)$ respectively. The initial energy E_0 of the electron is constant. From conservation of energy, we retrieve the familiar equation

$$E_0 \;=\; \frac{1}{2}\,|\dot{\vec{r}}(t)|^2 \;-\; \frac{1}{|\vec{r}(t)|}. \tag{7.1}$$

Without loss of generality, we assume that the motion of the electron is entirely confined to the $\hat{xz}$ plane. An angle θ_0 is defined which is the angle the initial radial trajectory makes with the $\hat{z}$ axis. The position and velocity of the electron in terms of x and z is then given by

$$x_0(t) \;=\; |\vec{r}_0(t)|\; sin\theta_0 \tag{7.2}$$

$$z_0(t) \;=\; |\vec{r}_0(t)|\; cos\theta_0 \tag{7.3}$$

$$\dot{x}_0(t) \;=\; |\dot{\vec{r}}_0(t)|\; sin\theta_0 \tag{7.4}$$

$$\dot{z}_0(t) \;=\; |\dot{\vec{r}}_0(t)|\; cos\theta_0. \tag{7.5}$$

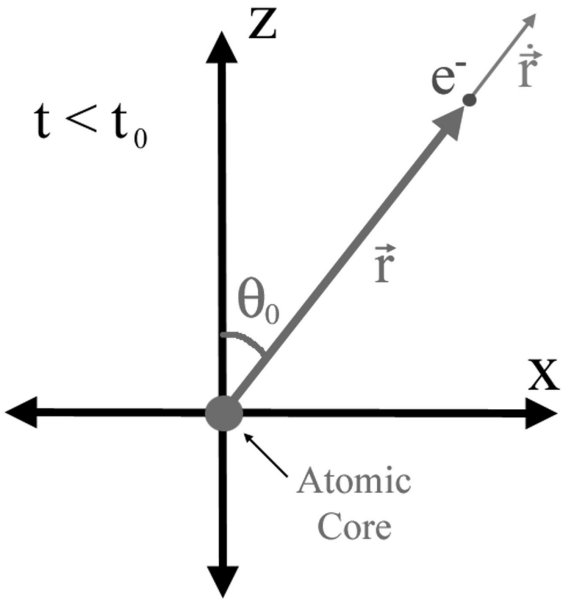

Figure 7.1: Schematic diagram showing the initial starting point for the analytic calculations of electron localization. The electron is shown in grey.

The next step is to determine the values of $\vec{r}_0(t)$ and $\dot{\vec{r}}_0(t)$ for a given value of E_0.

Equation 7.1 can be solved for $\dot{r}(t)$ and yields

$$\dot{r}(t) \;=\; \sqrt{2E_0 + \frac{2}{r(t)}}\;, \tag{7.6}$$

where $r(t) \equiv |\vec{r}(t)|$ and $\dot{r}(t) \equiv |\dot{\vec{r}}(t)|$. Equation 7.6 is separable and yields the differential relation

$$\sqrt{2}\;dt \;=\; \sqrt{\frac{r}{1+E_0 r}}\;dr\;. \tag{7.7}$$

Direct integration of equation 7.7 (with the aid of a symbolic integration program such as Mathematica) yields the messy relation:

$$t \;=\; \left(\frac{1}{2E_0}\right)\cdot\left[\;\sqrt{(r)(1+E_0 r)} \;-\; \left(\frac{1}{\sqrt{E_0}}\right)\;sinh^{-1}\sqrt{E_0 r}\;\right]. \tag{7.8}$$

Unfortunately, equation 7.8 is transcendental in r and must be inverted numerically to obtain an expression for $r(t)$. This is done in Mathematic through Newton's method, and an expression for $r(t)$ is obtained which can then be substituted into equation 7.6 to obtain values for $\dot{r}(t)$. Then, equations 7.2 through 7.5 yield expressions for the x and z position and momentum of the electron as a function of time.

To get a physical sense of this solution, if $E = -.0002$ a.u. $\approx$ -44 cm^{-1}, (corresponding to the binding energy of an $n = 50$ eigenstate) then at $t = 3$ ps,

$$r_0(3ps) \;=\; 3376.0 \quad \text{and} \quad \dot{r}_0(3ps) \;=\; 0.0139\ . \tag{7.9}$$

Similarly, if $E = 0$, and $t = 3$ ps,

$$r_0(3ps) \;=\; 4105.9 \quad \text{and} \quad \dot{r}_0(3ps) \;=\; 0.0221\ , \tag{7.10}$$

and for the initial conditions in the experiment in chapter 6: $E_0 = 15$ cm^{-1},

$$r_0(3ps) \;=\; 4331.0 \quad \text{and} \quad \dot{r}_0(3ps) \;=\; 0.0245\ . \tag{7.11}$$

7.2.3 HCP Interaction

The outgoing electron is allowed to evolve for a time t_0. At $t = t_0$, a HCP impulse of magnitude A is applied in the $-\hat{z}$ direction. Figure 7.2 shows a schematic drawing of the system for a given initial launch angle. Just after t_0, the position and momentum of the electron are now given by:

$$x(t_0) \;=\; |\vec{r}_0(t_0)|\ sin\theta_0 \tag{7.12}$$

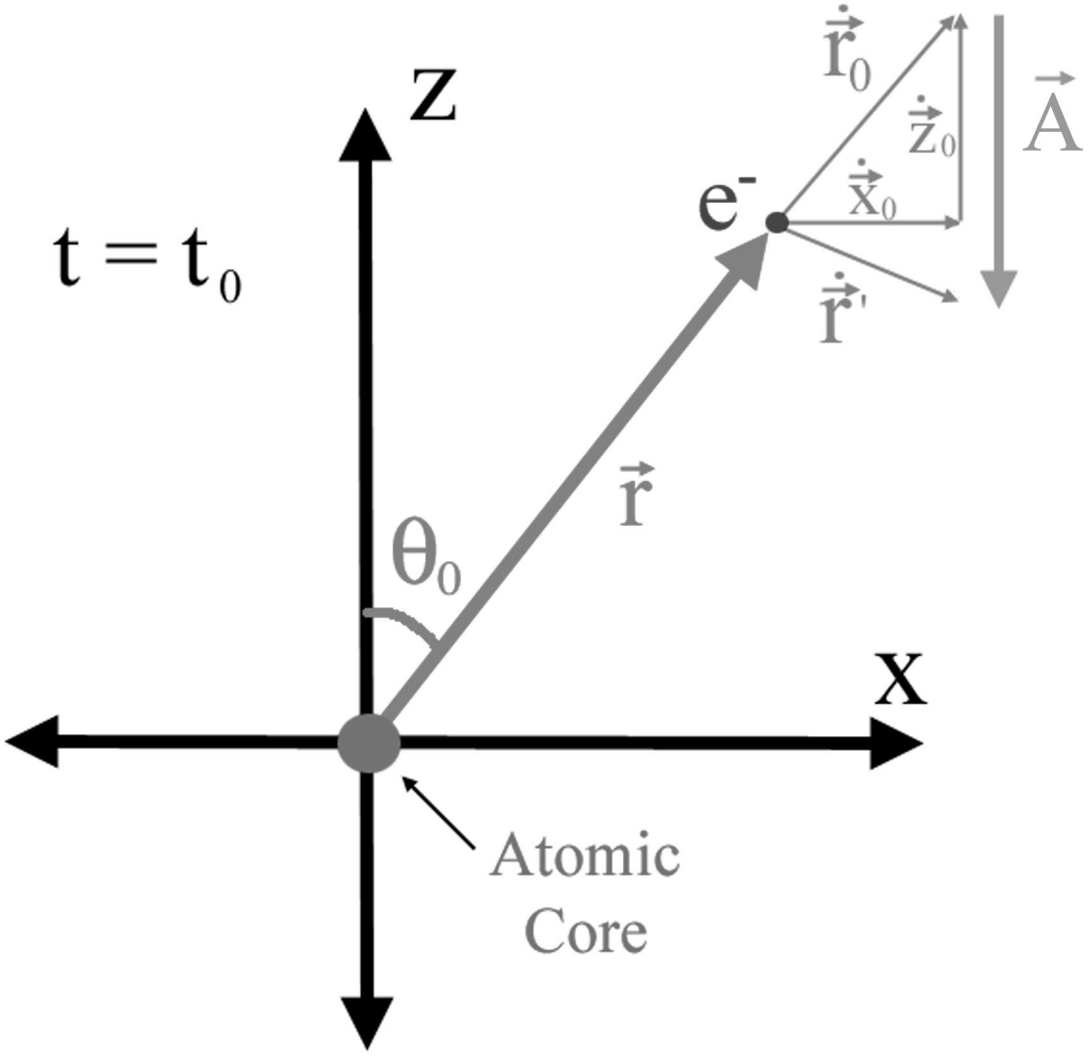

Figure 7.2: Schematic diagram of an electron as it feels the impulse $\vec{A}$ directed in the $-\hat{z}$ direction. Initially, the electron is moving radially outward at an angle θ_0 to the $\hat{z}$ axis. After the impulse, the $\hat{z}$ component of its velocity is changed by $-A$.

$$z(t_0) \;=\; |\vec{r}_0(t_0)|\; cos\theta_0 \tag{7.13}$$

$$\dot{x}(t_0) \;=\; |\dot{\vec{r}}_0(t_0)|\; sin\theta_0 \tag{7.14}$$

$$\dot{z}(t_0) \;=\; |\dot{\vec{r}}_0(t_0)|\; cos\theta_0 \;-\; A\;. \tag{7.15}$$

From these initial conditions, the subsequent motion of the electron can be calculated.

7.2.4 Determining Parameters of the Post-Impulse Motion

From this point on, we define $\vec{r}_0 \equiv \vec{r}(t_0)$ and $\dot{\vec{r}}_0 \equiv \dot{\vec{r}}(t_0)$ for ease of notation. The HCP breaks the convenient radial symmetry. The energy of the electron after the impulse is given by

$$E_f \;=\; \frac{1}{2}\Big(\dot{r}_0^2 \;+\; A^2 \;-\; 2A\dot{r}_0\; cos\theta_0\Big) \;-\; \frac{1}{r_0}\;, \tag{7.16}$$

where $r_0 \equiv |\vec{r}_0|$ and $\dot{r}_0 \equiv |\dot{\vec{r}}_0|$. A graphical representation for E_f as a function of θ_0 is given in figure 7.3 for representative values of E_0 and t_0.

To determine what values of initial launch angle θ_0 result in $E_f < 0$, equation 7.16 is solved for θ_0, yielding

$$cos\theta_0 = \frac{\dot{r}_0}{2A} \;+\; \frac{A}{2\dot{r}_0} \;-\; \frac{1}{r_0\dot{r}_0 A} \;-\; \frac{E_f}{A\dot{r}_0}\;. \tag{7.17}$$

An angle θ_c is defined by setting $E_f = 0$ in equation 7.17 and solving for the positive root of θ_0. For all $|\theta_0| < \theta_c$, $E_f < 0$ and the electron is bound. Similarly, if $|\theta_0| > \theta_c$ then $E_f > 0$. A graphical representation for θ_c as a function of A is given in figure 7.4 for representative values of E_0 and t_0.

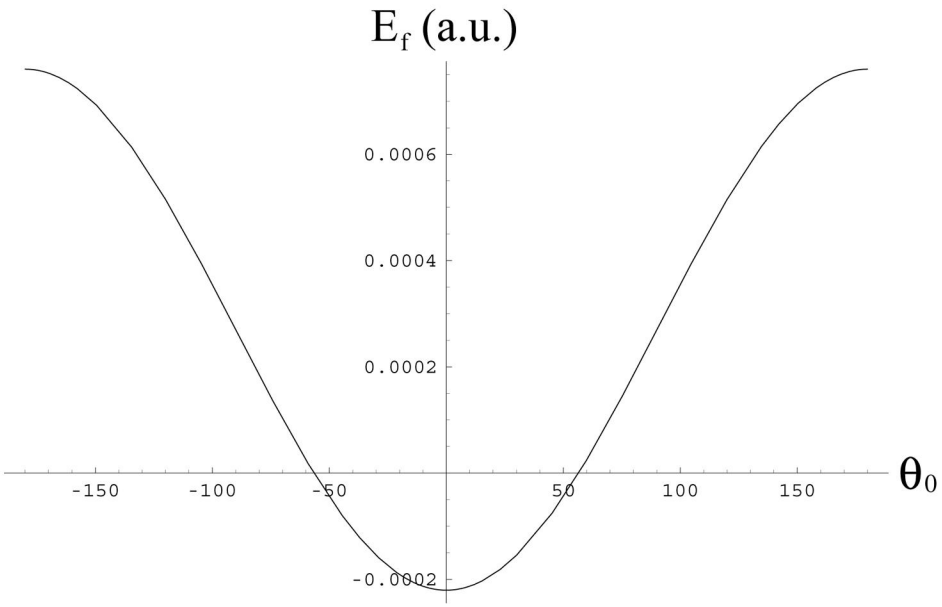

Figure 7.3: Final energy of an electron after interaction with a linear impulse in the $-\hat{z}$ direction as a function of initial launch angle, θ_0. For this figure, $A = 0.02$, $E_0 = 15$ cm^{-1}, and $t_0 = 3$ ps. Similar curves can be constructed for any initial values of E_0, A, and t_0.

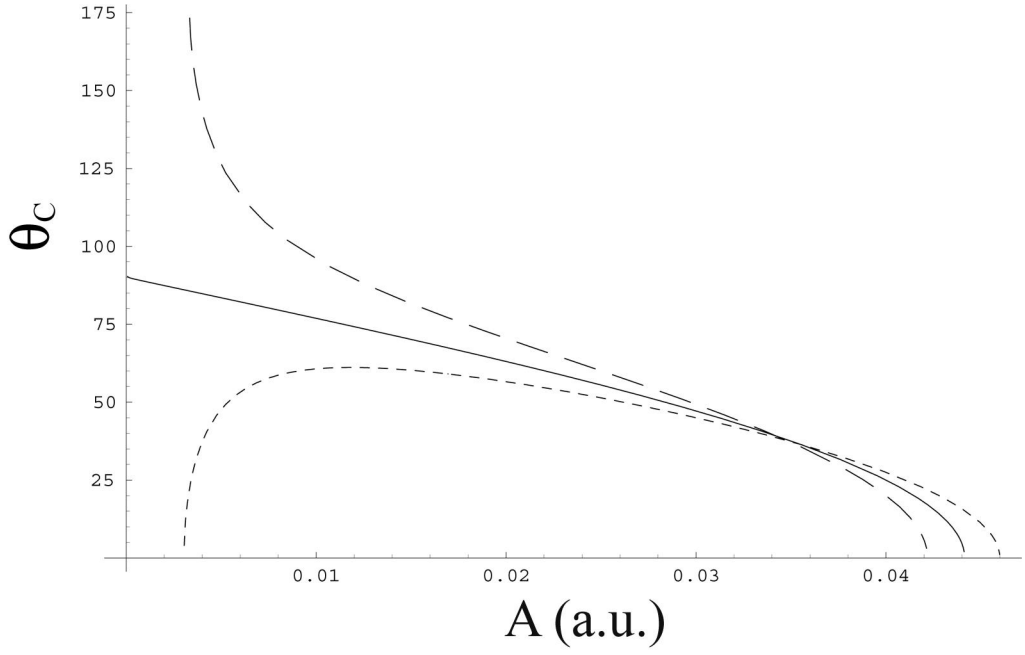

Figure 7.4: Critical launch angle θ_c such that for $\theta_0 = \theta_c$, $E_f = 0$ as a function of the impulse strength A. Here $t_0 = 3$ ps. In the solid curve $E_0 = 0$, in the long dashed curve $E_0 = -15$ cm^{-1} and in the short dashed curve $E_0 = 15$ cm^{-1}.

Another question which can be asked is: what combination of initial time delay t_0 and impulse strength A will lead to the most negative values of E_f? The impulse only affects the $\hat{z}$ component of the velocity vector. Therefore, an impulse which makes $|\dot{z}|$ as small as possible will result in the greatest decrease in E_f. As t_0 increases, the electron is farther and farther from the atomic core, however it is moving slower and slower due to the influence of the Coulomb potential. The impulse A which will cancel this motion similarly decreases with increasing values of t_0. Plotted in figure 7.5 is the impulse strength A which exactly cancels the initial momentum along $\hat{z}$ as a function of t_0. By zeroing $|\dot{z}|$, E_f is a minimum.

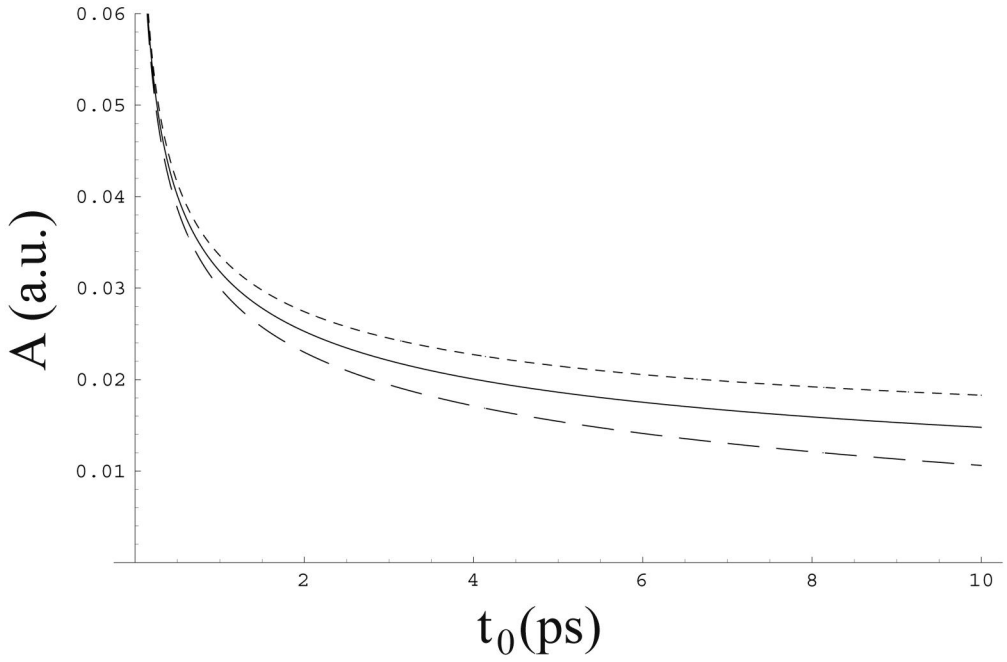

Figure 7.5: Impulse strength which results in the minimum value of E_f as a function of t_0. Points along this curve correspond to combinations of t_0 and A which exactly cancel the initial $\hat{z}$ momentum of the electron. The solid curve corresponds to $E_0 = 0$, the long dashed curve corresponds to $E_0 = -15$ cm^{-1} and the short dashed curve corresponds to $E_0 = 15$ cm^{-1}. The short dashed curve most closely represents the situation present in chapter 6.

In general, the angular momentum of the electron following the HCP is nonzero. To calculate ℓ, we use the familiar relation $\vec{\ell} = \vec{r} \times \dot{\vec{r}}$. Using the position and momentum of the electron immediately after the impulse, the angular momentum for all times $t > t_0$ is given by

$$\vec{\ell} = Ar_0 \, sin\theta_0 \, \hat{y} \; . \tag{7.18}$$

Now that the energy and angular momentum after the impulse are known, other quantities can be calculated. A useful one is the eccentricity of the orbit after interaction

with the impulse. We know from Goldstein [12] that the eccentricity of a Kepler orbit is given by:

$$e \;=\; \sqrt{1 \;+\; 2E\ell^2}\;. \tag{7.19}$$

Therefore, the eccentricity of the orbit that results after the continuum electron receives an impulsive kick of strength A at an angle θ_0 is obtained by combining equations 7.16, 7.18, and 7.19.

$$e \;=\; \sqrt{1 \;+\; \left(\dot{r}_0^2 \;+\; A^2 - 2A\dot{r}_0\; cos\theta_0 - \frac{2}{r_0}\right)\left(r_0^2 A^2\; sin^2\theta_0\right)} \tag{7.20}$$

The resulting eccentricity is shown in figure 7.6 as a function of initial launch angle, θ_0 for typical values of E_0 and A. Values of the eccentricity less than 1 correspond to elliptical (bound) orbits. Conversely, for $|\theta_0| > \theta_c$, the eccentricity is greater than 1 and the electron motion is unbounded.

The Kepler orbit period of the electron after its interaction with the HCP can be determined simply from semi-major axis a of its orbit [12]. Since we know both the angular momentum and eccentricity of the electron's orbit, we choose to express τ_K as

$$\tau_K \;=\; 2\pi a^{3/2} \;=\; 2\pi\left(\frac{\ell^2}{1 \;-\; e^2}\right)^{3/2}\;. \tag{7.21}$$

It should be noted that τ_K is independent of ℓ, however we choose to use ℓ, and e to determine a. Simple substitution of equations 7.18 and 7.20 into equation 7.21 yields the Kepler period as a function of E_0, t_0, A, and θ_0. Of course, this relation only holds for closed (bound) orbits where $E_f < 0$.

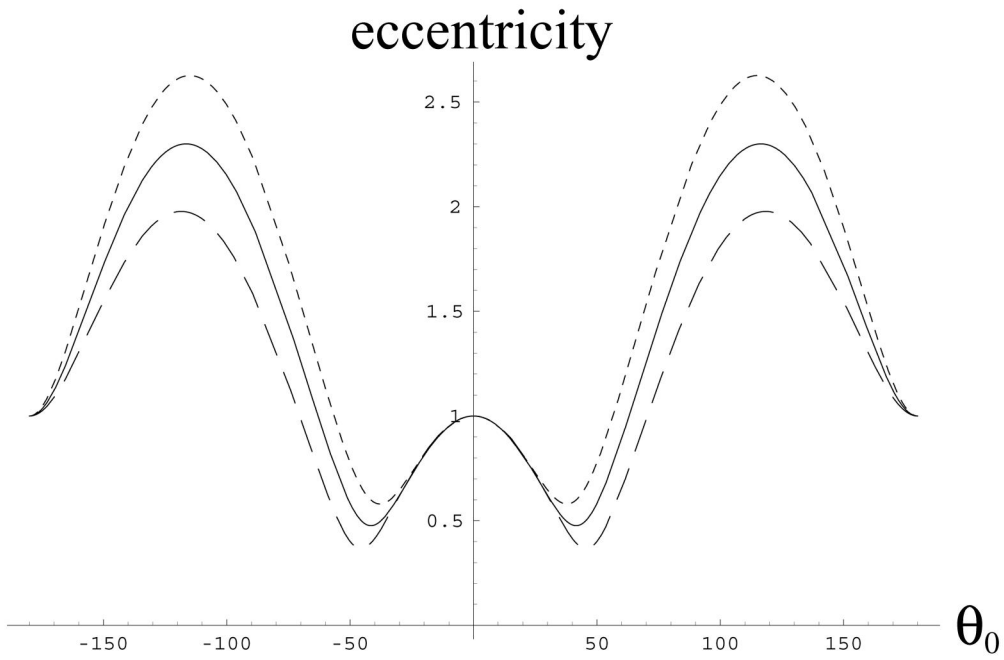

Figure 7.6: The eccentricity of the orbit that results from the HCP of magnitude $A = 0.02$ applied to an electron 3 ps after it is launched from the core, shown as a function of initial launch angle, θ_0. The short dashed, solid, and long dashed curves represent initial electron energies of $E_0 = +15$ cm^{-1}, 0, and -15 cm^{-1} respectively.

To get a feel for how variations in HCP magnitude affect the Kepler period of the recombined electron, we look at the limiting case where $\theta_0 = 0$ in figure 7.7. At $t_0 = 3$ ps, a minimum in the Kepler orbit time occurs at approximately $A = 0.022$. However, for a range of kick strengths ($0.015 \leq A \leq 0.035$) fairly uniform, bound motion occurs. To investigate both the effect of the impulse strength and launch angle on the Kepler period at the same time, a 3-D plot is created and shown in figure 7.8 which shows $\tau_K(A, \theta_0)$ for typical values of E_0 and t_0. Note that a large range of A and θ_0 values, yield similar Kepler periods for the recombined electron.

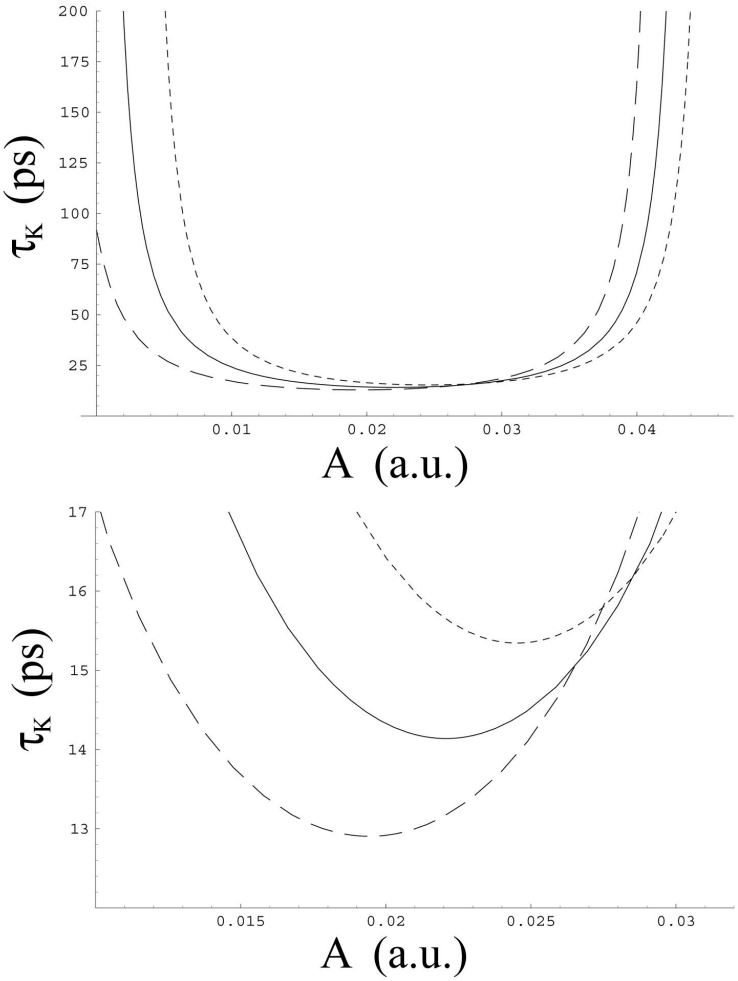

Figure 7.7: The Kepler period of an electron with $\theta_0 = 0$ after interacting with a HCP of magnitude A at $t_0 = 3$ ps. In both graphs, the short dashed, solid, and long dashed curves represent initial electron energies of $E_0 = +15$ cm^{-1}, 0, and -15 cm^{-1} respectively. The lower graph shows only a small range of τ_K and A values to highlight how the minimum value of τ_K varies with E_0 and A.

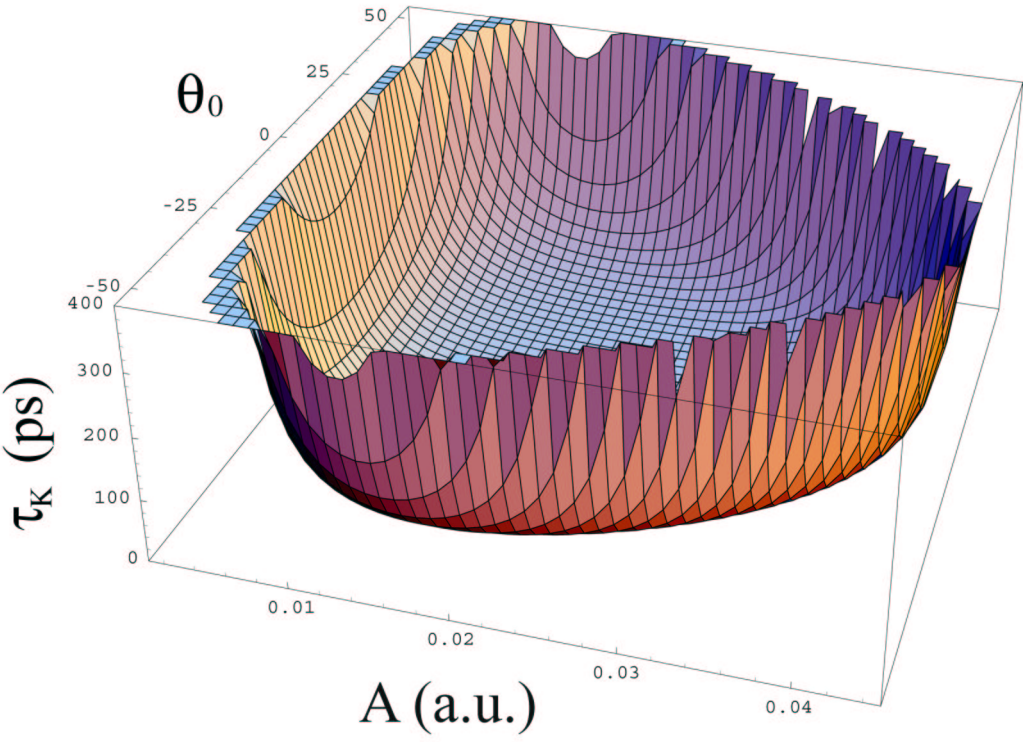

Figure 7.8: The Kepler period of an electron with initial launch angle θ_0 after interacting with a HCP of of magnitude A at $t_0 = 3$ ps. In this graph $E_0 = +15$ cm^{-1}. Therefore, the conditions shown here closely resemble the initial conditions in the experiment presented in chapter 6. A large section of the A, θ_0 parameter space leads to orbits with similar Kepler periods.

7.2.5 Orbital Dynamics

After the impulse, each bound electron performs an elliptical orbit. For any electron in an elliptical orbit, the radial distance from the origin to the electron is given by

$$\frac{\ell^2}{r} \;=\; 1 \;+\; e\; cos\; \phi \;, \tag{7.22}$$

where ϕ is measured from the outer turning point of the electron's orbit. Solving for ϕ yields,

$$cos\; \phi \;=\; \frac{1}{e}\left(\frac{\ell^2}{r} \;-\; 1\right). \tag{7.23}$$

Equation 7.23 can be used to determine the orientation of the electron's orbit after interaction with a HCP of magnitude A. An angle ϕ_0 is defined as the angle between the major axis of the new orbit of the electron and the electron's position immediately after the impulse. (See figure 7.9 for a schematic.) A new Cartesian coordinate system is defined to be along the major and minor axes of the elliptical motion of the electron following the impulse interaction. $+\hat{z}'$ is defined to be along the major axis of the orbit and pointed in the direction of the outer turning point of the orbit. Therefore, $-\hat{z}'$ points towards the inner turning point of the orbit. The $\hat{x}'$ axis lies along the minor axis of the new orbit. Therefore, ϕ_0 is the angle between the $-\hat{z}$ axis and the vector $\vec{r}_0$. To find a value for ϕ_0, we apply equation 7.23, resulting in

$$cos\; \phi_0 \;=\; \frac{1}{e}\left(\frac{\ell^2}{r_0} \;-\; 1\right). \tag{7.24}$$

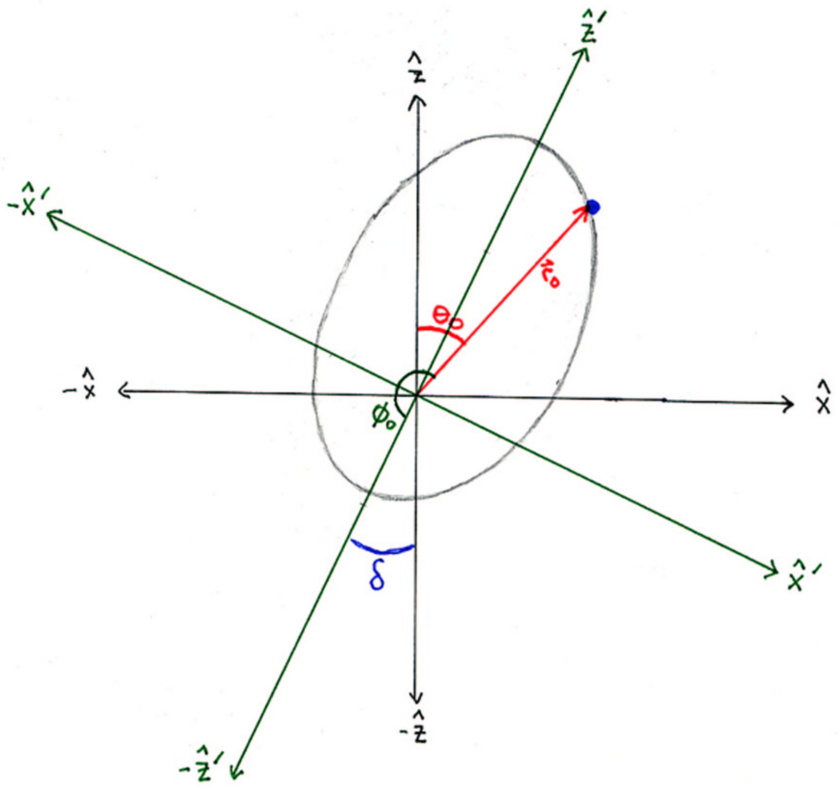

Figure 7.9: Important angles of the electron's motion instantaneously after interaction with a HCP of magnitude A applied in the $-\hat{z}$ direction. θ_0 is the angle that the initial motion of the electron makes with the $\hat{z}$ axis. The electron loses energy and becomes bound in an elliptical orbit at $t = t_0$. We define a new Cartesian coordinate system such that the major and minor axes of the new elliptical orbit form the axes of the new coordinate system. $+\hat{z}'$ is defined to be in the direction of the outer turning point of the new orbit and along the major axis. Therefore $-\hat{z}'$ is along the major axis of the new orbit and pointed in the direction of the inner turning point. The $\hat{x}'$ axis is the minor axis of the new orbit. The angle between the old and new axes is given by δ. The angle ϕ_0 is the angle that the electron's position at $t = t_0$ makes with the $-\hat{z}$ axis. ϕ_0 is defined to be zero at the inner turning point of the new elliptical orbit and measured positive in the clockwise direction in the $\hat{xz}$ plane.

Substitution of the values of e and ℓ from equations 7.20 and 7.18 yields the angle ϕ_0 as a function of E_0, θ_0, A, and t_0.

7.2.6 z Intercept Information

Finally, some information regarding the intersection of the electron's post-impulse orbit with the original kick axis can be obtained. Recall that the main goal of this section is to determine the degree of localization of the recombined wavepacket as a function of a variety of initial conditions. Due to the symmetry of the problem, localization is only possible along the axis which the HCP was applied. Therefore, determining where and when each orbit intersects this axis is crucial in determining the degree of wavepacket localization. For notational simplicity, we have defined the HCP to be incident along $-\hat{z}$. Therefore we seek to determine the z intercept position and timing as a function of the experimental parameters. It should be noted that there is no inherent symmetry about the $\hat{z}$ axis. The analysis presented here is equally valid for any choice of HCP kick axis.

Classical Trajectory Monte Carlo (CTMC) simulations suggest that a wide range of initial launch angles, θ_0 lead to similar values of z axis intercepts after interaction with a $-\hat{z}$ oriented HCP field [10,13]. To determine where a recombined electron's orbit will intersect the original z axis, the orbit equation is solved for r yielding

$$r \;=\; \frac{\ell^2}{1 \;+\; e\; cos\; \phi}\;. \tag{7.25}$$

The orbital radius vector $\hat{r}$ is entirely along the $+\hat{z}$ axis when $\phi = \phi_0 - \theta_0$, leading to

$$z_{int} = \frac{\ell^2}{1 + e\ cos\ (\phi_0 - \theta_0)} . \tag{7.26}$$

A symbolic expression for z_{int} in terms of A, t_0, E_0, and θ_0 is long and uninformative, and is therefore omitted. However a graphical representation of z_{int} is useful for visualizing the dynamics. In figure 7.10, z_{int} is shown as a function of the initial launch angle for two different values of impulse strength. Note that for $A \geq 0.023$, the z_{int} values are very similar over a large range of θ_0. This is shown more clearly in figure 7.11 by the large plateau of z_{int} values above $A = 0.023$. In this region, the values of z_{int} increase for increasing values of A, however z_{int} is approximately constant as a function of θ_0 when $\theta_0 < \theta_c$. Care must be taken in examining figure 7.11 however as not all values of A and θ_0 lead to bound orbits. Specifically, if $E_0 = +15$ cm^{-1} and $t_0 = 3$ ps, then for $A > 0.046$, no bound orbits exist regardless of the initial launch angle. Similarly, if $|\theta_0| > 57°$, then no value of impulse strength will result in bound orbits.

Figure 7.11 clearly shows that a diverse set of initial conditions may all lead to electron orbits which cross the kick axis (in this case the $\hat{z}$ axis) in approximately the same location. However, to show that the initial conditions are consistent with wavepacket localization, we must also show that each orbit crosses the kick axis *at the same time* as well. To determine *when* the electron crosses the z axis, (for that matter,

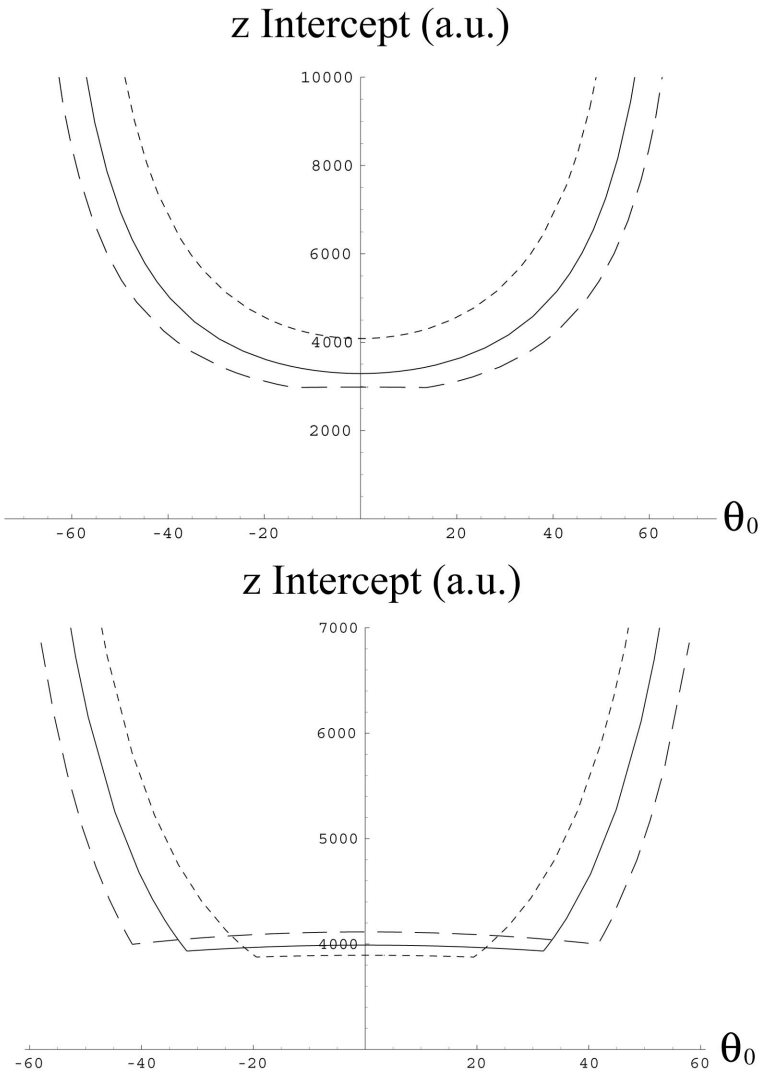

Figure 7.10: z_{int} as a function of θ_0 for two values of A. In the graph on the top, $A = 0.02$, while in the graph on the bottom, $A = 0.026$. In both graphs, the short dashed, solid, and long dashed curves represent initial electron energies of $E_0 = +15$ cm^{-1}, 0, and -15 cm^{-1} respectively. In both graphs $t_0 = 3$ ps. Note that once A passes a threshold value, a large range of θ_0 values result in very similar z intercepts.

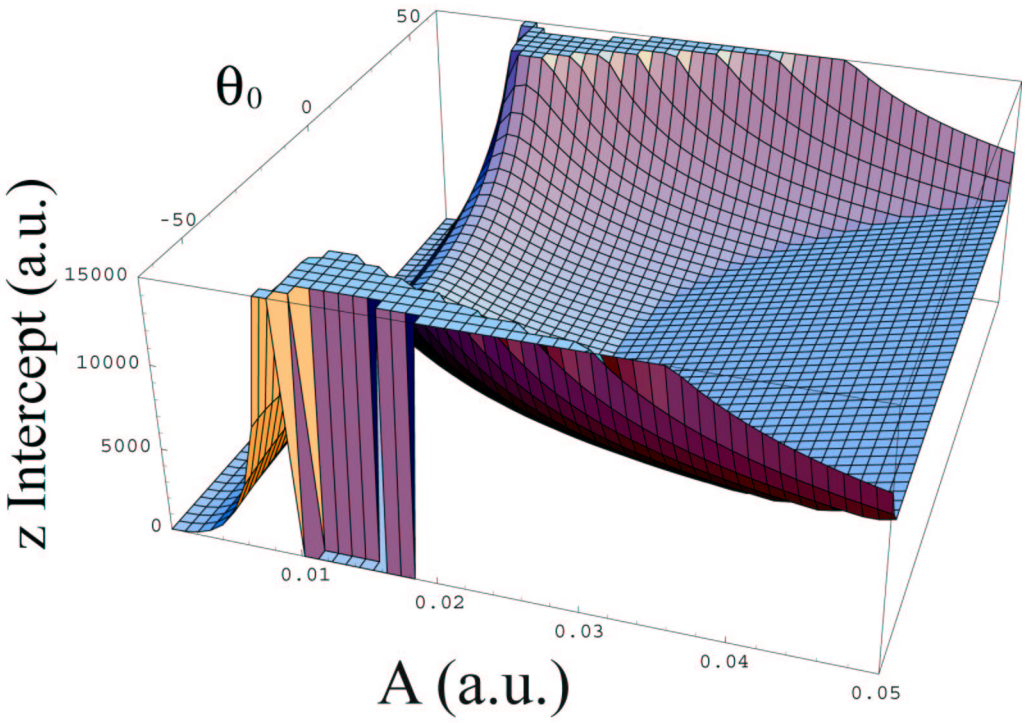

Figure 7.11: z_{int} as a function of θ_0 and A. For this graph $E_0 = +15$ cm^{-1} and $t_0 = 3$ ps.

to determine the time the electron reaches any given location in its orbit) we make use of Kepler's equation [12]

$$t \;=\; \left(\frac{\tau}{2\pi}\right)\,(\psi \;-\; e\;sin\;\psi)\;. \tag{7.27}$$

The variable ψ is known as the eccentric anomaly. ψ ranges from 0 to 2π and is defined by the relation

$$r \;=\; \left(\frac{\ell^2}{1 \;-\; e^2}\right)(1 \;-\; e\;cos\;\psi)\;. \tag{7.28}$$

The variables ϕ and ψ are related through the following equation [12]

$$tan\;\frac{\phi}{2} \;=\; \sqrt{\frac{1\;+\;e}{1\;-\;e}}\;tan\;\frac{\psi}{2}\;. \tag{7.29}$$

Therefore, to find the time when the electron's orbit crosses the z axis, we set $\phi = \phi_0 - \theta_0$ and solve for ψ with equation 7.29. Once the value of ψ is known, then we plug this value into equation 7.27 to determine when the electron crosses the z axis. Figure 7.12 shows the first z intercept time as a function of θ_0 and A for the approximate values of E_0 and t_0 which are present in the experiment in chapter 6. An "island" of initial θ_0 and A values leads to fairly short z intercept times. The center of this island in impulse strength corresponds to $A = .023$, $\theta_0 = 0$. These conditions lead to the shortest possible Kepler period of the recombined electron. The value of $A = .023$ is also roughly equal to the HCP kick magnitude which results in long lived modulations in the measured HCP probe ionization signal shown in figure 6.4.

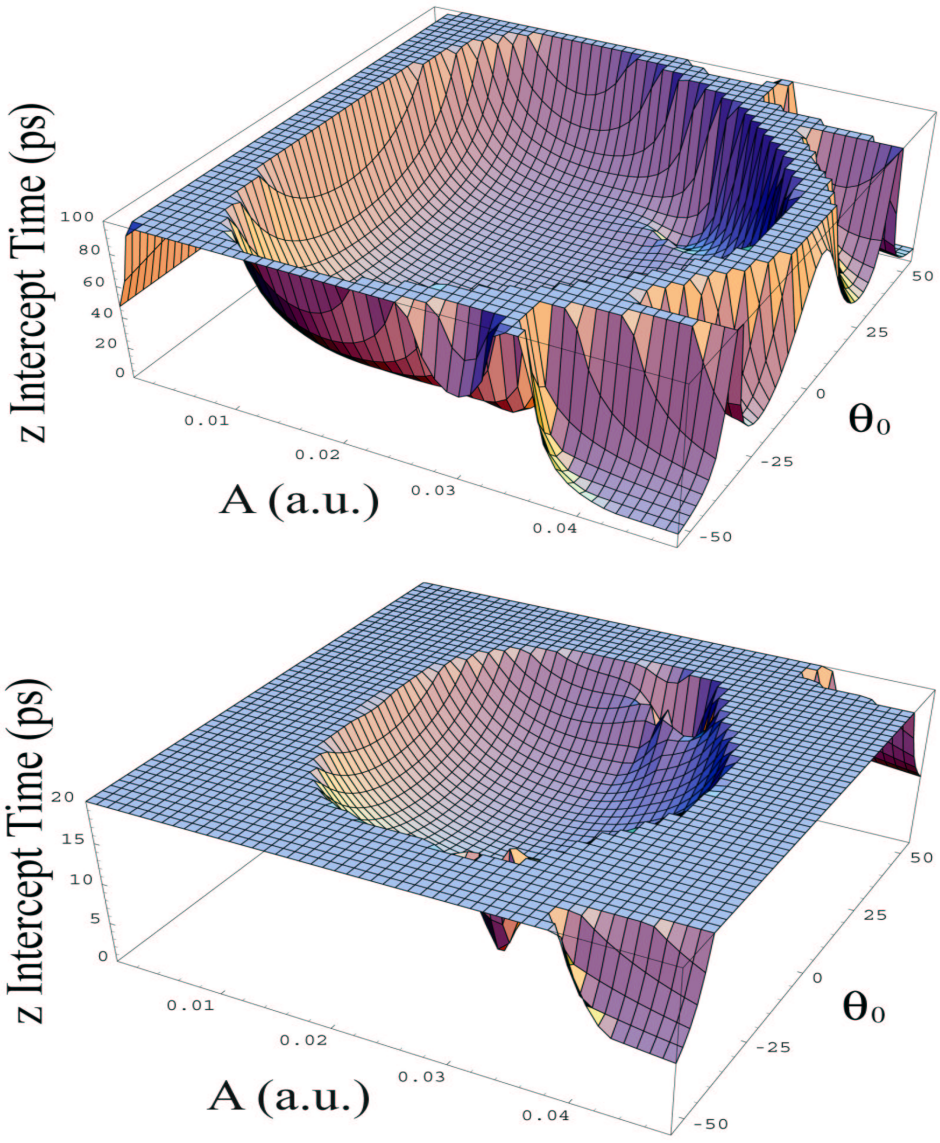

Figure 7.12: The time of the first $+z$ intercept as a function of θ_0 and A. Again, $E_0 = +15$ cm^{-1} and $t_0 = 3$ ps. In the lower graph, the time scale has been truncated to allow observation of conditions which lead to the shortest $+z$ intercept.

7.2.7 Conclusions

The main goal of this section was to demonstrate that a potentially diverse range of initial conditions all can lead to roughly the same localized wavepacket dynamics. In other words, a large portion of an initial distribution (with slightly different initial conditions) may wind up localized at the same point at the same time. We see that this is indeed the case. For a range of initial launch angles (roughly $-30^\circ \leq \theta_0 \leq 30^\circ$), HCP magnitudes ($0.02 \leq A \leq 0.03$), initial energy ($|E_0| \leq 15$ cm^{-1}), and launch times (2 ps $\leq t_0 \leq 4$ ps), most electron trajectories cross the $+\hat{z}$ axis at roughly the same time and in roughly the same place. Clearly, the more the initial conditions are narrowed, the tighter the localization becomes. However, a good deal of localization is expected for even the diverse initial conditions which are used in the HCP induced recombination in chapter 6.

Most of the graphs presented in this chapter are done under the same initial conditions for the launch of the continuum wavepacket, namely $E_0 = +15$ cm^{-1} and $t_0 = 3$ ps. These values are chosen to closely reproduce the experimental conditions that are used in the experimental work presented in chapter 6. Similar calculations have been performed for many different values of both E_0 and t_0, but the results do not provide any new information. To properly simulate the experimental parameters, calculations should be done for a range of initial launch times and initial energies and added together with the proper weighting. Performing these calculations analytically becomes

increasingly difficult. Therefore, instead of trying to extend the analytical calculations further, a shift to a completely numerical approach is indicated. To that end, in the following section we perform Classical Trajectory Monte Carlo (CTMC) simulations of HCP induced electron - ion recombination to investigate the range of initial conditions which lead to 3-D wavepacket localization.

7.3 Numerical Calculations of Localization

7.3.1 Introduction

The analytic methods described in the previous section can only be extended so far before the equations may not be solved in closed form, or even with only modest numerical techniques such as Newton's method. Most notably, for electric fields that are non-instantaneous, analytic solutions of the equations of motion are quite difficult. Therefore, to extend the analysis of the localized recombined wavepacket to interaction with non-instantaneous fields, several Classical Trajectory Monte Carlo (CTMC) ensemble simulations are performed. The technical details of the simulations are described in appendix B. In this section we present results from the simulations. These results are used to gain further understanding about the effect that a wide range of initial conditions have on the creation and subsequent evolution of a 3-D localized recombined wavepacket.

In the simulation, each electron in an ensemble of 25 000 points is launched from the core into a $m = 0$, $\ell = 2$ continuum orbit. The angle θ_0 that the major axis of the initial orbit makes with the $\hat{z}$ axis is randomly distributed between $-180°$ and $180°$. Without loss of generality, we assume that the orbit is confined to the $\hat{xz}$ plane. The results can then be rotated into the full 4π angular coordinate space. A time Δt after the electron leaves the core, it is subject to a 1 ps FWHM Gaussian HCP field. The polarity of the HCP is arbitrarily chosen so that the electron feels a kick in the $-\hat{z}$ direction. The results are independent of the initial choice of coordinate axes however. In this choice of orientation, the $\hat{z}$ axis is therefore defined to be the "kick" axis. The position and momentum of the electron is calculated numerically from $t = 0$ through some $t = t_{max}$. A classical electron probability distribution is created from the cumulative results at each time step [14]. The distributions from each time step are then combined and a movie of the electron probability is created which shows the position and momentum distributions for an ensemble of electrons for all times $0 \leq t \leq t_{max}$.

7.3.2 Movies

Unfortunately, the printed format of this thesis does not present an easy method to show movies of the time evolution of electron distributions. Therefore, a CD - ROM is included with the thesis which contains the movies discussed in the text. The printed figures in this section are a single frame from each movie. Each individual frame

presented in the printed format is chosen in an attempt show the main feature from the movie.

In each movie, a 1 ps FWHM HCP field interacts with an ensemble of electrons approximately 3 ps to 4 ps after the launch of the electrons from the atomic core. The initial motion is unbounded, with the initial energy of each electron in the ensemble chosen from a Gaussian distribution centered at approximately 15 cm^{-1} with a FWHM of 10 cm^{-1}. After HCP interaction, a portion of the electrons in the ensemble will have $E_f < 0$ and therefore be bound. These electrons execute elliptical orbits. This is shown in figure 7.13. It is important to keep in mind when examining the overall behavior of each ensemble that all the bound distribution shows is a bunch of elliptical orbits added together.

Figures 7.14, 7.15, and 7.16, show movies of the time evolution of classical electron probability densities before, during, and after interaction with a HCP field. Three individual cases of HCP kick strength are considered. Each distribution is assembled from 25 000 individual runs of a classical simulation. Probability density is shown in the vertical axis. The direction that the HCP kick is applied is chosen to be $-\hat{z}$. The HCP arrives approximately 4 ps after the initial launch of the electrons. In figure 7.14, the magnitude of the HCP field is chosen so that the momentum of an electron along the kick axis is zero after HCP interaction. In other words, the HCP field removes all the kinetic energy from an electron launched with $\theta_0 = 0$. This situation is referred to as

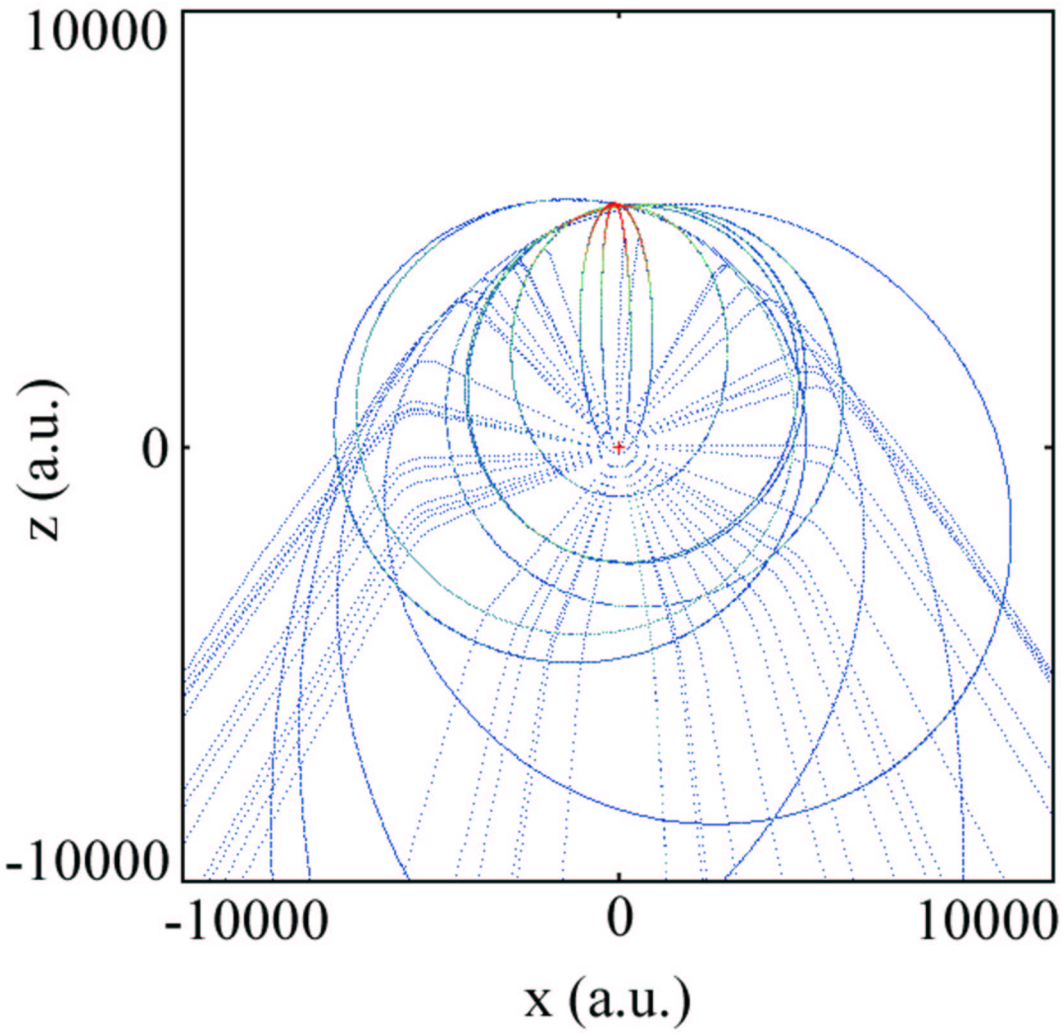

Figure 7.13: A single frame from a movie which shows 50 individual runs of the classical simulation of electron motion. Initially, each electron is launched into a $\ell = 2$ orbit from the atomic core with an energy E_0 chosen from a Gaussian distribution of energies centered at 15 cm^{-1}. The angle θ_0 that each electron's initial motion makes with the $\hat{z}$ axis is randomly chosen. A Gaussian HCP of maximum magnitude 4.5 kV/cm interacts with the system approximately 4 ps after the initial launch of the electrons. In this movie, the tracks of the electrons are displayed to demonstrate the elliptical nature of the electron orbits after the HCP interaction. Note that bound orbits intersect the $+\hat{z}$ axis at approximately the same location. Also note that electrons with small values of $|\theta_0|$ form the most tightly bound orbits. Red denotes greater probability for finding an electron at that location.

the "magic kick" case. For the "magic" HCP kick strength, a large spike in probability density occurs along the kick axis. This occurs approximately 22 ps after the launch of the electrons. The maximum in probability density recurs approximately every 22 ps. For the initial conditions presented here, this magic kick strength is 4.5 kV/cm.

If the magnitude of the HCP is weaker than magic kick strength, as in figure 7.15, the HCP does not remove all the kinetic energy from the $+\hat{z}$ directed outgoing electrons. This case is referred to as the "weak kick" case. In contrast, if the HCP field is stronger than the magic kick strength, as in figure 7.16, then electrons moving in the $+\hat{z}$ direction are turned around and have momentum directed along $-\hat{z}$ after HCP interaction. This situation is referred to as the "strong kick" case. In both the strong kick and weak kick cases, the large spike in probability density which occurs in the magic kick case does not occur. Figure 7.17 shows a plot of the maximum density of the electron distribution as a function of time for each of the three cases. After the first 50 ps of the simulations, no time dependent features are seen in the maximum density in either the weak or strong kick cases. However, a spike in probability density recurs every 23 ps in the magic kick case. This feature persists for several nanoseconds.

HCP interaction changes the energy of each electron by an amount

$$\Delta E \;=\; \vec{p}_e \cdot \vec{A} \;+\; \frac{1}{2}|\vec{A}|^2 \;, \tag{7.30}$$

where $\vec{p}_e$ is the momentum of the electron prior to HCP interaction and $\vec{A}$ is the HCP strength. (A full treatment of HCP interactions is contained in chapter 3, and an

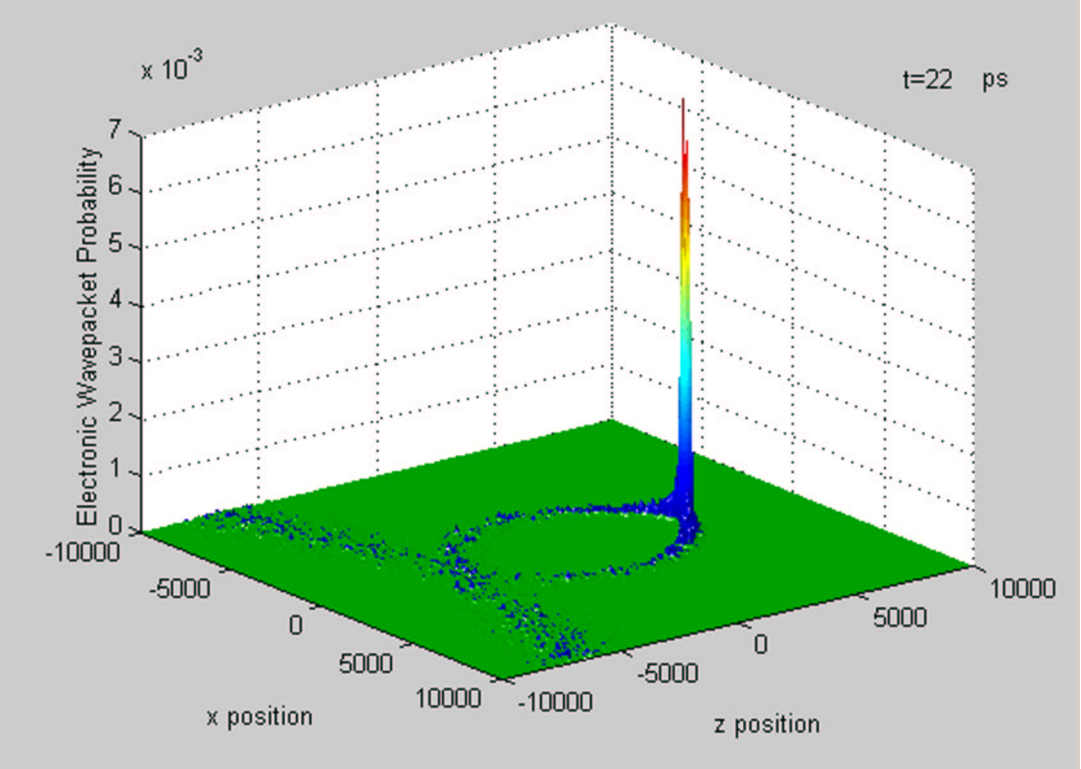

Figure 7.14: A single frame from a movie showing the time evolution of a classical electron probability density during interaction with a HCP. Probability density is shown in the vertical axis. The initial state is a classical $\ell = 2$ orbit launched from the atomic core with an energy E_0 chosen from a Gaussian distribution of energies centered at 15 cm^{-1}. The angle θ_0 that each electron's initial motion makes with the $\hat{z}$ axis is randomly chosen. A Gaussian HCP of maximum magnitude 4.5 kV/cm interacts with the system 4 ps after the initial launch of the electrons. This is the "magic kick" case discussed in the text. Note at approximately 22 ps after the launch of the electrons, a large spike in probability density forms along the $+\hat{z}$ axis. Over 50% of the bound population is located in the peak. The peak reforms several times throughout the duration of the simulation.

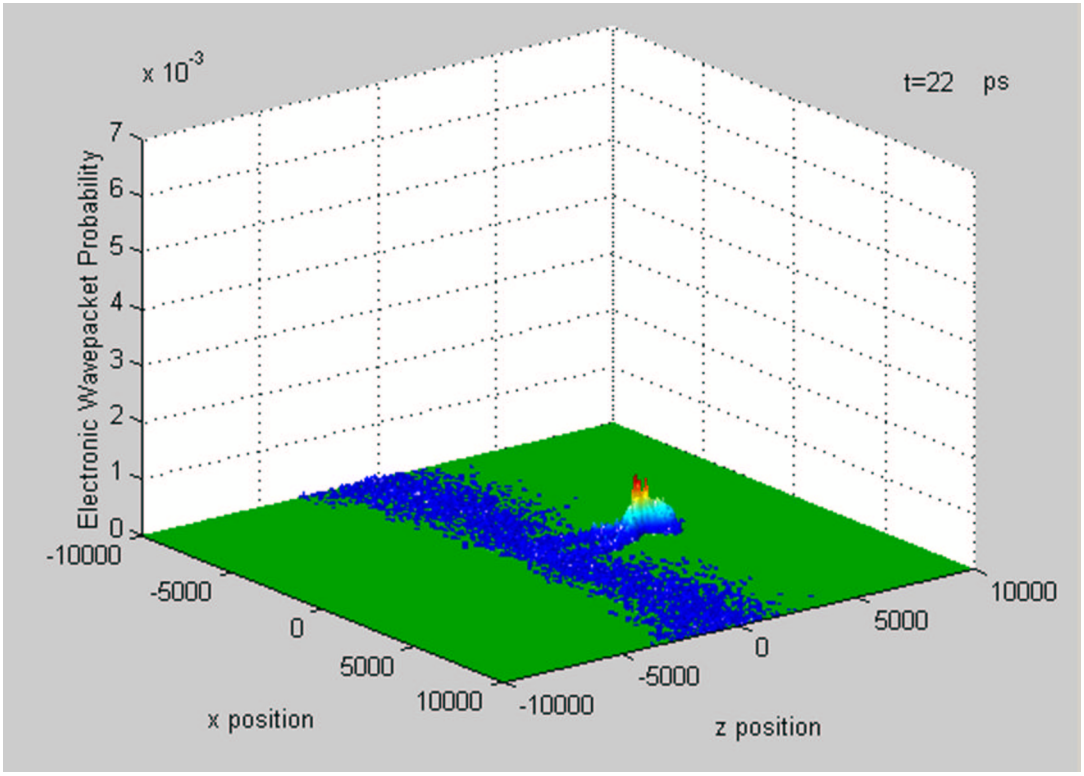

Figure 7.15: A single frame from a movie showing the time evolution of a classical electron probability density during interaction with a HCP. The distribution is assembled from 25 000 individual runs of a classical simulation. Probability density is shown in the vertical axis. This simulation contains the same parameters as figure 7.14, however the maximum HCP amplitude is reduced to 3 kV/cm. Note that the spike in probability density does not form as was seen in figure 7.14. This is the "weak kick" scenario discussed in the text.

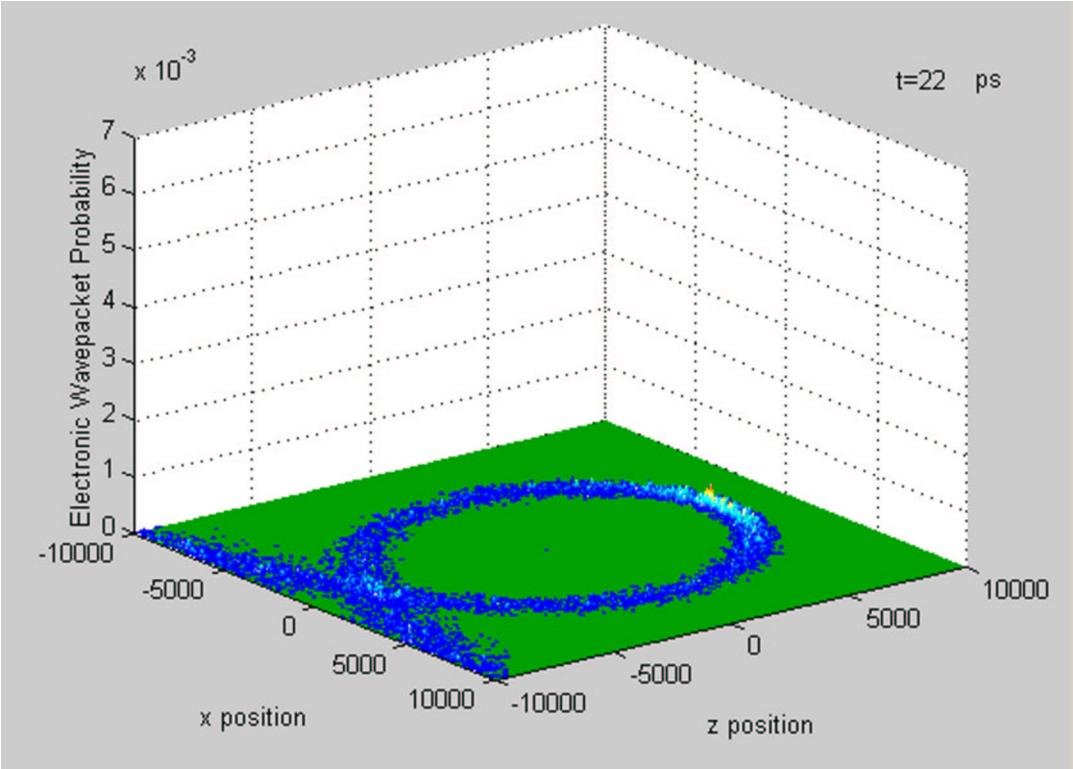

Figure 7.16: A single frame from a movie showing the time evolution of a classical electron probability density during interaction with a HCP. The distribution is assembled from 25 000 individual runs of a classical simulation. Probability density is shown in the vertical axis. This simulation contains the same parameters as figures 7.14 and 7.15, however the maximum HCP amplitude is increased to 5.5 kV/cm. No spike in probability density occurs. This is the "strong kick" scenario discussed in the text.

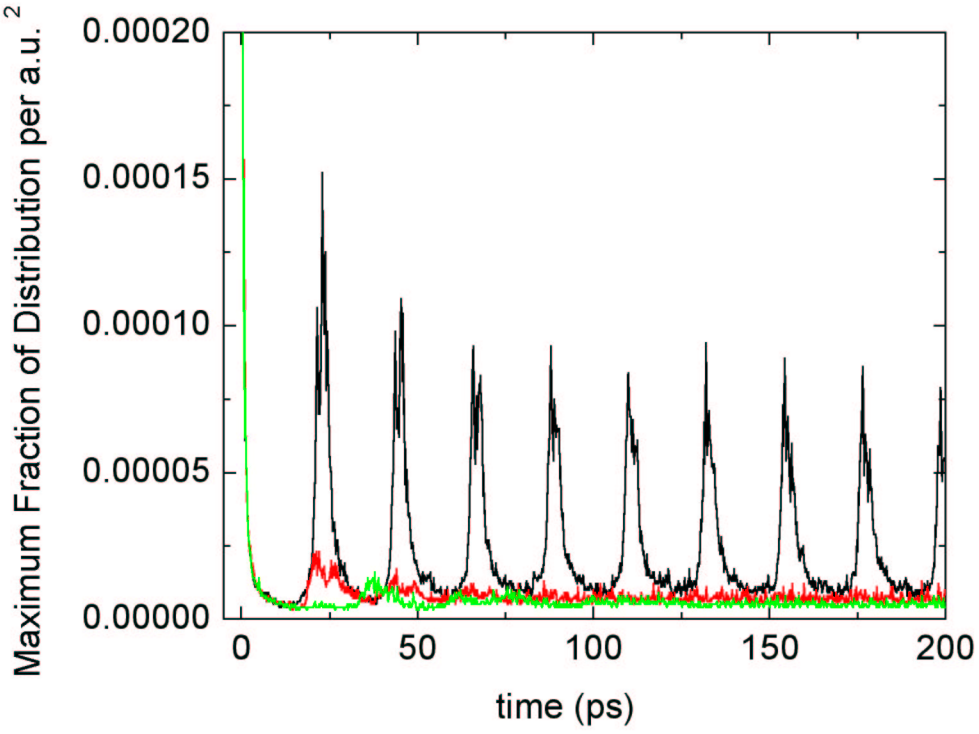

Figure 7.17: Maximum density of the classical electron distribution as a function of time after the launch of the continuum electrons. Initial conditions are discussed in the text. The black curve is for the magic kick strength case, the red curve is for the weak kick case, and the green curve is for the strong kick case. Only the magic kick case results in a recurring spike in the probability density.

explanation of HCP induced recombination is given in section 6.2.) The energy of an electron is a conserved quantity both before and after HCP interaction. Only *during* HCP interaction is E not conserved. Therefore, the energy distribution after HCP interaction reveals information about the fraction of the total electron distribution bound as well as the distribution of n states among the bound fraction. Figure 7.18 shows the energy distribution both before (E_0) and after (E_f) HCP interaction in the magic kick case. The energy distribution before HCP interaction is a Gaussian and centered at $E_0 = 15$ cm^{-1} as discussed previously. The E_f distribution is peaked near the lowest (bound) energies in the distribution. The lowest possible energy that an electron may have after HCP interaction is determined by its potential energy when it interacts with the HCP field. For the initial conditions in figure 7.18, $E_{f_{min}} = -40.5$ cm^{-1}, corresponding to a Rydberg orbit with principle quantum number of $n = 52$. A large fraction ($\approx 33\%$) of the bound population has energy between -40.5 cm^{-1} and -35 cm^{-1}, corresponding to $52 \leq n \leq 56$. For comparison, the E_f distributions in all three cases are shown in figure 6.13. The narrow peak in the E_f distribution broadens for both the weak and strong kick cases.

7.3.3 Time Evolution of Measurable Quantities

At each time step of the simulations, the position and momentum of each electron is recorded. The data is then complied to form position and momentum distributions as

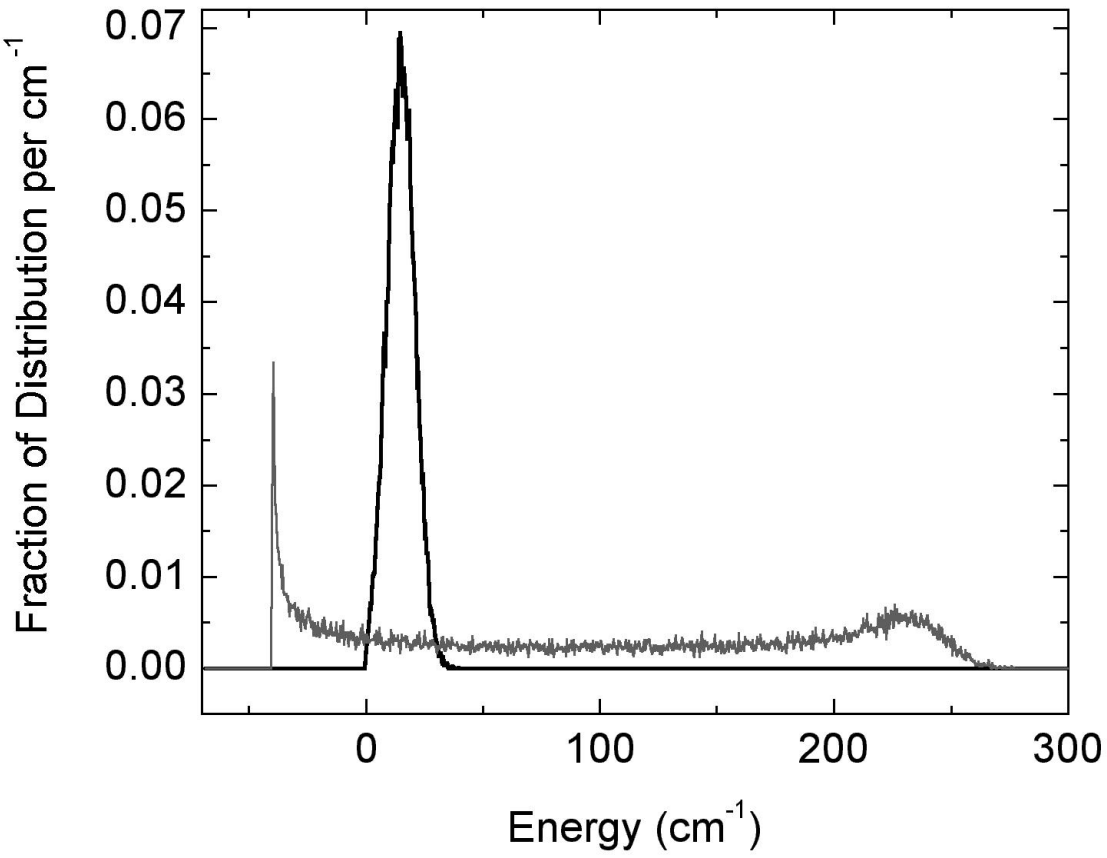

Figure 7.18: Energy distribution of a classical ensemble of electrons before (black curve) and after (grey curve) HCP interaction. The HCP field has a maximum strength of 4.5 kV/cm (magic kick case). The initial energy distribution is Gaussian and centered at approximately 15 cm^{-1} with a 10 cm^{-1} FWHM. Approximately 24% of the initial distribution has $E_f < 0$. Of that bound population, over 33% has principle quantum number $52 \leq n \leq 56$.

functions of time. In this way, classical distributions are created for the position and momentum along any axis. Figures 7.19 and 7.20 show the position and momentum along the $\hat{z}$ axis and $\hat{x}$ axis respectively for the classical electron distribution shown in figure 7.14. These distributions are for the magic kick case. For comparison, figure 7.21 shows the $\hat{z}$ momentum distribution in the weak kick and strong kick cases. Momentum plots such as those in figures 7.19(b), 7.20(b), and 7.21 can be directly compared to experimental momentum distributions obtained through the impulse momentum retrieval (IMR) method (see chapters 3 and 6).

When the $\hat{z}$ momentum distributions of the three kick strength scenarios are compared, one main feature is evident. Long lasting time dependent features only occur in the magic kick case. In both the weak and strong kick strength scenarios, all time dependent features wash out after the first 75 ps. In contrast, in the magic kick simulation the same oscillatory feature can be seen for up to several nanoseconds. Some dephasing occurs after each oscillation, however the basic structure remains. This is consistent with the plot of maximum wavepacket density shown in figure 7.17 This main recurring feature in the momentum distribution in figure 7.19(b) has the shape of a backwards "S". The crossover from positive to negative values of p_z generally occurs slowly as a function of time. In contrast, the switch from negative values of p_z to positive values is typically extremely rapid.

A low ℓ Rydberg electron moves very quickly past its inner turning point and then

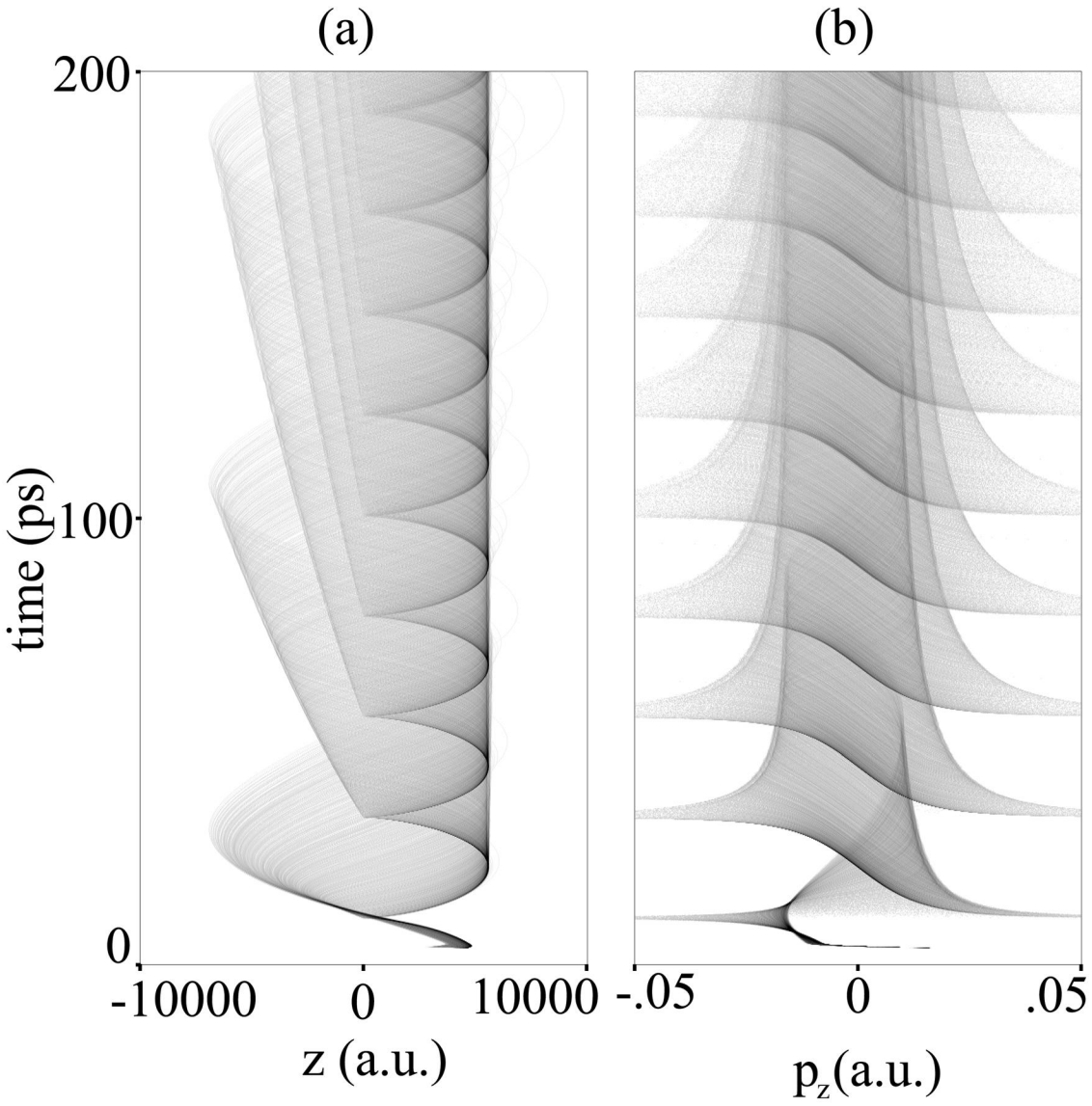

Figure 7.19: Classical position and momentum distributions measured along the $\hat{z}$ axis as functions of time for the magic kick simulation shown in figure 7.14. Note the asymmetry in the p_z distribution. The changeover from positive to negative values of momentum is very gradual. The switch from negative to positive values of momentum however occurs almost instantaneously.

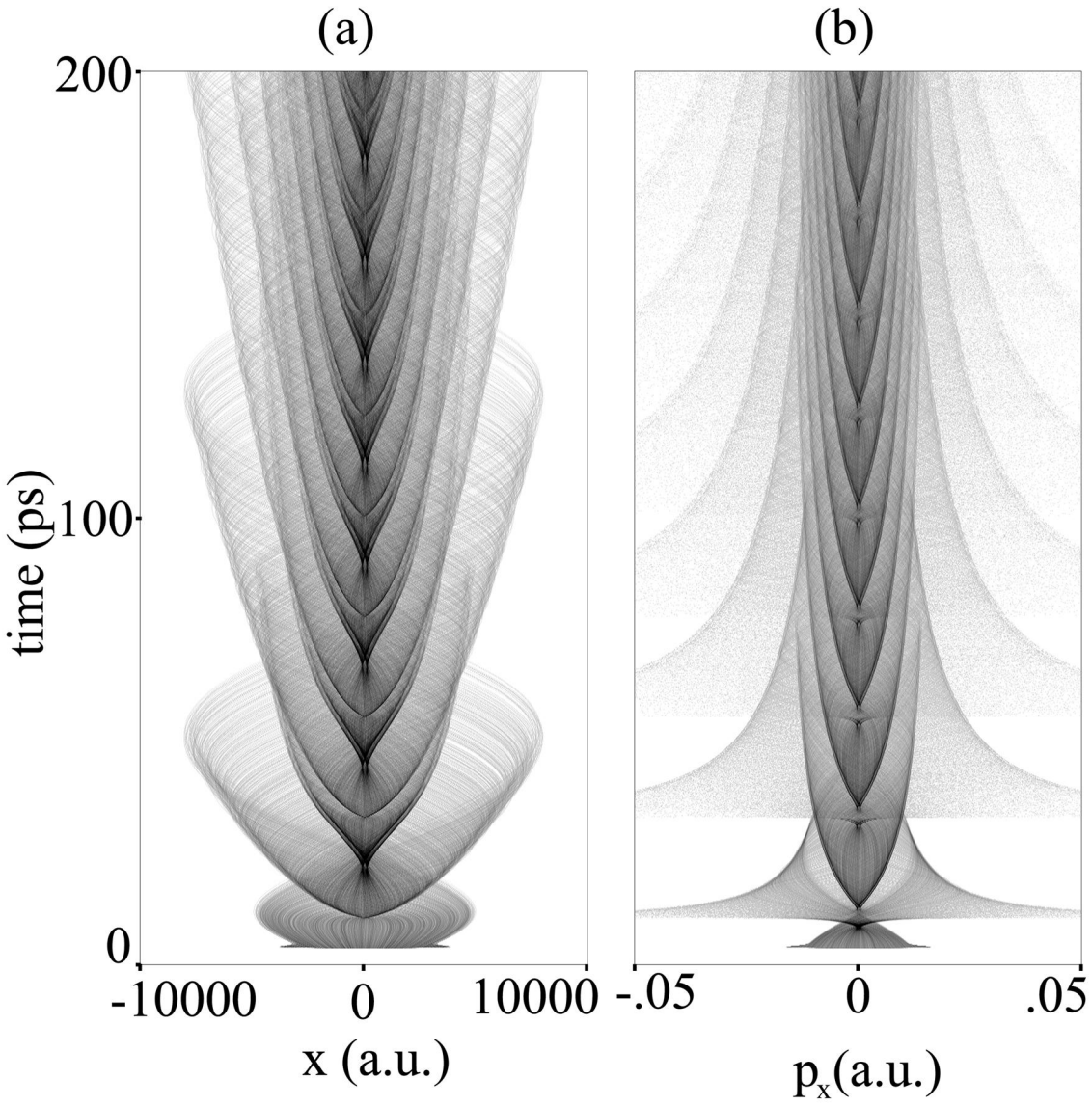

Figure 7.20: Classical position and momentum distributions measured along the $\hat{x}$ axis as functions of time for the magic kick strength simulation shown in figure 7.14. Note that the distributions are symmetric about $x = 0$. Therefore, there is no net motion of the electron distribution along the $\hat{x}$ axis.

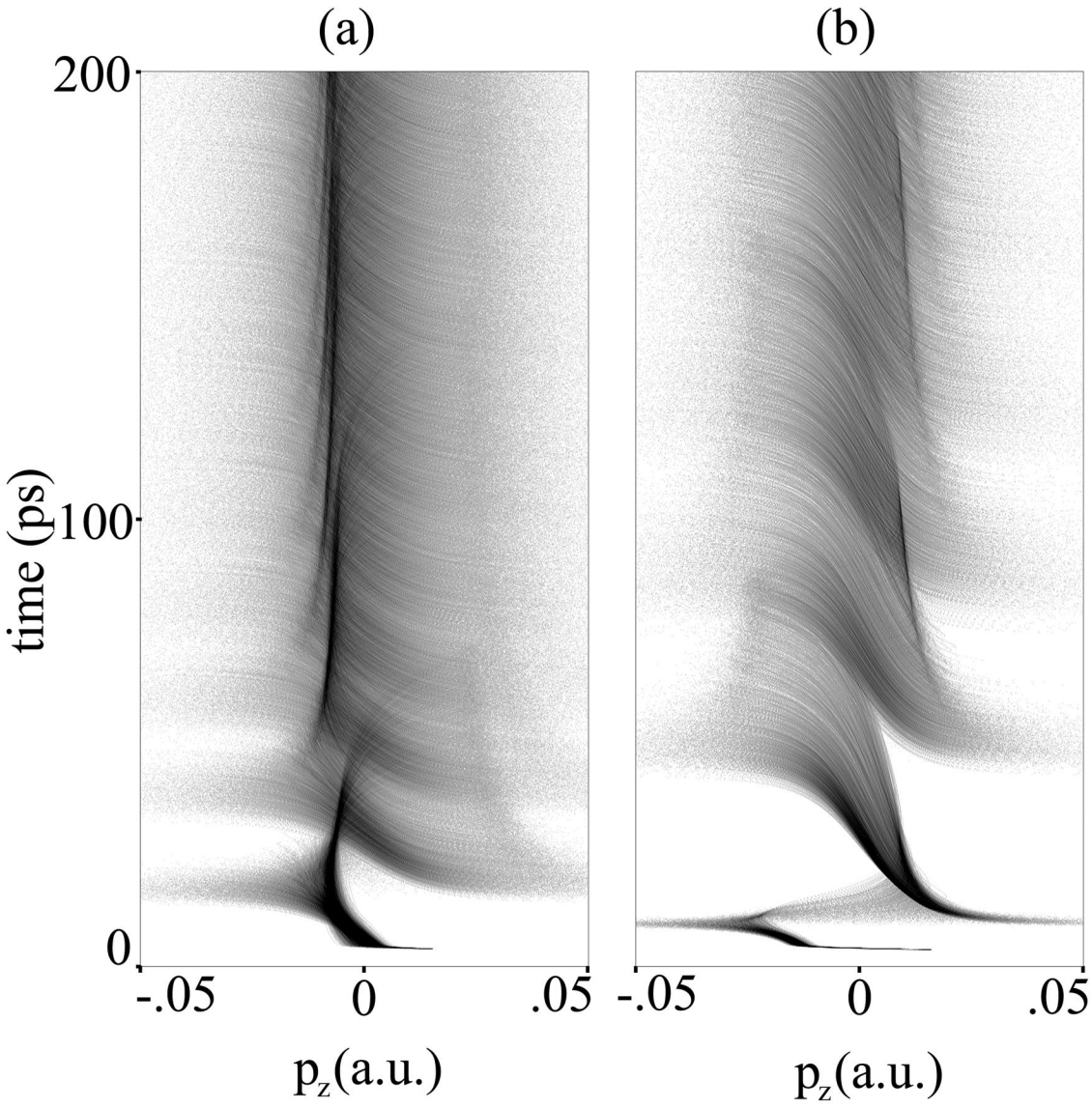

Figure 7.21: $\hat{z}$ momentum distributions as functions of time for the weak kick and strong kick regimes. (a) The weak kick case (HCP maximum field of 3 kV/cm). (b) The strong kick case (HCP maximum field of 5.5 kV/cm). All time dependent features wash out fairly quickly compared to the magic kick case shown in figure 7.19.

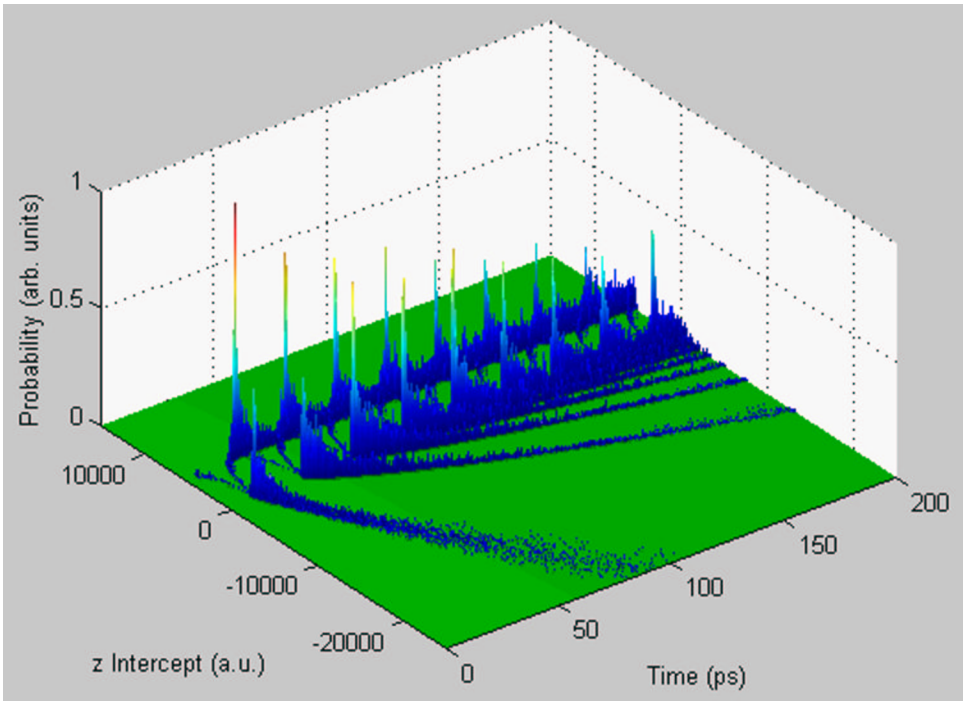

Figure 7.22: Probability distribution of z intercepts as a function of z value and t for the magic kick case. Almost all the electron orbits cross the $+\hat{z}$ axis at roughly the same value of $+z$. However, a significant fraction cross the $+\hat{z}$ axis at roughly the same time as well.

much more slowly through its outer turning point [12]. For a low ℓ Rydberg orbit oriented along the $\hat{z}$ axis with the outer turning point of its orbit along $+\hat{z}$, the change in the $\hat{z}$ component of the momentum from large negative to large positive values occurs very quickly. In contrast, the change from positive p_z to negative p_z is much slower. This can be seen by watching the low ℓ orbits oriented along the $\hat{z}$ axis present in figure 7.13.

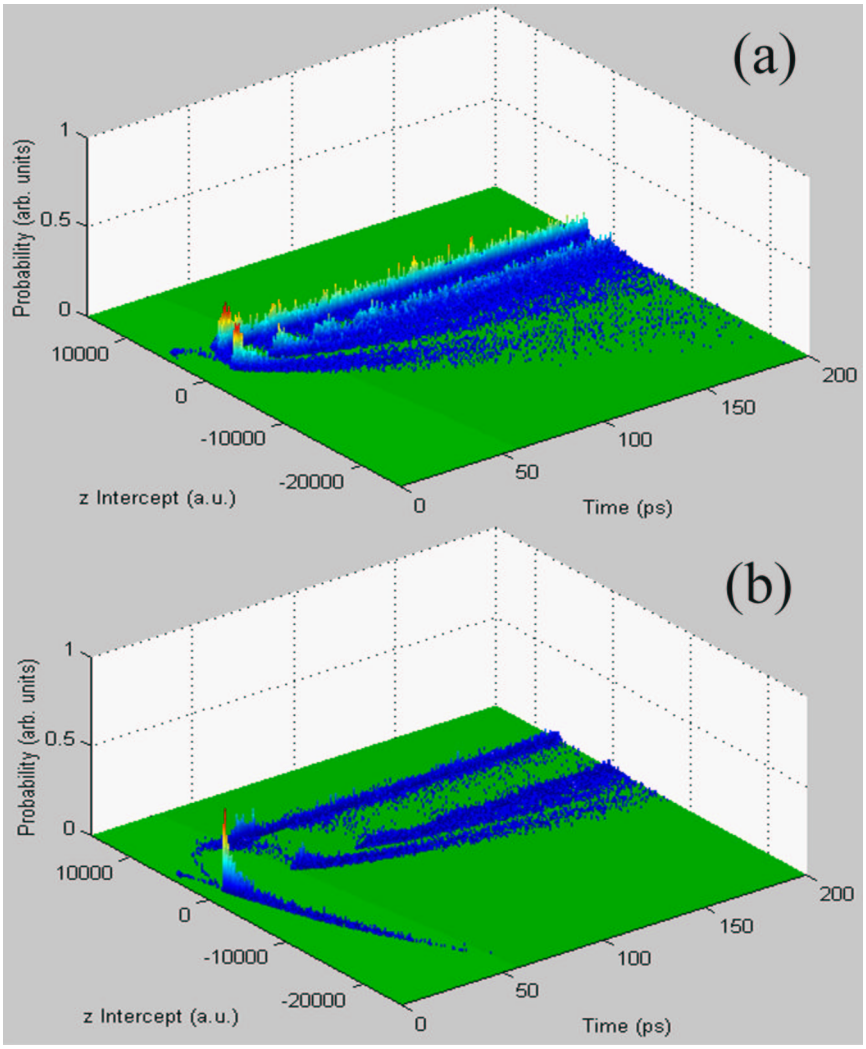

Figure 7.23: Probability distribution of z intercepts as a function of z value and t for (a) the weak kick case, and (b) the strong kick case. Even though many of the electron orbits cross the $+\hat{z}$ axis at roughly the same value of $+z$, *when* they cross the axis is not correlated in either case.

7.3.4 z Intercept Information

For a HCP kick in the $-\hat{z}$ direction, a maxima in the electron probability distribution occurs along the $+\hat{z}$ axis. Therefore, investigating the time and location of when each orbit crosses the $+\hat{z}$ axis yields some information about the degree of electron localization. Figure 7.22 is a density plot which shows when and where each orbit crosses the $\hat{z}$ axis in the magic kick case. Almost all electron orbits cross the $+\hat{z}$ axis in roughly the same location ($x = 0$, $y = 0$, and $z = z_{int}$). This is expected due to the analysis presented in section 7.2.6. However, *only* in the magic kick case do a large portion of the orbits cross the $+\hat{z}$ at approximately the same time as well. This is seen in figure 7.22 by the peak in probability which occurs for $z_{int} \approx 4600$ a.u. at 23 ps, 46 ps, 69 ps, and so on. This does not occur in either the weak or strong kick scenarios as shown in figure 7.23. Only the conditions which are defined in the magic kick case are consistent with a 3-D localized wavepacket.

7.3.5 Static Fields

The structure of the classical simulation program allows study of electron motion in any combination of electric fields and pulses. In the previous sections, only the effect of a single HCP field along the $\hat{z}$ direction is considered. One complication which can be added to the system is the application of a static field. It has been shown that it is possible to achieve some degree of 3-D wavepacket localization by exciting

an extremal red or blue Stark state and then applying a HCP kick to the state [9]. Instead of simulating a HCP interacting with an eigenstate of the Stark basis, in this section we simulate a Stark continuum wavepacket interacting with a HCP kick. The wavepacket has energy E above the classical field ionization limit, but below the field free continuum limit. The HCP recombine a portion of the initial state, creating a recombined wavepacket [10]. We investigate the amount of localization present in the recombined wavepacket as a function of kick strength and the angle between the HCP and the static field.

The static field breaks the spherical symmetry of the problem. Now, the initial launch angle, the static field direction, and the HCP field direction must be taken into account. As was shown in chapter 4, the orientations of the various fields have large influences on the subsequent electron motion. We arbitrarily choose the static field to be along the $+\hat{z}$ axis. We then simulate the motion of an electronic wavepacket in the static field after it feels a HCP kick along some axis. Again, the choice of coordinate systems is arbitrary and has no effect on the problem, however the *relative* angle between the HCP kick and the static field axis is important.

Shown in figures 7.24, 7.25, and 7.26 are movies of an electron distribution interacting with both a HCP and a static field. In all three cases, the initial state has energy centered around the location of the $n = 35$ state in zero field ($E_0 \approx -90$ cm^{-1}). A 450 V/cm static field is present in the $+\hat{z}$ direction in all three movies. The HCP field has

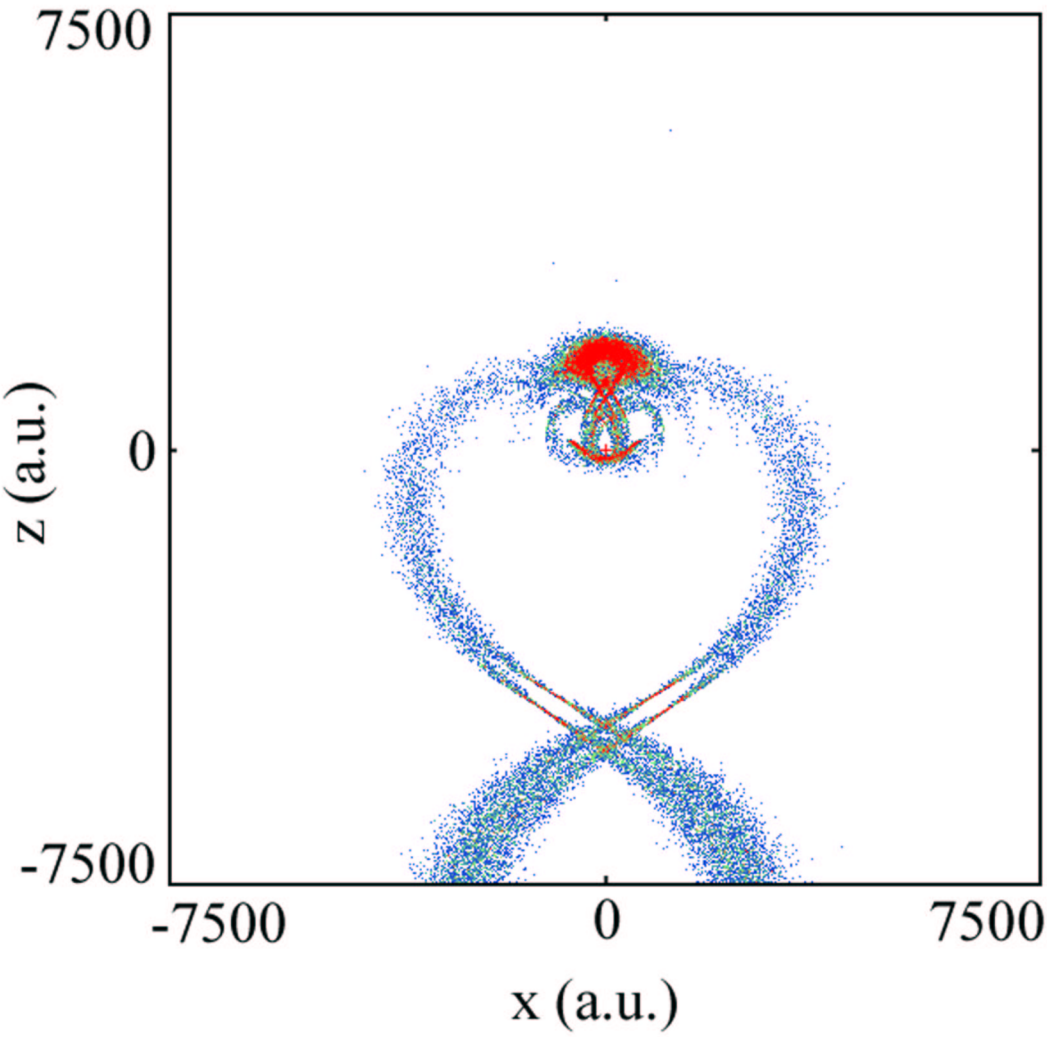

Figure 7.24: One frame from a movie of classical electron probability density as a function of time. The simulation which creates this movie consists of 25 000 individual electron trajectories. Each electron is launched with energy chosen from a Gaussian distribution centered at the zero field $n = 35$ bound state. A 450 V/cm static field is present and directed along $+\hat{z}$. Each electron has $\ell = \pm 2, m = 0$ and is launched from the inner turning point of its orbit. A HCP of maximum field 3 kV/cm interacts with the electrons 4 ps after the launch. The simulation runs for 100 ps and is 15 000 atomic units on a side. Red represents regions with greater electron probability density. A red box appears around the edge of the frame when the HCP field is at its maximum value.

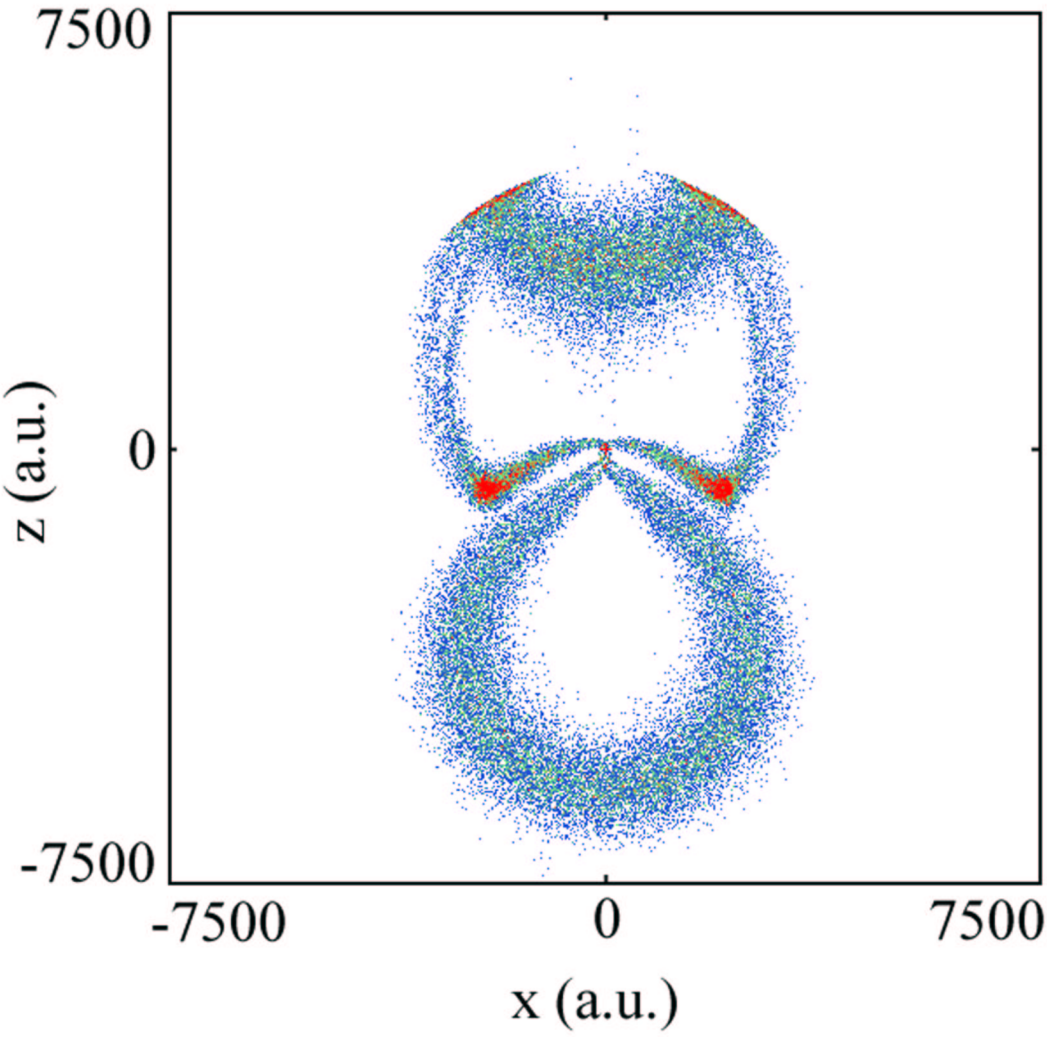

Figure 7.25: One frame from a movie of classical electron probability density as a function of time. The simulation which creates this movie consists of 25 000 individual electron trajectories. The initial conditions are the same as those in figure 7.24. The HCP field is oriented in the $-\hat{z}$ direction.

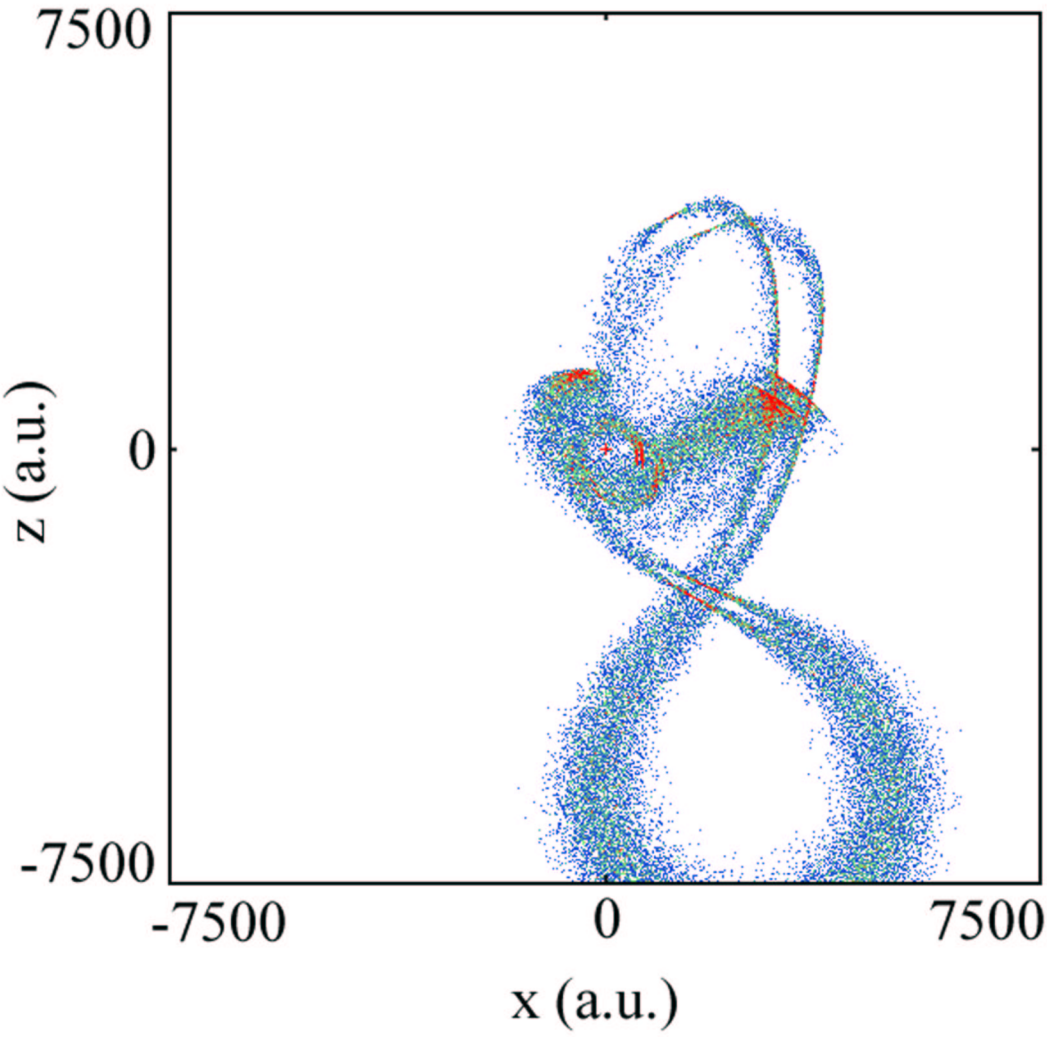

Figure 7.26: One frame from a movie of classical electron probability density as a function of time. The simulation which creates this movie consists of 25 000 individual electron trajectories. The initial conditions are the same as those in figure 7.24. The HCP field is oriented in the $+\hat{x}$ direction.

a maximum strength of 3 kV/cm. In figure 7.24, the HCP impulse is directed along the $-\hat{z}$ axis. In figure 7.25, the HCP impulse is directed along the $+\hat{z}$ axis, and in figure 7.26, the HCP impulse is along $+\hat{x}$. In each case, the movie shows the classical electron probability density as a function of time for $0 \leq t \leq 100$ ps. A red border appears around the edge of the frame in which the influence of the HCP field is maximum. Qualitative information can be gained from these distributions, such as the net value of the momentum along a given axis. Some amount of localization occurs in each case, however the amount of localization present in the static field simulations is significantly less than was observed in the zero field magic kick case.

7.3.6 Multiple HCPs

Another interesting situation which can be modeled by the classical calculations is the case of two separate HCP fields interacting with an atomic system. Often, experiments are performed which use two HCP fields. Frequently the second pulse is used as a probe of the dynamics created by the first one. Typically, the second HCP is used to perform IMR or some other measurement technique. Therefore, only the final energy of the system is measured at a time after both HCP interactions. However, interesting possibilities exist for manipulation of electron dynamics with two (or more) HCP fields [15]. One example is the creation of a "circular" electron state. A circular state is superposition of phase locked eigenstates with maximal ℓ and m values [16]. Classically,

a circular state resembles the Bohr picture of an electron orbit. Circular type states have been produced by exciting an extremal Stark state in a fixed n manifold [17]. However, these states are stationary. Some theoretical work has been done into possible creation of circular wavepackets [18], however such states have yet to be experimentally verified.

One possible method we propose for the creation of a circular state begins by localizing an electron away from the atomic core. This can be done through HCP induced recombination, as presented in chapter 6. Then, a second kick orthogonal to the first one, may set the localized distribution in circular motion around the atomic core. A simulation of this process is shown in figure 7.27. Even though some elements of the circular state are visible in the simulation, the variation in the energy and trajectory of each electron orbit make the creation of an "electron ball" circling the atomic core somewhat too simplistic of a picture.

7.3.7 Conclusions

The calculations presented in this section characterize a method of creating a localized electron distribution far from the atomic core with an impulsive field. Classical calculations provide an intuitive description of the dynamics of the localized distribution. These calculations show that up to 1/2 of the bound electron probability density can be localized in an extremely small region in space at a specific times. Furthermore, the calculations suggest several possible future experiments including the creation of a

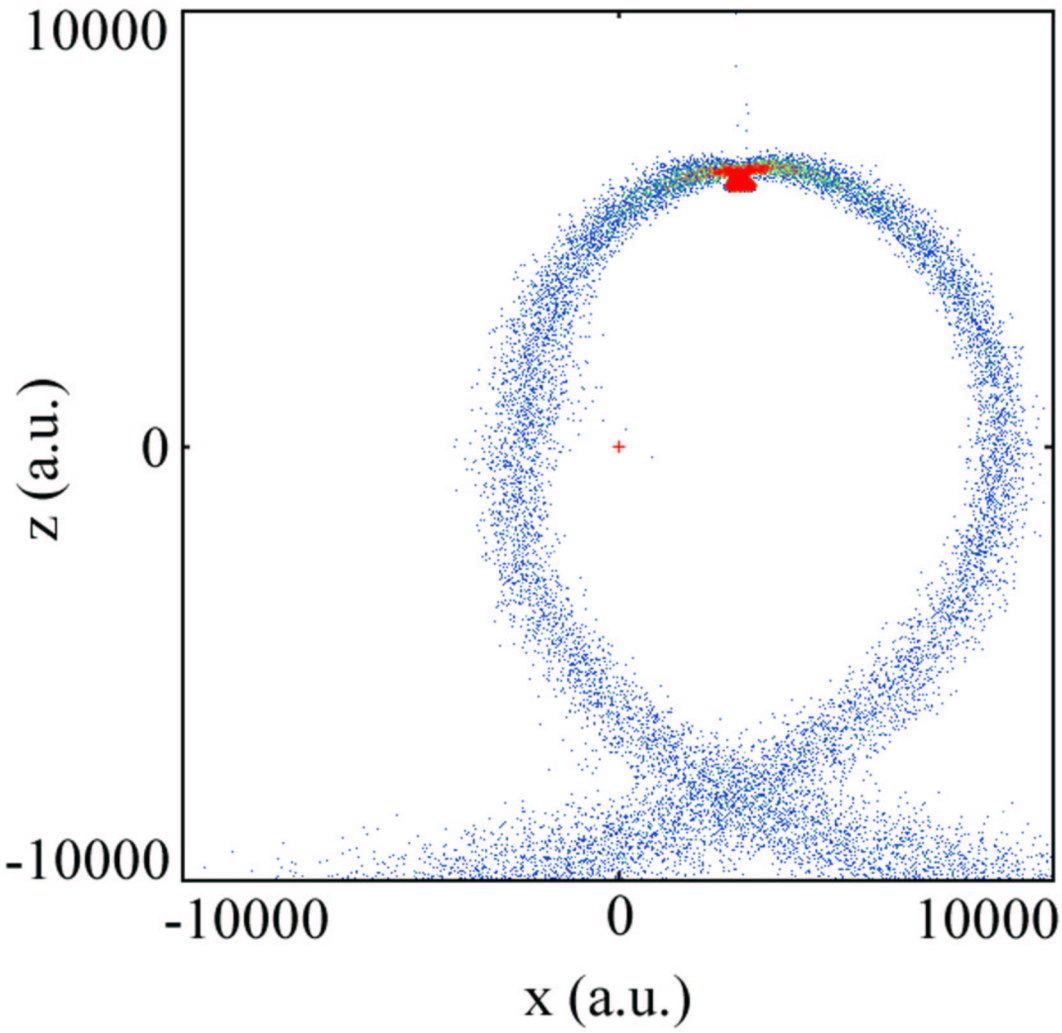

Figure 7.27: One frame from a movie of classical electron probability density as a function of time. The initial conditions are the same as those in figure 7.24. Two HCP fields interact with the system. The first HCP arrives 3 ps after launch of the electrons and is at the magic kick strength. A localization of the electron probability density is then formed on the $+\hat{z}$ axis at t=22 ps. At that time, a second HCP field of 2 kV/cm oriented in the $+\hat{x}$ direction interacts with the electrons. The time of the maximum of each HCP field is represented by a red box around the edge of the frame. The simulation is 20 000 atomic units on a side and runs for 100 ps.

circular state and the observation of interesting static field wavepacket dynamics. The simulations presented in this section show that HCP induced electron - ion recombination can produce a wavepacket localized in 3-D in a field free environment. Since this localization method is free of the complications presented by an applied static field, HCP recombination may be an attractive method to create localized wavepackets for future experiments in the area of quantum control.

Bibliography

[1] L.S. Brown, *Am. J. Phys.* **41**, 525 (1973).

[2] J.A. Yeazell and C.R. Stroud, Jr., *Phys. Rev. A* **35**, 2806 (1987); J.A. Yeazell and C.R. Stroud, Jr., *Phys. Rev. Lett.* **60**, 1494 (1988).

[3] G. Alber, H. Ritsch, and P. Zoller, *Phys. Rev. A* **34**, 1058 (1986); A. ten Wolde *et al. Phys. Rev. Lett.* **61**, 2099 (1988); J.G. Zeibel and R.R. Jones, *J. Phys. B* **34**, 1213 (2001).

[4] Z.D. Gaeta, M.W. Noel, and C.R. Stroud, Jr., *Phys. Rev. Lett.* **73**, 636 (1994); I. Bialynicki-Birula, M. Kaliński, and J.H. Eberly, *ibid.* **73**, 1777 (1994); R. Bluhm, V.A. Kostelecký, and B. Tudose, *Phys. Rev. A* **52**, 2234 (1995);

[5] M. Shapiro and P. Brumer, *J. Chem. Phys.* **97**, 6259 (1992).

[6] R.G. Littlejohn, *Phys. Rev. Lett.* **56**, 2000 (1986); M. Mallalieu and C.R. Stroud Jr., *Phys. Rev. A* **51**, 1827 (1995); R. Bluhm and V.A. Kostelecký, *Phys. Lett. A* **200**, 308 (1995); P. Bellomo, C.R. Stroud Jr., D. Farrelly, and T. Uzer, *ibid.*

58, 3896 (1998); J.A. Ramswell, V.G. Stavros, Q. Hong, and H.H. Fielding, *Phil. Trans. R. Soc. Lond. A* **356**, 363 (1998).

[7] C.O. Reinhold, J. Burgdörfer, M.T. Frey, and F.B. Dunning, *Phys. Rev. A* **54**, R33 (1996); M.T. Frey, F.B. Dunning, C.O. Reinhold, S. Yoshida, and J. Burgdörfer, *ibid.* **59**, 1434 (1999).

[8] S. Yoshida, C.O. Reinhold, and J. Burgdörfer, *Phys. Rev. Lett.* **84**, 1602 (2000).

[9] J. Bromage and C.R. Stroud, Jr., *Phys. Rev. Lett.* **83**, 4963 (1999).

[10] T.J. Bensky, M.B. Campbell, and R.R. Jones, *Phys. Rev. Lett.* **81**, 3112 (1998).

[11] F. Robicheaux, *Phys. Rev. A* **60**, 431 (1999).

[12] H. Goldstein, *Classical Mechanics, 2nd ed.*, Addison-Wesley Publishing Co., Reading, Massachusetts, (1980).

[13] See also the calculations presented in chapter 6.

[14] For a full description of how each successive electron position is determined see appendix B.

[15] B.E. Tannian *et al.*, *Phys. Rev. A*, **62**, 043402 (2001); B.E. Tannian *et. al.*, *ibid.* **64**, 021404 (2001); M. Klews and W. Schweizer, *ibid.* **64**, 053403 (2001).

[16] R. Bluhm and V.A. Kostelecký, *Phys. Rev. A* **51**, 4767 (1995).

[17] R.G. Hulet and D. Kleppner, *Phys. Rev. Lett.* **51**, 1430 (1983); D. Delande and J.C.Gay, *Europhys. Lett.* **5**, 303 (1988).

[18] Z. D. Gaeta, M. Noel, and C.R. Stroud, *Phys. Rev. Lett.* **73**, 636 (1994).

Chapter 8

Conclusions

Developed in this thesis are three experiments in which HCP fields are used to manipulate the environment of selected atomic systems. The three experiments study a variety of different atomic systems which are each relevant to real-world physical processes. In performing these experiments, we have advanced the technique of HCP assisted recombination in chapters 4 and 6, used HCPs to alter the dynamics of novel wavepackets in chapters 5 and 6, and developed the technique of dither impulse momentum retrieval.

Orthogonal Recombination

In this experiment, HCP fields are used to control the rates of artificial electron - ion recombination in a static electric field. For weak HCP fields ($A < 0.03$), the probability for recombination increases if the HCP field is oriented perpendicular to the static field.

The hydrogenic nature of high-m states created by the orthogonal geometry prevents sampling of the saddle point in the Stark potential by orbits located on the "uphill" side of the atom. This effect is important in properly determining the total electron - ion recombination rates in a microfield plasma environment.

Suppression of Autoionization

In chapter 5, we investigate how an autoionizing system responds to HCP interaction. Three separate configurations were investigated. Each configuration is representative of a time dependent field configuration present in the microfield environment of a neutral plasma. We find that HCP fields oriented parallel or antiparallel to a weak static field fail to stabilize the autoionizing system. Even though the HCP field populates states with high ℓ, the mixing of the angular momentum states in the static field ensures that each state contains some low ℓ character and is therefore not stable against autoionization. In contrast, HCP fields oriented orthogonal to a weak static field do suppress autoionization by approximately 10% by populating states with high values of m. These high m states are stable against autoionization, however the HCPs are only able to promote a small fraction of the initial distribution to high enough m to be stabilized. Even though stronger orthogonal HCP fields do promote a larger portion of the initial population to high m states, the amount of population which can be stabilized is capped due to direct ionization of the Rydberg electron by the HCP field.

Even so, the use of orthogonally oriented HCP fields as a probe for Rydberg electron dynamics in an autoionizing system may be possible.

Recombined Wavepacket Dynamics

In chapter 6, a HCP recombines a portion of an outgoing continuum wavepacket. The momentum distribution of the resulting recombined wavepacket is then probed by a second HCP through the lock-in IMR technique introduced in chapter 3. Results show momentum distributions consistent with the formation of a highly localized 3-D electron distribution located far from the atomic core. If HCP induced electron - ion recombination can be used to create spatially localized 3-D electronic wavepackets in a zero static field environment, then this method may be used as a starting point for a variety of quantum control experiments as well as a method to investigate the classical limit state of an atom.

Although a quantum mechanical simulation of the recombined wavepacket dynamics is technically possible for short times, the extremely large (infinite) number of states makes such an approach difficult. Instead, the large state density make classical (CTMC) simulations applicable. These simulations indicate that up to half of the bound (recombined) distribution can be localized in a small area of space. Furthermore, only a small range of HCP field strengths will result in wavepacket localization. This range is determined by the initial energy of the continuum wavepacket and the time

delay between the launch of the continuum packet and the arrival of the recombining HCP field. Analytical calculations are performed in chapter 7 which investigate how varying each of these initial parameters affects the degree of localization.

Future Projects

Research into HCP control of wavepacket dynamics is ongoing. Several experiments involving the manipulation of the three dimensionally localized wavepacket characterized in chapter 6 are possible. The realization of a circular, or planetary state can be attempted, as well as experiments which probe the correspondence between quantum mechanics and classical dynamics. Experiments involving quantum control of physical processes are facilitated by first creating a phase space localized wavepacket in a field free environment. When a series of control pulses is applied to this distribution, all portions of the distribution are affected in roughly the same manner. Localization through recombination may be a simple method of generating such an initial wavepacket.

In all the experiments presented in this thesis, the capabilities of the HCP field have been extended into new regimes. HCPs can be used to affect the environment of an atomic system in an impulsive way, as well as to measure the resulting dynamics. Overall, the experiments presented add to the general understanding of electron dynamics associated with physical processes.

Appendix A

Measuring Wavepacket Dynamics: Radial Rydberg Wavepacket Maps

A.1 Introduction

Results from the experiment presented in this appendix demonstrate the large parameter space of wavepacket dynamics which we can investigate through HCP interaction. Many individual radial Rydberg wavepackets are created, each with a slightly different average energy. The evolution of each wavepacket is then measured. Overall trends in the evolution of an entire class of wavepackets are thereby recovered. Unlike the experiments presented in chapters 4, 5, and 6, the HCP is used solely to *probe* the dynamics of an existing wavepacket, rather than to manipulate the environment in which

the wavepacket evolves.

Due to their high density of electronic states and long coherence times, isolated Rydberg atoms are pristine systems for investigating the correspondence between quantum and classical physics and for testing fundamental notions relevant to the manipulation and observation of quantum dynamics. Indeed, over the past two decades, a great number of experimental and theoretical studies of various aspects of Rydberg wavepacket dynamics have appeared in the literature [1]. One topic of continuing interest is the periodic "collapse" and "revival" of localized wavepacket structures as they move in the anharmonic Coulomb binding potential [2–6].

In this appendix, we examine the global revival structure for radial wavepackets, coherent superpositions of Rydberg states with different principal, but identical angular momentum quantum numbers. Previous experimental works have focussed on the revival properties of very specific wavepackets, each having a particular average energy and number of superimposed eigenstates [4,5]. Theoretical investigations have provided straightforward formulae for predicting the times at which fractional [3], integer [2], and "super" revivals [6] occur, but provide only limited information regarding the evolution of the wavepacket at times near the revivals. We have experimentally monitored the temporal evolution of an entire class of radial wavepackets over a continuous range of binding energies from 210 cm^{-1} to 10 cm^{-1} to explore the revival phenomena from a broader perspective. In addition, we present a time and energy scaling which aids in

the interpretation of the 3-dimensional wavepacket maps.

A.2 Experimental Details

In the experiment, a 5 ns dye laser promotes Ca atoms in a thermal atomic beam from the $4s4s$ ground state to an intermediate $4s4p$ level. The atoms are then exposed to a 1 ps laser pulse which transfers population from the $4s4p$ state to a coherent superposition of $4snd$ Rydberg levels. Because the $4s4p$ wavefunction has non-negligible amplitude only within a few atomic units of the Ca^+ ionic core, the wavepacket produced by the ps laser pulse is initially localized at a small radius. However, as time evolves, the wavepacket moves radially outward from the ionic core, reflects from the Coulomb potential at large radius, and returns to the nucleus. The anharmonicity of the Coulomb potential leads to spreading, or collapse, of the wavepacket and its eventual partial rephasing at fractional or integer revival times. The dynamical collapse and revival of the wavepacket is the principal interest of this appendix.

While several experimental methods now exist for viewing the complete motion of radial wavepackets [1, 8–12], we are most interested in the probability for finding the wavepacket at its initial location - near the ionic core. The time dependent probability for finding the electron near the nucleus, i.e. the recurrence strength, is monitored by partially ionizing the wavepacket with a 1 ps, unipolar HCP [13, 14]. Although HCP ionization is sensitive to the momentum of the electron, rather than its position, the

recurrence strength can still be obtained from the measurement [15, 16]. In relatively low HCP fields, ionization can occur if the electron has high momentum in the direction of the HCP "kick." For weak kicks, the electron only has sufficient momentum to ionize if it is near the nucleus when it is exposed to the HCP [13]. By monitoring the variation in the HCP ionization yield as a function of delay between the 1 ps laser pulse and the HCP, we obtain the time dependent recurrence strength.

The experimental apparatus and basic procedure are described in detail in chapter 2. Briefly, the 1 ps laser pulse is generated by frequency doubling the 120 fs, 787 nm output of an amplified Ti:Sapphire laser in a 2.0 cm long potassium dihydrogen phosphate (KDP) crystal. By tilting the entrance face of the crystal relative to the 787 nm fundamental beam, the frequency of the 1 ps pulse can be tuned to excite Rydberg wavepackets with average binding energies between 210 cm^{-1} and 10 cm^{-1}. The FWHM of the spectral bandwidth of the doubled light is approximately 17 cm^{-1}, independent of its central frequency. The HCP is generated and calibrated through the methods introduced in chapter 3. Before interacting with the atoms the HCP passes through a second GaAs wafer that acts to attenuate non-unipolar components of the pulse [17].

The ps laser beam and the ps HCP interact with the atoms between two parallel capacitor plates that are separated by approximately 1.2 cm (see figure 2.9). The ps beams counter-propagate beneath a 2.5 cm x 0.3 cm slit in the upper plate. Ions that

are formed through HCP ionization are pushed towards a single shot detector located immediately above the field plates [18]. Since atoms at different positions beneath the slit experience different relative delays between the ps laser pulse and the HCP, the position dependent ionization yield is directly related to the time dependent recurrence strength for the wavepacket [18]. Recurrence maps are produced by recording the time dependent recurrence signal as a function of the frequency of the ps laser pulse, i.e. the wavepacket binding energy.

A.3 Results

A HCP ionization vs. time delay curve for a wavepacket with a binding energy of $E = 122.3$ cm^{-1}, kicked by a HCP with an amplitude, $F_{HCP} = 5.5$ kV/cm, is shown in figure A.1. Clearly some ionization of the wavepacket occurs independent of its evolving location and structure. A better measure of the wavepacket recurrence strength is obtained from the normalized signal variation, $S_E(\tau)$. $S_E(\tau)$ is generated by first subtracting the *delay-averaged* ionization yield from the *delay-dependent* ionization signal, and then dividing that difference by the averaged yield. To accurately monitor changes in the wavepacket probability distribution near the nucleus, it is also important to maintain the HCP ionization yield at a level that is much less than unity. Over the range of binding energies studied, the HCP field amplitude, F_{HCP} that produces a few percent ionization for a given Rydberg eigenstate, $n\ell$, scales as n^{-2}, i.e. linearly with

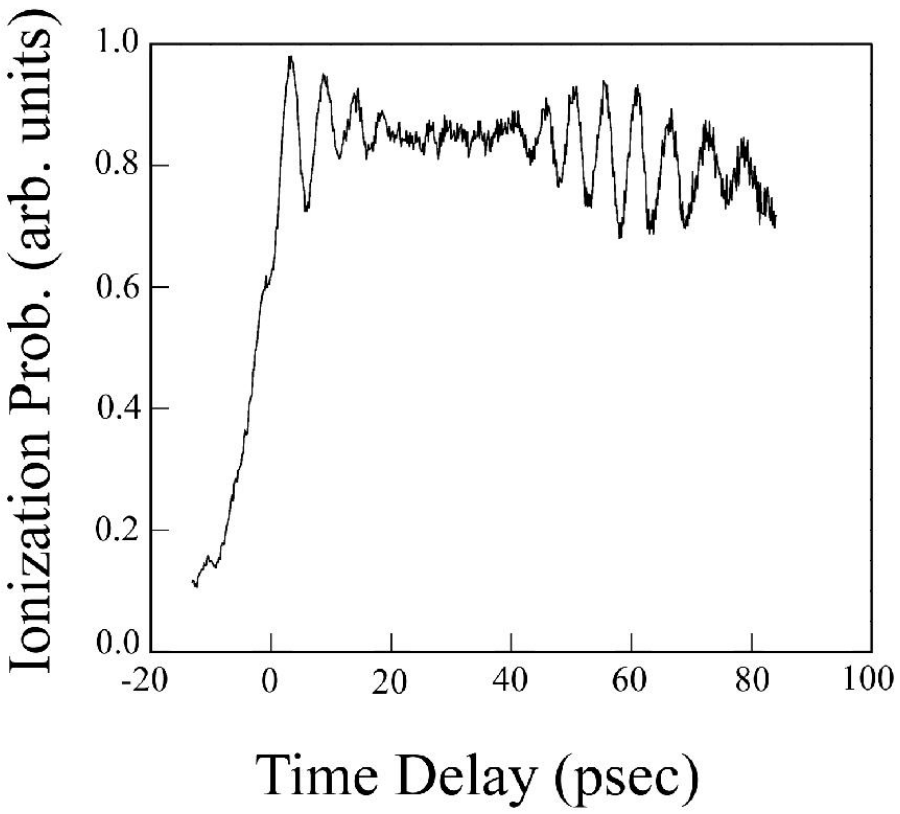

Figure A.1: HCP ionization probability as a function of delay following the excitation of a radial wavepacket with average principal quantum number, $N = 29.95$. The HCP field amplitude is approximately 5.5 kV/cm.

binding energy. [13] Therefore, F_{HCP} is varied linearly with the frequency of the ps laser to generate consistent recurrence strength curves for wavepackets with different binding energies.

Recurrence maps are produced by combining recurrence data at fixed binding energy, E, into a 2-dimensional array. A typical map is shown as a density plot in figure A.2 with dark areas representing regions of high recurrence probability. At early times

and at all energies, strong oscillations in the recurrence strength are evident as the radial wavepacket moves between the inner and outer turning points of the Coulomb potential. The recurrence strength reaches a maximum when the wavepacket is closest to the ionic core. The Kepler period of the wavepacket oscillations increases significantly, $\tau_K = 2\pi N^3$, as the classically allowed radial region increases with decreasing binding energy. We define the average principal quantum number, N, in terms of the wavepacket binding energy $N = \frac{1}{\sqrt{2E}}$. The fundamental frequency of the Kepler motion of the wavepacket is the energy difference between adjacent Rydberg eigenstates in the wavepacket, $\omega_K \approx N^{-3}$. After a few periods, the wavepacket disperses and only minimal amplitude modulations appear in the recurrence map.

At longer times the wavepacket rephases and strong amplitude modulations reappear in the recurrence map. These "integer" wavepacket revivals have been studied in detail and occur at regular intervals separated by the revival period, $\tau_{rev} = 2\pi N^4/3$ [6]. Three different integer revivals are observed for the more tightly bound wavepackets with low values of N. Smaller amplitude recurrence modulations due to partial rephasing of the packet at "fractional revival" times are apparent at times between the integer revivals [3, 5]. However, in general these higher frequency oscillations are not well resolved with the 1 ps pump and probe pulse durations used in this experiment.

The recurrence modulations near the integer revival times have an energy dependence that is strikingly different from that during the initial "primary" Kepler orbits.

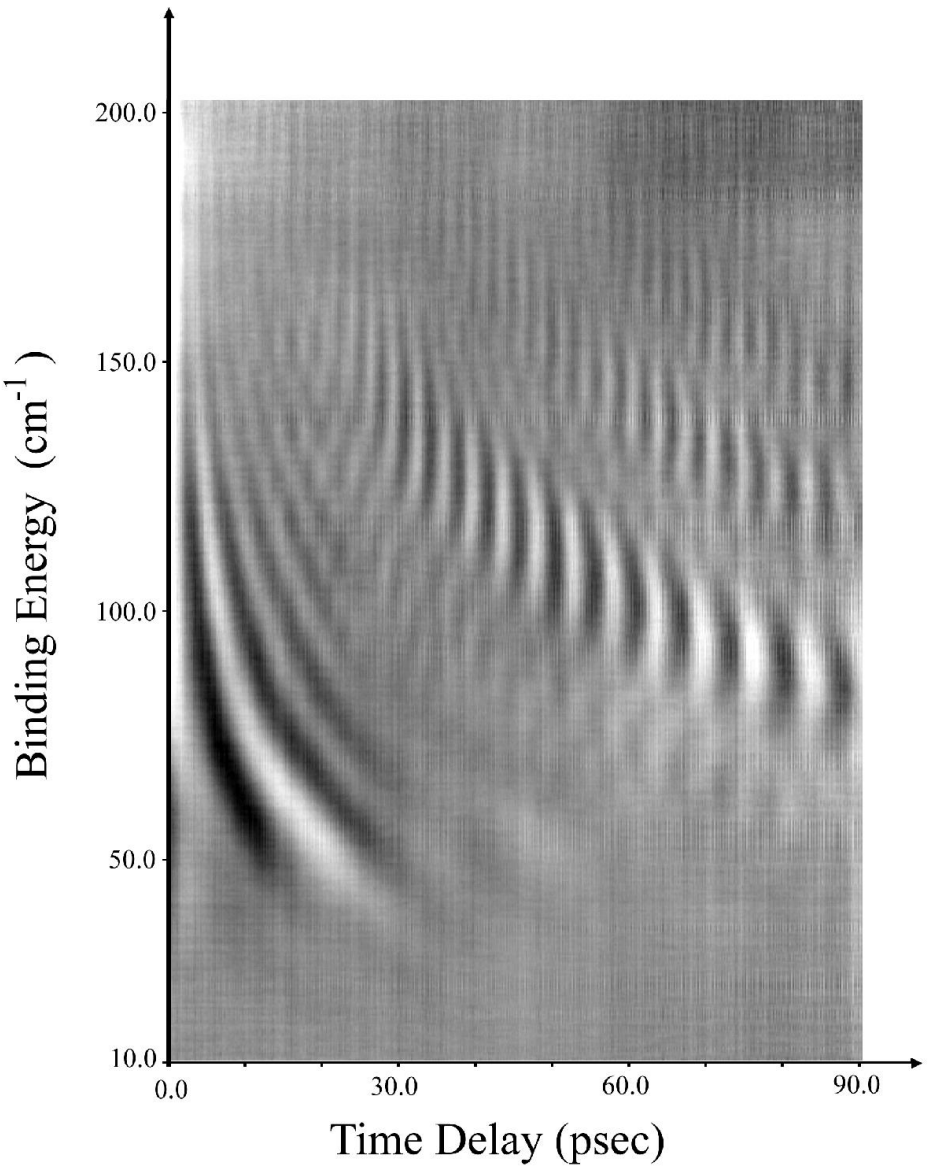

Figure A.2: Map of recurrence strength vs. delay vs. binding energy for radial wavepackets produced using a laser pulse with a fixed bandwidth of 17 cm^{-1} as described in the text. Dark(light) regions denote high(low) recurrence strength.

The temporal location of a specific *primary* recurrence maximum increases in direct proportion to the Kepler period with decreasing binding energy, i.e. increasing N. However, the recurrence maxima near each *revival* time appear to have the opposite dependence, moving toward shorter times with increasing values of N. The difference in the energy dependences of the primary and revival recurrences suggest that there are fundamental distinctions between these two phenomena, in spite of the fact that the maxima have similar amplitudes and modulation periods.

In an attempt to study the complex, energy dependent revival phenomena in more detail, we use scaled coordinates for displaying the recurrence maps. These scaled maps are reminiscent of the recurrence maps generated via Fourier transforming frequency domain Stark spectra in scaled energy coordinates [19–21]. We define an energy-dependent scaled-time coordinate, $\tau = t/2\pi N^3$ and a scaled-energy coordinate, $\epsilon = N^{-3}/\gamma$, where γ is the FWHM of the excitation laser's frequency spectrum. The physical significance of the two coordinates is straightforward. τ counts the number of Kepler periods for a wavepacket at a particular energy, and $1/\epsilon + 1$ is the number of constituent eigenstates in the wavepacket. The recurrence map of figure A.2 is redisplayed in scaled coordinates in figure A.3. As anticipated, the primary recurrences appear as vertical lines on the scaled map, with each line centered at an integer value of τ. However, the full and fractional wavepacket revivals appear along lines that appear to extend radially from the origin.

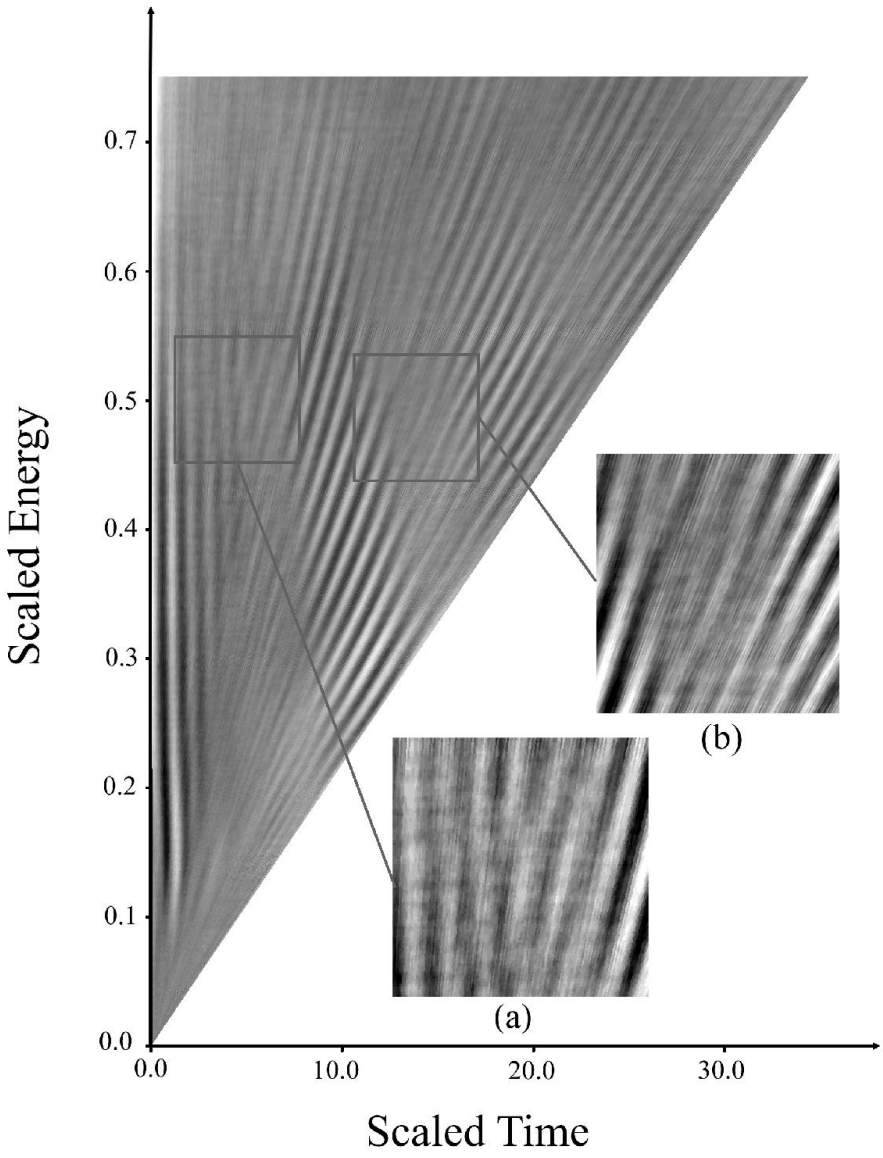

Figure A.3: Recurrence data identical to that shown in Figure A.2 but displayed using scaled coordinates as described in the text. Primary wavepacket recurrences appear as vertical lines at integer values of the Kepler period, while integer and fractional revivals fall along approximately straight lines that pass through the origin. The insets (a) and (b) provide enlarged views of regions of the map where the recurrence strength in single lines bifurcates along additional paths. A different greyscale normalization is used in the insets to improve the visibility of the intermediate strength modulations.

Radial lines of the observed form, $\epsilon = \tau/k,\ k = 1, 2, 3, ..,$ have a simple physical interpretation. A wavepacket with scaled energy ϵ has $1/\epsilon + 1$ constituent eigenstates. Since the approximate energy spacing between adjacent eigenstates is N^{-3}, the energy splitting between the extreme states is $\Delta \cong N^{-3}/\epsilon$. Hence, periodic rephasing of the extreme states occurs over time intervals, $T = 2\pi/\Delta \cong \tau\epsilon$. The kth rephasing of the extreme states occurs when $k = \tau\epsilon$, i.e. when $\epsilon = \tau/k$.

Apparently the fundamental period associated with revival structure is $\epsilon\tau_K$ rather than τ_K, and the energy dependence of both fractional and full revivals is marked by the radial lines in the recurrence map. However, the recurrence strength at different radial lines varies with position within the map, and depends critically on the details of the wavepacket. Bifurcations and coalescence of the recurrence lines can be seen in the insets of figure A.3. It is important to note that while recurrence strength is not uniformly high along the entire length of each radial line in the map, the strong recurrences that are observed always appear along (or very near) these lines.

We can simulate the structure found in the scaled maps by numerically constructing a coherent superposition of Rydberg eigenstates, and then computing the time dependent probability for finding the wavepacket within a small sphere surrounding the ionic core (see figure A.4). A standard Numerov integration algorithm is used to compute the stationary radial eigenfunctions. As in the experiment, the simulations assume that the wavepacket is produced near the ionic core using a transform-limited laser pulse with a

bandwidth, $\gamma = 17$ cm^{-1}. Wavepackets with different scaled-energies are generated by changing the average frequency in the excitation laser pulse, rather than changing γ. The results shown in figure A.4 are obtained assuming a sphere radius of $R = 9$ a.u., but the global properties of the map are insensitive to the precise value of R. Because of the higher temporal resolution available in the simulation, structure associated with fractional as well as full wavepacket revivals is apparent.

An additional feature of the map scaling is that the scaled energy roughly defines the highest fractional revival orders (i.e. smallest fraction 1/2, 1/3, 1/4, ...) that can be observed. The shortest possible period for a partial revival is $\epsilon\tau_K$. So, for example, 1/3 revivals are the fastest periodic features at $\epsilon = 0.33$ while features with periods of $\tau_K/5$ are expected near $\epsilon = 0.2$. These periodicities are more apparent in the simulated results due to the limited experimental resolution described previously.

A.4 Conclusions

In summary, we have investigated the revival structure of radial wavepackets as a function of time and binding energy using HCP ionization as a probe. We introduce a set of scaled coordinates that enables us to distinguish differences between recurrences during primary as opposed to revival orbits. Notably, the energy bandwidth of the packet rather than the inverse Kepler period plays the dominant role in determining the energy dependence of the revival structure.

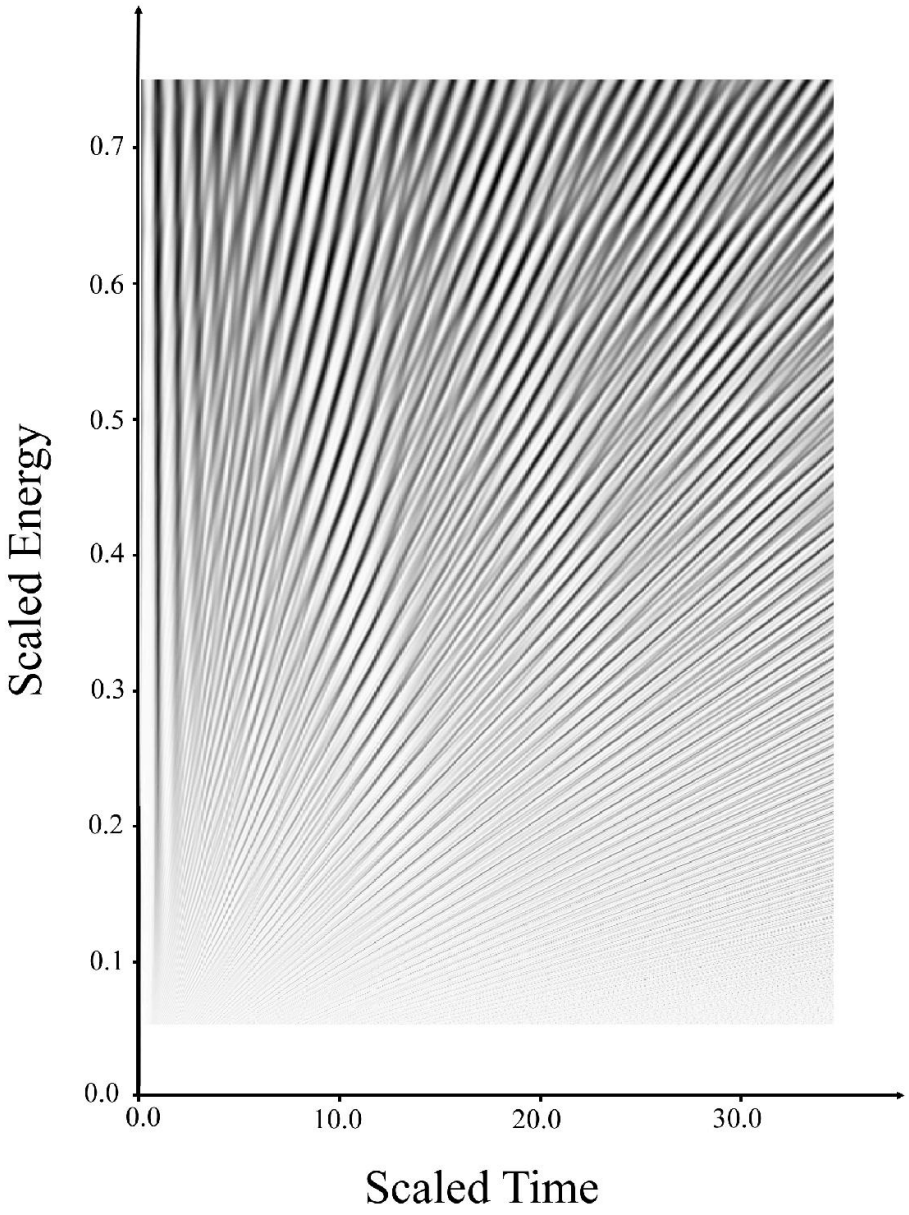

Figure A.4: Numerical simulation of a recurrence map as described in the text. The appearance of the map is very similar to the experimental version shown in figure A.3 with the exception that the recurrence strength has been calculated for much longer time delays at high values of N. Also, fractional revivals are much more clearly seen due to the arbitrarily high temporal resolution of the numerical simulation.

Bibliography

[1] R.R. Jones and L.D. Noordam, *Ad. At. Mol. and Opt. Phys.* **38** 1 (1997) and references therein.

[2] J.R. Parker and C.R. Stroud, *Phys. Rev. Lett.* **56**, 716 (1986).

[3] Ish. Averbukh and N.F. Perelman, *Phys. Lett. A* **139**, 449 (1989).

[4] J.A. Yeazell, M. Mallalieu, and C.R. Stroud, *Phys. Rev. Lett.* **64**, 2007 (1990).

[5] J.A. Yeazell and C.R. Stroud, *Phys. Rev. A* **43**, 5153 (1991).

[6] R. Bluhm and V.A. Kostelecký, *Phys. Rev. A* **51**, 4767 (1995).

[7] A. ten Wolde, L.D. Noordam, A. Lagendijk, and H.B. van Linden van den Heuvell, *Phys. Rev. Lett.* **61**, 2099 (1988).

[8] L.D. Noordam and R.R. Jones, *J. Mod. Opt.* **44**, 2515 (1997) and references therein.

[9] T.C. Weinacht, J. Ahn, and P.H. Bucksbaum, *Phys. Rev. Lett.* **80**, 5508 (1998).

[10] C. Leichtle, W.P. Schleich, I.Sh. Averbukh, and M. Shapiro, *Phys. Rev. Lett.* **80**, 1418 (1998).

[11] R.R. Jones, *Phys. Rev. A* **57**, 446 (1998).

[12] R.R. Jones and M.B. Campbell, *Phys. Rev. A* **61**, 013403 (1999).

[13] R.R. Jones, D. You, and P.H. Bucksbaum, *Phys. Rev. Lett.* **70**, 1236 (1993).

[14] D. You, R.R. Jones, D.R. Dykaar, and P.H. Bucksbaum, *Opt. Lett.* **18**, 290 (1993).

[15] C. Raman, C.W.S. Conover, C.I. Sukenik, and P.H. Bucksbaum, *Phys. Rev. Lett.* **76**, 2436 (1996).

[16] R.R. Jones, *Phys. Rev. Lett.* **76**, 3927 (1996).

[17] N.E. Tielking, T.J. Bensky, and R.R. Jones, *Phys. Rev. A* **51**, 3370 (1995).

[18] M.B. Campbell, T.J. Bensky, and R.R. Jones, *Opt. Express* **1**, 197 (1997).

[19] U. Eichmann, D. Richter, D. Wintgan, and W. Sandner, *Phys. Rev. Lett.* **61**, 2438 (1998).

[20] M.L. Keeler and T.J. Morgan, Phys. Rev. Lett. **80**, 5726 (1998).

[21] S.N. Pisharody, J.G. Zeibel, R.R. Jones, *Phys. Rev. A* **61**, 063405 (2000).

Appendix B

Classical Numerical Simulations

B.1 Introduction

An example of the predictive power of classical mechanics was demonstrated by Edmond Halley in the 16^{th} century. By knowing where a comet was at one instant in time, and knowing its trajectory, he was able to predict where the comet would be for all future times, as well as determine where it had been in the past. He accurately predicted the comet's return 76 years later to within 2 weeks [1]. For this feat, the comet today bears his name. Small perturbations to the orbit of the comet by other bodies which Halley had not considered prevented a more accurate determination. In a similar manner, we can use classical mechanics to predict the motion of a classical electron to a certain level of accuracy, while trying to recognize the shortcomings of this method. In this section,

a method for using classical mechanics to model the interaction between a Rydberg electron and a set of external fields is presented.

The use of classical techniques to model atomic systems has its advantages and disadvantages. Classical analyses tend to yield physical intuition about a system and are generally far easier to implement than quantum mechanical models. However, since atoms are inherently quantum systems, classical mechanics can at best yield a good approximation of the true system. Performing a classical analysis of an atomic system is very straightforward in principle. The equations of motions can be integrated for an electron subject to an attractive Coulomb force and some set of external fields. Many details and complexities must be overcome however before obtaining a viable classical model of an atomic system. The first complication arises from the fact that except for extremely simple cases, the equations of motion are not integrable in closed form. It is therefore necessary to model the system with numerical methods. Fortunately, a large number of algorithms exist in the literature to aid in this process. The vast majority of these routines are cataloged in *Numerical Recipes* [2]. Much of the computer code developed for the simulations presented in this thesis is based on routines from that text. In addition, some of the classical simulation techniques presented here are developed from the previous work of T.J. Bensky [3].

B.2 Numerical Integration

We begin an analysis with Newton's second law

$$\sum_i \vec{F}_i \;=\; \frac{d\vec{p}}{dt} \;=\; M\frac{d^2\vec{r}}{dt}\;. \tag{B.1}$$

The sum over i includes all the forces acting on a given particle of mass M. Since we will consider only the motion of an electron in atomic units, from this point on $M \equiv 1$. Equation B.1 is not directly useful in determining $\vec{v}(t)$ or $\vec{r}(t)$. To determine $\vec{v}(t)$ and $\vec{r}(t)$, equation B.1 must be integrated for the particular set of forces which we are interested in. In general this integration is not possible in closed form and therefore the position and velocity of the electron are not simple closed form expressions.

Through numerical integration, values of $\vec{v}(t)$ and $\vec{r}(t)$ can be determined through a recursive approach. Numerical integration proceeds by advancing the state of a system in small, incremental time steps during which all forces acting on the system can be considered constant. If the initial position and velocity are known at a time $t = t_0$, then the first step of the numerical integration process yields $\vec{v}(t_1)$ and $\vec{r}(t_1)$ where $t_1 = t_0 + \Delta t$. Here, Δt is some small time step. For this approach to be valid, the forces acting on the electron must not change significantly over Δt, or at worst must change in a manner which can be predicted. Once $\vec{v}(t_1)$ and $\vec{r}(t_1)$ are found, these values are input as the initial conditions for the next time step. In this way, the time dependent position and velocity of the electron are eventually determined for all times.

As long as the starting position and velocity are known, as well as all the forces acting on the electron, $\vec{v}(t)$ and $\vec{r}(t)$ can be determined through numerical integration. After calculating $\vec{v}(t)$ and $\vec{r}(t)$, other important physical quantities can also be determined. These include the energy, angular momentum, linear momentum, and Runga-Lenz vector.

B.3 Electron Orbital Motion

For the analysis of this section, the atomic system is most easily pictured in an astrophysical manner. Consider the atomic core like the sun and the electron like Halley's comet, moving in some highly elliptical, fairly low angular momentum state. An angle θ is defined as the angular coordinate of the electron's position such that $\theta = 0$ when the electron is at its inner turning point. In the absence of external fields, the radial position as a function of θ is given by

$$r(\theta) \;=\; \frac{\ell^2}{1 + e cos(\theta - \theta_0)} \;. \tag{B.2}$$

The angular momentum is given by $\ell = r^2\dot{\theta}$ and the eccentricity of the orbit is given by $e = \sqrt{1 + 2E\ell}$, where E is the total energy of the electron [4]. A problem arises however when we desire to predict the time dynamics of the electron. Equation B.2 yields only $\vec{r}(\theta)$ and not $\vec{r}(t)$. Therefore, determining the time dependence of $\vec{r}$ and $\vec{v}$ is more complicated. The angle θ is related to another quantity ψ (called the eccentric

anomaly) by

$$cos\theta \;=\; \frac{cos\psi - e}{1 - ecos\psi}. \tag{B.3}$$

Furthermore, a transcendental relationship exists between ψ and t [4],

$$\frac{2\pi t}{\tau} \;=\; \psi - esin\psi \;. \tag{B.4}$$

The parameter τ is the orbital period of the electron. Combining equations B.2, B.3, and B.4 is not possible analytically. However, this combination of equations can be combined numerically, yielding values for $\vec{r}(t)$ and $\vec{v}(t)$. Section 7.2 is dedicated to these calculations. Obtaining solutions becomes even less tractable however with the introduction of external, time dependent electric fields. Therefore, direct numerical integration of the equations of motion is typically the preferred manner to calculate orbital dynamics.

B.4 Computational Implementation

For a single electron moving in a Coulomb potential free of any external fields, the differential equations of motion are given by

$$\frac{d^2\vec{r}}{dt^2} \;=\; -\frac{\vec{r}}{r^3} \;. \tag{B.5}$$

In equation B.5, $\vec{r}$ is the position vector of the electron. Contained in equation B.5 are three non-separable second order differential equations. (One equation for each

coordinate.) However, in order to apply standard numerical integration techniques, it is more advantageous to reduce equation B.5 into six, first order differential equations [2]. Doing so yields

$$\frac{dr_x}{dt} = v_x \ , \tag{B.6}$$

$$\frac{dr_y}{dt} = v_y \ , \tag{B.7}$$

$$\frac{dr_z}{dt} = v_z \ , \tag{B.8}$$

$$\frac{dv_x}{dt} = -\frac{r_x}{r^3} \ , \tag{B.9}$$

$$\frac{dv_y}{dt} = -\frac{r_y}{r^3} \ , \tag{B.10}$$

and

$$\frac{dv_z}{dt} = -\frac{r_z}{r^3} \ . \tag{B.11}$$

Note that the Coulomb force has been broken down into components and included in equations B.9 through B.11. Numerical integration of these six first order differential equations yields $\vec{r}(t)$ and $\vec{v}(t)$ for all time. Adding an external or time dependent force to the system involves only adding an additional term to the right hand side of equations B.9 through B.11 during integration. The relative simplicity by which field terms can be added is the advantage of this technique, when compared to the direct solution begun in equations B.2 through B.4.

B.5 Initial Conditions

Since the numerical integration routine is recursive, it is essential that correct initial conditions are supplied for $\vec{r}(t_0)$ and $\vec{v}(t_0)$. Six initial conditions are required to solve equations B.6 through B.11. Without loss of generality, the simulation can be confined to a plane (let's choose $\hat{xy}$). Following the numerical integration, the results are then rotated from the $\hat{xy}$ plane into any other orientation appropriate to the situation being studied. Due to this initial choice of orientation, $z(t_0) = 0$ and $v_z(t_0) = 0$. To obtain the four other initial conditions, an initial orbit angle θ_0 is chosen. The initial position is then given by

$$r_{x_0} \;=\; r(\theta_0)cos\theta_0 \quad \text{and} \quad r_{y_0} \;=\; r(\theta_0)sin\theta_0 \;, \tag{B.12}$$

where $r(\theta_0)$ is given by the equation B.2. Since the velocity is simply the derivative of the position, the initial velocity is given by

$$v_{x_0} \;=\; \dot{r}(\theta_0)cos\theta_0 \;-\; \frac{\ell}{r(\theta_0)sin\theta_0} \tag{B.13}$$

$$v_{y_0} \;=\; \dot{r}(\theta_0)sin\theta_0 \;+\; \frac{\ell}{r(\theta_0)cos\theta_0} \;, \tag{B.14}$$

where we have made use of the fact that $\ell = r(\theta_0)^2\dot{\theta_0}$. Here, $r(\theta_0)$ is again given by equation B.2, and its time derivative, $\dot{r}(\theta_0)$ is given by

$$\dot{r}(\theta_0) \;=\; \pm\sqrt{\frac{2}{r(\theta_0)} - \frac{1}{n^2} - \frac{\ell^2}{r(\theta_0)^2}} \;. \tag{B.15}$$

The positive root of $\dot{r}(\theta_0)$ is chosen for $0 \leq \theta_0 \leq \pi$, corresponding to motion of the electron *away* from the core. Similarly, the negative root of $\dot{r}(\theta_0)$ is chosen for $\pi \leq \theta_0 \leq$

2π.

If we only wish to observe a single electron's motion from a single initial location, then a value of θ_0 is arbitrarily chosen, the initial values of $\vec{r}(t_0)$ and $\vec{v}(t_0)$ are calculated from equations B.12 through B.14, and the numerical integration is performed. In most situations however, we are concerned with an ensemble of atoms in a laboratory environment and not a single atom. Therefore, many initial conditions must be chosen and the results from each event averaged to obtain physically meaningful values of observable quantities such as E, ℓ, $< r >$, $< v >$, etc.

Some manner for selecting a meaningful ensemble of starting positions is needed. The problem is that the electron's motion is not uniform as a function of θ. The electron moves quickly past the atomic core at its inner turning point, and then much more slowly as it moves towards its outermost radial position. For a low ℓ Rydberg orbit, the electron typically spends more than 90% of the time in the "outer half" of its orbit [4]. Therefore, choosing starting positions for the numerical integration which are located uniformly around the orbit will not accurately reproduce the physics of the system. Instead, the selection of appropriate initial conditions must be done in a manner which takes into account the time spent in each part of the electron's orbit.

To properly choose an ensemble of initial conditions, we introduce the concept of classical probability density. We define dP as the probability that an electron is found in a small volume element along its orbit. Furthermore, dP is related to a small change

in time by

$$dP \;=\; \frac{dt}{\tau_K}\;, \tag{B.16}$$

where, dP is the differential probability that a particle spends a time dt at a given point in its orbit. $\tau_K = 2\pi n^3$ is the Kepler period of the orbit. The time differential dt can be expressed in terms of a small radial differential dr by

$$dt \;=\; \frac{dr}{\dot{r}}\;. \tag{B.17}$$

Here $\dot{r}$ is the velocity of the electron at $r+dr$ and is given in equation B.15. Combining equations B.15, B.16, and B.17 gives the expression

$$dP \;=\; \frac{dr}{2\pi n^3\sqrt{\frac{2}{r}-\frac{1}{n^2}-\frac{\ell^2}{r^2}}}\;. \tag{B.18}$$

Equation B.18 gives the differential classical probability of finding a Rydberg electron with radius between r and $r+dr$ [3]. When choosing the initial positions for an ensemble of electrons in Rydberg states, it is necessary that the points be weighted by this probability density function. An effective method for achieving this proper weighting involves solving Kepler's equation (equation B.4) for ψ at equally spaced values of t between 0 and τ_K. The resulting values of ψ are then used to determine appropriately spaced values of θ from equation B.3. Values of θ found in this manner are properly distributed.

B.6 Initial Orientation

In choosing the initial conditions, the orbit was confined to the $\hat{xy}$ plane. Experimentally however, the atoms are confined to an initial value of m, but not to a single orientation in a plane. In order to reproduce the dynamics of a real ensemble of atoms, a series of three rotations is performed on $\vec{r}$ and $\vec{v}$ which rotate the system into a randomly oriented orbit. For most of the simulations performed in this thesis, we initially choose $m = 0$ [5]. The rotations are performed in the same technique as the Euler angle rotations defined in Goldstein [4]. First, the initial position and velocity vectors are rotated about the $\hat{z}$ axis by an angle ϕ, randomly chosen between 0 and 2π. The major axis of the elliptical orbit is now defined as the $\hat{\xi}$ axis. Second, a rotation of $\pi/2$ about the $\hat{\xi}$ axis is performed. The axis normal to the plane of the orbit is now defined to be $\hat{z}'$. Finally, a rotation around the $\hat{z}'$ axis by a random angle between 0 and 2π is performed. This combination of three rotations results in all possible $m = 0$ orientations. A large number of individual trials must then be performed to create a statistically meaningful distribution due to the random numbers used in the simulation to seed the initial conditions.

B.7 Stepsize

In numerical integration, the position of a particle changes from one time step to another through the equation

$$x_{new} \;=\; x_{old} + \frac{dx}{dt}\Delta t \;. \tag{B.19}$$

In this recursive method, the old position and velocity are used to determine the new position, then the old position is replaced by the new value and the process is repeated. The main assumption in this method is that the forces are constant over the time step interval Δt. Determining an optimal value of Δt is crucial in successfully performing the numerical integration. If Δt is too large, fast fluctuations in the applied forces are averaged out and the approximation to the real system breaks down. If Δt is too small, then the time required to perform the integration becomes prohibitively long.

A problem arises when numerically integrating the equations of motion of a Rydberg orbit. When the electron is near the core, very small steps of Δt must be taken to accurately reproduce the very strong and quickly changing Coulombic force near the atomic core. When the electron is far from the core however, the forces acting on the system vary slowly, and large Δt steps are preferred. To satisfy these two somewhat opposing conditions, an *adaptive* stepsize is used. In an adaptive stepsize routine, the size of the next step is determined by the error introduced by the previous step. Therefore in the case of a Rydberg orbit, small time steps are taken when the electron is near the atomic core and larger ones are taken during the rest of the orbit.

B.8 Performing the Integration

In summary, the steps required to perform the numerical integration are as follows. First, the initial conditions are determined.

1. A random time t in the interval $[0, 2\pi n^3]$ is chosen.
2. Kepler's equation (B.4) is solved numerically for the eccentric anomaly, ψ.
3. The initial orbit angle, θ_0 is computed.
4. Initial values of (x, y, z, v_x, v_y, v_z) are calculated from the initial choices of electron energy, ℓ, and m.
5. The initial positions are rotated to a randomly oriented orbit.

Next, the integration loop parameters are set. These include the initial Δt stepsize, the initial time, and the final time. Then the functional values of the derivatives are set. These are equations B.6 through B.11, along with any additional terms due to forces arising from external static fields, HCP fields, etc. This is how the numerical integration is customized to any particular set of environmental conditions or field geometry. A fourth order Runga-Kutta routine is chosen for the numerical integration [2]. After the initial conditions and initial parameters are set, the six parameters (x, y, z, v_x, v_y, v_z) are advanced recursively from their initial value to their values at the final time by the Runga-Kutta routine. The exact details of the routine are omitted here, however, they are described in detail in [2].

B.9 External Fields

As mentioned before, adding an external field and or a HCP field to the system is done by adding an additional term to equations B.9 through B.11. For example, if we wanted to apply a static field along $\hat{y}$ and Gaussian shaped HCP fields along the $\hat{x}$ and $\hat{z}$ axes, equations B.9 through B.11 would become:

$$\frac{dv_x}{dt} = -\frac{r_x}{r^3} + F_{HCPx}\, e^{-(t-t_{0x})^2/2\sigma_x^2} \tag{B.20}$$

$$\frac{dv_y}{dt} = -\frac{r_y}{r^3} + F_{static} \tag{B.21}$$

$$\frac{dv_z}{dt} = -\frac{r_z}{r^3} + F_{HCPz}\, e^{-(t-t_{0z})^2/2\sigma_z^2}\ . \tag{B.22}$$

In equation B.20, t_{0x} is the arrival time of the maximum of the $\hat{x}$ polarized HCP field and σ_x^2 is its width. In equation B.22, t_{0z} is the arrival time of the maximum of the $\hat{z}$ polarized HCP field and σ_z^2 is its width. HCP fields and external fields may be added along any axis independently by simply adding the appropriate terms.

B.10 Conclusions

The basic computing framework of the classical simulations presented in this appendix are applicable to the modeling of various physical systems. The programs discussed in this appendix are used to (i) model HCP ionization of a Rydberg eigenstate to aid in HCP calibration (chapter 3), (ii) model HCP induced ionization of a wavepacket in a

static field (chapter 4), and (iii) simulate electron - ion recombination dynamics in zero field (section 7.3). In all cases, the agreement between the classical calculations and experiment is adequate to gain intuition about the system being simulation. In some cases the agreement between the classical calculations is even remarkably good. In addition, the added conceptual insight gained from a classical picture of very complex systems is quite helpful.

Bibliography

[1] P. Lancaster-Brown, *Halley and His Comet*, Blandford Press, London, (1985).

[2] W.H. Press, S.A. Teukolsky, W.T. Vetterling, and B.P. Flannery, *Numerical Recipes in C, 2nd ed.*, Cambridge University Press, Cambridge, (1992).

[3] T.J. Bensky, *Rydberg Atoms & Half Cycle Pulses*, Ph.D. Thesis, University of Virginia, (1998).

[4] H. Goldstein, *Classical Mechanics, 2nd ed.*, Addison-Wesley Publishing Co., Reading, Massachusetts, (1980).

[5] The orientation $m = 0$ is chosen for the initial starting condition in the numerical simulation as the polarization of the laser pulses in the laboratory environment is entirely vertical. This experimental alignment initially produces entirely $m = 0$ orbits, with no classical projection of angular momentum along the $\hat{z}$ axis. Altering the calculations to initially populate other values of m is straightforward.

Appendix C

Quantum Simulations

C.1 Introduction

Lots of insight is gained from classical modeling of atomic systems. However, to legitimately claim full understanding of an atomic system requires knowledge of quantum mechanics. In this appendix, we present details of how the quantum mechanical simulations presented in chapter 5 are performed. Furthermore, additional simulations of an atomic system interacting with a time dependent electric field are presented which demonstrate the simulation techniques. Simulations presented in this appendix are performed for calcium, although adaptation to any other atomic system with known quantum defects is trivial.

The main difficulty with quantum calculations of Rydberg atoms is the extremely

large number of basis states necessary to perform meaningful calculations. Only with recent advances in computing technology is it possible to address such calculations. If we assume that the magnetic quantum number m is constant, then there are $n - m$ angular momentum states for each n state [1]. A typical calculation includes tens of n states. Transition probabilities must be calculated between all possible initial and final states within the large basis set at each time step. Computational difficulties are magnified when the process of direct field ionization needs to be considered [2]. As $n \rightarrow \infty$, the number of basis states becomes infinite. A good deal of work has been done in dealing with field ionization quantum mechanically and the transition from bound to continuum states [3], however this added complexity is beyond the scope of the calculations presented here.

C.2 Time Dependent Perturbation Theory

The goal in most quantum mechanical calculations is to solve the Schrödinger wave equation for a given Hamiltonian $\hat{H}$. In the most general case, the wave equation can be written

$$i\hbar \frac{\partial}{\partial t}\psi \;=\; \hat{H}\psi \;. \tag{C.1}$$

In time dependent perturbation theory, the Hamiltonian has explicit time dependence

$$\hat{H} \;=\; \hat{H}_0 \;+\; \hat{V}(t) \;, \tag{C.2}$$

where $\hat{H}_0$ is the unperturbed, time *independent* Hamiltonian, and $\hat{V}(t)$ is the time *dependent* perturbation. For a system evolving due to the Hamiltonian in equation C.2, energy is not conserved. Therefore, no stationary states of the system exist for the Hamiltonian in equation C.2 [1].

We define a state $\phi_k^{(0)}$ to be a time independent eigenstate of the unperturbed system. An arbitrary solution to the unperturbed wave equation may be written

$$\psi \;=\; \sum_k a_k \; \phi_k^{(0)} \; e^{-iE_k t/\hbar} \;, \tag{C.3}$$

where the coefficients a_k are a set of time independent complex state amplitudes. Similarly, if we want to solve the full wave equation with the perturbation given by equation C.1 we look for solution of the form

$$\psi \;=\; \sum_k a_k(t) \; \phi_k^{(0)} \; e^{-iE_k t/\hbar} \;. \tag{C.4}$$

The only difference between the two arbitrary solutions presented in equations C.3 and C.4 is the time dependence of the a_k terms. We have expressed the wavefunction of the full Hamiltonian given in equation C.2 in terms of the eigenstates of the unperturbed, time independent Hamiltonian $\hat{H}_0$. Substitution of equations C.4 and C.2 into equation C.1 yields

$$\begin{aligned} i\hbar\Big[\sum_k \frac{d}{dt}\Big(a_k(t)\Big)\phi_k^{(0)} \; e^{-iE_k t/\hbar} + \sum_k a_k(t)\frac{d}{dt}\Big(\phi_k^{(0)} \; e^{-iE_k t/\hbar}\Big)\Big] \\ = \; \sum_k \Big(\hat{H}_0 \; + \; \hat{V}(t)\Big) \; a_k(t) \; \phi_k^{(0)} \; e^{-iE_k t/\hbar} \;. \end{aligned} \tag{C.5}$$

Recalling that the unperturbed states satisfy the relation

$$i\hbar \frac{\partial}{\partial t}\Big(\phi_k^{(0)}\ e^{-iE_k t/\hbar}\Big) \ = \ \hat{H}_0 \ \Big(\phi_k^{(0)}\ e^{-iE_k t/\hbar}\Big) \ , \tag{C.6}$$

equation C.5 reduces to

$$i\hbar \ \sum_k \phi_k^{(0)}\ e^{-iE_k t/\hbar}\ \frac{d}{dt}a_k(t) \ = \ \sum_k a_k(t)\hat{V}(t)\phi_k^{(0)}\ e^{-iE_k t/\hbar} \ . \tag{C.7}$$

Multiplying both sides of equation C.7 by $\phi_j^{(0)*}$ and integrating yields

$$i\hbar \ \frac{d}{dt}\Big(a_j(t)\Big) \ = \ \sum_k a_k(t) < \phi_j^{(0)}|\hat{V}(t)|\phi_k^{(0)} > e^{-i\omega_{jk}t} \ , \tag{C.8}$$

where ω_{jk} is defined as

$$\omega_{jk} \ = \ \frac{E_j^{(0)} - E_k^{(0)}}{\hbar} \ . \tag{C.9}$$

To apply the general perturbative approach given in equation C.8 to the problem of an atom in a time dependent electric field, the unperturbed eigenstates $\phi_k^{(0)}$ are taken to be the normal spherical harmonic eigenstates, $|n\ell m >$. The perturbation $\hat{V}(t)$ is defined to be

$$\hat{V}(t) \ = \ F_x(t)\ x \ + \ F_y(t)\ y \ + \ F_z(t)\ z \ . \tag{C.10}$$

The three Cartesian field components in equation C.10 can each be independently varied depending on the configuration of the fields in the experiment. Substituting into equation C.8 and employing atomic units ($\hbar \equiv 1$), we have

$$i \ \frac{d}{dt}a_j(t) \ = \ \sum_k a_k(t) < n_j\ell_j m_j|\hat{V}(t)|n_k\ell_k m_k > e^{i(E_j - E_k)t} \ , \tag{C.11}$$

The Cartesian components of the perturbation can each be expressed in terms of spherical tensor operators to perform the integration. They are given by

$$x = r \frac{1}{\sqrt{2}}(C^1_{-1} - C^1_1) \tag{C.12}$$

$$y = r \frac{1}{\sqrt{2}}(C^1_{-1} + C^1_1) \tag{C.13}$$

$$z = r\, C^1_0. \tag{C.14}$$

The reduced spherical tensor operators C^ℓ_m are related to the familiar spherical harmonics Y^m_ℓ by

$$C^\ell_m = \sqrt{\frac{4\pi}{2\ell+1}}\, Y^m_\ell \,. \tag{C.15}$$

The perturbation matrix element $V_{jk}(t) \equiv < n_j \ell_j m_j | \hat{V}(t) | n_k \ell_k m_k >$ then becomes

$$\begin{aligned} V_{jk}(t) = & < n_j \ell_j | r | n_k \ell_k > \Big[\Big(\frac{F_x(t) + F_y(t)}{\sqrt{2}} \Big) < \ell_j m_j | C^1_{-1} | \ell_k m_k > \\ & + \Big(\frac{F_x(t) - F_y(t)}{\sqrt{2}} \Big) < \ell_j m_j | C^1_1 | \ell_k m_k > + \Big(F_z(t) \Big) < \ell_j m_j | C^1_0 | \ell_k m_k > \Big]. \end{aligned} \tag{C.16}$$

Finally, to determine the state of the system as a function of time, the set of coupled differential equations given by

$$i \frac{d}{dt} a_j(t) = \sum_k a_k(t) V_{jk}(t) e^{i(E_j - E_k)t} \tag{C.17}$$

must be solved by some means.

C.3 Numerical Integration

Equation C.17 defines a set of coupled, first order differential equations. Due to the size of the basis set of the atomic system, it is advantageous to apply numerical techniques at this point to determine the time dependent state distribution [4]. A fourth order Runga-Kutta adaptive stepsize integration routine is used to perform the numerical integration. The routine is similar to the one developed for the classical simulations (see appendix B), however it has been modified to handle complex numbers and a much larger number of coupled equations. In the classical simulations, six first order differential equations are solved to completely determine the motion of an electron. In the quantum mechanical calculations, one first order coupled differential equation exists to describe the time dependent complex state amplitude of each basis state. In a typical quantum mechanical simulation, thousands of coupled differential equations are solved simultaneously.

Initially, an upper and lower bound on n are chosen which define the size of the basis set for the calculation. The lower bound is labeled n_L and the upper bound n_H. For a typical calculation done in this thesis, $n_L \approx 10$ and $n_L \approx 40$. We have developed a method of giving a sequential index i to each allowed $|n\ell m>$ state in the range $n_L \leq n \leq n_H$. In our indexing scheme, first the m value is incremented, then the ℓ, and finally the n. Therefore, the state $n = n_L, \ell = n_L - 1, m = -(n_L - 1)$ corresponds to $i = 0$, the state $n = n_L, \ell = n_L - 1, m = -(n_L - 2)$ has $i = 1$, and so on. The index

for each $|n\ell m>$ state is given by the relation

$$\begin{aligned} i(n,\ell,m) &= \frac{1}{6}\Big((2n^3-3n^2+n)-(2n_L^3-3n_L^2+n_L)\Big) \\ &\quad + \frac{1}{2}\Big(n^2-n+|m|+2nm\pm m^2\Big) \;+\; \ell \;-\; |m| \;. \end{aligned} \tag{C.18}$$

The + sign in equation C.18 is for $m<0$, and the − sign is for $m>0$. For example, if $n_L=20$, then the state $|20,19,-19>\equiv|\phi_0>$, the state $|20,0,0>\equiv|\phi_{190}>$, and the state $|30,5,-3>\equiv|\phi_{6438}>$. The index i runs from $i=0$ to i_{max}, where

$$i_{max} \;=\; \frac{1}{6}(2n_H^3+3n_H^2+n_H-2n_L^3+3n_L^2-n_L-6)\;, \tag{C.19}$$

and contains one element for every $|n\ell m>$ state. This indexing method simplifies the labeling of the basis state vector when designing computer code. Through equation C.18, the state vector can be written as a single vector with index ranging from $i=0$ to $i=i_{max}$.

To begin a calculation, an initial state vector is chosen. This is the state of the system at $t=0$. Frequently, the initial state is simply a $m=0$, nd Rydberg eigenstate. For example, if an electron is excited directly to a $n=22,\ell=2,m=0$ eigenstate, then the real amplitude of the $|22,2,0>$ state is set to unity and the real and complex amplitudes of every other state in the basis set are zero. If the system is instead excited with a broad bandwidth laser pulse, then several different n states may be excited simultaneously and a Gaussian distribution of initial real amplitudes is used for the initial state. A third possibility is the initial excitation of a Stark state. In this case,

one (or several) states with parabolic quantum number(s) k are initially excited. The calculations are performed in the spherical harmonic basis, so the initial Stark state(s) must be rotated from the parabolic basis ($|nkm>$) into the spherical ($|n\ell m>$) basis to determine an initial state distribution. Techniques for performing such rotations are discussed in section D.1.3.

After setting the initial state, the value of the electric field along each axis is specified for all times t. If the electric field is static, then a constant value is used throughout. Static fields may be applied along any direction by simply specifying the Cartesian components separately. Time varying electric fields (such as the field of a HCP) are specified at each value of time in a separate file which is read into the program at runtime. The precise temporal shape of the pulse may be adjusted to any form by specifying the pulse shape in the input file. A typical electric field profile used to simulate a HCP is shown in figure 3.2. The absolute height and temporal width of the time varying field are scaled to user input values. A subroutine within the numerical integration returns values for F_x, F_y, and F_z for any given value of time within $0 \leq t \leq t_{max}$.

All the time dependence in equation C.16 is contained in the profile of the electric fields and is outside of the interaction matrix elements. Therefore, it is only necessary to calculate each matrix element once, instead of at every time step during the numerical integration routine. Furthermore, due to angular momentum selection rules, a large

number of the matrix elements are zero. For example, a basis set that contains all possible $|n\ell m>$ states from $10 \leq n \leq 35$, contains 14624 elements. However, out of almost 214 million possible interaction matrix elements, only 1416635 are nonzero. These are calculated at the beginning of the simulation and stored in an array to be accessed at each time step of the numerical integration. Each of the radial matrix elements $< n_j \ell_j |r| n_k \ell_k >$ is calculated for calcium by a Numerov numerical integration [10]. The angular matrix elements are calculated from the Wigner-Eckhart theorem [11] and are given by

$$< \ell' m' |C^1_M| \ell m > \;\; = \;\; (-1)^{m'} \sqrt{(2\ell'+1)(2\ell+1)} \begin{pmatrix} \ell' & 1 & \ell \\ 0 & 0 & 0 \end{pmatrix} \begin{pmatrix} \ell' & 1 & \ell \\ -m' & M & m \end{pmatrix} . \tag{C.20}$$

Once the initial state is chosen, the matrix elements are calculated, and some initial value of stepsize is selected, the integration routine proceeds to advance the initial state through the first time step. The nature of numerical integration assumes that the perturbation does not change during each time step. In other words, the values of the components of the electric field are assumed to be constant during each time step. After the first step, the resulting state distribution is recorded in a file and then becomes the initial state distribution for the second time step. The size of the next step is determined adaptively based on the error of the previous step. The adaptive stepsize technique allows small time steps to be taken when the electric field is changing very rapidly and much larger steps when the field is effectively constant. The integration

proceeds in this way until the final time step. After the final step, the final state distribution is recorded.

As an example of the quantum calculations, the state redistribution due to two HCP fields interacting with an initial $|22, 2, 0>$ Rydberg eigenstate is calculated. The first HCP is polarized along the $\hat{z}$ axis and the second is polarized along $\hat{x}$ and follows the first in time by 1 ps. Each HCP has a FWHM of 0.8 ps. A small ($\sim$10 V/cm) static electric field persists for the duration of the simulation along each HCP axis to simulate the slow return to zero offset of the experimentally generated HCPs [5]. The simulation runs for 4 ps. The final $|n\ell m>$ state vector is integrated along each of the three quantum numbers to recover final n, ℓ, and m distributions. These final state distributions are shown in figure C.1. The values of n_L and n_H are 10 and 35 respectively. The magnetic quantum number m is measured with respect to the $\hat{z}$ axis. For larger values of HCP field strength, more of the initial population is transferred to high angular momentum states. At 4 kV/cm all the n states have been populated up to n_H. Therefore, for HCP fields greater than 4 kV/cm, more n states must be included in the simulation to prevent artificial "reflection" of population from the edge of the basis set. Eventually, as the HCP field strength increases further, direct HCP ionization begins to occur and the simulation is no longer valid in its current form.

Since the full state distribution is recorded at each time step, it is possible to calculate the time dependent population in each quantum state *during* HCP interaction

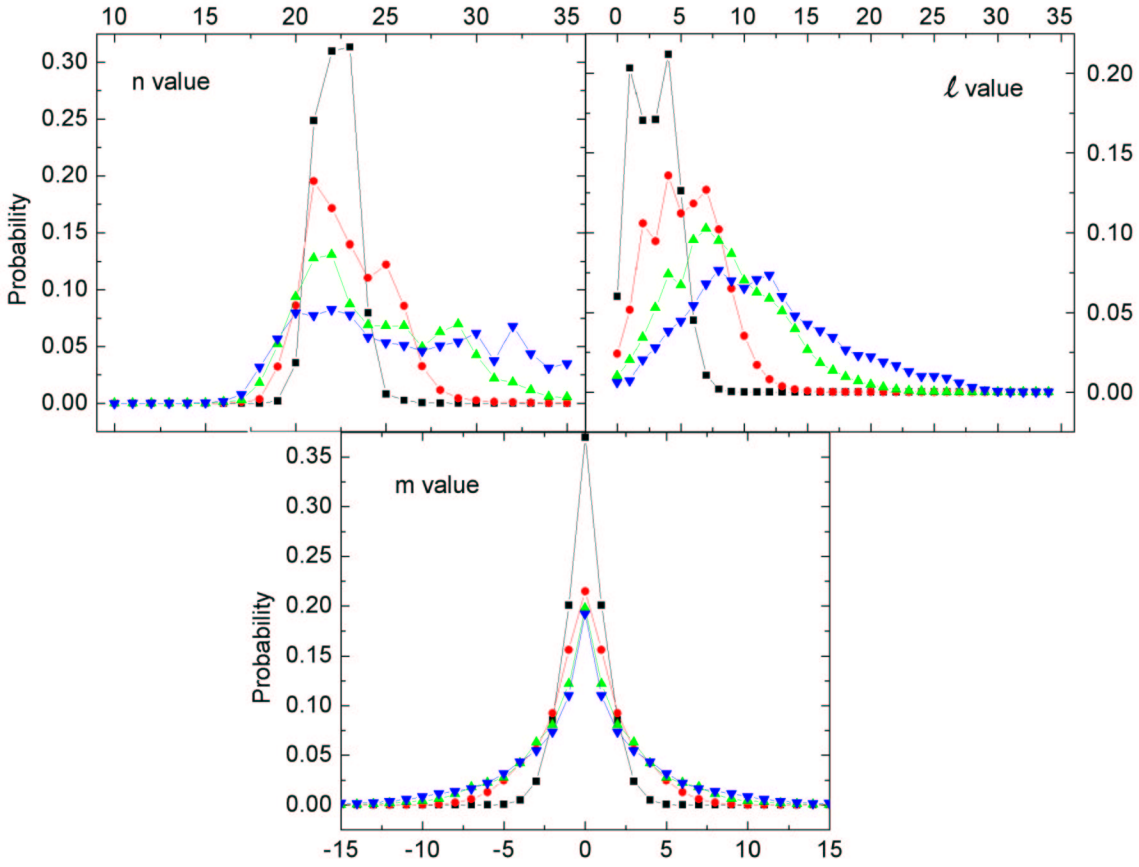

Figure C.1: Final $|n\ell m>$ state distributions resulting from the quantum mechanical simulation of two orthogonally polarized HCP fields interacting with an initial $|22, 2, 0>$ Rydberg eigenstate in Ca. The four curves in each graph represent HCP fields with maximum strengths of 1 kV/cm (black), 2 kV/cm (red), 3 kV/cm (green), and 4 kV/cm (blue). For the m state distribution, m is measured along the $\hat{z}$ axis.

as well as after it. If we look at the n state distribution for the simulation discussed above, we see that the entire population lies initially in $n = 22$. As the HCP field increases, more and more population is transferred to neighboring n states. The rate of population transfer is proportional to the strength of the HCP field. Figure C.2(a) shows the time dependent n state population in some selected n values. Note that after the first HCP field interacts with the system, a little over 10% of the initial population resides in $n = 30$. After the second pulse though, the amount of population in each n state is very similar. Time dependent state distributions are shown in figure C.2(b) for the ℓ state character. Population shifts very rapidly between ℓ states during the maximum of the first HCP field at approximately $t = 0.4$ ps. After the second HCP field is over, more population actually resides in $\ell = 15$ than it does in $\ell = 2$.

If no electric fields are present in either the $\hat{x}$ or $\hat{y}$ directions, then m is a good quantum number and the matrix elements $V_{jk}(t)$ reduce to

$$V_{jk}(t) \;=\; < n_j \ell_j | r | n_k \ell_k > \; \Big(F_z(t) \Big) < \ell_j m | C_0^1 | \ell_k m > \;\; . \tag{C.21}$$

If this simplification can be made then the calculations are greatly reduced as only one value of m must be considered in the perturbation matrix. In this case, the number of interaction matrix elements is greatly decreased and many more n states can be considered in the basis without winding up with an unmanageable number of calculations. A similar calculation is performed to that shown in figure C.1, however only a single HCP is applied, polarized along the $\hat{z}$ axis. The initial state is again $|22, 2, 0>$. m is

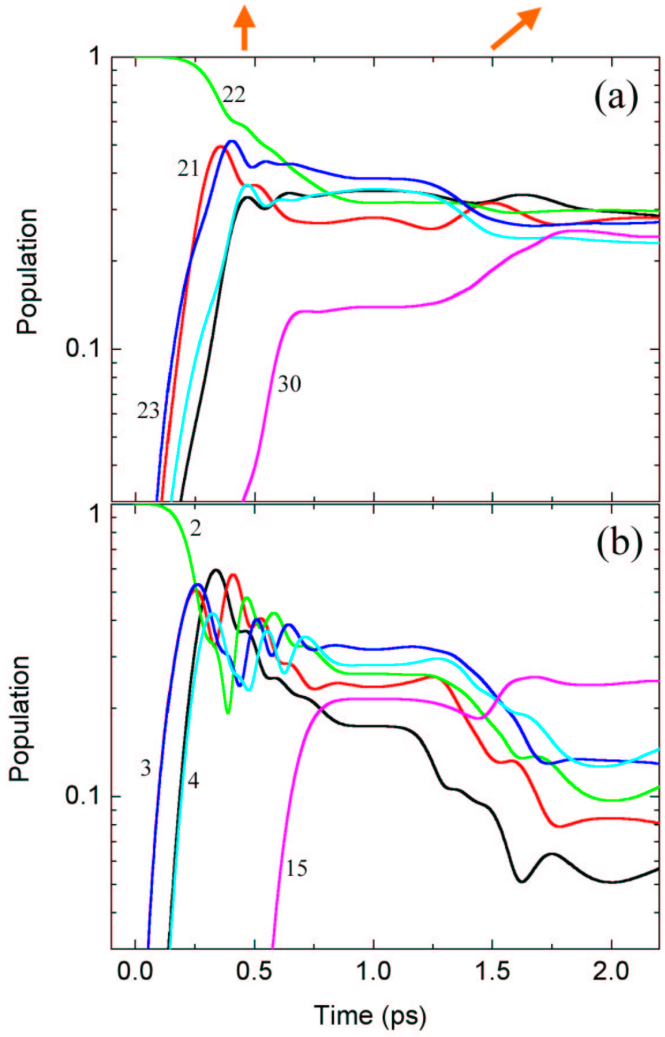

Figure C.2: Quantum mechanical simulation of the time evolution of selected n and ℓ states in the presence of two HCP fields separated in time by 1 ps. The first HCP is polarized along $\hat{z}$ and has a maximum value of 4 kV/cm at $t = 0.4$ ps. The second HCP is polarized along $\hat{x}$ and also has a maximum value of 4 kV/cm at a time $t = 1.4$ ps. The relative timing of the maxima of the HCP fields is indicated by the orange arrows. (a). Population in selected n states as a function of time. Shown are $n = 20, 21, 22, 23, 24,$ and 30. Initially, the population in $n = 22$ is 1. Very little of the $n = 30$ state is populated after the first HCP. By the end of the second HCP however, the amount of population in $n = 30$ is roughly the same as the other n states. (b). Population in selected ℓ states as a function of time for $\ell = 0, 1, 2, 3, 4,$ and 15. The population is initially all in $\ell = 2$.

uniquely determined to be zero (when measured along the $\hat{z}$ axis) for the duration of the simulation. The simulation runs for 4 ps. The final $|n\ell 0>$ state vector is integrated along both n and ℓ to recover the final distributions of both quantum numbers. Results from the simulation are shown in figure C.3. n values from $10 \leq n \leq 90$ are included in the simulation.

If we look at the n state distribution for a HCP field of maximum strength 8 kV/cm (the blue curve in the left graph in figure C.2), we can already begin to see the effect of the boundary reflection. Peaks in the n state probability occur at $n = 41$ and $n = 53$. These features are artifacts which arise from artificially limiting the size of the basis set. Increasing n_H will decrease these features, however if the HCP field is strong enough to directly ionize the Rydberg electron, then no matter how many bound states we include in the simulation, boundary reflections are present. Once these reflections begin to occur, the simulation is no longer valid.

C.4 Ionization

C.4.1 Direct Ionization

Extending the quantum simulations presented above to include the possibility of direct field ionization involves many computational difficulties. In this situation, a nonzero probability exists for making transitions to any of an infinite number of continuum

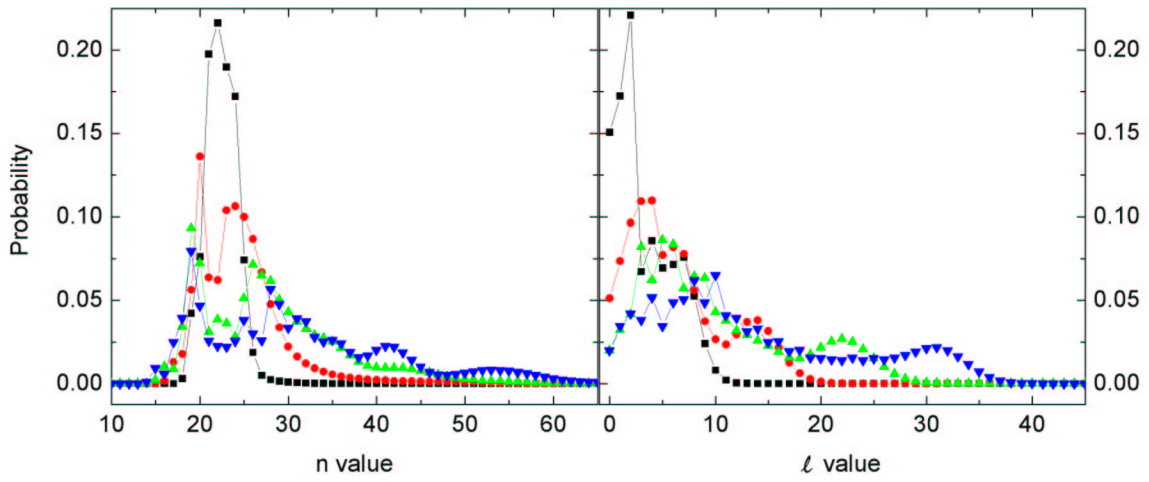

Figure C.3: Final $|n\ell 0>$ state distributions resulting from the quantum mechanical simulation of a HCP field polarized along $\hat{z}$ interacting with a initial population of $|22, 2, 0>$ atoms in Ca. The four curves represent HCP fields with a maximum strength of 2 kV/cm (black), 4 kV/cm (red), 6 kV/cm (green), and 8 kV/cm (blue).

states. This scenario is sidestepped in the quantum simulations presented here by defining a very high n state as the effective continuum limit. If any of the initial population is contained in states with $n \geq n_{limit}$ after any time step, then that population is removed from the simulation and counted as ionized. In this way, the initial population is depleted due to "direct ionization". This limit introduces some artificial reflection of population back down to lower n values. Any population lying in high n states which are slightly below n_{limit} are energetically allowed to make transitions to n states above n_H (the highest n state in the simulation). Since the matrix elements to make these transitions are artificially absent from the basis set, the population must instead move back to lower n values. Reflection effects are reduced by increasing the number of n

values between n_{limit} and n_H but are not completely eliminated.

C.4.2 Autoionization

In the auto-ionizing system (doubly excited Ca) considered in chapter 5), AI typically occurs in the following manner

$$4pnd \;\rightarrow\; 4s^+ \;+\; \epsilon(\ell \pm 1) \quad \text{or} \quad 4pnd \;\rightarrow\; 3d^+ \;+\; \epsilon(\ell \pm 1)\;. \tag{C.22}$$

To simulate the effect of AI in the quantum simulations, population is removed from each state after each time step according to the calculated AI rate for that state, as long as both valence electrons are excited. In the simulation, AI is "turned on" at some time Δt_{ICE} following the HCP interaction. This is the experimental analogy of performing an inner electron isolated core excitation (ICE) [6].

The AI rates for calcium are calculated from Fermi's golden rule in the isolated resonance approximation [7, 8],

$$\Gamma \;=\; 2\pi| < f|V|i > |^2\;. \tag{C.23}$$

The matrix element V is the combined interaction matrix element between the initial state and all possible final states [1, 7, 8]. The total AI rate is assumed to be the sum of the AI rates into the $4s$ and $3d$ continua. For ease of notation, we denote the inner electron as electron 1 and the outer electron as electron 2. V can be written

$$V \;=\; \left\langle n_1'\ell_1'\;\epsilon\ell_2'\;J\middle|\frac{1}{r_{12}}\middle|4p_{3/2}\;n_2\ell_2\;J\right\rangle\;, \tag{C.24}$$

where we have ignored the spin of electron 2. The scalar quantity r_{12} is defined to be the distance between the two electrons. In calcium, the possible values of n_1' and ℓ_1' are $4s_{1/2}$, $3d_{3/2}$, and $3d_{5/2}$. In this section, only AI rates for $n_1'\ell_1' = 4s_{1/2}$ are computed. Similar calculations are performed for the $3d$ continua. The total AI rates used in the quantum simulations are a sum of the contributions from each $n_1'\ell_1'$.

The $\frac{1}{r_{12}}$ operator in equation C.24 can be expanded in terms of spherical harmonics. Keeping only the dipole term in the expansion yields [8]

$$V \;=\; \left\langle 4s_{1/2}\ \epsilon\ell_2'\ J\right|\left(\frac{r_1}{r_2^2}\right)\mathbf{C}_1^{(1)}\cdot\mathbf{C}_2^{(1)}\left|4p_{3/2}\ n_2\ell_2\ J\right\rangle . \tag{C.25}$$

The components of the spherical harmonic vectors $\mathbf{C}_i^{(1)}$ are given by equation C.15. The two radial matrix elements in equation C.25 can be separated and written in terms of electron 1 and electron 2 respectively. The angular matrix elements are coupled. Therefore, V can be written

$$V \;=\; <4s_{1/2}|r_1|4p_{3/2}>\left\langle \epsilon\ell_2'\right|\frac{1}{r_2^2}\left|n_2\ell_2\right\rangle\left\langle s_{1/2}\ \ell_2'\ J\right|\mathbf{C}_1^{(1)}\cdot\mathbf{C}_2^{(1)}\left|p_{3/2}\ \ell_2\ J\right\rangle . \tag{C.26}$$

The inner electron radial matrix element is calculated using the method of Lindgard and Nielsen and yields $1.439a_0$ [9]. The radial matrix element of the outer electron is calculated using a Numerov integration technique adapted for continuum wavefunctions [10]. The angular matrix element is separated through decoupling of the angular momenta of the two electrons [11]. The decoupling involves summing over all possible values of each of the coupling constants which leads to the same final state. A matrix

element is calculated for every allowed value of the parameters j, J, and M. Here j is the ℓs coupled angular momentum of electron 1, J is the total coupled angular momentum, and M is the $\hat{z}$ projection of J. For each value of these three parameters, the angular matrix element is given by

$$\left\langle (s_{1/2})j'\ \ell_2'\ JM \middle| \mathbf{C}_1^{(1)} \cdot \mathbf{C}_2^{(1)} \middle| (p_{3/2})j\ \ell_2\ JM \right\rangle\ =$$
$$(-1)^{j'+\ell+J} \left\{ \begin{array}{ccc} J & \ell_2' & j \\ 1 & j' & \ell_2 \end{array} \right\} < (s_{1/2})j' || \mathbf{C}_1^{(1)} || (p_{3/2})j > \times < \ell_2' || \mathbf{C}_2^{(1)} || \ell_2 > \ . \tag{C.27}$$

The quantity in braces is a Wigner 6-J symbol and the remaining matrix elements are reduced matrix elements [11]. Since the outer electron's spin is neglected, the reduced matrix element for the outer electron is given by

$$< \ell_2' || \mathbf{C}_2^{(1)} || \ell_2 > \ = \ (-1)^{\ell_2} \left(\begin{array}{ccc} \ell_2 & 1 & \ell_2' \\ 0 & 0 & 0 \end{array} \right) \sqrt{(2\ell_2+1)(2\ell_2'+1)}\ . \tag{C.28}$$

The spin contribution must be considered when evaluating the reduced angular matrix element for the inner electron. From Edmonds [11], the first angular matrix element in equation C.27 is given by

$$< (s_{1/2})j' || \mathbf{C}_1^{(1)} || (p_{3/2})j > \ =$$
$$\sqrt{3} \sum_{m,m',q} (-1)^{j-m} \left(\begin{array}{ccc} j & 1 & j' \\ -m & q & m' \end{array} \right) < (s_{1/2})j'm' | C_1^{(1)}(q) | (p_{3/2})jm > . \tag{C.29}$$

ℓn	15	18	21	25	30	35	40
0	50.1	28.9	18.2	10.8	5.76	.721	.0106
1	52.3	30.2	19.0	11.2	6.49	4.08	2.74
2	22.5	13.0	8.17	4.84	2.80	1.76	1.18
3	6.17	3.59	2.27	1.35	.781	.492	.330
4	1.11	.655	.418	.251	.146	.0925	.0621
5	.135	.0825	.0536	.0326	.0192	.0122	.00826
6	.0115	.00742	.00497	.00309	.00185	.00119	$8.08e^{-4}$
7	$7.06e^{-4}$	$4.90e^{-4}$	$3.42e^{-4}$	$2.20e^{-4}$	$1.35e^{-4}$	$8.79e^{-5}$	$6.02e^{-5}$
8	$3.13e^{-5}$	$2.42e^{-5}$	$1.79e^{-5}$	$1.21e^{-5}$	$7.64e^{-5}$	$5.07e^{-6}$	$3.52e^{-6}$
9	$1.00e^{-6}$	$9.01e^{-7}$	$7.25e^{-7}$	$5.19e^{-7}$	$3.43e^{-7}$	$2.33e^{-7}$	$1.64e^{-7}$
10	$2.30e^{-8}$	$2.56e^{-8}$	$2.29e^{-8}$	$1.78e^{-8}$	$1.24e^{-8}$	$8.71e^{-9}$	$6.26e^{-9}$
11	$3.68e^{-10}$	$5.52e^{-10}$	$5.71e^{-10}$	$4.90e^{-10}$	$3.66e^{-10}$	$2.67e^{-10}$	$1.97e^{-10}$

Table C.1: Calculated $4s$ continua autoionization rates for selected n,ℓ states in calcium in cm^{-1}.

The index q ranges over all possible $\hat{z}$ projections of ℓ. In this case, since $\ell = 1$, $q = -1$,0, or 1. m is the $\hat{z}$ projection of the combined angular momentum (j) of the inner electron.

To calculate the total value of the angular matrix element in equation C.26, matrix elements must be calculated for all allowed values of J, M, and j. The angular and radial matrix elements are then combined to determine the total $4s$ continua AI rate for each $|n, \ell, m >$ outer electron state in the quantum simulation. Selected AI rates are shown in table C.4.2. Rates for $\ell \geq 8$ are sufficiently small that the lifetime of the $4p_{3/2}$ inner excited state is shorter than the average time for autoionization.

C.4.3 Calculated Survival Probability

After the AI rates and the direct ionization are factored into the quantum simulations, a more accurate picture of the final state distribution emerges. We perform a simulation of the amount of ionization (due to both AI and direct ionization) as a function of time for Ca atoms subjected to a HCP field with low amplitude static negative tail. This simulation is similar to the calculations performed in chapter 5. AI is "turned on" at $t = 2$ ps and the simulation runs for 3 ns (approximately the spontaneous emission time of the $4p_{3/2}$ state). The un-ionized population is shown as a function of time in figure C.4. The initial Rydberg state is $n = 22$, $\ell = 2$, $m = 0$. Similar calculations are possible with any given combination of field pulses and static fields. For the initial parameters in this simulation, less than 1% of the initial population remains bound, regardless of the HCP field strength.

C.5 Rotation of Bases

When time dependent electric fields are applied along more than one axis, determining the "good" axis of the problem becomes difficult. The "good" axis is defined as the axis of the resultant field vector. Along this axis, m_r is a good quantum number, where m_r is the projection of the angular momentum along the resultant axis. If the direction of the resultant vector is constant throughout the entire simulation, then the m distribution

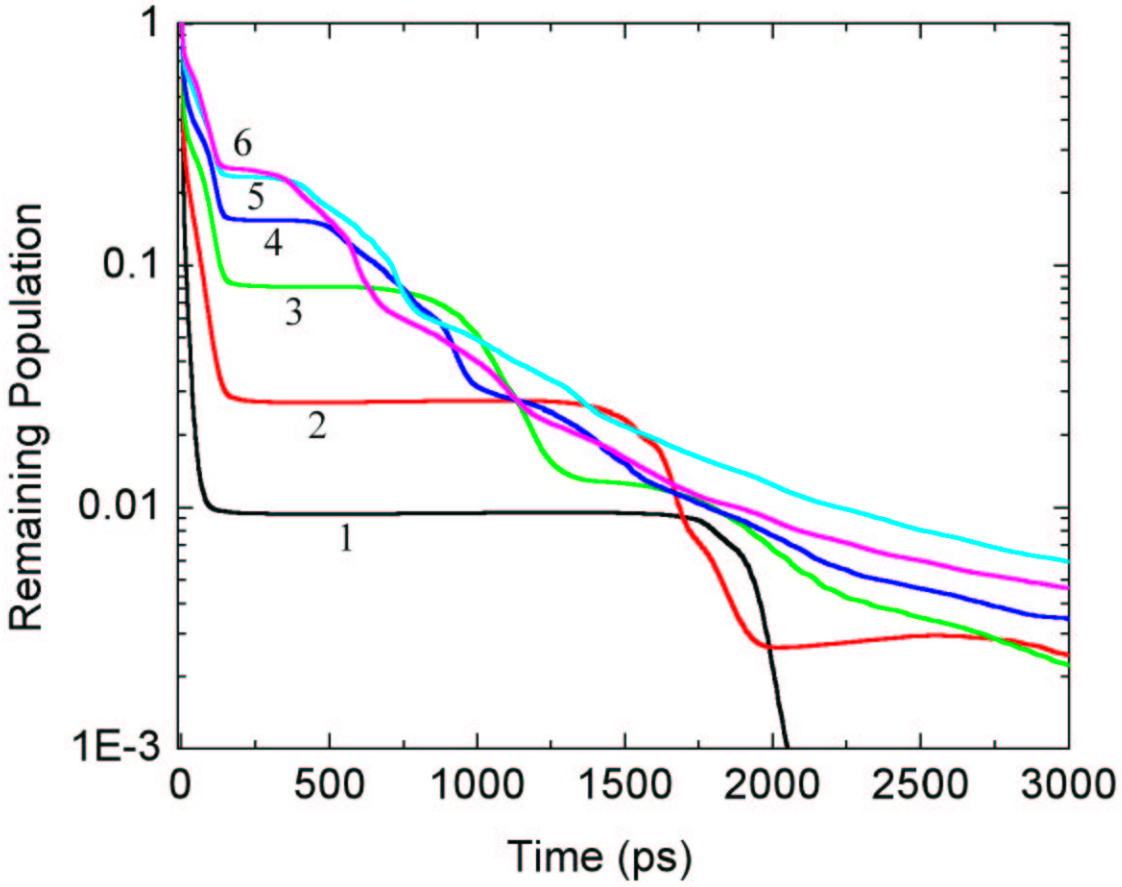

Figure C.4: Calculated survival probability of a $|22, 2, 0>$ initial Rydberg state subjected to a single HCP along the $\hat{z}$ axis of maximum field F. Following the HCP, a small static field is applied which has magnitude proportional to F to simulate the effect of the long negative tail on an experimentally generated HCP. Population is removed from the simulation due to both direct ionization and autoionization as discussed in the text. HCP fields of $F = 1, 2, 3, 4, 5, 6$ kV/cm are considered. Note the final population is greatest for $F = 5$ kV/cm. For $F > 5$ kV/cm, direct ionization instead of AI becomes as the main ionization mechanism.

along the resultant axis is unchanged. However, if the direction of the resultant field vector varies during the simulation, the m distribution along the resultant axis will also change. Also, the m distribution along any axis other than the resultant axis is time dependent and will change.

In the quantum simulations presented here, we measure only the final state m distribution. As the "good" axis may have changed drastically during the course of a quantum simulation, to ensure that we are measuring the m distribution along the correct (resultant) axis, we simply measure the m distribution along *every* axis. Typically, some set of candidates for the good axis of the problem is obvious. For example, if HCP fields of equal magnitude are applied along both the $+\hat{x}$ and $+\hat{z}$ axes, then the good axis of the problem is $\frac{1}{\sqrt{2}}(\hat{x}+\hat{z})$. When static fields are applied as well as HCP fields, the choice of the good axis is no longer straightforward, however we are able to at least narrow the choices down to a plane.

We define the axis $\hat{u}$ as being in the $\hat{xz}$ plane and making an angle θ with the $+\hat{z}$ axis. We also define an angular momentum operator $\hat{L}_u$ by the relation $\hat{L}_u|\ell m >_u = m_u|\ell m >_u$. The states $|\ell m >_u$ are eigenstates in the $\hat{u}$ basis with corresponding quantum numbers m_u. To project an m state distribution measured along $\hat{z}$ onto the $\hat{u}$ axis, we define an operator $\hat{L}_\theta$, given by

$$\begin{aligned} \hat{L}_\theta &= cos\theta\hat{L}_z + sin\theta\hat{L}_x \\ &= cos\theta\hat{L}_z + \left(\frac{sin\theta}{2}\right)\left(\hat{L}_+ + \hat{L}_-\right), \end{aligned} \tag{C.30}$$

where the $\hat{L}_+$ and $\hat{L}_-$ operators are the typical ladder operators along the $\hat{z}$ axis as defined in Landau and Lifshitz [1]. If the operator $\hat{L}_\theta$ acts on a state $|\ell m>$ in the $\hat{z}$ basis, the result is given by

$$\begin{aligned}\hat{L}_\theta\ |\ell m> \ &=\ (cos\theta)m|\ell m> \\ &+\ \left(\frac{sin\theta}{2}\right)\Big(\sqrt{(\ell-m)(\ell+m+1)}\ |\ell(m+1)> \\ &+\ \sqrt{(\ell+m)(\ell-m+1)}\ |\ell(m-1)>\Big)\ . \end{aligned} \tag{C.31}$$

A matrix is created of all allowed eigenvalues of $\hat{L}_\theta$ acting on the states $|\ell m>_z$. The matrix is tridiagonal. Its eigenvalues and eigenvectors are determined numerically [4]. The eigenvectors form a new rotation matrix which projects the m distribution of a state from the $\hat{z}$ basis to the new $\hat{u}$ basis. Therefore, if we measure a final state m distribution only along $\hat{z}$, we can rotate this distribution through any angle θ and see what the m distribution looks like along that axis.

As a test of the m rotation technique, a quantum simulation of a HCP field interacting with a Rydberg state is performed in a similar manner as discussed above. In this simulation however, the initial state is chosen such that $m = 0$ when measured along the $\hat{x}$ axis. In the $\hat{z}$ basis, this state has the form

$$|22,2,0>_x\ =\ \sqrt{\frac{3}{8}}\ |22,2,-2>_z\ -\ \frac{1}{2}\ |22,2,0>_z\ +\ \sqrt{\frac{3}{8}}\ |22,2,2>_z\ . \tag{C.32}$$

The HCP field is applied along the $\hat{x}$ axis. Despite the obvious choice of the preferred axis of integration ($\hat{x}$), the simulation is still performed in the $\hat{z}$ basis. The final state

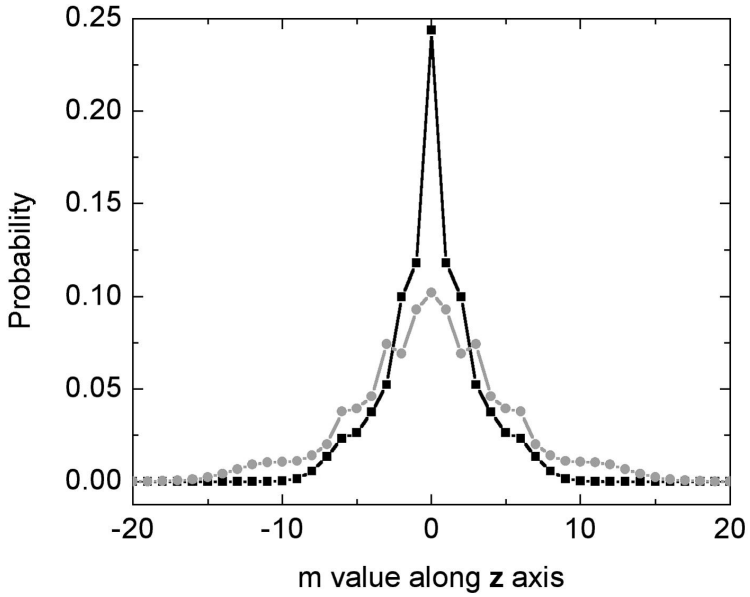

Figure C.5: An initial $|22, 2, 0>_x$ state is subject to a single HCP along the $\hat{x}$ axis of maximum field F. Following the HCP, a small static field is applied which has magnitude proportional to F to simulate the effect of the long negative tail on an experimentally generated HCP. The m distribution along the $\hat{z}$ axis is shown for HCP maximum fields of 2 kV/cm (black curve) and 4 kV/cm (grey curve). No population removal due to AI is performed in this simulation. The simulation runs for 2 ps and the basis set contains all n such that $10 \leq n \leq 35$.

m distribution along $\hat{z}$ is shown in figure C.5. When the final m distribution is rotated to the $\hat{x}$ axis, the entire population returns to $m = 0$. Since the initial population is entirely $m = 0$ along the good axis, and the fields are all applied along that axis, the final state distribution must also be $m = 0$ along this axis. The fact that the integration is performed along some other axis ($\hat{z}$) which is not the good axis of the problem leads to a complicated distribution of m values along that axis. However, the physical symmetry is still preserved throughout the simulation. In figure C.6 the m

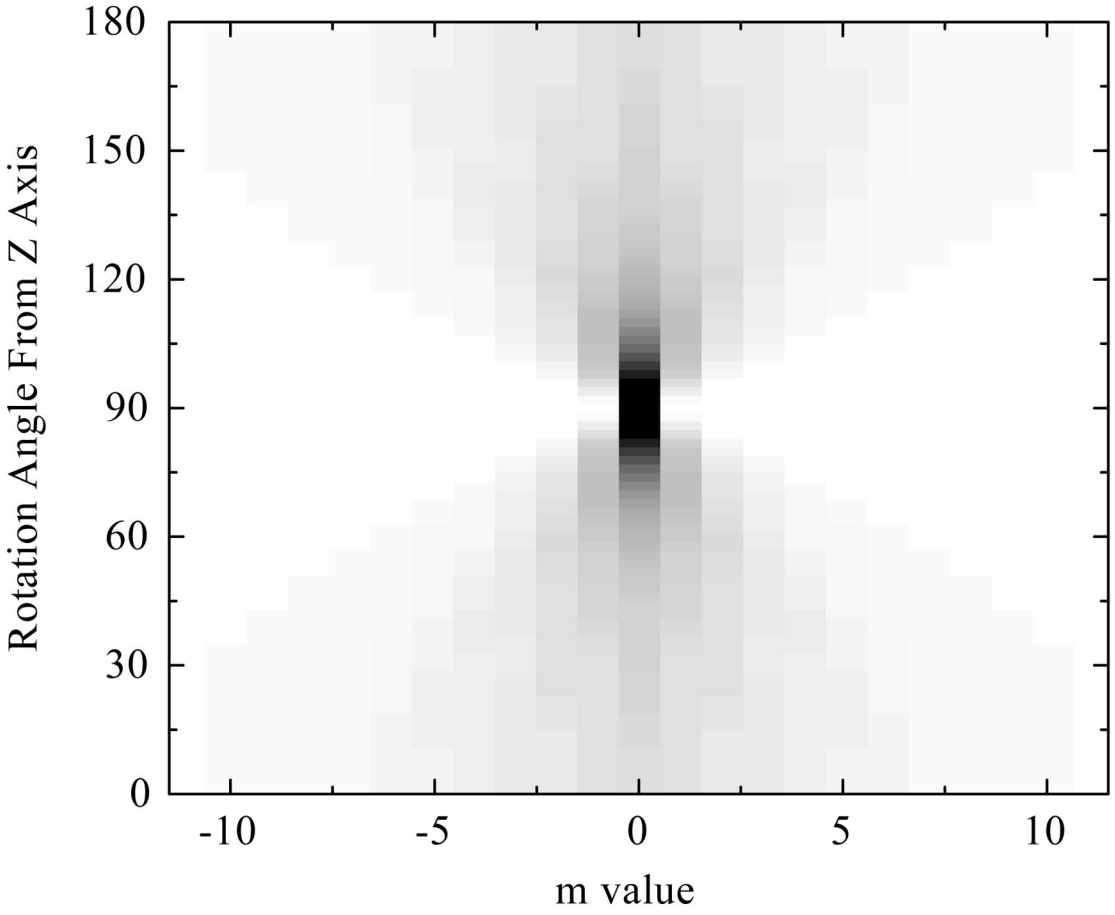

Figure C.6: An initial $|22, 2, 0>_x$ state is subject to a single HCP along the $\hat{x}$ axis of maximum field of 4 kV/cm. Following the HCP, a static field of 10 V/cm is applied along $\hat{x}$ to simulate the effect of the long negative tail of an experimentally generated HCP. The m probability distribution is shown in greyscale for m measured along all axes from $+\hat{z}$ to $-\hat{z}$. Due to the symmetry of the problem, the entire population has $m = 0$ along the $\hat{x}$ axis. The simulation runs for 2 ps and the basis set contains all n such that $10 \leq n \leq 35$.

distribution is shown for all axes in the $\hat{xz}$ plane. The complex distribution of values seen when m is measured along $\hat{z}$ collapses when the axis of measurement is changed from $+\hat{z}$ to $+\hat{x}$.

Choosing the correct axis to measure the m distribution is critical to understanding the electron dynamics of a given experiment. Even though the simulation above indicated a electron distribution containing high m values (see figure C.5), in fact we have just chosen a poor direction to measure the m distribution. To properly determine "what the atom thinks" the m distribution is, it is necessary to measure the m distribution along the good axis of the problem.

C.6 Conclusions

Quantum mechanical simulations are less intuitive and frequently more difficult than classical simulations. However, nature is inherently quantum mechanical. To properly understand the dynamics of an atomic system, quantum simulations are needed. The simulation methods presented in this appendix are fairly straightforward and useful, even if some approximations have been made for ease of computation and implementation. The goal of this appendix and the programs generated through the methods described here is to provide a fully quantum mechanical method to simulate physical processes. These simulations can be compared with experimental data such as the data presented in chapter 5.

Bibliography

[1] L.D. Landau and E.M. Lifshitz, *Quantum Mechanics, 3rd ed.*, Pergamon Press, Oxford, (1977).

[2] T. Brabec and F. Krausz, *Reviews of Modern Physics* **72**, 545 (2000).

[3] F. Robicheaux, *Phys. Rev. A* **60**, 431 (1999).

[4] W.H. Press, S.A. Teukolsky, W.T. Vetterling, and B.P. Flannery, *Numerical Recipes in C, 2nd ed.*, Cambridge University Press, Cambridge, (1992).

[5] The HCP profile used in the quantum calculations is identical to that used in the classical simulations and is shown graphically in figure 3.2. See chapter 3 for a full description of the experimental HCP profile and characteristics.

[6] J.G. Story, D.I. Duncan, and T.F. Gallagher, *Phys. Rev. Lett.* **71**, 3431 (1993); R.R. Jones, *Phys. Rev. A* **58**, 2608 (1998); W.E. Cooke, T.F. Gallagher, S.A. Edelstein, and R.M. Hill, *Phys. Rev. Lett.* **40**, 178 (1978).

[7] R.R. Jones, *Double Rydberg States of Barium*, Ph.D. Thesis, University of Virginia, (1990).

[8] R.R. Jones and T.F. Gallagher, *Phys. Rev. A* **38**, 2846 (1988); R.R. Jones and T.F. Gallagher, *ibid.* **39** 4583 (1989).

[9] A. Lindgard and S.E. Nielsen, *At. Data Nucl. Data Tables* **19**, 597 (1977).

[10] M.L. Zimmerman, *Phys. Rev. A* **20**, 225 (1979).

[11] A.R. Edmonds, *Angular Momentum in Quantum Mechanics*, Princeton University Press, Princeton, (1960).

Appendix D

The Stark Effect

Before studying the system of an atom in a static field, one must realize that atoms in externally applied electric fields (also known as a "Stark" fields) have already been the subject of considerable research [1–4]. Even though the problem is difficult to solve exactly for arbitrary atoms, if the electric field is relatively weak (below the field ionization limit) then perturbation theory can be applied to obtain approximate positions of the energy levels [1]. In this appendix, we apply a perturbative approach to gain an introductory understanding of the Stark effect.

In the first section of this appendix, an introduction to the Stark problem and to parabolic coordinates in general is given. This enables the reader to more easily follow arguments presented in chapters 4 and 5. Then, a treatment of the Stark problem specifically dealing with non-hydrogenic atoms is presented. Finally, a brief discussion

of how we calculate Stark maps of non-hydrogenic atoms is given.

D.1 Analytic Calculations for Hydrogenlike Atoms

D.1.1 Introduction

The presence of an external static electric field breaks the spherical symmetry of the Coulomb potential [1]. The lack of spherical symmetry means ℓ is no longer a good quantum number and angular momentum is no longer conserved. Eigenstates of the Stark potential do not have a well defined value of ℓ, nor well defined parity. In this treatment of the Stark effect, it is assumed without loss of generality that the static field is applied along the $\hat{z}$ axis such that $\vec{F} = F\hat{z}$. Furthermore, we choose to perform calculations in the "length" gauge given by $V = \vec{E} \cdot \vec{r}$. The analysis in this section is done for the purely hydrogenic case where the Coulomb potential is valid for all $r > 0$. The results will be extended to non-hydrogenic atoms through the use of quantum defect theory in the following section.

The time independent Schrödinger equation for a hydrogen atom in a static field is given by

$$\left(\frac{\nabla^2}{2} + E + \frac{Z}{r} - Fz\right)\psi \;=\; 0. \tag{D.1}$$

This system may be solved directly through matrix diagonalization, however perturbation theory can also be used to obtain approximate solutions. This is useful if the

basis set is quite large and therefore the matrix diagonalization is difficult. Although the system may be treated in spherical coordinates, the symmetry of the problem lends itself to parabolic coordinates [2]. The coordinate transformations from spherical to parabolic coordinates are given by

$$\xi \;=\; r+z\;, \quad \eta \;=\; r-z\;, \quad \text{and} \quad \phi = tan^{-1}\Big(\frac{y}{x}\Big)\;, \tag{D.2}$$

and the volume element is $dV \;=\; \frac{1}{4}(\xi+\eta)d\xi d\eta d\phi$. In parabolic coordinates, the Schrödinger equation (D.1) becomes

$$\frac{\partial}{\partial\xi}\Big(\xi\frac{\partial\psi}{\partial\xi}\Big)+\frac{\partial}{\partial\eta}\Big(\eta\frac{\partial\psi}{\partial\eta}\Big)+\Big(\frac{1}{4\xi}+\frac{1}{4\eta}\Big)\frac{\partial^2\psi}{\partial\phi^2}+\Big[\frac{1}{2}E(\xi+\eta)+Z-\frac{1}{4}F(\xi^2-\eta^2)\Big]\psi \;=\; 0. \tag{D.3}$$

Equation D.3 is separable, having solutions of the form

$$\psi \;=\; u_1(\xi)u_2(\eta)e^{\pm im\phi}. \tag{D.4}$$

For the rest of this appendix, we define the magnetic quantum number to be positive. Therefore, $m = |m|$. This is the reason for the $\pm$ in equation D.4. Any time when negative values of m are to be included, they will be included explicitly as $\pm m$.

Two differential equations result from the separation performed in equation D.4,

$$\frac{\partial}{\partial\xi}\Big(\xi\frac{\partial u_1}{\partial\xi}\Big)+\Big(\frac{1}{2}E\xi+Z_1-\frac{m^2}{4\xi}-\frac{1}{4}F\xi^2\Big)u_1 \;=\; 0 \tag{D.5}$$

and

$$\frac{\partial}{\partial\eta}\Big(\eta\frac{\partial u_2}{\partial\eta}\Big)+\Big(\frac{1}{2}E\eta+Z_2-\frac{m^2}{4\eta}+\frac{1}{4}F\eta^2\Big)u_2 \;=\; 0\;. \tag{D.6}$$

Z_1 and Z_2 are the amounts of nuclear charge seen by the electron and m is the projection of the angular momentum on the $\hat{z}$ axis [2]. The total core charge Z in equation D.1 is the sum of the separation constants Z_1 and Z_2. It is worth noting that the eigenvalues of equations D.5 and D.6 are Z_1 and Z_2 respectively, rather than the energy E, as in equation D.1. Our intention is to expand the eigenvalues in powers of the field F. We begin with zeroth order perturbation theory, where the field term is ignored altogether ($F = 0$).

D.1.2 Zero Field Solution

To solve the second order differential equations D.5 and D.6 for $F = 0$, four boundary conditions are needed. We examine the asymptotic behavior of the differential equations to determine these boundary conditions. A useful quantity ϵ is defined as $\epsilon \equiv \sqrt{-2E}$ for ease of notation. As $\xi, \eta \to 0$,

$$u_1^{(0)}(\xi) \ \sim \ \xi^{m/2} \quad \text{and} \quad u_2^{(0)}(\eta) \ \sim \ \eta^{m/2} \ . \tag{D.7}$$

The superscripts on the u_1 and u_2 eigenfunctions indicate these are zeroth order solutions. Furthermore, as $\xi, \eta \to \infty$,

$$u_1^{(0)}(\xi) \ \sim \ e^{-\xi\epsilon/2} \quad \text{and} \quad u_2^{(0)}(\eta) \ \sim \ e^{-\eta\epsilon/2} \ . \tag{D.8}$$

With these boundary conditions, polynomial solutions are sought of the form

$$u_1^{(0)}(\xi) \ = \ \xi^{m/2} e^{-\xi\epsilon/2} f_1(\xi) \quad \text{and} \quad u_2^{(0)}(\eta) \ = \ \eta^{m/2} e^{-\eta\epsilon/2} f_2(\eta) \ . \tag{D.9}$$

A change of variables is made for convenience. We define $x \equiv \epsilon\xi$, and $y \equiv \epsilon\eta$. The resulting second order differential equations

$$x\frac{d^2 f_1}{dx^2} + (m+1-x)\frac{df_1}{dx} + \left(\frac{Z_1^{(0)}}{\epsilon} - \frac{m+1}{2}\right)f_1 \;=\; 0 \tag{D.10}$$

and

$$y\frac{d^2 f_2}{dy^2} + (m+1-y)\frac{df_2}{dy} + \left(\frac{Z_2^{(0)}}{\epsilon} - \frac{m+1}{2}\right)f_2 \;=\; 0 \tag{D.11}$$

are solved by the associated Laguerre polynomials. The superscripts on the parabolic separation constants Z_1 and Z_2 again indicate these are zeroth order perturbation values. The resulting solutions are given by

$$f_1(x) \;=\; L^m_{n_1+m}(x) \quad \text{and} \quad f_2(y) \;=\; L^m_{n_2+m}(y)\ . \tag{D.12}$$

Since f_1 and f_2 must remain finite at large values of ξ and η respectively, the parameters n_1 and n_2 must be non-negative integers. Therefore,

$$n_1 \;=\; \frac{Z_1^{(0)}}{\epsilon} - \frac{m+1}{2} \quad \text{and} \quad n_2 \;=\; \frac{Z_2^{(0)}}{\epsilon} - \frac{m+1}{2}\ . \tag{D.13}$$

Rearranging for $Z_1^{(0)}$ and $Z_2^{(0)}$ we find

$$Z_1^{(0)} \;=\; \left(n_1 + \frac{m+1}{2}\right)\epsilon \quad \text{and} \quad Z_2^{(0)} \;=\; \left(n_2 + \frac{m+1}{2}\right)\epsilon\ . \tag{D.14}$$

Solving for $Z = Z_1^{(0)} + Z_2^{(0)}$, we find

$$\frac{Z}{\epsilon} \;=\; n_1 + n_2 + m + 1\ . \tag{D.15}$$

Equation D.15 can then be solved for the energy E, resulting in

$$E_0 \;=\; \frac{-\epsilon^2}{2} \;=\; -\frac{Z^2}{2(n_1+n_2+m+1)^2}\;. \tag{D.16}$$

Since the field free energy levels are well known ($E_n = -\frac{Z^2}{2n^2}$), from equation D.16 we derive a relation between n_1, n_2, m, and n,

$$n \;=\; n_1+n_2+m+1\;. \tag{D.17}$$

The variables n_1 and n_2 are known as the parabolic quantum numbers and are related to the amount of charge on the either side of the $\hat{z}$ axis [1].

To obtain the actual parabolic eigenfunctions $u_1^{(0)}(\xi)$ and $u_2^{(0)}(\eta)$ (defined by equations D.5 and D.6), the normalization conditions

$$\int_0^\infty u_1^2(\xi)d\xi = 1 \quad \text{and} \quad \int_0^\infty u_2^2(\eta)d\eta = 1 \tag{D.18}$$

are applied. The resulting normalized parabolic eigenfunctions are

$$u_1^{(0)}(\xi) \;=\; \frac{n_1!^{\frac{1}{2}}}{(n_1+m)!^{\frac{3}{2}}} e^{-\epsilon\xi/2}\xi^{m/2}\epsilon^{(m+1)/2}L^m_{n_1+m}(\epsilon\xi) \tag{D.19}$$

and

$$u_2^{(0)}(\eta) \;=\; \frac{n_2!^{\frac{1}{2}}}{(n_2+m)!^{\frac{3}{2}}} e^{-\epsilon\eta/2}\eta^{m/2}\epsilon^{(m+1)/2}L^m_{n_2+m}(\epsilon\eta)\;. \tag{D.20}$$

Unlike the spherical eigenfunctions, the eigenfunctions given in equations D.19 and D.20 are not symmetric with the plane $z = 0$. If $n_1 > n_2$, a larger part of the charge distribution lies on the positive side of z, while the reverse is true if $n_1 < n_2$ [1]. The parabolic eigenfunctions are shown in figure D.1 for $n = 8$, $m = 0$ [5].

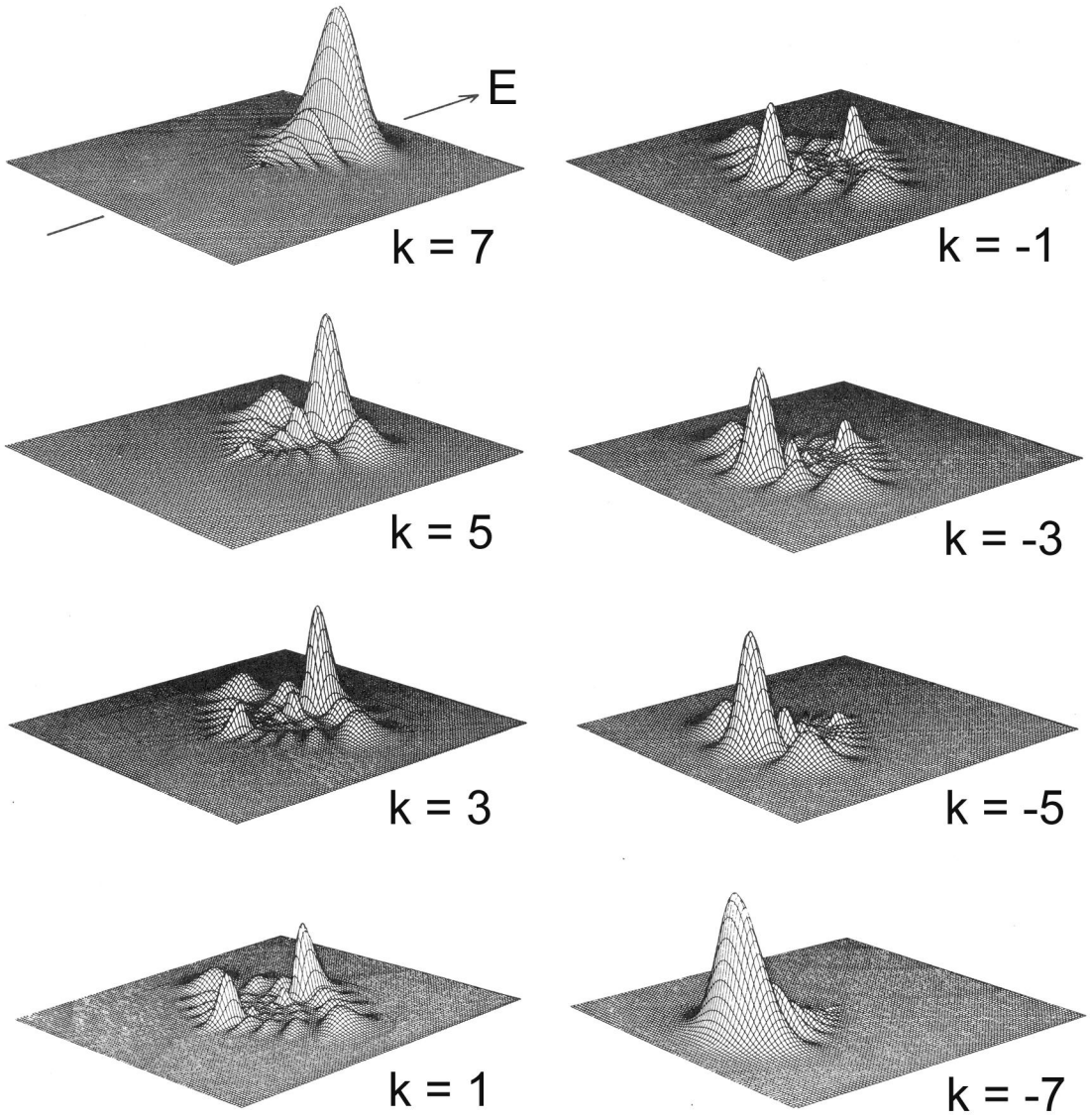

Figure D.1: Hydrogenic charge distributions of the parabolic eigenstates for $n = 8$, $m = 0$ [5]. The parabolic quantum number k is defined to be $n_1 - n_2$. The overall dipole moments of the distributions are obvious. The nodes of each eigenstate form families of parabolas.

D.1.3 Changing Bases

Both the parabolic eigenfunctions and the familiar spherical eigenfunctions form complete, orthonormal bases. Since both sets span the same Hilbert space, it is therefore possible to perform projections of a state in one space into the other. We define the variable k as the projection of the electric dipole moment along the $\hat{z}$ axis. k is given by the difference between the parabolic quantum numbers n_1 and n_2. A state $|n_1, n_2, m>$ can be written

$$|n_1, n_2, m> \equiv |nkm> = \sum_{\ell} a_{\ell,k} \, |n\ell m> \ . \tag{D.21}$$

The states $|n\ell m>$ are the standard spherical angular momentum states and the coefficients $a_{\ell,k}$ are the Clebsch-Gordan coefficients $< n\ell m|nkm >$. The $a_{\ell,k}$ coefficients are most typically given in the form of a Wigner 3J symbol as [6]

$$< n\ell m|nkm > = (-1)^m \sqrt{2\ell+1} \begin{pmatrix} \frac{1}{2}(n-1) & \frac{1}{2}(n-1) & \ell \\ \frac{1}{2}(m+k) & \frac{1}{2}(m-k) & -m \end{pmatrix} . \tag{D.22}$$

A very similar relation to equation D.21 is used to perform the inverse transformation, if desired. A given $|n\ell m>$ state can be written as a coherent sum of Stark states of the form

$$|n, \ell, m> = \sum_{k} a_{k,\ell} \, |nkm> \ . \tag{D.23}$$

The matrix elements $< nkm|n\ell m >$ in equation D.23 are the same as the $< n\ell m|nkm >$ matrix elements from equation D.21. Such projections are useful if a given angular momentum state is excited in zero field, and then subsequently subjected to an electric

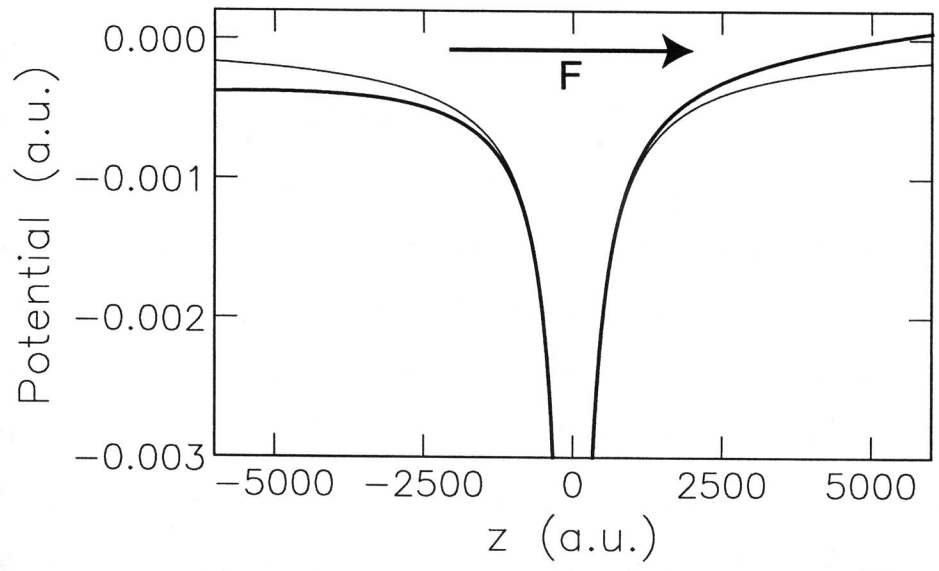

Figure D.2: The combined Coulomb and static field potentials (known as the Stark potential). The direction of the higher potential is known as the "uphill" or "blue" part, while the region of lower potential is known as the "downhill" or "red" part. The zero field Coulomb potential is shown in the light curve for reference.

field. Then an initial spherical state can be expressed in terms of a superposition of Stark states.

D.1.4 First Order Perturbation Theory

Extending the analysis of the parabolic system to first order in perturbation theory involves re-introduction of the linear field terms from equations D.5 and D.6. The first order perturbation to the eigenvalues is given by

$$Z_1^{(0,1)} \;=\; Z_1^{(0)} + Z_1^{(1)} \;=\; Z_1^{(0)} + \frac{1}{4}\left(\frac{F}{\epsilon^2}\right) < u_1^{(0)}|\xi^2|u_1^{(0)} > \qquad \text{(D.24)}$$

and

$$Z_2^{(0,1)} \;=\; Z_2^{(0)} + Z_2^{(1)} \;=\; Z_2^{(0)} - \frac{1}{4}\Big(\frac{F}{\epsilon^2}\Big) < u_2^{(0)}|\eta^2|u_2^{(0)} > \;\;, \tag{D.25}$$

where the field free eigenfunctions $u_1^{(0)}$ and $u_2^{(0)}$ are given by equations D.19 and D.20 respectively. Calculating the matrix element in equation D.24 yields

$$< u_1^{(0)}|\xi^2|u_1^{(0)} > \;\;=\;\; \int_0^\infty \xi^2 u_1^2(\xi)d\xi \;\;=\;\; \frac{n_1!}{(n_1+m)!^3} \;\int_0^\infty \epsilon^{m+1}\xi^{m+2}e^{-\epsilon\xi}(L^m_{n_1+m}(\epsilon\xi))^2 d\xi \;. \tag{D.26}$$

Solving the integral in equation D.26 and combining with equation D.14 results in [1]

$$Z_1^{(0,1)} \;=\; \epsilon\Big(n_1 + \frac{m+1}{2}\Big) + \frac{1}{4}\Big(\frac{F}{\epsilon^2}\Big)(6n_1^2 + 6n_1m + m^2 + 6n_1 + 3m + 2) \;. \tag{D.27}$$

Performing similar calculations for $Z_2^{(0,1)}$ results in a similar expression,

$$Z_2^{(0,1)} \;=\; \epsilon\Big(n_2 + \frac{m+1}{2}\Big) - \frac{1}{4}\Big(\frac{F}{\epsilon^2}\Big)(6n_2^2 + 6n_2m + m^2 + 6n_2 + 3m + 2) \;. \tag{D.28}$$

Combining equations D.27 and D.28 and solving for ϵ, keeping only first order F terms yields

$$\epsilon \;=\; \frac{Z}{n} - \frac{3}{2}F\Big(\frac{n}{Z}\Big)^2(n_1 - n_2) \;. \tag{D.29}$$

Therefore, to first order in F, the energy levels are given by

$$E_1 \;=\; -\frac{1}{2}\epsilon^2 \;=\; -\frac{Z^2}{2n^2} + \frac{3}{2}\frac{Fn}{Z}(n_1 - n_2) \;. \tag{D.30}$$

The parabolic eigenfunctions given by equations D.19 and D.20 are unchanged in first order perturbation theory. This is the main advantage of solving the Stark problem in

parabolic coordinates. The energy levels exhibit a linear shift depending on the value of the parabolic quantum number k. States with higher energies ($k > 0$ and $n_1 > n_2$) are known as "uphill" or blue states as the states are shifted to higher (bluer) frequencies with increasing field. Likewise, states with lower energies ($k < 0$ and $n_1 < n_2$) are known as "downhill" or red states. The potential is shown in figure D.2, illustrating the uphill and downhill sides.

A constant of interest is the averaged value of the field term, $< Fz >$. We find that

$$< Fz > \;=\; \frac{3}{2} F \Big(\frac{n}{Z} \Big) (n_1 - n_2) \; . \tag{D.31}$$

Dividing by the field F, we find

$$< z > \;=\; \frac{3}{2} \frac{n^2}{Z} \Big(\frac{n_1 - n_2}{n} \Big) \;=\; < r >_s M_z \; . \tag{D.32}$$

The quantity $< z >$ is the averaged dipole moment induced by the field, M_z is the z projection of the Runga-Lenz vector, and $< r >_s$ is the average radial position of an ns orbital. The Runga-Lenz vector $\vec{M}$ is a constant of the motion. The $\hat{z}$ projection of $\vec{M}$ is also given by $< cos\theta >_s$ and defines the cosine of the angle that an s orbital makes with the $\hat{z}$ axis in a given Stark state [7,8]. By definition, $-1 \leq M_z \leq 1$.

D.1.5 Stark Maps

A plot of all the energy levels for a given n state as a function of both energy and field is known as a Stark map. An example of a Stark map section for hydrogen is shown

in figure D.3. All the Stark states with a given n value make up one Stark manifold. The Stark states in a given manifold with the largest energy shifts (extremal states) are determined by setting the value of k to

$$k \;=\; \pm\,(n-m-1)\;. \tag{D.33}$$

In equation D.33, the + sign refers to the bluest state, while the − sign refers to the reddest state of a given n manifold. The width of a manifold is defined as the energy spacing between the reddest and bluest states. The width is given by

$$\Delta E_{manifold} \;=\; \frac{3Fn}{Z}(n-m-1)\;. \tag{D.34}$$

For small values of m and large values of n (the typical experimental conditions studied in this thesis), equation D.34 is approximated by

$$\Delta E_{manifold} \;\approx\; \frac{3Fn^2}{Z}\;. \tag{D.35}$$

Also of interest is the energy spacing between individual Stark states within one n manifold. This spacing is determined by using adjacent values of n_1 and n_2 in equation D.30 and is given by $\Delta E_{Stark} = 3Fn/Z$.

As the field strength is further increased, states from adjacent Stark manifolds begin to cross. The crossing occurs at a field F_c when the downward shifted energy of the reddest state of the $(n+1)^{th}$ manifold and the upward shifted energy of the bluest state of the n^{th} manifold are equal. To determine F_c, the zero field energy difference of the

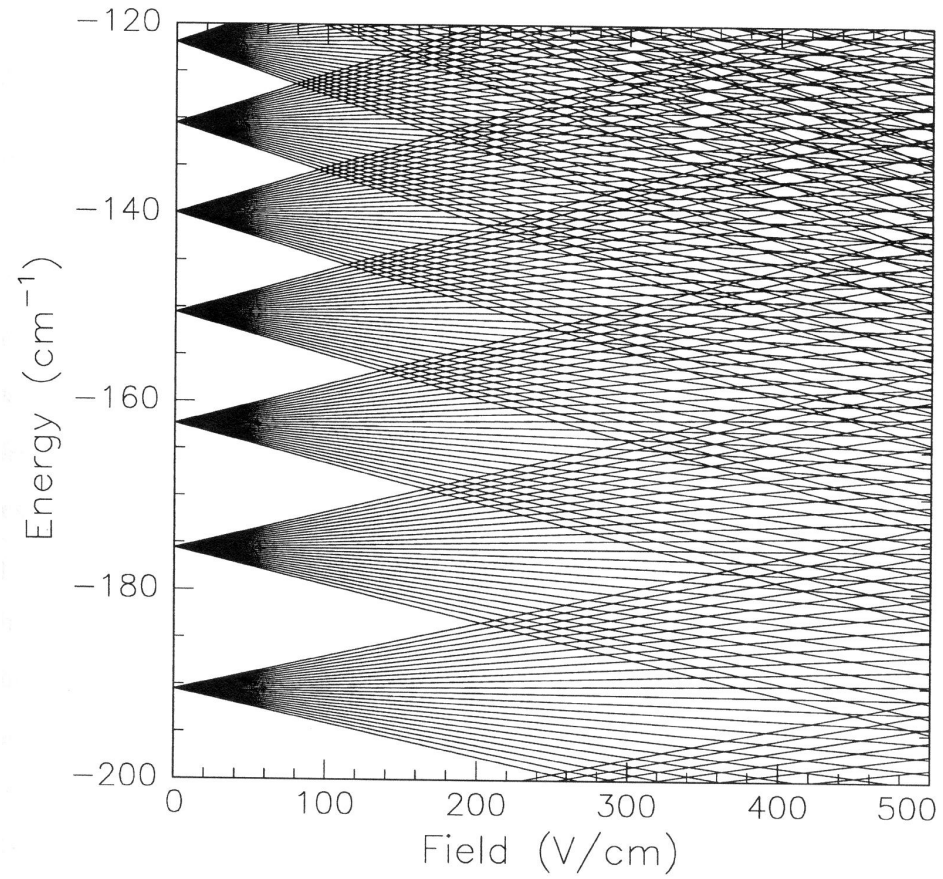

Figure D.3: A Stark map section of hydrogen ($m = 0$).

two states is set equal to the sum of the two Stark shifts.

$$E_{n+1} - E_n = -\Delta E_{red}(n+1) + \Delta E_{blue}(n) \tag{D.36}$$

$$-\frac{Z^2}{2(n+1)^2} + \frac{Z^2}{2n^2} = \frac{1}{Z}\left(\frac{3}{2}F_c(n+1)(n-m) + \frac{3}{2}F_c(n)(n-m-1)\right) \tag{D.37}$$

$$\frac{Z^3}{2n^2}\left(1 - \frac{1}{(1+\frac{1}{n})^2}\right) = \frac{3}{2}F_c(2n^2 - 2mn - m) \tag{D.38}$$

In the case where $n \gg 1$ and $m \ll n$, equation D.38 can be solved for F_c yielding

$$F_c \approx \frac{Z^3}{3n^5} \; . \tag{D.39}$$

The field given in equation D.39 is known as the Inglis - Teller limit. For field values greater than this limit, adjacent n manifolds cross. The value of the Inglis - Teller limit in equation D.39 only strictly applies in the case of hydrogenlike atoms [9].

D.1.6 Higher Order Effects

For increasing field strengths, the effects of higher order perturbation terms must be considered. Introducing the second order perturbative term to equation D.24 yields

$$Z_1^{(0,1,2)} = Z_1^{(0)} + \frac{F}{4}\frac{1}{\epsilon^2} < u_1^{(0)}|\xi^2|u_1^{(0)} > + \left(\frac{F}{4}\right)^2 \sum_{n_1' \neq n_1} \frac{|(\xi^2)_{n_1 n_1'}|^2}{Z_1^{(0)}(n_1) - Z_1^{(0)}(n_1')} \ . \quad \text{(D.40)}$$

All non-diagonal matrix elements of the ξ^2 matrix vanish if $n_1' > n_1 + 2$ or $n_1' < n_1 - 2$. The remaining nonzero elements are given by

$$(\xi^2)_{n_1,n_1-1} = -\frac{2}{\epsilon^2}(2n_1 + m)\sqrt{n_1(n_1+m)} \quad \text{(D.41)}$$

$$(\xi^2)_{n_1,n_1-2} = \frac{1}{\epsilon^2}\sqrt{n_1(n_1-1)(n_1+m)(n_1+m-1)} \ . \quad \text{(D.42)}$$

The denominator in equation D.40 can be simplified as

$$Z_1^{(0)}(n_1) - Z_1^{(0)}(n_1') = \epsilon(n_1 - n_1') \ . \quad \text{(D.43)}$$

Evaluation of only the second order term in equation D.40 yields

$$Z_1^{(2)} = \frac{1}{32}\frac{F^2}{\epsilon^5}(m + 2n_1 + 1)[8m^2 + 34(2mn_1 + 2n_1^2 + m + 2n_1) + 36] \ . \quad \text{(D.44)}$$

An expression for $Z_2^{(2)}$ is similarly derived. Combining results for the first 2 orders

for Z, we obtain

$$Z \;=\; (Z_1^{(0)} + Z_2^{(0)}) + (Z_1^{(1)} + Z_2^{(1)}) + (Z_1^{(2)} + Z_2^{(2)}) \tag{D.45}$$

$$Z \;=\; \epsilon n \;+\; \frac{3}{2}\Big(\frac{Fn}{\epsilon^2}\Big)(n_1 - n_2) \;-\; \frac{1}{16}\Big(\frac{F^2 n}{\epsilon^5}\Big)[17n^2 + 51(n_1 - n2)^2 - 9m^2 + 19]\;. \tag{D.46}$$

Equation D.46 results in a value of the hydrogenic Stark energy levels correct to second order in the field,

$$E_2 \;=\; -\frac{1}{2}\epsilon^2 \;=\; -\frac{Z^2}{2n^2} \;+\; \frac{3}{2}\frac{Fn}{Z}(n_1 - n_2) \;-\; \frac{1}{16}F^2\Big(\frac{n}{Z}\Big)^4[17n^2 - 3(n_1 - n2)^2 - 9m^2 + 19]\;. \tag{D.47}$$

Unlike the linear Stark shift, the quadratic shift depends explicitly on the magnitude of the magnetic quantum number m. Furthermore, in second order the parabolic eigenstates are no longer the good eigenstates of the problem. The quadratic shift is always negative and always lowers the energy of the Stark states. In the experiments presented in this thesis, the effect of the quadratic Stark shift is neglected, although some effects are discussed in [10]. At field strengths in which second order perturbation techniques become necessary, other strong field effects such as direct field ionization may also occur. This effect is an integral part of the experiment presented in chapter 4. A description of direct field ionization is therefore presented in the analysis there.

D.2 Non-Hydrogenic Atoms

D.2.1 Introduction

A derivation of the hydrogenic energy levels in the presence of an external electric field was presented in section D.1. In this section, the previous analysis is extended to non-hydrogenic atoms. A brief discussion of quantum defects is presented, followed by a description of the method used to generate non-hydrogenic Stark maps. Finally, some examples of calculated Stark maps are presented for non-hydrogenic atoms.

D.2.2 Quantum Defects

The analysis of the Stark effect in non-hydrogenic atoms depends heavily on quantum defect theory [2, 9, 11–13]. To gain an understanding of the role quantum defects have in the Stark problem, a cursory treatment of quantum defect theory is presented here. We start with the field free radial Schrödinger equation in spherical coordinates for an electron in a Coulomb potential, given by

$$\frac{\partial^2 \chi}{\partial r^2} \; + \; 2\Big[E \; + \; \frac{Z}{r} \; - \; \frac{\ell(\ell+1)}{2r^2}\Big]\chi \; = \; 0 \; . \tag{D.48}$$

A parameter ν is defined by $E \; = \; -\frac{1}{2\nu^2}$, where E is the total energy of the electron. For negative values of E (bound electrons) the most general solution to equation D.48 is given by [9]

$$\chi(\ell, r, \nu) \; \propto \; f(\ell, \nu, r) cos(\pi\delta_\ell) \; - \; g(\ell, \nu, r) sin(\pi\delta_\ell) \; . \tag{D.49}$$

The functions $f(\ell,\nu,r)$ and $g(\ell,\nu,r)$ are individual orthonormal solutions to equation D.48 which must satisfy appropriate boundary conditions. By examining the behavior of $f(\ell,\nu,r)$ and $g(\ell,\nu,r)$ as $r \rightarrow 0$ and $r \rightarrow \infty$ these boundary conditions can be determined. As $r \rightarrow 0$, it is required that

$$f(\ell,\nu,r) \;\rightarrow\; r^{\ell+1} \quad \text{and} \quad g(\ell,\nu,r) \;\rightarrow\; r^{-\ell}\,, \tag{D.50}$$

and when $r \rightarrow \infty$,

$$f(\ell,\nu,r) \;\rightarrow\; u(\ell,\nu,r)sin(\pi\nu) - v(\ell,\nu,r)e^{i\pi\nu} \tag{D.51}$$

$$g(\ell,\nu,r) \;\rightarrow\; -u(\ell,\nu,r)cos(\pi\nu) + v(\ell,\nu,r)e^{i\pi(\nu+1/2)}\,. \tag{D.52}$$

The functions $u(\ell,\nu,r)$ and $v(\ell,\nu,r)$ are given by [9]

$$u(\ell,\nu,r) \;\equiv\; (-1)^{\ell}\sqrt{\nu}\frac{1}{\pi}\left(\frac{2r}{\nu}\right)^{\nu} e^{r/\nu}\sqrt{\Gamma(\nu-\ell)\Gamma(\nu+\ell+1)} \tag{D.53}$$

$$v(\ell,\nu,r) \;\equiv\; (-1)^{\ell}\sqrt{\nu}\left(\frac{\nu}{2r}\right)^{\nu} e^{-r/\nu}\frac{1}{\sqrt{\Gamma(\nu-\ell)\Gamma(\nu+\ell+1)}}\,. \tag{D.54}$$

In the case of a hydrogenic atom, it is necessary that $\chi(\ell,r,\nu)$ be finite at $r = 0$. Therefore, δ_ℓ must be an integer due to the behavior of the function $g(\ell,\nu,r)$ in equation D.49. Furthermore, the coefficient of $u(\ell,\nu,r)$ must vanish as $r \rightarrow \infty$. This requires that $sin(\pi\nu) = 0$, or that ν be an integer. This is the typical quantization condition for hydrogenlike atoms [1]. In non-hydrogenic atoms however, the requirement that $\chi(\ell,r,\nu)$ be finite as $r \rightarrow 0$ is relaxed due to the non-Coulombic behavior of the potential near $r = 0$. The remaining boundary condition, that the wavefunction not explode as

$r \rightarrow \infty$ is satisfied if $sin[\pi(\nu + \delta_\ell)] = 0$. Therefore, $\nu + \delta_\ell$ must take on integer values. The quantity δ_ℓ is known as the quantum defect.

The field free energy of a given n, ℓ state in a non-hydrogenic atom is given by

$$E = -\frac{1}{2(n - \delta_\ell)^2} . \tag{D.55}$$

Table D.2.2 shows quantum defects for the first four ℓ values of calcium [14]. In practice, quantum defects vary as a function of both n and ℓ. In most cases, the variation as a function of n is small and quantum defect values are simply quoted for each value of ℓ. This is the case for the s, p, and $\ell > 2$ series in calcium. However the presence of a perturbing state shifts the quantum defects of the d states strongly as a function of n. In general for a given ℓ state, the larger the size of the atomic core, the larger the value of the quantum defects. Also, the smaller the ℓ value for a given n state, the larger the quantum defect. In both cases, smaller quantum defects indicate less overlap with the atomic core.

Low ℓ states of non-hydrogenic atoms in zero field are not degenerate with the rest of the ℓ manifold due to their nonzero quantum defects. In a weak field, high ℓ states with $\delta_\ell \approx 0$ fan out just like hydrogenic states and form a Stark manifold. However, states with non-negligible quantum defects are not affected by the weak static field to first order. In this case, the energy difference between the low ℓ states and high ℓ states of a given manifold is large when compared to the spacing between individual Stark

n	δ_s	δ_p	δ_d	δ_f
15	2.34	1.88	0.819	.085
16	2.34	1.88	0.862	.085
17	2.34	1.88	0.901	.085
18	2.34	1.88	0.939	.085
19	2.34	1.88	0.975	.085
20	2.34	1.88	1.007	.085
21	2.34	1.88	1.036	.085
22	2.34	1.88	1.059	.085
23	2.34	1.88	1.082	.085
24	2.34	1.88	1.110	.085
25	2.35	1.88	1.119	.085
26	2.35	1.88	1.135	.085
27	2.35	1.88	1.150	.085
28	2.35	1.88	1.168	.085
29	2.35	1.88	1.177	.085
30	2.35	1.88	1.175	.085
31	2.35	1.88	1.186	.085
32	2.35	1.88	1.192	.085
33	2.35	1.88	1.199	.085
34	2.35	1.88	1.197	.085
35	2.35	1.88	1.210	.085

Table D.1: Experimentally obtained values for the quantum defects in calcium [14].

states. The first order correction to the energy level positions is given by

$$\Delta E_{low\ell} \propto \frac{|<low\ell state|Fz|high\ell state>|^2}{E_{low\ell} - E_{high\ell}} . \tag{D.56}$$

In the weak field case, the zero field energy difference in the denominator is many times larger than the spacing between adjacent states in the hydrogenic portion of the Stark manifold ($|<Fz>|^2$). Due to the large factor in the denominator, the energy shift of the low ℓ states in weak fields is almost zero. However, as F increases, the states in the high ℓ manifold spread out. Once the extremal state in the hydrogenic portion of

the Stark manifold reaches the zero field energy of a low ℓ state, then the numerator in equation D.56 becomes much larger due to the increased interaction between the states. The energies of the low ℓ states then shift from their zero field values. In effect, each low ℓ states is repelled by the rest of the Stark manifold.

It is useful to determine the field at which a given low ℓ state encounters the high ℓ, hydrogenic states of the rest of the Stark manifold. To calculate this field value, the zero field energy of the low ℓ state is set equal to the energy of the closest hydrogenic n state in the linear Stark approximation, yielding

$$-\frac{1}{2(n-\delta_\ell)^2} = -\frac{1}{2n^2} + \frac{3}{2}F_0 n(1-n-m)\ , \qquad 0 \le \delta_\ell \le 0.5, \qquad \text{(D.57)}$$

$$-\frac{1}{2[(n-1)-\delta_\ell]^2} = -\frac{1}{2n^2} + \frac{3}{2}F_0 n(n-m-1)\ , \qquad 0.5 \le \delta_\ell \le 1.0. \qquad \text{(D.58)}$$

In equations D.57 and D.58, n is the principle quantum number of the closest hydrogenic manifold above the low ℓ state being considered and δ_ℓ is given $mod(1)$ such that $0 \le \delta_\ell \le 1$. If $n \gg 1$, then equation D.57 or D.58 can be solved for F_0 yielding

$$F_0 = \frac{2\delta_\ell}{3n^5}\ . \qquad \text{(D.59)}$$

At static field values greater than F_0, all the ℓ states are mixed together in the Stark manifold and ℓ is no longer a good quantum number for any value of ℓ.

At even higher values of F, near the Inglis - Teller limit, states from adjacent manifolds begin to interact. Unlike the hydrogenic case however, states from neighboring manifolds never cross. Instead, they experience "avoided crossings". Due to the pres-

ence of the atomic core, the reddest and bluest states do not lie completely on opposite sides of the atom. Classically, each state samples the side of the atom which is forbidden in the hydrogenic case [7]. The Kepler orbits do not close, and red states eventually become blue states, and vice versa.

D.2.3 Calculated Stark Maps

The full Hamiltonian for non-hydrogenic atoms in an electric field is not separable in parabolic coordinates. Neither ℓ, nor k is a good quantum number when F is above the Inglis - Teller limit. To properly determine the atomic energy levels, a perturbation matrix must be diagonalized [15] which contains all the states in every manifold. For computational reasons, the perturbation matrix is typically limited to all the manifolds within a given area of interest. Furthermore, since the parabolic eigenstates are no longer the eigenstates of the system, the advantage of separating the problem in parabolic coordinates is removed. Therefore, we return to the spherical $|n\ell m>$ basis to perform the integration.

The elements of the perturbation matrix are determined from

$$< n'\ell'm'|\hat{H}|n\ell m > \;\; = \;\; \delta_{n'n}\delta_{\ell'\ell}\delta_{m'm}E_{n\ell} \;\; + \;\; < n'\ell'm'|\vec{F}\cdot\vec{z}|n\ell m > \;\; . \qquad \text{(D.60)}$$

Equation D.60 can be separated into

$$< n'\ell'm'|\hat{H}|n\ell m > \;\; = \;\; -\frac{1}{2(n-\delta_\ell)^2} \;\; + \;\; F < n'\ell'|r|n\ell >< \ell'm'|cos(\theta)|\ell m > \;\; . \qquad \text{(D.61)}$$

The radial matrix elements $< n'\ell'|r|n\ell >$ are no longer trivial in the non-hydrogenic case. They are calculated numerically using a Numerov routine similar to the method of Zimmerman [16]. The angular matrix elements $< \ell'm'|cos(\theta)|\ell m > = < \ell'm'|C_0^1|\ell m >$ are unchanged from the hydrogenic case however and are given by [17]

$$< \ell'm'|C_0^1|\ell m > = (-1)^{m'}\sqrt{(2\ell'+1)(2\ell+1)} \begin{pmatrix} \ell' & 1 & \ell \\ 0 & 0 & 0 \end{pmatrix} \begin{pmatrix} \ell' & 1 & \ell \\ -m' & 0 & m \end{pmatrix}. \tag{D.62}$$

If we define the static field to be in the $\hat{z}$ direction, then only dipole transitions ($\Delta\ell = \pm 1$, $\Delta m = 0$) are possible. Therefore, equation D.62 reduces to

$$< (\ell+1)m|C_0^1|\ell m > = (-1)^m\sqrt{(2\ell+3)(2\ell+1)} \begin{pmatrix} \ell+1 & 1 & \ell \\ 0 & 0 & 0 \end{pmatrix} \begin{pmatrix} \ell+1 & 1 & \ell \\ -m & 0 & m \end{pmatrix}, \tag{D.63}$$

$$< (\ell+1)m|C_0^1|\ell m > = \sqrt{\frac{(\ell+1)^2 - m^2}{(2\ell+3)(2\ell+1)}}. \tag{D.64}$$

To create a non-hydrogenic Stark map, first all allowed matrix elements are calculated, then a Jacobian matrix diagonalization is performed for a given value of static field F [18]. The eigenvalues of the perturbation matrix are determined in the diagonalization routine. These are the eigenenergies of the system. In principle the diagonalization is straightforward, however if a Stark map is desired which covers a large number of n manifolds, diagonalization of a 1000 by 1000 element matrix may be required. Furthermore, to create the Stark map, the diagonalization must be performed for many values of F over the region of interest. The computational requirements

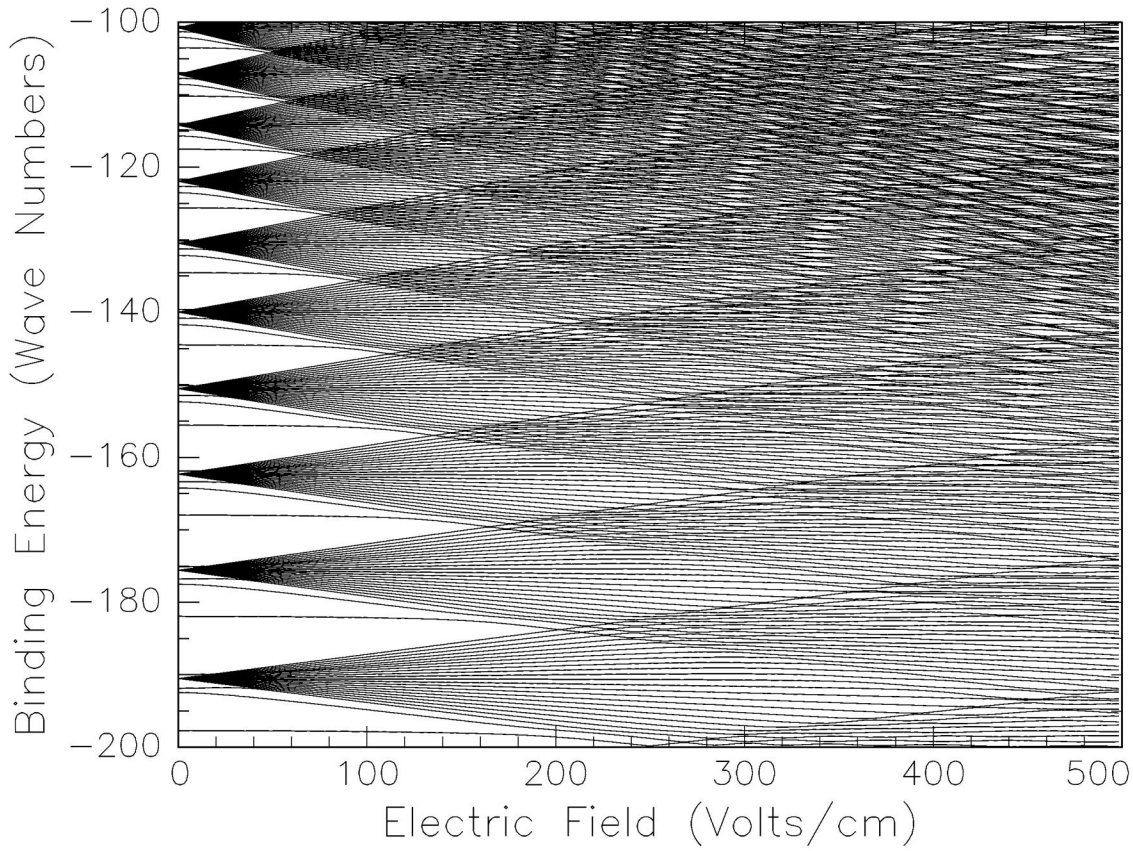

Figure D.4: A Stark map section of calcium ($m = 0$). All $|n\ell 0>$ states are included for $20 \leq n \leq 38$.

quickly become large. The resulting energy levels are only accurate in the region where direct field ionization does not occur.

Figure D.4 shows a section of a Stark map for calcium with $m = 0$. To reproduce the level structure for the range of energies in figure D.4 up to a field of $F = 500$ V/cm, it is necessary to include n values from $20 \leq n \leq 38$. When more states are included, the position of the energy levels at $F = 500$ V/cm shifts by less than 0.1

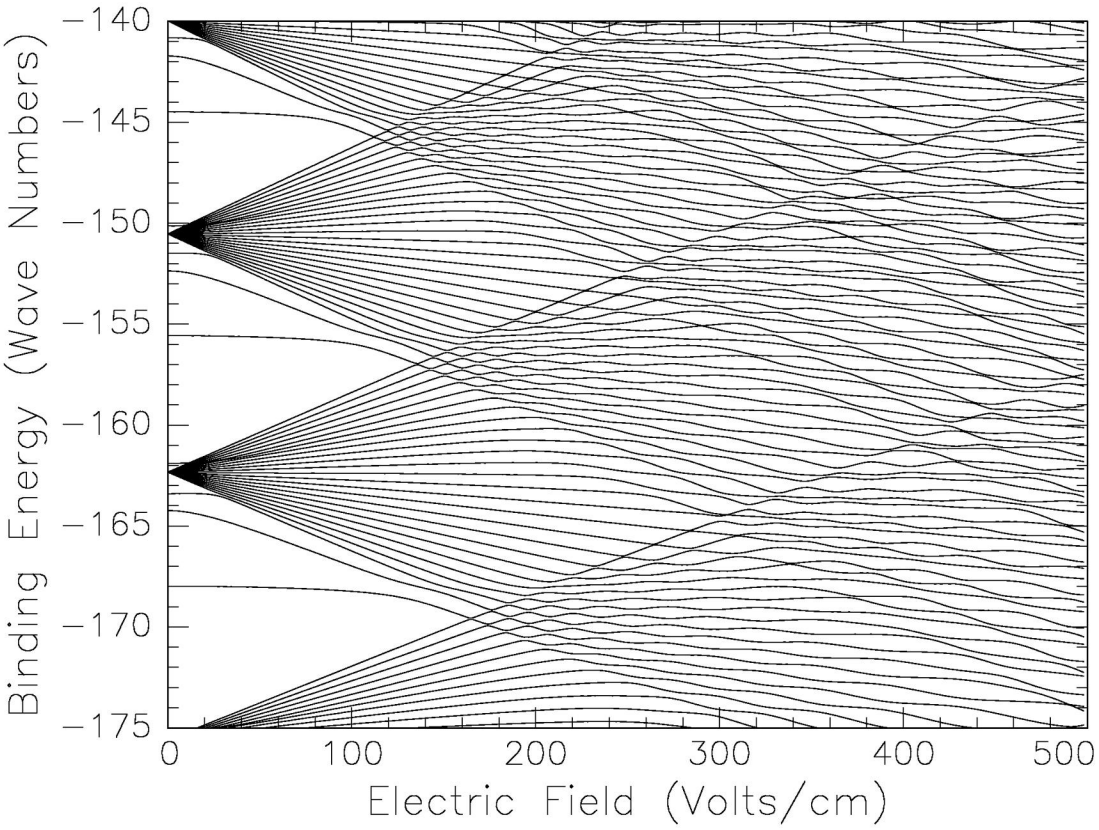

Figure D.5: Smaller region of the $m = 0$ Stark map of calcium that shows avoided level crossings.

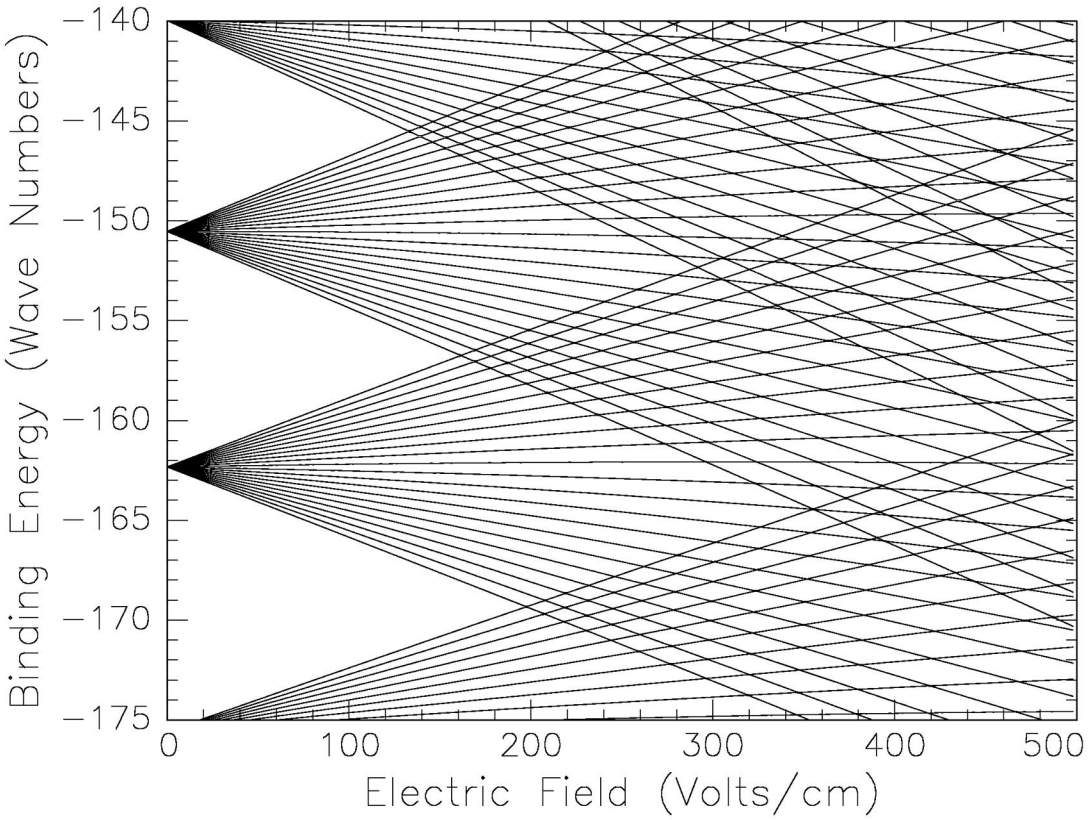

Figure D.6: Smaller region of the $m = 4$ Stark map of calcium. Due to the negligible quantum defects for $\ell > 3$ in calcium, the Stark map is essentially hydrogenic and no avoided crossings are seen.

cm^{-1}. The perturbation matrix for $20 \leq n \leq 38$ contains 551 states. In figure D.5, a smaller portion of the $m = 0$ Stark map is shown so that the avoided crossings can be seen in greater detail. For a given value of m, the allowed values of ℓ vary from $m \leq \ell \leq n - 1$. As the value of m is increased, low ℓ states are forbidden. Therefore, for $m \geq 3$, the Stark map appears essentially hydrogenic. Figure D.6 shows the same region of the Stark map as shown in figure D.5, but for $m = 4$ instead of $m = 0$. Note that all the avoided crossings have vanished. Classically this results from the fact that states with higher m values never come close enough to the atomic core to sample the small r deviation from the Coulombic potential. The behavior of these orbits therefore is entirely hydrogenic. This effect is explored experimentally in chapter 4. In that experiment, it is found that increasing the m value leads to hydrogenic behavior in a non-hydrogenic system.

It is possible to gain more information from the perturbation matrix generated by equation D.60 than just energy level positions. While the eigenvalues of the perturbation matrix determine the energy levels, the eigenvectors can be used to project out a given ℓ state character from the Stark map. Two examples of calculated Stark map sections with the oscillator strengths taken into account are shown in figures D.7 and D.8 for calcium with $m = 0$ and $m = 4$ respectively. Note the simple, hydrogenic nature of the $m = 4$ Ca Stark map compared to the much more complicated structure of the $m = 0$ Ca map. In figure D.7, the d state character is projected out to simulate

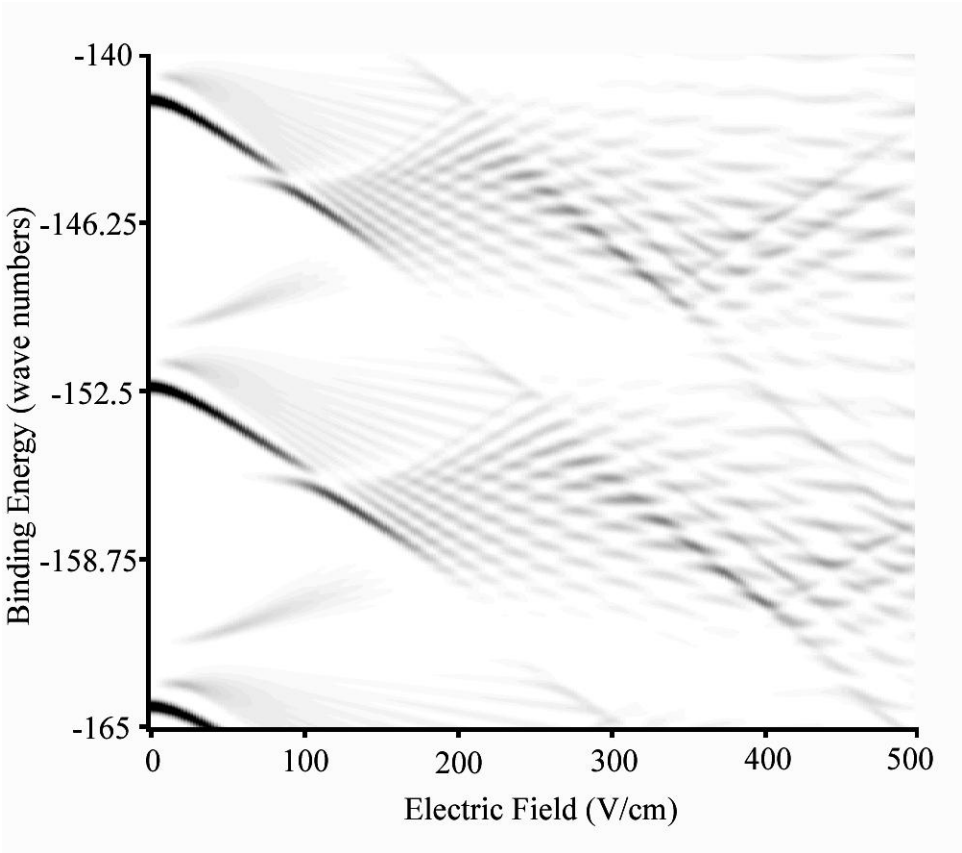

Figure D.7: A section of the $m = 0$ Stark map of calcium where the oscillator strengths have been included. The manifold is initially excited by populating the $\ell = 2$ (d) state, as is done in the experiments presented in chapter 5 and in [10]. Included in the calculation are states with $24 \leq n \leq 30$.

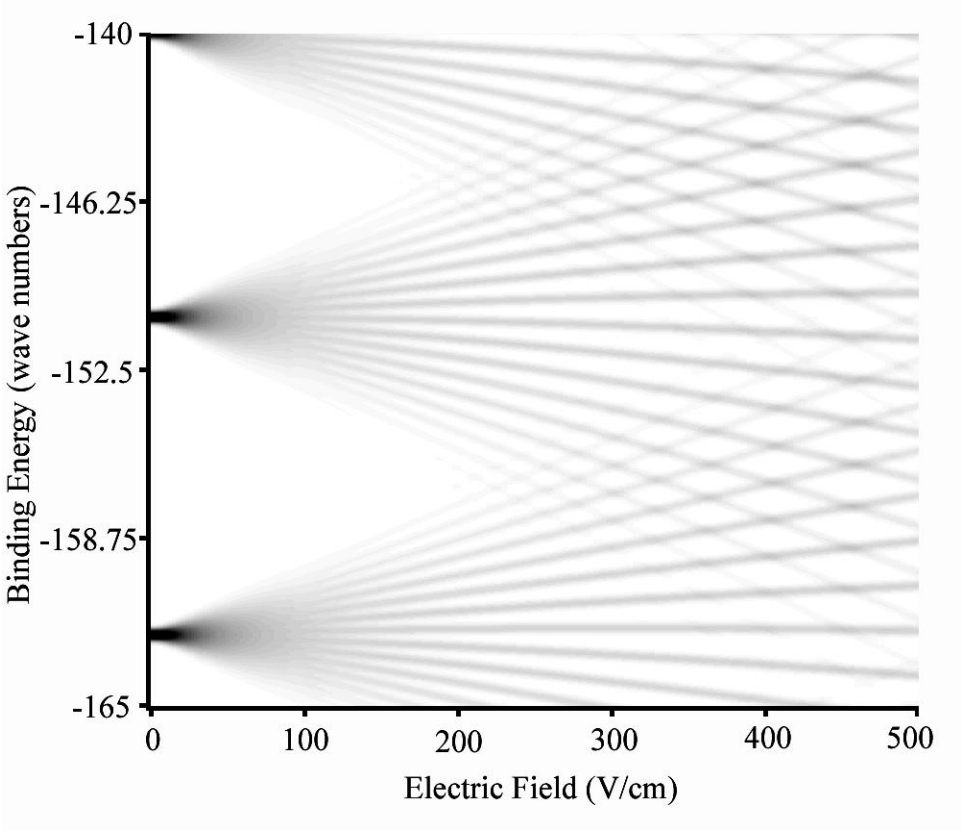

Figure D.8: A section of the $m = 4$ Stark map of calcium where the oscillator strengths have been included. Each of the ℓ states is populated equally. The behavior is essentially hydrogenic. Again, states with states with $24 \leq n \leq 30$ have been included in the calculation.

photoexcitation into the Stark Rydberg states from a p state. In figure D.8, all the high ℓ states are projected equally.

D.2.4 Conclusions

Even though the problem of a non-hydrogenic atom in an external electric field is not solvable in closed form, approximate positions of the energy levels and the associated oscillator strengths can be predicted through numerical and perturbative methods. Once the values of the quantum defects are known for a given atom, the analysis presented in this section can be applied to determine the energy levels and oscillator strengths. These techniques are applicable for electric fields weaker than the field ionization limit. Knowing the level positions and excitation probabilities is useful for understanding the dynamics of an atomic system. Care must be taken when trying to extend the techniques presented here out of their range of validity. As the field increases, other factors such as field ionization quickly become important [2].

Bibliography

[1] H.A. Bethe and E.E. Salpeter, *Quantum Mechanics of One and Two Electron Atoms*, Plennum Publishing Co., New York, (1977).

[2] T.F. Gallagher, *Rydberg Atoms*, Cambridge University Press, Cambridge, (1994).

[3] D. Kleppner, M.G. Littman, and M.L. Zimmerman, *Rydberg States of Atoms and Molecules*, R.F. Stebbings and R.B. Dunning *eds.*, Cambridge University Press, Cambridge, (1983).

[4] An extensive treatment of parabolic coordinates and DC Stark fields is presented in *Class Notes on Atomic Physics* by R.R. Jones.

[5] R.F. Stebbings and F.B. Dunning, *Rydberg States of Atoms and Molecules*, Cambridge University Press, Cambridge, (1983).

[6] Park, *Z. für Physik*, 155 (1960).

[7] T.P. Hezel, C.E. Burkhardt, M. Ciocca, and J.J. Leventhal, *Am. J. Phys.* **60**, 324 (1992).

[8] E. Luc-Koenig and A. Bachelier, *J. Phys. B* **13**, 1743 (1980).

[9] R. Freeman and D. Kleppner, *Phys. Rev. A* **14**, 1614 (1976).

[10] S.N. Pisharody, J.G. Zeibel, and R.R. Jones, *Phys. Rev. A* **61**, 063405 (2000).

[11] U. Fano, *Phys. Rev. A* **2**, 353 (1970).

[12] S.A. Bhatti, C.L. Cromer, and W.E. Cooke *Phys. Rev. A* **24**, 161 (1981).

[13] M.J. Seaton, *Rep. Prog. Phys.* **46**, 167, (1983).

[14] J.A. Armstrong, P. Esherick, and J.J. Wynne, *Phys. Rev. A* **15**, 180 (1977).

[15] M.G. Littman, M.L. Zimmerman, T.W. Ducas, R.R. Freeman, and D. Kleppner, *Phys. Rev. Lett.* **36**, 788 (1976).

[16] M.L. Zimmerman, *Phys. Rev. A* **20**, 225 (1979).

[17] A.R. Edmonds, *Angular Momentum in Quantum Mechanics*, Princeton University Press, Princeton, (1960).

[18] W.H. Press, S.A. Teukolsky, W.T. Vetterling, and B.P. Flannery, *Numerical Recipes in C, 2nd ed.*, Cambridge University Press, Cambridge, (1992).